

**Accurate and Reliable
Mobile Robots Localization
Based on
Secondary Radar
and
Multi-Modal Sensor Fusion**

**Genaue und zuverlässige Ortung
mobiler Roboter basierend auf
Sekundärradar und multimodaler Sensorfusion**

Der Technischen Fakultät
der Friedrich-Alexander-Universität
Erlangen-Nürnberg

zur
Erlangung des Doktorgrades Dr.-Ing.

vorgelegt von
Herrn Dipl.-Ing. Yassen Dobrev
aus Sofia, Bulgarien

Als Dissertation genehmigt
von der Technischen Fakultät
der Friedrich-Alexander-Universität Erlangen-Nürnberg

Tag der mündlichen Prüfung: 19.09.2018
Vorsitzender des Promotionsorgans: Prof. Dr.-Ing. Reinhard Lerch
Gutachter: Prof. Dr.-Ing. Martin Vossiek
Univ.-Prof. DI Dr. Andreas Stelzer

*Sometimes you win,
sometimes you lose.
learn*

John C. Maxwell

*You cannot connect the dots looking forward;
you can only connect them looking backwards.*

Steve Jobs

Abstract

Service robots are expected to rapidly grow in spread and importance in the years to come. Service robots are autonomous mobile robots performing useful tasks for humans, excluding manufacturing operations. Thus, they frequently operate in unstructured and dynamic indoor environments among humans.

A crucial prerequisite for the efficient and safe operation of such devices is the reliable and accurate localization. Although widely spread for global positioning and navigation, satellite-based technologies such as GPS cannot provide sufficient reliability and accuracy in many outdoor and virtually all indoor scenarios. As service robots frequently operate indoors, an alternative is needed. Many promising approaches have been demonstrated in the past, however, no technology has yet managed to reach mass-market adoption for indoor localization.

The aim of this work is to present a powerful alternative for indoor and outdoor local positioning based on secondary radar combining range and angle measurements. This combination allows for accurate and reliable localization with much less infrastructure compared to state-of-the-art multilateration and multiangulation techniques. This is thoroughly studied based on a frequency-modulated continuous-wave (FMCW) single-input multiple-output (SIMO) secondary radar. The theoretical limits on the achievable measurement accuracy are shown and analyzed in multiple experiments. The effect of intrinsic and extrinsic error sources on range and angle estimation accuracy is also studied.

An indoor localization system for healthcare service robots is developed using the proposed radar device. Using multi-modal sensor data fusion with an ultrasonic device and odometry, accurate and robust positioning is achieved and verified in three real-life scenarios. Another system for 6-degrees-of-freedom (DOF) service robot localization for planetary exploration missions based on the same concept is analyzed theoretically in terms of achievable accuracy. Measurement campaigns in three different scenarios show the advantages of the approach to combine range and angle measurements for 6-DOF localization. The versatility and flexibility of the proposed concept is also proved by a successful participation in the Microsoft Indoor Localization Competition 2016 and a UAV 3D localization experiment demonstration.

Zusammenfassung

In den nächsten Jahren ist ein starkes Wachstum im Bereich der Servicerobotik zu erwarten. Serviceroboter sind autonome mobile Roboter, die für Menschen nützliche Aufgaben ausführen, ausgenommen Industrieroboter. Sie agieren häufig in unstrukturierten, dynamischen Indoorumgebungen unter Menschen.

Eine entscheidende Voraussetzung für die effiziente und sichere Operation solcher Roboter ist die zuverlässige und genaue Ortung. Satellitenbasierte Technologien wie GPS können keine ausreichende Zuverlässigkeit und Genauigkeit in vielen Outdoor- und faktisch allen Indoorszenarien bereitstellen, obwohl sie weit verbreitet für globale Lokalisierung und Navigation sind. Da Serviceroboter oft im Indoor agieren, ist eine Alternative notwendig. Zahlreiche vielversprechende Ansätze wurden in der Vergangenheit demonstriert, jedoch konnte bis jetzt keine Technologie eine breite Verbreitung im Bereich der Indoorortung finden.

Das Ziel dieser Arbeit ist, eine leistungsfähige Alternative für Indoor- und Outdoorortung basierend auf Sekundärradar, das Abstands- und Winkelmessungen kombiniert, vorzustellen. Im Vergleich zu Multilaterations- und Multiangulations-Techniken nach dem Stand der Technik ermöglicht diese Kombination die Ortung mit viel geringeren Infrastrukturanforderungen. Basierend auf einem single-Input multiple-Output (SIMO) frequenzmodulierten Dauerstrich-Sekundärradar (FMCW-Sekundärradar) wurde dies gründlich untersucht. Die theoretischen Grenzen der erreichbaren Genauigkeit wurden aufgezeigt und in zahlreichen Experimenten analysiert. Der Einfluss der intrinsischen und extrinsischen Fehlerquellen auf die Abstands- und Winkelschätzungsgenauigkeit wurden ebenfalls studiert.

Basierend auf dem vorgestellten Radargerät wurde ein Indoorortungssystem für Krankenhaus-Serviceroboter entwickelt. Unter Einsatz von multimodaler Sensordatenfusion mit einem Ultraschallsensor und Odometrie konnte genaue und zuverlässige Ortung erreicht und in drei realen Szenarien demonstriert werden. Ein weiteres System zur Serviceroboterortung mit 6 Freiheitsgraden (DOF) für die Planetenerforschung basierend auf dem gleichen Konzept wurde bezüglich der erreichbaren Genauigkeit analysiert. Messkampagnen in drei verschiedenen Szenarien zeigen die Vorteile des Ansatzes, Abstands- und Winkelmessungen für 6-DOF-Ortung zu kombinieren. Die Flexibilität des vorgestellten Konzepts wurde auch durch die erfolgreiche Teilnahme an der Microsoft Indoor Localization Competition 2016 und ein Experiment zur 3D-UAV-Ortung demonstriert.

Preface / Vorwort

Diese Arbeit entstand während meiner Tätigkeit als wissenschaftlicher Mitarbeiter am Lehrstuhl für Hochfrequenztechnik der Friedrich-Alexander-Universität Erlangen-Nürnberg.

Herrn Prof. Dr.-Ing. Martin Vossiek danke ich für die Möglichkeit der Durchführung dieser Doktorarbeit an seinem Lehrstuhl und für die produktive Zusammenarbeit.

Herrn Univ.-Prof. DI Dr. Andreas Stelzer danke ich für die Bereitschaft, das Koreferat dieser Arbeit zu übernehmen.

Meiner Frau Kalina, meiner Familie und meinen Freunden danke ich für die Unterstützung. [На съпругата ми Калина, на моето семейство и на моите приятели благодаря за подкрепата.]

Ich danke noch folgenden ehemaligen, gegenwärtigen bzw. potentiell zukünftigen Kollegen: Dr.-Ing. Maximilian Pöpperl, Michael Gottinger und Martin Schütz für die zahlreichen fachlichen und überfachlichen Diskussionen; Johanna Geiß für die Zusammenarbeit an der Personenortung und dem LED-System; Denys Shmakov, Igor Bilous und Christoph Mammitzsch von der Symeo GmbH für die Radar-Hardware und -Software; Dr.-Ing. Tobias Gindele von der Robert Bosch GmbH und Matthias Lutz von der HS Ulm für die gute Zusammenarbeit im Projekt iserveU; dem LHFT Ortungsteam: Tatiana Pavlenko für die Antennen(arrays), Sergio Flores für das Ultraschallsystem, Christoph Reustle und Albert Marschall für die Diskussionen über Ortung; Dr.-Ing. Peter Gulden, CTO der Symeo GmbH für die Möglichkeit zu lernen; Melanie Lipka für das Mini-LPR; Fabian Kirsch für die Diskussionen über Kalmanfilter; Dr.-Ing. Gang Li für die Diskussionen über 3D räumliche Optimalfilter; Dr.-Ing. Randolph Ebelt für die Diskussionen über Phasenrauschen; Dr.-Ing. Haowei Wang für die Diskussionen über Schritterkennung; meinem Bruder, Yavor Dobrev für die UAV Messungen.

Und den Kollegen von meiner ersten abgebrochenen Promotion: Dr.-Ing. Pascal Volkert, Dr.-Ing. Daniel Schäfer und Prof. Dr.-Ing. Chihao Xu für die Zusammenarbeit an den OLED Treiberschemata und die schöne Zeit am Lehrstuhl für Mikroelektronik an der Universität des Saarlandes; Dr.-Ing. Tobias Jung, Dr.-Ing. Marc Albrecht, and the display team for the great time at Apple in Cupertino.

Yassen Dobrev
Nürnberg, 1. April 2018

Contents

1	Introduction	1
1.1	State of the Art of Positioning Technology	2
1.2	Multilateration vs. RTOF + DOA	7
1.3	Outline and Contribution of this Work	9
2	24 GHz FMCW SIMO Secondary Radar	11
2.1	Operating Principle and Signal Model	11
2.2	Hardware Description	16
2.3	Distance Measurement	18
2.3.1	Ranging Precision in Ideal Environment	18
2.3.1.1	Phase Noise	18
2.3.1.2	AWGN	22
2.3.1.3	Measurement Results	26
2.3.2	Ranging Accuracy in a Long Narrow Corridor	27
2.4	Direction of Arrival Estimation	31
2.4.1	3D Spatial Matched Filter	31
2.4.2	Antenna Arrays	34
2.4.3	Efficient Implementation	36
2.4.3.1	Grid-Based Processing (Brute Force / Exhaustive Search)	37
2.4.3.2	Solution with the Gauss-Newton Algorithm	37
2.4.3.3	Comparison	39
2.4.4	CRLB	41
2.4.5	Calibration	42
2.4.5.1	Signal Model	42
2.4.5.2	Simulation	43
2.4.5.3	Measurement Results	48
2.4.6	Ring Array	53
2.5	3D RTOF + DOA Positioning	57
2.5.1	Unbiased Estimator	57
2.5.2	CRLB for 3D RTOF + DOA Positioning	59
2.5.3	Measurement Results	62

3 Probabilistic Sensor Fusion for Mobile Robot Localization Applications	69
3.1 Bayes Filter	69
3.2 Kalman Filter	71
3.3 Extended Kalman Filter (EKF)	72
3.4 Geometric Interpretation of the Covariance Matrix	74
4 iserveU: Health-Care Service Robot Indoor Positioning	77
4.1 Motivation	77
4.2 WLPS for Healthcare Service Robots	79
4.3 System Overview and Prerequisites	80
4.4 State Vector and Motion Model	84
4.5 Fusing Static Radar Node Measurements	89
4.5.1 Using Elevation to Support Distance Estimation	91
4.5.2 2D EKF for Static Radar Node Measurements	92
4.5.3 1D EKF for Static Radar Node Measurements	97
4.6 Fusing Mobile Radar Node Measurements	98
4.7 Fusing Ultrasonic Measurements	104
4.7.1 Wall-Finding Ultrasonic Sensor	104
4.7.2 Ultrasonic Virtual Tag	104
4.7.3 EKF for Ultrasonic Sensor	107
4.8 Using Mahalanobis Distance to Improve Reliability and Integrity	112
4.9 Initialization / Kidnapped-Robot Case	115
4.10 Relative Positioning of a Person	115
4.11 System Implementation	122
4.12 Results	125
4.13 Hybrid Localization	135
4.14 Conclusion	136
5 TransTerrA: 6 DOF Mobile Robot Localization for Planetary Exploration	137
5.1 Motivation	138
5.2 Comparison of Positioning Techniques	139
5.2.1 Multilateration	140
5.2.2 Multiangulation	144
5.2.3 RTOF+DOA	145
5.3 EKF for 6 DOF Positioning	150
5.3.1 Motion Model	150
5.3.2 EKF for 3D Position	152
5.3.3 EKF for 3D Orientation	154
5.3.4 System Implementation	159
5.3.5 Results	159
5.4 Conclusion	165

6 Further Applications	167
6.1 Microsoft Indoor Localization Competition	167
6.2 UAV Localization	171
6.2.1 CRLB	173
6.2.2 Results	173
7 Conclusion and Outlook	177
A Geometric Functions	179
A.1 Euclidean Distance	179
A.2 Angle	179
A.3 Wrap Angle	180
A.4 Basis Transformation	180
B Evaluation of Positioning Systems	183
B.1 3D Position	183
B.2 3D Orientation	184
B.3 Quantifying Positioning Quality	185
B.4 CRLB and DOP	188
List of Student Theses Supervised	191
Bibliography	193
CV	209

Acronyms

ADC	Analog-to-Digital Converter
AGV	Automated/Autonomous Ground Vehicle
AMCL	Adaptive Monte Carlo Localization
AOA	Angle of Arrival
AWGN	Additive White Gaussian Noise
CCD	Charge-Coupled Device
CMKF	Converted Measurements Kalman Filter
COTS	Commercial Off-The-Shelf
CRLB	Cramér-Rao Lower Bound
DFT	Discrete Fourier Transform
DGPS	Differential Global Positioning System
DOA	Direction of Arrival
DOF	Degree of Freedom
DSP	Digital Signal Processing
DWNA	Discrete White Noise Acceleration model
EDM	Electronic Distance Measurement
EKF	Extended Kalman Filter
FDM	Frequency Division Multiplexing
FFT	Fast Fourier Transform
FIM	Fisher Information Matrix
FMCW	Frequency-Modulated Continuous-Wave
FPGA	Field-Programmable Gate Array
FSCW	Frequency-Stepped Continous Wave
FSK	Frequency-Shift Keying
FSPL	Free-Space Path Loss
GNSS	Global Navigation Satellite System
GPS	Global Positioning System

IF	Intermediate Frequency
IMU	Inertial Measurement Unit
IR	Infrared
ISM	Industrial, Scientific, Medical
ITA	Intelligent Transport Assistant
LADAR	LAser Detection And Ranging
LED	Light Emitting Diode
LiDAR	Light Detection and Ranging
LNA	Low-Noise Amplifier
LO	Local Oscillator
LOS	Line of Sight
LPR	Local Positioning Radar
LPS	Local Positioning System
LUT	Lookup Table
MBW	Mainlobe Beamwidth
MC	Monte Carlo Simulation
MCL	Monte Carlo Localization
MCU	Microcontroller Unit
MOPSO	Multi-Objective Particle Swarm Optimization
MP	Multipath
NLOS	Non-Line of Sight
PLL	Phase-Locked Loop
QR	Quick Response
RF	Radio Frequency
RFID	Radio-Frequency IDentificationa
RGB-D	Red, Green, Blue, Depth
RMSE	Root-Mean-Square Error
ROS	Robot Operating System
RSS	Received Signal Strength
RTK	Real Time Kinematic
RTOF	Round-Trip Time of Flight
Rx	Receive
SDS-TWR	Symmetrical Double-Sided Two-Way Ranging
SIMO	Single-Input Multiple-Output

SLAM	Simultaneous Localization and Mapping
SLL	Sidelobe Level
SNR	Signal-to-Noise Ratio
SPI	Serial Peripheral Interface
TDM	Time Division Multiplexing
TDOA	Time Difference of Arrival
TOA	Time of Arrival
TOF	Time of Flight
Tx	Transmit
UAV	Unmanned Aerial Vehicle
UWB	Ultra-Wideband
VCO	Voltage-Controlled Oscillator
WLPS	Wireless Local Positioning System

1 Introduction

With the onset of artificial intelligence, autonomously operating machines will become an integral part of our daily life. While self-driving cars are still in active research [1], the sector of service robotics is already developing rapidly with an annual growth of 20-30 % [2]. One of the main challenges for safe and robust context-aware service robots is the accurate and reliable localization, which is imperative for successful navigation.

An example, where service robots are being successfully employed, is the area of logistics [3], where local positioning systems enable autonomous mobile robots to transport goods in warehouses, factories, and harbors. Another novel use case with great potential are healthcare service robots for repetitive transportation tasks in hospitals like the one shown in Fig. 1.1.

Service robots frequently need to operate among humans and other robots, in indoor or in cramped outdoor environments. These scenarios pose a serious challenge for the state-of-the-art positioning technologies. The aim of this work is to explore secondary radar combining range and angle measurements as an alternative.



Fig. 1.1: Intelligent Transport Assistant (ITA) for transportation tasks in hospitals, developed in the project iserveU (see Chapter 4).

1.1 State of the Art of Positioning Technology

GNSS Probably the most well-known and wide-spread positioning technology is the global positioning system (GPS), which is one of several available global navigation satellite systems (GNSS). The 3D position of a receiver can be determined by receiving a signal from at least 4 GPS satellites based on the time-of-arrival (TOA) measurement principle and trilateration. The satellites must be accurately synchronized and for this reason are equipped with expensive high-precision atomic clocks. The receiver on the other hand can use cheaper clocks since its clock bias can also be estimated from the measurements [4]. GPS thus provides global coverage with an accuracy of a few meters using low-cost receivers.

In order to improve the accuracy, a static reference receiver at precisely known coordinates can additionally be employed to compensate for common-mode errors e.g. caused by the signal propagation through the atmosphere. This technology is known as differential GPS (DGPS) [5] and has a typical accuracy in the range of 10 cm. Real Time Kinematic (RTK) satellite navigation further uses the signal carrier wave's phase to reach an accuracy of 1 cm. Using multiple receivers and tightly-coupled sensor fusion, it is also possible to estimate the heading, mitigate multipath effects and reach accuracies of less than 1 cm under favorable conditions [6].

The inherent drawback of GNSS is that at least 4 satellites need to be visible at any moment to provide a position estimate. This problem can be mitigated by fusing the (D)GPS measurements with vehicle motion sensors such as inertial sensors or odometers when the satellite signal is shortly unavailable [5]. This is the case in cities, where tall buildings can shadow the signal or cause multi-path reflections (urban canyons). Indoor environments will also remain out of reach for GPS due to signal attenuation and reflection, even if high-sensitivity receivers are employed [7]. Extraterrestrial exploration missions represent another scenario where an alternative positioning system is needed, as no GNSS are available on other planets or moons.

As evident from this example, GNSS is not able to provide accurate and reliable positioning in several situations, which are particularly interesting for autonomously operating mobile robots. An alternative for indoor or high-precision outdoor scenarios is provided by local positioning systems (LPS). The following sections outline some of the available concepts.

Ultrasound Ultrasound propagates as a mechanical wave causing oscillation of the particles in a given medium. It has a frequency beyond that of audible sound, i.e. beyond 20 kHz. Some animals, e.g. bats and dolphins use it for echolocation to locate and identify objects and prey. Due to the relatively low frequencies, it

is also rather inexpensive to realize in hardware.

Many local positioning systems based on ultrasound have been presented in the past. In one of the earliest attempts, the Active Bat system [8], a mobile beacon is triggered via a radio signal to send an ultrasonic pulse to a grid of static receivers. The receivers are reset by a wired signal at the same time as the radio signal is sent. As electromagnetic waves travel approximately 6 orders of magnitude faster than acoustic waves, the TOA at the receivers can be determined by measuring the time interval between the reset signal and receiving the ultrasonic pulses. The 3D position of the beacon can then be determined by multilateration after converting the TOA to ranges using the known propagation speed of sound.

The ultrasonic system Cricket developed by the MIT Laboratory for Computer Science also provides 3D indoor localization [9]. In contrast to Active Bat, it relies on static emitters and mobile receivers, enabling decentralized positioning. The positioning is again based on TOA measurements and multilateration.

While both systems feature excellent accuracy in the range of a few centimeters, they have several drawbacks inherent to ultrasound. Due to the impedance mismatch between air and standard piezoelectric materials and the high signal attenuation in air [10], the maximum operating range of ultrasonic systems is limited to approximately 10 m. This means, that many sensors are necessary to cover larger areas as e.g. in [11], which leads to high installation and maintenance cost. Multipath propagation can also decrease the positioning performance. An additional error source is the speed of sound in air which is dependent on the temperature. Furthermore, certain everyday actions performed by humans indoors such as typing on a keyboard generate ultrasound which can interfere with the positioning signals [12].

Camera Since vision is the dominant sense of humans, which we also use for navigation, it is natural to attempt to use cameras and computer vision algorithms for positioning [13]. Using a single camera, only the angles to an object in the scene can be determined. Employing additional cameras, also the distance to an object can be measured using triangulation. However, the accuracy is dependent on the distance between the cameras, which is unfavorable for mobile applications.

There exist several approaches to camera-based positioning [14]. Some systems try to detect landmarks with known locations in the environment and then perform triangulation to find the position of the camera. This has the advantage that no additional infrastructure is needed. Other systems use markers instead (quick-response (QR) codes, light-emitting diodes (LED) or other coded

targets), which increases the robustness of the system, but requires that the environment is equipped with markers beforehand [15]. Such systems provide dm to cm accurate localization [16]. The commercially available system OptiTrack [17] relies on multiple static cameras surrounding a test volume. The cameras can recognize and track markers, which enables tracking the 3D position and 3D orientation of an object in the test volume with sub-millimeter accuracy for optimal configurations.

Structured-light cameras also pose a powerful localization concept. By projecting an infrared (IR) pattern and analyzing its geometrical distortion due to the reflection on objects, such cameras provide RGB-D (Red, Green, Blue, Depth) data. By matching it to a known map or by performing SLAM (Simultaneous Localization and Mapping) it is possible to determine the position of a mobile robot. One popular example is the Microsoft Kinect camera [18]. A structured-light camera is also used in the now deprecated Google Project Tango [19].

Due to the falling prices of computing power and charge-coupled device (CCD) sensor chips, camera-based positioning systems are becoming increasingly attractive. However, the maximum measurement range is relatively low, depending on the size of the markers being used. Moreover, the performance can deteriorate in very dark or very bright environments depending on the operation principle. Fog, rain and dust also have severe negative impact on optical systems.

Laser Scanner Laser scanners (or LiDAR/LADAR – Light Detection and Ranging / LAser Detection And Ranging), e.g. the popular commercially available systems of the companies SICK [20] and Velodyne [21] are another example of a powerful scanning system, which can be used for localization. The distance to an object can be determined by measuring the round-trip time-of-flight (RTOF) of a pulsed infrared laser beam from the emitter to the object and back to the receiver. A 2D or 3D point cloud representation of the environment can be obtained by additionally employing a rotating mirror and/or multiple channels [22]. The measured point cloud can then be matched to a map to perform localization by using e.g. Monte Carlo Localization (MCL) [23], freely available in the amcl package of the robotic framework ROS [24].

While such systems achieve excellent accuracy in the range of 1 cm [25] and provide a map of their surroundings, which is especially important for navigation and collision avoidance, they also have some inherent drawbacks. They can become unreliable in dynamic environments when the map changes. Bars and rods can remain undetected due to the limited angular resolution of the laser scanner, which can lead to collisions. Glass doors and windows can also be

problematic depending on the laser wavelength used. As simpler laser scanners only perform a 2D scan in a plane, many objects with strongly varying profile in height can pose a problem. For example, only a table's legs and not the plate will be detected, which can lead to collisions. Using additional lasers in elevation direction is technically possible, but expensive. The relatively high cost and the mechanically moving parts can also limit the use of laser scanners in many applications. Similar to other optical systems, their performance can quickly deteriorate, when dust, fog or rain are present.

Received Signal Strength The strength of an electromagnetic wave diminishes by the power of two of the traveled distance due to free-space path loss (FSPL). Most commercial off-the-shelf (COTS) radio chips provide received signal strength (RSS) values for the received signals. Thus, in theory, the range between the transmitter and the receiver can be calculated from the RSS based on a signal-propagation model. This is utilized e.g. in the SpotON positioning system [26] using a multilateration approach with several transmitters at known locations. Another option is to use a technique called “fingerprinting”, where a radio map of a building is created. The measured RSS values are then matched to the map to determine the receiver position as in Microsoft’s system called “RADAR” [27]. Such maps, however, need to be frequently updated to account for any changes in the environment, such as adding or removing furniture.

RSS-based positioning is very attractive due to its simplicity and due to the fact, that it can use already available infrastructure, such as Wi-Fi access points and COTS components. However, it has inherently poor accuracy, as the signal strength is strongly influenced by multipath reflections at walls and furniture. Typical reported accuracies lie in the range of several meters [28] which is insufficient for indoor navigation.

Ultra-Wideband and FMCW Due to the extensive research performed in the area of GNSS, most microwave-based wireless local positioning systems (WLPS) are also based on the time-of-arrival (TOA) or time-difference-of-arrival (TDOA) measurement principles [29]. Such systems in general consist of multiple static devices at known positions distributed across the measurement area (instead of satellites in space) and one or more mobile devices.

As the range estimation accuracy and resolution is in general proportional to the signal bandwidth, multiple localization systems based on ultra-wideband (UWB) signals have been proposed and several have made it to commercial products [30]. A system is referred to as UWB, when its bandwidth is more than 20 % of its center frequency or over 500 MHz in the USA or over 50 MHz in Europe [31]. One such system is Zebra Technologies’ [32] Dart UWB sys-

tem. It comprises multiple static Dart Sensors, which are synchronized over a wired connection. Using UWB pulses in the frequency range from 5.94 GHz to 7.12 GHz, it is capable of locating a large number of active RFID tags using the TDOA measurement principle with an accuracy of 30 cm [33]. Another example is Time Domain's¹ PulsON UWB chip series [34] with a range measurement accuracy of 5 cm [35]. Ubisense's [36] smart space platform also uses UWB pulses, but combines TDOA with angle-of-arrival (AOA). Using this approach only 2 measurements are necessary for 3D positioning (instead of 4 without AOA) [37]. Nanotron Technologies' nanoLOC system uses symmetrical double-sided two way ranging (SDS-TWR) to estimate the distance between two wireless nodes operating in the 2.4 GHz ISM band. The reported accuracy is better than 1 m [38]. A popular low-cost solution is DecaWave's [39] ScenSor DW1000 chip, which is compliant to the IEEE 802.15.4-2011 UWB standard. With a bandwidth of 500-900 MHz using two-way ranging its accuracy in range is below 10 cm even in indoor scenarios [40].

The Locata system is another example of a WLPS designed to enable localization at places where GPS is not available [41]. Using a network of time-synchronized transmitters (pseudolites) and GNSS-similar localization principles it achieves accuracies in the range of 1-10 cm by also utilizing the carrier phase.

The company Abatec's [42] LPM (local position measurement) system uses a frequency-modulated continuous-wave (FMCW) radar in the 5.8 GHz industrial, scientific, medical (ISM) band to locate a car on a race track. By arranging several static base stations around the measurement site and using a reference transponder at a known position to synchronize them, the position of a mobile transponder can be estimated based on TDOA and multilateration. The reported accuracy is 10 cm up to a range of 500 m [43]. The company Symeo² [44] also uses FMCW in its RTOF local positioning radar (LPR[®]) devices [45]. A wireless local positioning system (WLPS) for container terminal logistics using Symeo's LPR[®] combining inverse TDOA (ITDOA) and RTOF is presented in [46].

UWB systems can achieve very good accuracy, since the range resolution is in general proportional to the bandwidth. This is especially important in indoor applications to mitigate the effect of multipath reflections. However, the transmit power of UWB systems is limited by legal radiation regulations. This is necessary to prevent interference on existing communication systems [31]. Due to the relatively low power of UWB systems, their maximum measurement range is in general limited to a few tens of meters.

¹ Acquired by 5D Robotics in 2016 and by Humatics Corp. in 2018.

² Symeo GmbH was acquired by Analog Devices, Inc. in 2018.

Interim Conclusion As the previous sections show, a broad range of technologies are being used for localization. They utilize a wide band of the electromagnetic spectrum, starting from radio waves and microwaves in the MHz/GHz range and going up to infrared and visible light in the THz range. Mechanical waves such as sound and ultrasound in the kHz range are also being used. However, none of the proposed systems has yet managed to reach mass market adoption, but have mostly remained niche products for specific applications.

This list of positioning systems is in no way complete, but barely attempts to give an overview of the problem of positioning from different perspectives. More thorough surveys can be found in [16], [29], [47], and [48]. Dead-reckoning positioning systems based for example on inertial measurement units (IMU) are not discussed in this work as they have limited accuracy and reliability due to accumulated error caused by sensor bias and drift.

The fact that none of the technologies mentioned in Section 1.1 provides a universal solution for the positioning problem demonstrates its complexity. While certain systems provide very good accuracy, their cost and requirement for complex infrastructure is a limiting factor. Other systems are cheap and simple, but their accuracy or measurement range is insufficient for many applications. This suggests, that a combination of multiple sensor types with complementary properties could outperform a system based on a single technology. Furthermore, a cost reduction and a broader adoption could be achieved by reducing the infrastructure required by the localization system.

1.2 Multilateration vs. RTOF + DOA

The overview in Section 1.1 shows that the vast majority of positioning systems is based on the multilateration positioning principle. As shown in Fig. 1.2 (a), this method can be used to determine the position of a mobile node (Node 0) relative to several static nodes at known positions (Node 1...3). Multilateration can be applied to both 2D and 3D positioning problems based on measurements to at least 3 resp. 4 static nodes³. It can be used in conjunction with the RTOF, TOA, TDOA and RSS measurement principles.

For RTOF and TOA, the distance $d_n = c_0 \cdot \tau_n$ between the mobile node and the static node n can be determined from the time a signal needs to travel the distance between the nodes τ_n and the speed of propagation c_0 . From geometric considerations the mobile node then lies on the intersection point of circles (or spheres in the 3D case) around the static nodes. The same principle applies for RSS, with the difference that the signal attenuation instead of

³Excluding the case of degenerated layouts, e.g. when the static nodes lie on a straight line.

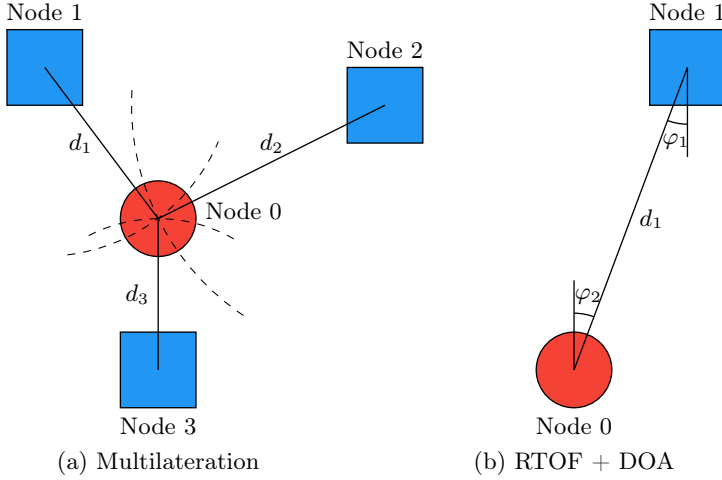


Fig. 1.2: Positioning based on (a) Multilateration; (b) RTOF combined with DOA.

the time-of-flight is evaluated to determine d_n . For TDOA, the distance difference $d_{n,m}$ from the mobile node to the static nodes n and m is derived from the difference of the traveled times. The mobile node position is then on the intersection of hyperbolas (or hyperboloids in the 3D case) around the static nodes [49]. As real measurements rarely intersect in a point and for the case of over-determined measurement constellations, the problem can be solved e.g. by using least-squares optimization [50].

While multilateration allows for precise localization by only using relatively simple range-measuring sensors, it has some inherent drawbacks. Multiple nodes are necessary to determine the target position. Hence, complex infrastructure is required and there is high installation and maintenance cost and effort if a large area needs to be covered. Furthermore, this leads to lower reliability, as multiple measurements to different units are required to obtain a single estimate for the target position. This means that if the measurement to one of the static nodes fails, e.g. due to missing line-of-sight (LOS) or due to multipath fading, no positioning can be performed⁴. This problem can be mitigated by carefully choosing the static nodes' positions or by simply increasing their number. This is already being done in GPS-based positioning systems by incorporating the

⁴Assuming that only 3 or 4 nodes are available for 2D or 3D positioning, respectively.

satellites of other GNSS systems to increase the reliability e.g. in urban canyons.

An alternative solution for localization is shown in Fig. 1.2 (b). It is based on the combination of the RTOF and the direction-of-arrival (DOA) measurement principles. Using this approach, it is possible to determine the 2D position of Node 0 by performing a single RTOF+DOA measurement, thus determining the distance d_1 and the azimuth angle φ_1 (3D positioning is possible by additionally measuring the elevation angle ϑ_1). This means that only a single static node and a single measurement is sufficient for a 2D or 3D position estimate. Furthermore, by measuring the azimuth angle φ_2 to Node 1, Node 0 can determine its orientation in 2D (the measurement of both the azimuth and the elevation angles to at least two static nodes is necessary for the complete 3D orientation).

As this system concept reduces the required number of static nodes (and thus the system cost) and increases the reliability, it will be examined in this work based on several application scenarios.

1.3 Outline and Contribution of this Work

This work is organized as follows:

Chapter 1 gives a short overview of the state-of-the-art of localization technology with focus on local positioning. A simple comparison between the proposed concept of combining RTOF and DOA measurements and the classic multilateration and multiangulation approaches is made.

In Chapter 2, the secondary FMCW radar device used is presented and examined. The intrinsic (noise, calibration) and extrinsic (multipath) error sources are analyzed in theory and in experiments. The achievable positioning accuracy in 3D using only 2 radar devices is derived and demonstrated.

Chapter 3 provides an overview of the basics of probabilistic sensor fusion with focus on mobile robot localization.

In Chapter 4, a 3 degrees of freedom (DOF) local positioning system for healthcare service robots based on the approach from Chapter 2 and multimodal sensor data fusion with further complementary sensors is presented. Using a demonstrator system capable of real-time operation, it is shown that the proposed concept achieves very good accuracy and reliability with minimum infrastructure in three challenging real-life indoor scenarios. Large portions of this chapter have been submitted in the form of two journal papers to IEEE Access [51] and IEEE Transactions on Microwave Theory and Techniques.

Chapter 5 presents another application where a mobile robot for space exploration applications is located with 6 DOF. A comparison of the expected accuracy of the proposed approach and state-of-the-art multilateration and multiangulation is performed. The feasibility of the concept is demonstrated in three

realistic scenarios.

Chapter 6 presents two further applications proving the versatility and flexibility of the presented approach. The successful participation in the Microsoft Indoor Localization Competition 2016 shows the effectiveness of the approach, as the proposed system outperformed others, which used a much larger bandwidth. Accurate 3D localization of a UAV is also demonstrated.

Chapter 7 concludes the work with some final comments and an outlook.

Appendix A defines several geometric functions frequently used throughout this work. Appendix B contains some remarks regarding the evaluation of positioning systems.

2 24 GHz FMCW SIMO Secondary Radar

This work is based on an 8-channel single-input multiple-output (SIMO) FMCW secondary radar operating in the 24 GHz ISM band with a bandwidth of 250 MHz. The FMCW radar waveform is widely used and well-known as it, among others, allows for relatively easy hardware implementation, requires low baseband bandwidth and low peak power, and also has relatively good resistance to interference [52]. Using a secondary radar has the advantage that the SNR depends with $1/R^2$ with range R opposed to $1/R^4$ for primary radar. The radar used here was developed by the company Symeo GmbH and is based on the Local Positioning Radar (LPR[®]) measurement principle.

2.1 Operating Principle and Signal Model

The radar system consists of at least two secondary SIMO FMCW radar nodes. Each node has N receive (Rx) channels and 1 transmit (Tx) channel. The generic measurement geometry is depicted in Fig. 2.1. Assuming a common global coordinate system, the 3D positions of Rx antenna n of radar node m is given by the vector $\mathbf{r}_{\text{Rx},m,n}$; that of the Tx antenna by $\mathbf{r}_{\text{Tx},m}$. Both radars are identically constructed in hardware and software. They need to be coarsely pre-synchronized in time before the measurement cycle in order to obtain an intermediate frequency (IF) within the passband of the baseband filter. This is done over an IEEE 802.15.4 link or over frequency-shift keying (FSK) communication in the 24 GHz band. The achieved pre-synchronization accuracy is in the range of $\Delta t = \pm 100$ ns [53].

The system is based on signals with linear frequency modulation with a lower frequency f_1 , duration T , and bandwidth B . The resulting sweep rate is denoted as $\mu = B/T$. During each measurement cycle one node assumes the role of a master and the second node that of a slave as illustrated in Fig. 2.2.

Synchronization The master initiates the measurement cycle at time $t = t_0$ by sending an upsweep from f_1 to $f_1 + B$ and a subsequent downsweep back to f_1 . At time $t = t_0 + \Delta t$ the slave's local oscillator (LO) generates a local upsweep and downsweep pair with the same parameters, but with an additional frequency offset of $f_a + \Delta f$. The term f_a is a known additional offset included to ensure a positive frequency after mixing and to ensure that the primary radar responses

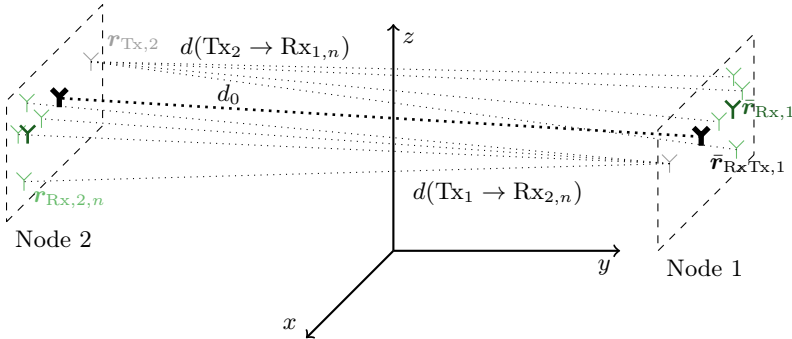


Fig. 2.1: Measurement geometry with $N = 4$ Rx antennas. The Rx antennas in node m with coordinates $\mathbf{r}_{Rx,m,n}$ are denoted by thin green antenna symbols Υ ; the Tx antennas $\mathbf{r}_{Tx,m}$ by thin grey Υ . The thick green Υ denotes the centroid $\bar{\mathbf{r}}_{Rx,m} = \frac{1}{N} \sum_{n=1}^N \mathbf{r}_{Rx,m,n}$ of the Rx antenna array of node m . The thick black Υ signifies the Rx/Tx centroid $\bar{\mathbf{r}}_{RxTx,m} = \frac{1}{2}(\bar{\mathbf{r}}_{Rx,m} + \mathbf{r}_{Tx,m})$.

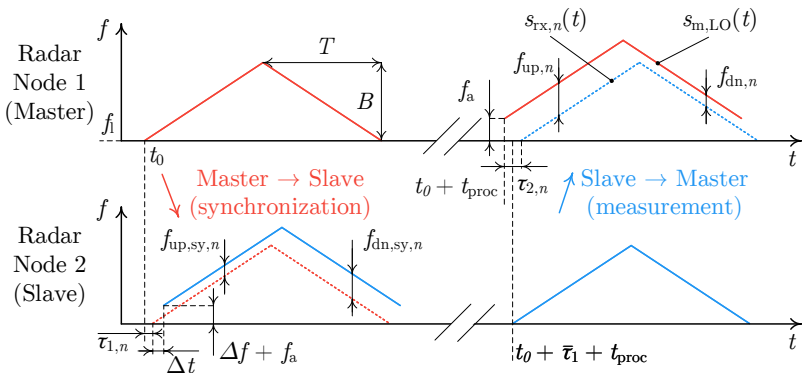


Fig. 2.2: LPR[®] operation principle: synchronization and measurement sequence. Not to scale.

don't overlap with the secondary signals. The terms Δt and Δf account for the fact, that both devices are only coarsely synchronized in time and frequency and can be either positive or negative.

As can be seen in Fig. 2.1, after the propagation time

$$\tau_{1,n} = \frac{d(\text{Tx}_1 \rightarrow \text{Rx}_{2,n})}{c_0} = \frac{\|\mathbf{r}_{\text{Rx},2,n} - \mathbf{r}_{\text{Tx},1}\|}{c_0} \quad (2.1)$$

the master FMCW ramps are received by the slave Rx channels and mixed with the LO sweeps. $\|\cdot\|$ denotes the Euclidean norm (cf. Appendix A.1). After low-pass filtering, two baseband signals are obtained from the two FMCW ramps in every channel n . The frequencies $f_{\text{up,sy},n}$ and $f_{\text{dn,sy},n}$ of these signals can be determined e.g. by using the fast Fourier transform (FFT). As shown in [54], these are used for very precise synchronization between the master and the slave node with respect to time and frequency by calculating the unknown offsets Δt and Δf for time and frequency by

$$\begin{aligned} \Delta t &= \frac{f_{\text{dn,sy},n} - f_{\text{up,sy},n}}{2\mu}, \\ \Delta f &= \frac{f_{\text{dn,sy},n} + f_{\text{up,sy},n}}{2} - f_a. \end{aligned} \quad (2.2)$$

As the time and frequency offsets Δt and Δf are equal in all Rx channels, the baseband signals can be combined to obtain an averaged estimate using the estimators presented in Section 2.3.1.2. The slave node is hence precisely synchronized relative to the point in time $t_0 + \bar{\tau}_1$ with

$$\bar{\tau}_1 = \frac{1}{N} \sum_{n=1}^N \tau_{1,n} = \frac{\|\bar{\mathbf{r}}_{\text{Rx},2} - \mathbf{r}_{\text{Tx},1}\|}{c_0}. \quad (2.3)$$

The time of flight $\bar{\tau}_1$ thus corresponds to the distance from the Tx antenna of the master node to the geometric center of the Rx antenna array of the slave node (cf. Fig. 2.1).

As evident from Eq. (2.2) both the upsweep and the downsweep are necessary to determine the time and frequency offsets between the nodes. However, no information about the distance between both nodes is available during synchronization, as the time t_0 is unknown. It is necessary to repeat this precise synchronization step before every measurement, as the clocks of the two radar nodes drift apart for various reasons (thermal variations, mechanical shock, etc.). A clock rate difference of 1 ppm over a time of 100 ms would cause a ranging error of approximately 15 m. Therefore, it is crucial to synchronize the stations both in time and in frequency. A more detailed description of the synchronization

procedure can be found in [54].

Measurement After a known and predefined processing time t_{proc} , the slave responds with an upsweep and a downsweep at time $t = t_0 + \bar{\tau}_1 + t_{\text{proc}}$ (assuming ideal synchronization). These are received by the Rx antennas of the master node, mixed with its LO sweeps started at time $t = t_0 + t_{\text{proc}}$ and low-pass filtered to obtain IF signals with the frequencies $f_{\text{up},n}$ and $f_{\text{dn},n}$ in channel $n = 1 \dots N$. Again a known offset frequency of f_a is added to the local sweeps. For simplicity, we assume that this offset is equal in the synchronization and measurement as well as in both up and down sweeps.

In the following paragraphs, the signal model for the baseband measurement signal will be derived. Although the derivations apply for the up ramp, the equations for the down ramp can be obtained in analogous fashion. During the measurement procedure, the locally generated up ramp in the master radar node $s_{\text{m,LO}}(t)$ can be modeled as

$$s_{\text{m,LO}}(t) = \cos(2\pi(f_i + f_a)t + \pi\mu t^2 + \phi_{\text{LO}}), \quad (2.4)$$

with the unknown starting phase of the LO ramp ϕ_{LO} . The amplitude is modeled as unity, since it is irrelevant for this analysis. The signal $s_{\text{Rx},n}(t)$ received in channel $n = 1 \dots N$ is

$$s_{\text{Rx},n}(t) = \cos(2\pi f_i(t - \tau_{\text{rt},n}) + \pi\mu(t - \tau_{\text{rt},n})^2 + \phi_{\text{Rx}}). \quad (2.5)$$

The phases ϕ_{Rx} are caused by the unknown starting phase of the slave ramp and the signal propagation from the slave to the master. The term $\tau_{\text{rt},n}$ is the round-trip time of flight of the signal which is the sum of the time-of-flight $\bar{\tau}_1$ from the master Tx antenna to the slave Rx array centroid during synchronization plus the time-of-flight $\tau_{2,n}$ from the slave Tx antenna to master Rx antenna n during the measurement:

$$\tau_{\text{rt},n} = \bar{\tau}_1 + \tau_{2,n} = \bar{\tau}_1 + \frac{\|\mathbf{r}_{\text{Rx},1,n} - \mathbf{r}_{\text{Tx},2}\|}{c_0}. \quad (2.6)$$

Multiplying $s_{\text{Rx},n}(t)$ from Eq. (2.5) with $s_{\text{m,LO}}(t)$ from Eq. (2.4) in a mixer results in a signal component with a frequency of more than $2f_i$ and a second component with a frequency close to f_a . By low-pass filtering the result and by removing some in general negligible terms, the resulting IF signal $s_n(t)$ can be expressed as

$$\begin{aligned} s_{\text{up},n}(t) &= \text{low-pass}\{s_{\text{m,LO}}(t) \cdot s_{\text{Rx},n}(t)\} \\ &\approx A_n \cos(2\pi(f_a + \mu\tau_{\text{rt},n})t + 2\pi f_i\tau_{\text{rt},n} + \phi_0) \end{aligned} \quad (2.7)$$

with the unknown phase term $\phi_0 = \phi_{\text{LO}} - \phi_{\text{Rx}}$ and the amplitude A_n . It is evident from Eq. (2.7) that the frequency as well as the phase of the resulting signal depend on $\tau_{\text{rt},n}$. Deriving the phase of $s_n(t)$ w.r.t. to t and dividing by 2π yields the momentary frequencies $f_{\text{up},n}$ and $f_{\text{dn},n}$ from Fig. 2.2:

$$\begin{aligned} f_{\text{up},n} &= f_a + \mu\tau_{\text{rt},n}, \\ f_{\text{dn},n} &= f_a - \mu\tau_{\text{rt},n}. \end{aligned} \quad (2.8)$$

Again, a peak search can be used to determine these frequencies from the DFT spectrum (using the up ramp as an example):

$$S_{\text{up},n}(f) = A_n W_f(f - f_{\text{up},n}) \exp\left(j(2\pi f_1 \tau_{\text{rt},n} + \phi_0)\right), \quad (2.9)$$

where W_f denotes the window function frequency response.

Based on Eq. (2.8), the round-trip distance $d_{\text{rt},n}$ in channel n using the up ramp can be calculated by

$$d_{\text{rt},n} = \tau_{\text{rt},n} c_0 = \frac{c_0 T}{B} (f_{\text{up},n} - f_a). \quad (2.10)$$

Replacing the frequency axis in the spectrum from Eq. (2.9) with a distance axis according to Eq. (2.10) yields

$$S_n(d) = A_n W_d(d - d_{\text{rt},n}) \exp\left(j\left(\frac{2\pi}{\lambda} d_{\text{rt},n} + \phi_0\right)\right), \quad (2.11)$$

with the wavelength $\lambda = f_1/c_0$ and the window function frequency response converted to range W_d .

Combining the spectra of all N Rx channels as shown in Section 2.3.1.2, an estimate for the round-trip time $\bar{\tau}_{\text{rt}}$ is obtained:

$$\begin{aligned} \bar{\tau}_{\text{rt}} &= \frac{1}{N} \sum_{n=1}^N \tau_{\text{rt},n} = \bar{\tau}_1 + \bar{\tau}_2 = \frac{\|\bar{\mathbf{r}}_{\text{Rx},2} - \mathbf{r}_{\text{Tx},1}\|}{c_0} + \frac{\|\bar{\mathbf{r}}_{\text{Rx},1} - \mathbf{r}_{\text{Tx},2}\|}{c_0} \\ &= 2 \frac{\|\bar{\mathbf{r}}_{\text{RxTx},1} - \bar{\mathbf{r}}_{\text{RxTx},2}\|}{c_0} = 2 \frac{d_0}{c_0}. \end{aligned} \quad (2.12)$$

As can be seen from the comparison of Eq. (2.12) with Fig. 2.1, the measured round-trip time $\bar{\tau}_{\text{rt}}$ is proportional to the distance d_0 between the Rx/Tx centroids of both nodes. This distance is independent of the relative position and orientation of both nodes. Hence, setting the coordinate systems of both nodes in the Rx/Tx centroids decouples the RTOF and DOA estimation problems. This consideration and Eq. (2.3) are valid in the array far field, i.e. for distances

d_0 for which applies:

$$d_0 > \frac{2D^2}{\lambda} \approx 1.6 \text{ m}, \quad (2.13)$$

where $D = 10 \text{ cm}$ is the array size. This condition is satisfied for virtually all problems and situations considered in this work. For near-field scenarios, the 3D spatial matched filter (holography) from Section 2.4.1 has to be used.

Combining the result of the up and down ramps from Eq. (2.8), a compensation of the Doppler effect can be achieved in case the radar nodes are not static during the measurement (this is not considered in the presented model and will not be discussed further in this work)

$$\tau_{\text{rt},n} = \frac{T}{2B} \cdot (f_{\text{up},n} - f_{\text{dn},n}). \quad (2.14)$$

A more detailed derivation and description of the basic operating principle of the deployed system can be found in [54]. Several 1D and 2D localization applications based on this system are presented in [45].

The azimuth and elevation angles of the impinging signal (respectively, of the slave node) are estimated by analyzing the phase differences of $s_n(t)$ between the Rx channels using digital beamforming. This will be discussed in greater detail in Chapter 2.4.

The radar nodes are connected with each other over an IEEE 802.15.4 or an FSK link in the 24 GHz band in a dynamic network, which also serves coarse time synchronization and communication purposes. Measurements with multiple radar nodes can be done in a time-division multiplexing (TDM) manner, which, however, leads to a reduced measurement rate. Alternatively, frequency division multiplexing (FDM) can be implemented by using different frequency offsets in the response of the slave nodes. While this approach is favorable for its higher measurement rate, it reduces the maximum unambiguous range, since it divides the baseband bandwidth among the participating radar nodes.

2.2 Hardware Description

Each radar node consists of a radio-frequency (RF) board and a digital-signal-processing (DSP) board as shown in Fig. 2.3. A planar sparse antenna array comprising 8 patch antennas is connected to the RF board using flexible phase-stable HUBER+SUHNER Astrolab minibend coaxial cables.

On the DSP board an FPGA is responsible for precisely scheduling the stages of the synchronization and measurement process. The FFT calculation of the signals and the subsequent peak search in the resulting spectrum is also performed on the FPGA. The microcontroller unit (MCU) is used to program the

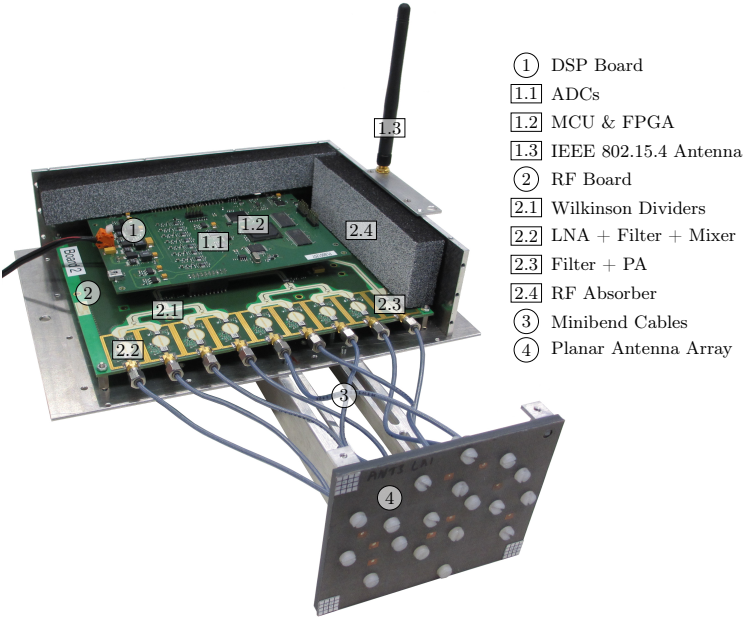


Fig. 2.3: 24 GHz secondary radar. Adapted from [55].

phase-locked loop (PLL) chip on the RF board and the IEEE 802.15.4 radio chip. It is also in charge of the coarse pre-synchronization and of determining the time slot to use in the node network.

During signal transmission, the FMCW ramps are generated by a fractional-N PLL, which is programmed over SPI (serial peripheral interface) by the MCU. A 12 GHz voltage-controlled oscillator (VCO) is controlled by the PLL. Before eventually reaching the Tx antenna, the FMCW ramp is doubled in frequency, band-pass filtered and amplified.

In receiving mode the Tx path is disabled by switching off the frequency doubler. The 8 received 24 GHz FMCW ramps are amplified by a low-noise amplifier (LNA) and band-pass filtered. By using a cascade of Wilkinson power dividers, the 12 GHz FMCW VCO signal is distributed and mixed with the received signals in subharmonic mixers. The resulting IF signals are digitized by differential 14-bit ADCs with sampling frequency $f_s = 8 \text{ MHz}$ and sent to the FPGA for further processing. The hardware used was also presented in [56].

The system parameters are summarized in Table 2.1.

Table 2.1: System parameters of the FMCW radar used.

Parameter	Value
Lower frequency f_l	24 GHz
Sweep bandwidth B	250 MHz
Sweep duration T	1.024 ms
Output power	13 dBm
IF bandwidth $f_s/2$	4 MHz

2.3 Distance Measurement

The expected accuracy of a positioning system strongly depends on the performance of the sensors used. Therefore, it is important to perform an analysis of the error sources and verify the system performance in different environments.

2.3.1 Ranging Precision in Ideal Environment

In an ideal environment without any systematic errors which can be caused for example by multipath (MP) propagations distorting the line-of-sight (LOS) signal, the system performance depends only on radar-internal error sources. These cause only statistical errors and limit the ranging precision of the system. One way to describe the best achievable performance in this case is the Cramér-Rao Lower Bound (CRLB). It gives a lower bound for the variance of an unbiased estimator [57]. The main noise sources for secondary radar systems have been recognized as thermal and quantization noise, which can be modeled as additive white Gaussian noise (AWGN), and phase noise.

2.3.1.1 Phase Noise

As recognized in [58] and [59], the phase noise is the dominant limiting factor for the localization precision for the employed measurement method as described in Section 2.1 at high signal-to-noise ratio (SNR), i.e. when the noise power of white thermal noise is low relative to the signal power. The CRLB used in [59] to describe the localization precision σ_d is

$$\sigma_d \geq \frac{c_0}{2B} \sqrt{\frac{1}{\pi^2 \eta} \left(1 + \frac{1}{\eta}\right)} \quad (2.15)$$

as given by [60] and similarly in [57]. As can be seen from Eq. (2.15), the measurement precision depends only on the sweep bandwidth B and the signal-to-

noise ratio (SNR) η . While the bandwidth is a known system design parameter and is limited by technical factors and legal regulations, the SNR needs further study.

Equation (2.15), however, fails to model the fact, that the CRLB decreases as the observation time (sweep duration) is increased¹. Therefore, in this work the CRLB σ_f for frequency estimation from [61], [57], and [58] was used instead:

$$\sigma_f \geq \frac{f_s}{2\pi} \sqrt{\frac{12}{\eta N(N^2 - 1)} F_{\text{wnd}}}, \quad (2.16)$$

with the sampling frequency f_s , the number of samples $N = Tf_s$, and the degradation factor F_{wnd} depending on the window used given by [62]. The SNR can be calculated by integrating the measured normalized phase noise spectrum $L(f)$ from Fig. 2.4 as shown in [63]:

$$\eta = \frac{P_S}{P_N}, P_S = \frac{1}{2}, P_N = \int_{f_l}^{f_u} L(f) df, \quad (2.17)$$

with the signal and noise power P_S and P_N , respectively. The lower integration limit f_l was approximated by $1/T$ (lower-frequency components present a nearly constant phase offset over the whole baseband); the upper integration limit f_u was chosen as the low-pass filter corner frequency $f_s/2$. The derivation of σ_d from σ_f will be shown later in this section.

To verify the validity of Eq. (2.16), a Monte Carlo (MC) simulation based on the measured phase noise profile from Fig. 2.4 was conducted. The simulations confirmed the N^{-3} dependence of the bound σ_f on the observation duration. However, the value predicted by Eq. (2.16) differed from the MC result by a constant scaling factor, since Eq. (2.16) (as well as Eq. (2.15)) is only valid for additive white Gaussian Noise (AWGN). The effect of phase noise $\phi_{\text{PN}}(t)$ on a single-tone signal $s(t)$ with amplitude A and frequency f can be approximated as

$$s(t) = A \cos(2\pi ft + \phi_{\text{PN}}(t)) \approx A \cos(2\pi ft) - A \sin(2\pi ft) \phi_{\text{PN}}(t), \quad (2.18)$$

assuming $\phi_{\text{PN}}(t)$ is small, zero-mean, Gaussian and having a normalized power spectral density as in Fig. 2.4. Although Gaussian and approximately additive, it is nonwhite and thus Eq. (2.16) is not completely accurate, as the covariance matrix for colored noise is non-diagonal. MC simulations, where the phase noise was assumed white concurred with Eq. (2.16) demonstrating the correctness of this consideration. Eq. (2.18) also demonstrates why increasing the signal

¹Unless implicitly considered in the SNR η .

amplitude A does not improve the performance – the phase noise power is also scaled by A .

A more accurate analytical result can be obtained by computing the covariance matrix of the signal and using it to obtain the Fisher information matrix (FIM) as shown for the general Gaussian case in [57]. The effect of phase noise on frequency estimation is also considered in [64] and [65]; an analytical expression for white phase noise (modeled as a Wiener process) is given in [66]. A more accurate calculation of the CRLB in the presence of phase noise is beyond the scope of this work. As shown in [59] and as valid for the parameters used here, ADC quantization noise is much lower than the phase noise and is therefore neglected.

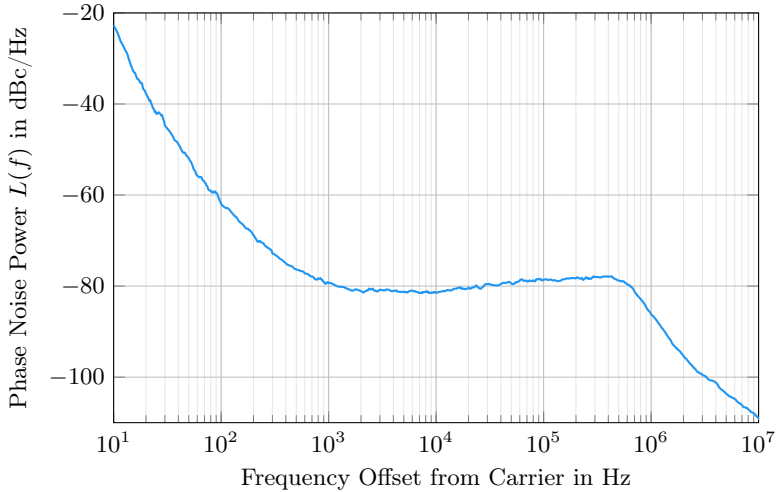


Fig. 2.4: Measured phase noise spectrum of the 24 GHz CW signal.

A series of MC simulations was conducted in order to examine the error propagation during the synchronization and measurement process. Up and down FMCW ramps for the Rx and LO signal in the slave with the system parameters from Table 2.1 were generated. Phase noise with a phase-noise profile according to the measurement in Fig. 2.4 was added. The mixing process was simulated and a band-pass filter was applied to the result to obtain the baseband signal. By computing the FFT and performing a peak search with quadratic interpolation, the standard deviation of the synchronization signal frequencies $f_{\text{up,sy}}$ and $f_{\text{dn,sy}}$

from Fig. 2.2 was estimated to

$$\sigma_{f_{sy}} \approx 5.5 \text{ Hz}. \quad (2.19)$$

This value corresponds to $\sqrt{2}\sigma_f$ from Eq. (2.16) as it results from mixing the Rx and LO signals whose noise is uncorrelated. The standard deviation of the calculated time offset from Eq. (2.2) is

$$\begin{aligned} \sigma_{\Delta t} &= \sqrt{\mathbb{E}\{(\Delta t - \mathbb{E}\{\Delta t\})^2\}} \\ &= \frac{1}{2\mu} \sqrt{\mathbb{E}\{(f_{dn,sy} - f_{up,sy} - \mathbb{E}\{f_{dn,sy} - f_{up,sy}\})^2\}} \\ &= \frac{1}{2\mu} \sqrt{\mathbb{E}\{((f_{dn,sy} - \mathbb{E}\{f_{dn,sy}\}) - (f_{up,sy} - \mathbb{E}\{f_{up,sy}\}))^2\}} \\ &= \frac{1}{2\mu} \sqrt{\underbrace{\sigma_{f_{sy}}^2 - 2 \mathbb{E}\{(f_{dn,sy} - \mathbb{E}\{f_{dn,sy}\}) \cdot (f_{up,sy} - \mathbb{E}\{f_{up,sy}\})\}}}_{=0, \text{uncorrelatedness}} + \sigma_{f_{sy}}^2 \\ &= \frac{1}{\sqrt{2}\mu} \sigma_{f_{sy}}. \end{aligned} \quad (2.20)$$

For the standard deviation of the estimated frequency offset we obtain analogously

$$\sigma_{\Delta f} = \sigma_{\Delta t} = \frac{1}{\sqrt{2}\mu} \sigma_{f_{sy}}. \quad (2.21)$$

The starting point of the measurement ramps is triggered by a clock with ns accuracy. However, this is insufficient for precise range measurements. Therefore, to compensate the time offset Δt , frequency offsets proportional to Δt with opposite signs are added to the start frequency measurement ramps. The accuracy of the frequency offset is limited by the PLL step size [53], which is $f_{step} = 30.4 \text{ Hz}$ for the given system. As shown in [67], this causes a discretization error, with an approximately uniform distribution $\mathcal{U}(-\frac{f_{step}}{2}, \frac{f_{step}}{2})$ with a standard deviation of

$$\sigma_{disc} = \frac{f_{step}}{\sqrt{12}}. \quad (2.22)$$

The uncertainty of the time synchronization, expressed as the standard deviation of the quantized measurement ramp start frequency is then

$$\sigma_{f,disc} = \sqrt{(\sigma_{\Delta t}\mu)^2 + \sigma_{disc}^2}. \quad (2.23)$$

Eq. (2.23) describes the uncertainty caused by the synchronization process neglecting the error caused by imperfect frequency synchronization as it has no

direct effect in Eq. (2.14). It causes an additional timing error due to the clock rate differences during the relatively short time of 14 ms between the synchronization and the measurement.

As the oscillators in both stations have similar characteristics, the value from Eq. (2.19) can be reused to describe the effect of phase noise on the measurement:

$$\sigma_{f,\text{ms}} = \sqrt{\sigma_{f_{\text{sy}}}^2 + \sigma_{\text{disc}}^2}. \quad (2.24)$$

$\sigma_{f,\text{ms}}$ is the covariance of the IF frequencies from Eq. (2.8). Finally, by using Eq. (2.14) and (2.10), the range uncertainty is

$$\sigma_d = \frac{c_0 T}{4B} \sqrt{2\sigma_{f,\text{ms}}^2} = 4.1 \text{ mm}. \quad (2.25)$$

In order to verify the expected ranging precision, a series of measurements was conducted. The error distribution for 1000 stationary measurements at a constant distance of 1.5 m is shown in Fig. 2.5. As evident from the plot, the error has an approximately Gaussian distribution with $\sigma_d \approx 6.8 \text{ mm}$. The measured error is larger than the predicted, probably due to further less significant unmodeled error sources and multipath reflections, since the measurements were done in a laboratory environment and not in an anechoic chamber. Although stationary, multipath reflections do not only change the mean of the resulting distribution, but also the standard deviation, as they are decorrelated from the LOS by the difference in time of flight (as shown e.g. in [68]).

2.3.1.2 AWGN

At low SNR (large distances), AWGN becomes dominant over the phase noise [58]. In this case, the use of multiple channels, as available in the system at hand, can improve the detectability of the signal. No improvement can be achieved against phase noise, as it is identical in all channels.

Several estimators of the distance d were compared in a series of MC simulations based on the model in Eq. (2.11). The analyzed estimators which all basically calculate the mean distance to the target in all channels are:

1. Estimator “1 channel”: Determine d from peak search in FFT magnitude of 1 channel (with subsequent quadratic peak interpolation):

$$d_{1 \text{ channel}} = \arg \max_d |S_1(d)|. \quad (2.26)$$

2. Estimator “mean”: Determine d from peak search in FFT magnitude in all N channels separately (with subsequent quadratic peak interpolation)

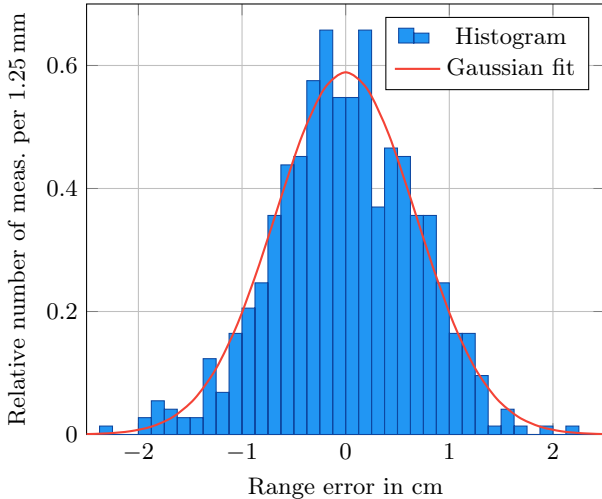


Fig. 2.5: Measured error distribution for a stationary measurement scenario.

and calculate mean:

$$d_{\text{mean}} = \frac{1}{N} \sum_{n=1}^N \arg \max_d |S_n(d)| . \quad (2.27)$$

3. Estimator “sumabs”: Determine d from peak search in the sum of the FFT magnitudes of all N channels (with subsequent quadratic peak interpolation):

$$d_{\text{sumabs}} = \arg \max_d \left(\sum_{n=1}^N |S_n(d)| \right) . \quad (2.28)$$

This estimator relies upon the narrowband assumption (the signal bandwidth B is so narrow or the array size is so small, that there is a significant overlap of the peaks in the spectra of all channels despite the TOF differences between them [69]). This is valid for the system used.

4. Estimator “holo”: Determine d assuming the azimuth and elevation angles φ_{az} and ϑ_{el} to the target can be accurately determined or are known. The angles can then be used to manipulate the phase in each channel to obtain

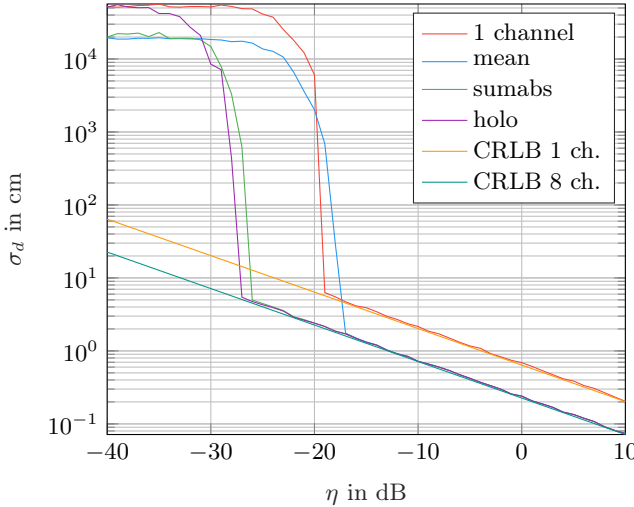


Fig. 2.6: Comparison of 4 range estimators for varying SNR (see text) and corresponding CRLB.

constructive interference of all channels:

$$d_{\text{holo}} = \arg \max_d \left(\sum_{n=1}^N S_n(d) e^{-j\phi_n(\varphi_{\text{az}}, \vartheta_{\text{el}})} \right). \quad (2.29)$$

This estimator is equivalent to using a 3D spatial matched filter (also known as holography or wideband beamforming), as described in Eq. (2.36) and Fig. 2.15 for the case when the angles to the target can successfully be estimated.

1000 MC simulation runs were performed while varying the SNR for a radar with parameters as in Table 2.1 and antenna array as in Fig. 2.16 (a) using the 4 estimators with different noise realizations. The signal model from Eq. (2.7) was extended by an AWGN noise term $N_n(t) \sim \mathcal{N}(0, \sigma_N^2)$ which was band-limited to $f_s/2$:

$$s_n(t) = A_n \cos(2\pi(f_a - \mu t_{\text{rt},n})t - 2\pi f_l t_{\text{rt},n}) + N_n(t). \quad (2.30)$$

Eq. (2.16) was used for the CRLB σ_f for 1 channel. For 8 channels $\sigma_f/\sqrt{8}$ can be used due to the uncorrelatedness of the noise in the channels. The SNR η

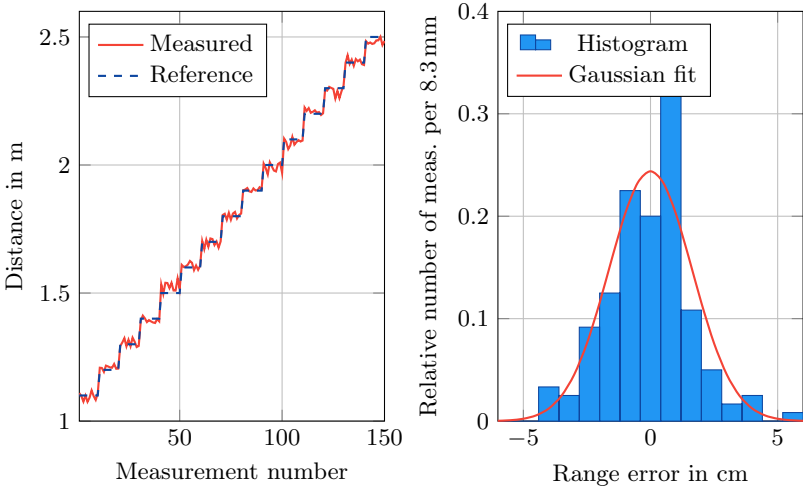


Fig. 2.7: Measured and reference distance (left). Error histogram (right).

was defined as

$$\eta_{\text{lin}} = \frac{E\{s_n^2(t)\}}{E\{N_n^2(t)\}} = \frac{0.5A^2}{\sigma_N^2}, \eta = 10 \log_{10} \eta_{\text{lin}}. \quad (2.31)$$

The result of the MC simulations and the corresponding CRLB are shown in Fig. 2.6. As evident from the graph, all estimators asymptotically reach the CRLB as the SNR (or the number of samples) becomes sufficiently large. However, some estimators reach the CRLB “faster” than others, they are thus capable of detecting a signal at lower SNR.

As expected, the worst estimator is the FFT-based “1 channel” as it uses data from only a single channel. The estimator “mean” is somewhat better, due to the introduced averaging of several results with independent noise. “sumabs” is an even better estimator, because the averaging here is performed in the magnitude of the raw data, which leads to a higher SNR of the summed magnitude (signal sums up, noise averages out). “holo” is the best FFT-based estimator, as the summation here is performed phase-coherently. This leads to an even better SNR of the sum.

Although “holo” performed best, its computational cost is also very high (unless the angles to the target are known beforehand). “sumabs” has almost equal performance at a much lower computational cost. “sumabs” also has good re-

sistance against multipath fading, when most of the channels report correct distance, but the others are severely disturbed (this case is not handled well by “mean”). Therefore, the estimator “sumabs” was used throughout this work.

2.3.1.3 Measurement Results

A measurement series at varying distances was conducted to verify the accuracy of the system. One radar node was stationary and a second node was mounted on a high-precision linear guide (model Isel LEZ 3) and moved away from the first one from 1.1 to 2.5 m in 10 cm steps. 10 measurements were done per range step. The results are shown in Fig. 2.7. As can be seen from the plot, the measurement closely matches the reference values and achieves an accuracy of $\sigma_d \approx 1.64$ cm. The error is larger than the static measurement error from Fig. 2.5, since it was again conducted in a laboratory environment. Different multipath components lead to varying systematic errors at each measurement step, which leads to lower accuracy.

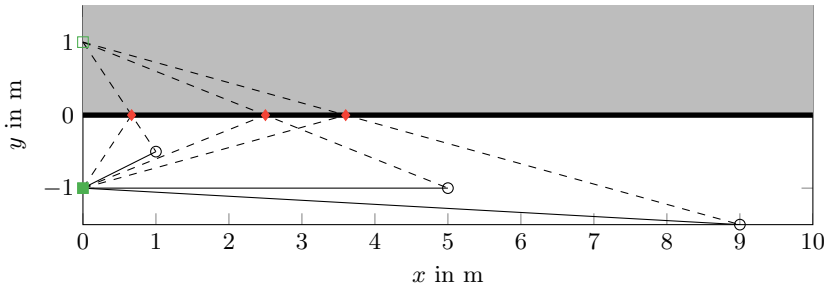


Fig. 2.8: Top view of a long narrow corridor with one wall denoted as a thick black line. White denotes the space inside the corridor; grey denotes an occupied area inside the wall. The transmitter is shown as a filled green square. The LOS paths to a target, shown as a black circle at 3 different positions, are plotted as solid black lines. The reflection points on the wall are shown as red diamonds; the corresponding MP components are illustrated as dashed lines. Given the geometry, a virtual transmitter can be defined as illustrated by the empty green rectangle.

2.3.2 Ranging Accuracy in a Long Narrow Corridor

Long narrow corridors are of particular importance for the applications this work focuses on (see the scenarios in Section 4.12). They represent a very difficult problem for wireless localization systems due to the relatively strong and numerous multipath reflections caused by the floor, ceiling, and walls. Furniture and door frames which are often present in corridors cause further multipath components.

To illustrate this, a scenario consisting of a transmitter close to an ideal smooth reflecting surface was considered as shown in Fig. 2.8. This is representative for a radar unit at a distance of 1 m from a wall in a long narrow corridor. Assuming ideal specular reflections at the surface, which is modeled as infinite in the xz plane, the ray-tracing approach can be used to simulate the resulting propagation paths. This results in the LOS paths denoted by the continuous black lines and in the MP paths shown as dashed black lines in the figure. Given the geometry, a virtual transmitter can be defined by mirroring the real transmitter at the reflecting surface to aid the intuitive interpretation of the problem. For simple scenarios, this can be used to improve the localization as shown in [70]. However, in the case of indoor localization in a corridor, in the ideal case such a reflection occurs at least at both walls, at the floor and at the ceiling making such an approach less promising. The path length difference between the LOS and the MP component for a transmitter in the middle of a 2 m-wide corridor and a receiver moving away from it in the middle of the corridor was

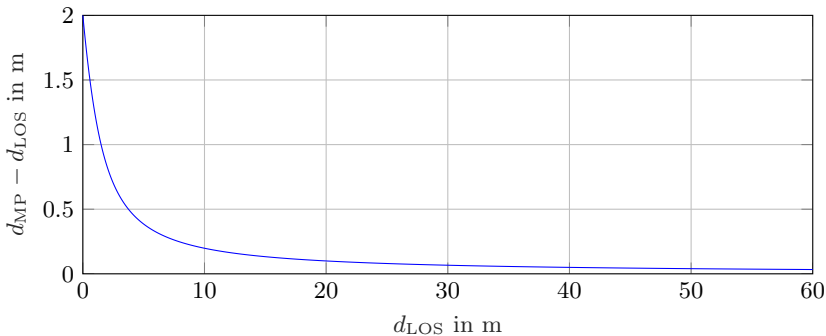


Fig. 2.9: Path length difference between the LOS component d_{LOS} and the MP component d_{MP} for a transmitter and receiver placed in the middle of a 2 m-wide corridor at a distance d_{LOS} apart.

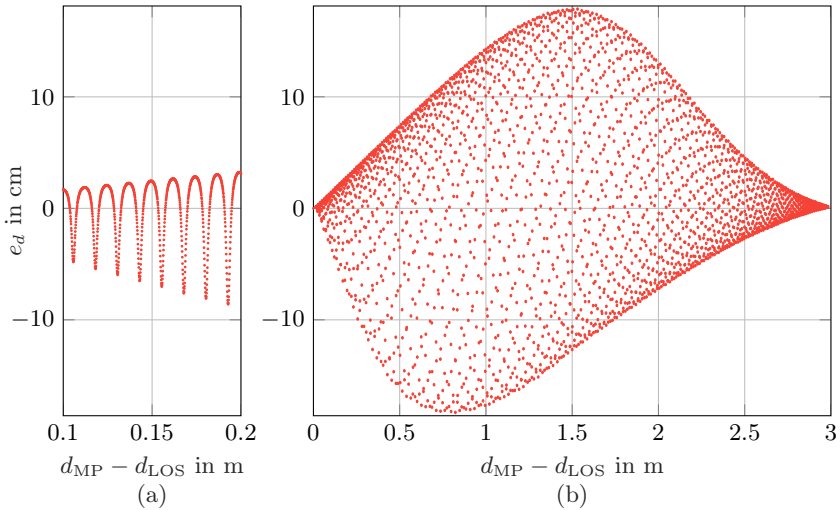


Fig. 2.10: Simulation of the range error e_d for the superposition of a LOS and a MP component for range difference $d_{\text{MP}} - d_{\text{LOS}} = 0.1 \dots 0.2 \text{ m}$ (a) and $0 \dots 3 \text{ m}$ (b). Both signals impinge from $\varphi_{\text{az}} = 0^\circ, \vartheta_{\text{el}} = 0^\circ$.

calculated and plotted in Fig. 2.9. As evident, the path length difference quickly decreases as the distance between the transmitter and the receiver increases. For a secondary radar system with the parameters from Table 2.1, the resolution in range is $\Delta d_{\min} \approx 2\frac{c_0}{B} \approx 2.4$ m, where the factor 2 is valid for a Hann window². Thus, the MP component quickly becomes indistinguishable from the LOS and impairs the range estimation accuracy.

To study this effect, a simulation was performed. A LOS component with amplitude A_{LOS} and of constant length d_{LOS} and a multipath signal with amplitude $A_{\text{MP}} = 0.5A_{\text{LOS}}$ and length d_{MP} were assumed and superimposed linearly in every channel n according to

$$S_n(d) = A_{\text{LOS}} W(d - d_{\text{LOS},n}) \exp \left(j \left(\frac{2\pi}{\lambda} d_{\text{LOS},n} \right) \right) + A_{\text{MP}} W(d - d_{\text{MP},n}) \exp \left(j \left(\frac{2\pi}{\lambda} d_{\text{MP},n} \right) \right). \quad (2.32)$$

²The resolution of secondary radar is lower than that of a primary radar given by $\Delta d_{\min, \text{primary}} \approx 2 \frac{c_0}{2B}$, because only the one-way time-of-flight is considered.

The result for a MP impinging from $\varphi_{az} = 0^\circ, \vartheta_{el} = 0^\circ$ is shown in Fig. 2.10 for a single channel. The length difference $d_{MP} - d_{LOS}$ was varied in the range $0.1 \dots 0.2\text{ m}$ (a) and $0 \dots 3\text{ m}$ (b) in steps of 1 mm. As can be seen, the range estimation error e_d varies within $-18 \dots 18\text{ cm}$ for the parameters used. The simulation also shows that the range error can vary strongly by several cm for a 1 mm variation of the difference between the signals due to the superposition of the two waves with relatively quickly varying phases. This variation is almost zero-mean and can roughly be modeled as Gaussian³.

For a MP impinging from $\varphi_{az} = 10^\circ, \vartheta_{el} = 10^\circ$, the result in Fig. 2.11 is obtained for the 4 estimators from Section 2.3.1.2. It can be seen that the estimators relying on multiple channels perform better than the single-channel estimator in this case, as the length difference between the MP and the LOS component varies in every channel and the error partially averages out. This is not the case for $\varphi_{az} = 0^\circ, \vartheta_{el} = 0^\circ$, since here the range difference is almost identical in all channels. For the simulations, it was assumed that the two signals can be resolved neither in distance, nor in angle.

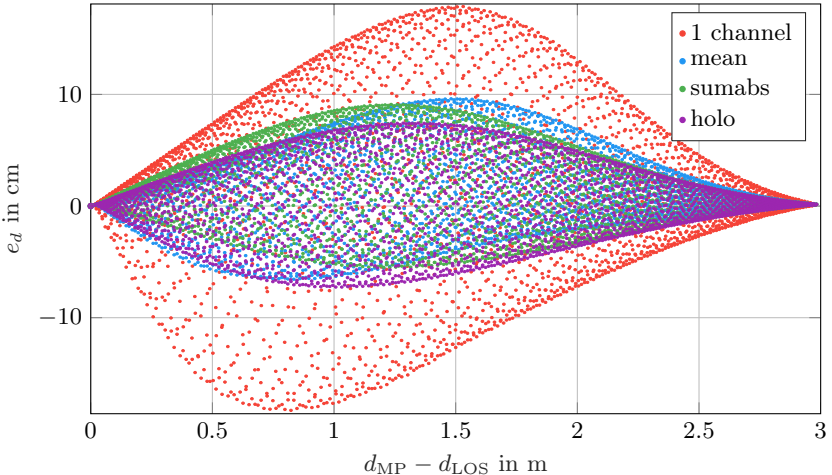


Fig. 2.11: Simulation of the range error e_d for the superposition of a LOS and a MP component with range difference $d_{MP} - d_{LOS}$ for 4 different estimators. The LOS signal impinges from $\varphi_{az} = 0^\circ, \vartheta_{el} = 0^\circ$, the MP from $\varphi_{az} = 10^\circ, \vartheta_{el} = 10^\circ$.

³This is a coarse, but important assumption for the algorithms in Chapter 3.

Albeit simplified, this simulation demonstrates the effect of multipath propagation on ranging accuracy. This was also closely studied e.g. in [71] and [72]. Extensive models were developed by in [73] and [74]. They basically model the arrival times of the multipath components by a Poisson distribution and their amplitudes as a Rayleigh (in [73]) or a Ricean (in [74]) distribution. The multipath signals arrive in clusters emanating from the building topology. For the problem at hand, only the first cluster is of interest, as the others have virtually no effect on the localization accuracy.

To verify the validity of these observations, a measurement was conducted in a 2 m-wide corridor in Cauerstr. 6, FAU Erlangen-Nürnberg (the scenario is depicted in Fig. 4.25). One radar node was static and the second node was moved away from it at a constant height along the corridor. The resulting FFT spectrum for a single measurement in all 8 Rx channels is shown in Fig. 2.12. The one-way channel response for 110 measurements at a distance from 10 m to 20 m is shown in Fig. 2.13. As a comparison, the predicted amplitude decaying with a time constant of 20 ns as described by the Saleh-Valenzuela model in [73] is shown. As can be seen, the model approximately matches the measurement.

Another measurement series in the same environment was conducted to determine the range estimation accuracy of the system. 475 measurements were

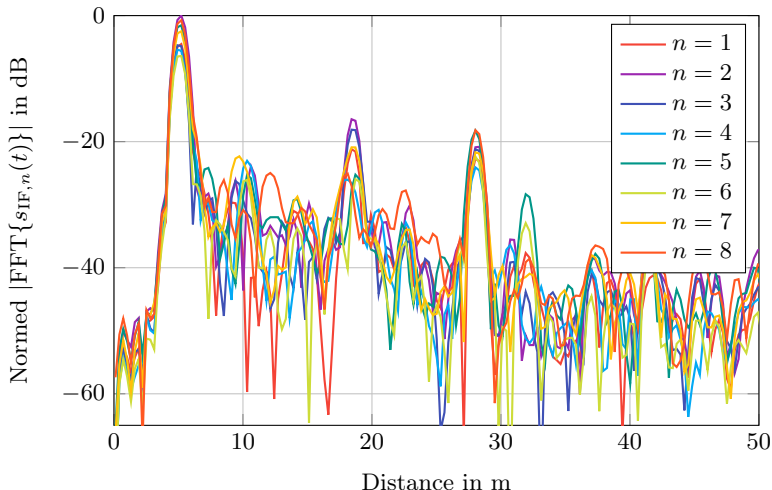


Fig. 2.12: Absolute values of the FFT spectrum of the received signals in channels $n = 1 \dots 8$ for a distance $d = 0 \dots 50$ m.

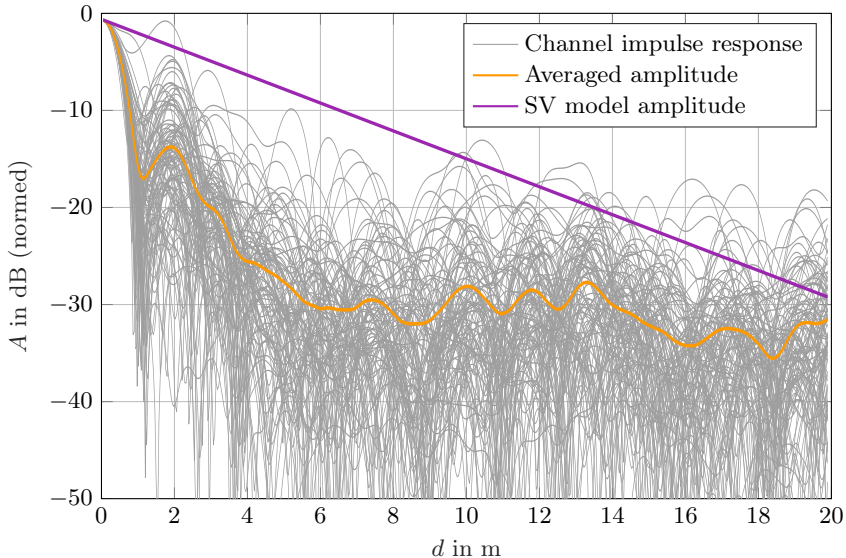


Fig. 2.13: Measured FFT spectrum in a corridor and Saleh-Valenzuela model prediction.

made at a distance from 3 m to 25 m using a mobile robot. A Leica TS30 total station was used as a reference (cf. Section B.1). The ranging standard deviation was 7.45 cm with approximately Gaussian distribution. This proves the validity of the aforementioned considerations and demonstrates the suitability of the proposed system for indoor localization for applications as in Chapter 4.

2.4 Direction of Arrival Estimation

As outlined in Section 1.2, combining RTOF with DOA measurements has significant advantages over multilateration-based approaches. This section focuses on the coherent processing of the Rx signals for DOA angle estimation.

2.4.1 3D Spatial Matched Filter

While the distance to the target is estimated by temporal sampling of the impinging signal at different points in time, the DOA angles are estimated by spatial sampling using multiple antennas at different spatial positions at the

same time. By computing the Fourier transform of Eq. (2.7) and converting it from the frequency domain to the spatial domain by replacing the frequency axis with a distance axis according to Eq. (2.10) we obtain the ideal signal model

$$\begin{aligned} S_n(d) &= A_n W(d - d_{\text{rt},n}) \exp\left(j\left(\frac{2\pi}{\lambda} d_{2,n}\right)\right) \\ &= A_n W(d - d_{\text{rt},n}) \exp(j\phi_n), \end{aligned} \quad (2.33)$$

with the signal amplitude A_n , the wavelength $\lambda = f_1/c_0$, and the window function frequency response W . The round-trip distance $d_{\text{rt},n} = \bar{d}_1 + d_{2,n}$ is the sum of the distance $\bar{d}_1 = \bar{\tau}_1 c_0$ from the Tx antenna on the master to the Rx array on the slave and the distance $d_{2,n} = \tau_{2,n} c_0$ from the slave's Tx antenna to the master's Rx antenna n (see Fig. 2.1 and Eq. (2.3) and (2.6)). While \bar{d}_1 has no effect on the baseband signal phase, it acts as a constant offset on the signal frequency due to the synchronization process. The signal phase ϕ_n in channel n depends only on $d_{2,n}$.

Given the model in Eq. (2.33) and assuming unity amplitude, we can construct the 3D spatial matched filter $H_{3D,n}$ as

$$\begin{aligned} H_{3D,n}(\|\mathbf{r}_{\text{Rx},n} - \mathbf{r}_{\text{Tx,h}}\|) &= S_n^*(\|\mathbf{r}_{\text{Rx},n} - \mathbf{r}_{\text{Tx,h}}\|) \\ &= \exp\left(-j\frac{2\pi}{\lambda}\|\mathbf{r}_{\text{Rx},n} - \mathbf{r}_{\text{Tx,h}}\|\right), \end{aligned} \quad (2.34)$$

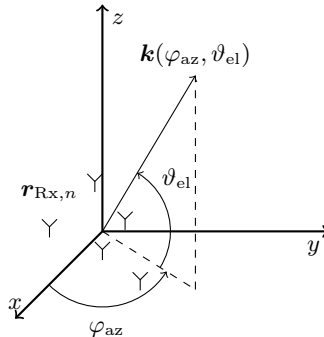


Fig. 2.14: DOA estimation problem geometry. The Rx antennas are denoted by the antenna symbol Υ . The origin of the array coordinate system is in the geometric center of the array. The antenna positions $\mathbf{r}_{\text{Rx},n}$ are known in this coordinate system.

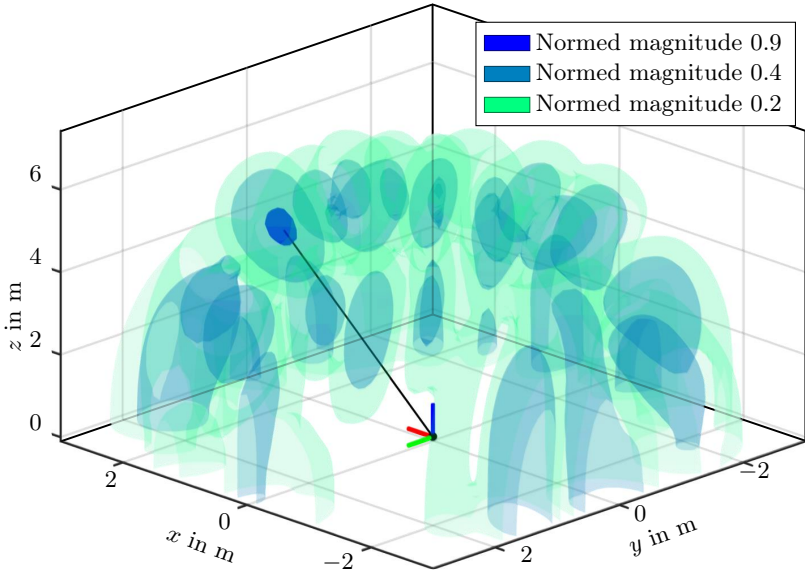


Fig. 2.15: Normalized magnitude of 3D spatial matched filter response $\mathbf{I}(\mathbf{r}_{\text{Tx},h})$. The Rx antenna array of the master lays in the xy plane. The black line denotes the LOS path between the target and the array coordinate system origin. Adapted from [55].

where $*$ denotes the complex conjugate operator. As shown in Fig. 2.14, the vector $\mathbf{r}_{\text{Rx},n} = [x_n \quad y_n \quad z_n]^T$ is the known 3D position of the n th antenna element. The vector $\mathbf{r}_{\text{Tx},h} = [x_h \quad y_h \quad z_h]^T$ is the hypothetical target position in 3D (the target is the slave's Tx antenna). The response to the matched filter for a hypothetical target location $\mathbf{r}_{\text{Tx},h}$ can be calculated by

$$\mathbf{I}(\mathbf{r}_{\text{Tx},h}) = \left| \sum_{n=1}^N S_n(\|\mathbf{r}_{\text{Rx},n} - \mathbf{r}_{\text{Tx},h}\|) \cdot H_{3D,n}(\|\mathbf{r}_{\text{Rx},n} - \mathbf{r}_{\text{Tx},h}\|) \right|. \quad (2.35)$$

By evaluating (2.35) at every voxel in a given 3D range $\mathbf{R}_{\text{search}} \in \mathbb{R}^3$ using measured data, the holographic image in Fig. 2.15 was obtained. Assuming

there is only 1 target in the search range, its position is

$$\mathbf{r}_{\text{Tx,res}} = \arg \max_{\mathbf{r}_{\text{Tx,h}} \in \mathcal{R}_{\text{search}}} \mathbf{I}(\mathbf{r}_{\text{Tx,h}}). \quad (2.36)$$

In this example, the correct position $\mathbf{r}_{\text{Tx}} = [1.4 \text{ m} \quad 1.0 \text{ m} \quad 2.4 \text{ m}]^T$ in the Rx array coordinate system was determined. As evident from the distribution, multiple other weaker local maxima are available. These are not real targets, but phantom targets caused by the side lobes of the array response and the window function.

2.4.2 Antenna Arrays

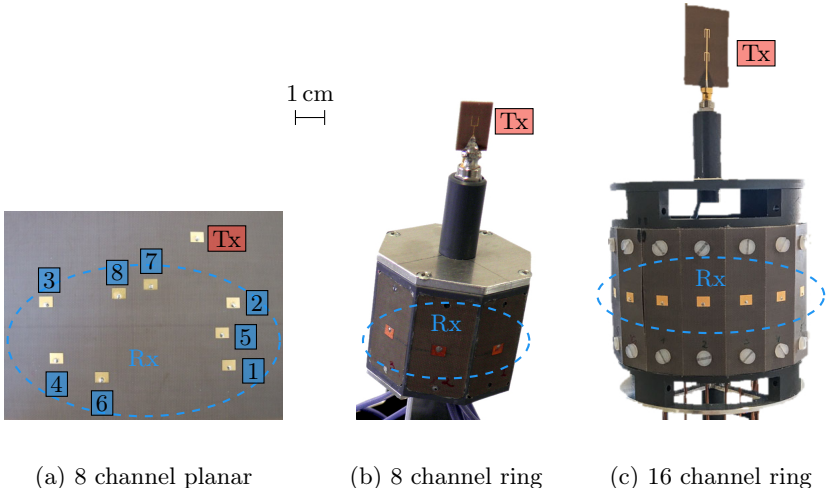


Fig. 2.16: Used antenna arrays: a) 8 channel planar antenna array with Rx channels numbered 1 ... 8; b) 8 channel ring antenna array; c) 16 channel ring antenna.

For primary radar applications, low sidelobe level (SLL) is required, as otherwise a sidelobe can be easily mistaken for a target. Uniform linear arrays (ULA) and uniform rectangular arrays (URA) with element spacing $\lambda/2$ are commonly used, as they offer the smallest SLL and maximum unambiguous range. The disadvantage is the relatively small aperture size which results in a large mainlobe beamwidth (MBW) and thus a lower resolution and accuracy.

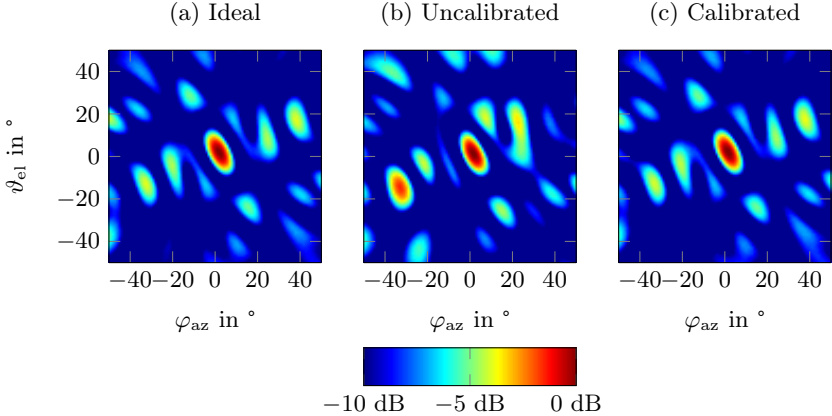


Fig. 2.17: Normalized array response for an impinging signal from $\varphi_{\text{az}} = 2^\circ$, $\vartheta_{\text{el}} = 1^\circ$ in dB. a) Ideal simulated array response. b) Measured array response before calibration. A strong sidelobe is present at $\varphi_{\text{az}} = -35^\circ$, $\vartheta_{\text{el}} = -15^\circ$. c) Measured array response after calibration. SLL improved to close to ideal values.

Secondary-radar-based positioning applications, on the other hand, have much more relaxed requirements regarding SLL, since – in the absence of multipath – the slave radar node is the only target. This makes it possible to design sparse antenna arrays with a relatively low number of elements and large aperture and thus a narrow MBW and high accuracy. This comes at the cost of a high SLL which makes them sensitive to multipath interference.

Fig. 2.16 depicts the antenna arrays used in this work. A 2D planar array consisting of 8 Rx and 1 Tx linearly polarized patch antennas is shown in a). A multi-objective particle swarm optimization (MOPSO) stochastic algorithm was used to design an antenna array geometry as a trade-off between MBW and SLL as described in [75]. Thanks to its 2D structure, this array is capable of measuring both azimuth and elevation angles and has an unambiguous range of $\sqrt{\varphi_{\text{az}}^2 + \vartheta_{\text{el}}^2} < 60^\circ$. As evident from the simulated array response in Fig. 2.17 a), the array has a SLL ≈ -3.7 dB and a MBW $\approx 10^\circ$ at boresight. The MBW becomes wider at larger angles, as at such angles the projected array aperture is reduced.

For applications, where omnidirectional coverage in azimuth is important, the “ring” arrays in Fig. 2.16 b) and c) were used. These consist of 8 (16) patches

placed on the walls of an 8-sided (16-sided) prism. Because the signal coming from any direction is received by at least 3 (5) patches, these arrays provide a coverage of 360° in azimuth and $\pm 45^\circ$ in elevation. The Tx antenna used has approximately equivalent radiation pattern. Due to mechanical constraints, the antenna elements were spaced at distances $> \lambda/2$ which causes ambiguities in the array response. To resolve these, the signal amplitude was additionally used as shown in Section 2.4.6. Unfortunately, it is not possible to reliably estimate the elevation DOA using the ring arrays.

2.4.3 Efficient Implementation

In order to enable real-time DOA estimation, it is necessary to implement the algorithms efficiently on an embedded platform. Calculating the 3D matched filter response $\mathbf{I}(\mathbf{r}_{\text{Tx},h})$ from Section 2.4.1 is very costly and is shown here for illustrative purposes only. Such an approach (holography) is necessary in situations where the target is in the array near-field as described by Eq. (2.13). However, for the application at hand, the array far-field approximation is valid and the impinging signal can be modeled as a plane wave. Furthermore, under the narrow-band assumption [69], the signal model from Eq. (2.33) simplifies to

$$\begin{aligned} S_n(d) &= A_n W(d - d_{\text{rt},n}) \exp\left(j\left(\frac{2\pi}{\lambda} d_{2,n}\right)\right) \\ &\approx A_n W(d - 2d_0) \exp\left(j\left(\frac{2\pi}{\lambda} d_{2,n}\right)\right). \end{aligned} \quad (2.37)$$

It is thus assumed that the signal varies only in phase, but not in frequency along the array aperture. This greatly reduces the computational effort by first conducting a 1D peak search to estimate d_0 as described in Section 2.3 and then a 2D peak search for azimuth and elevation. The corresponding 2D matched filter (delay-and-sum beamformer [76]) assuming plane wave propagation is given by

$$H_{2D,n}(\varphi_h, \vartheta_h) = \exp(-j\mathbf{k}^T(\varphi_h, \vartheta_h) \mathbf{r}_{\text{Rx},n}), \quad (2.38)$$

where the hypothetical azimuth and elevation angles to the target are φ_h and ϑ_h , respectively. As shown in Fig. 2.14, the wave vector $\mathbf{k}(\varphi_h, \vartheta_h)$ is defined as

$$\mathbf{k}(\varphi_h, \vartheta_h) = \frac{2\pi}{\lambda} \begin{bmatrix} \cos \varphi_h \cos \vartheta_h \\ \sin \varphi_h \cos \vartheta_h \\ \sin \vartheta_h \end{bmatrix}. \quad (2.39)$$

The 2D matched filter response is given by

$$\mathbf{I}(\varphi_h, \vartheta_h) = \left| \sum_{n=1}^N S_n(2d_0) \cdot H_{2D,n}(\varphi_{az}, \vartheta_{el}) \right|, \quad (2.40)$$

where d_0 is the estimated distance to the target. The angles φ_{az} and ϑ_{el} then maximize $\mathbf{I}(\varphi_h, \vartheta_h)$:

$$\begin{bmatrix} \varphi_{az} \\ \vartheta_{el} \end{bmatrix} = \arg \max_{[\varphi_h, \vartheta_h] \in \Psi_{\text{search}}} \mathbf{I}(\varphi_h, \vartheta_h), \quad (2.41)$$

with the array-dependent 2D angle search range Ψ_{search} . The far-field approximation causes errors $< 0.1^\circ$ at distances > 1 m for the antenna arrays used.

Eq. (2.41) poses a piecewise convex nonlinear optimization problem with no closed analytic-form solution and needs to be solved by other means. Two approaches were studied with respect to the efficiency on an embedded hardware platform.

2.4.3.1 Grid-Based Processing (Brute Force / Exhaustive Search)

The evaluation of $\mathbf{I}(\varphi_h, \vartheta_h)$ on a grid in Ψ_{search} represents the most straightforward method to obtain the global maximum. However, as evident from Eq. (2.38), a relatively large number of trigonometric functions needs to be calculated at every grid-point. This takes a relatively long processing time, especially on embedded hardware and might not be suitable for real-time operation, even when efficient approximations of the trigonometric functions are used (e.g. the algorithm CORDIC, Taylor expansion or curve fit [77]).

However, since $\mathbf{I}(\varphi_h, \vartheta_h)$ is repeatedly evaluated on a constant grid, the trigonometric functions at the grid-points can be pre-computed in advance and stored in a lookup table (LUT). A further optimization can be achieved by first finding the maximum of $\mathbf{I}(\varphi_h, \vartheta_h)$ on a coarse grid and performing a subsequent search on a fine-grid around the maximum to accurately determine the angle-of-arrival. A parabolic fit can additionally be used to further increase the accuracy of the result. This approach greatly reduces the processing time. An example of grid-based processing is shown in Fig. 2.18 a). The black circles denote the coarse grid and the filled black dots the fine grid. As can be seen, the direction of arrival was correctly estimated to $\varphi_{az} = -8^\circ$, $\vartheta_{el} = 2^\circ$.

2.4.3.2 Solution with the Gauss-Newton Algorithm

The Gauss-Newton algorithm is a method for solving convex nonlinear least-squares problems [78]. It can be derived from the Newton's optimization method

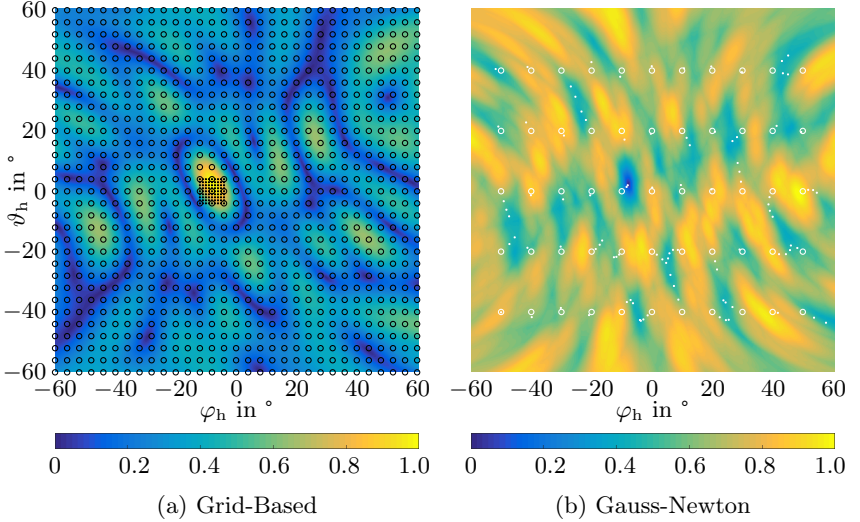


Fig. 2.18: Digital beamforming using a) Grid-based processing; b) Gauss-Newton method.

by ignoring the second-order derivative terms in the Hessian matrix. This simplification makes it particularly suited for real-time implementation [79]. In order to use it to solve the problem in Eq. (2.41), an objective function \mathbf{F}_x needs to be defined, which can be minimized in the least-squares sense. \mathbf{F}_x is obtained from Eq. (2.40) by rewriting it to

$$\mathbf{F}_x = \begin{bmatrix} \cos(\mathbf{k}^T(\varphi_{az}, \vartheta_{el})\mathbf{r}_{Rx})^T - \Re\{\mathbf{s}\} \\ \sin(\mathbf{k}^T(\varphi_{az}, \vartheta_{el})\mathbf{r}_{Rx})^T - \Im\{\mathbf{s}\} \end{bmatrix}, \quad (2.42)$$

with $\mathbf{r}_{Rx} = [\mathbf{r}_{Rx,1}, \dots, \mathbf{r}_{Rx,N}]$ and $\mathbf{s} = [S_1(2d_0), \dots, S_N(2d_0)]^T$. The goal of the Gauss-Newton algorithm is then to minimize

$$\sum_{n=1}^{2N} F_{x,n}^2(\mathbf{x}) \quad (2.43)$$

for the optimization variable $\mathbf{x} = [\varphi_{az} \quad \vartheta_{el}]^T$. We thus have $2N$ equations and 2 unknowns. The algorithm is started with an initial guess $\mathbf{x}^{(0)}$ and proceeds

with the next iteration i to determine

$$\boldsymbol{x}^{(i+1)} = \boldsymbol{x}^{(i)} - \Delta \boldsymbol{x}^{(i)}, \quad (2.44)$$

with the step

$$\Delta \boldsymbol{x}^{(i)} = (\mathbf{J}_{\mathbf{F}_x}^T \mathbf{J}_{\mathbf{F}_x})^{-1} \mathbf{J}_{\mathbf{F}_x}^T \mathbf{F}_x(\boldsymbol{x}^{(i)}). \quad (2.45)$$

The elements of the Jacobian matrix $\mathbf{J}_{\mathbf{F}_x}$ are given by

$$[\mathbf{J}_{\mathbf{F}_x}]_{m,n} = \frac{\partial F_{x,n}(\boldsymbol{x}^{(i)})}{\partial x_n}. \quad (2.46)$$

The step calculation process can thus be interpreted as a linear least-square approximation of the original nonlinear problem.

Since the function \mathbf{F}_x is only piecewise convex, the estimate \boldsymbol{x} in Eq. (2.44) mostly converges to a local minimum. Therefore, the algorithm needs to be started multiple times with different initial guesses to find the global minimum.

The result of applying the Gauss-Newton method to the beamforming problem is shown in Fig. 2.18 b). As evident, the algorithm could successfully find the global minimum and thus the angle of arrival by evaluating the function at only a fraction of points in $\Psi_{\text{search}} = \pm 60^\circ$ in azimuth and elevation (denoted as white filled dots). The overall runtime of the algorithm applied to the beamforming problem from Eq. (2.38) could be greatly reduced by choosing appropriate initial guess points in Ψ_{search} (denoted as white circles) and applying heuristic termination conditions for slowly converging iterations.

2.4.3.3 Comparison

In order to verify the performance of the proposed solutions, they were both implemented on an embedded platform using the programming language C. A set of measurement data was recorded to test the algorithms with respect to accuracy and runtime. While both methods successfully found the global maximum in every measurement with equal accuracy (to the numeric precision used), there was a difference in the runtime. The Gauss-Newton algorithm had a runtime varying by up to 13 % depending on the number of necessary iterations with a mean of 15 ms. The grid-based method using a LUT for the trigonometric functions on the other hand had an almost constant processing time with a mean of 9 ms.

The comparison shows an advantage for the latter method due to the lower and more stable processing time. The reason for the worse performance of the Gauss-Newton method is that although it evaluates much fewer points, each iteration is more costly due to the many multiplications necessary to solve the linearized least-squares problem to determine the next iteration step in Eq.

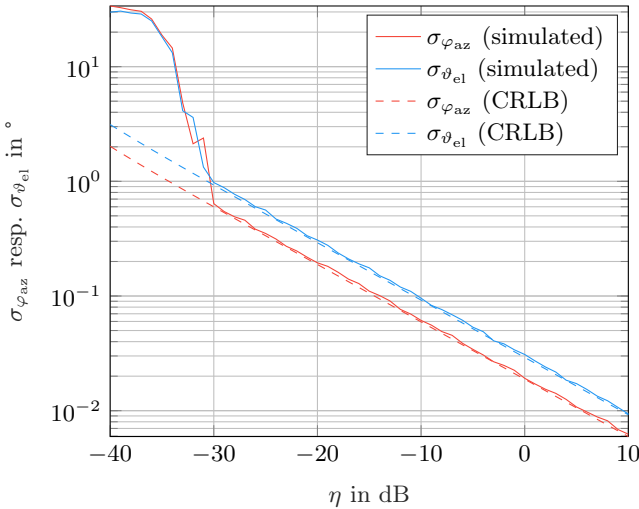


Fig. 2.19: MC simulation and CRLB for 2D DOA for the planar array from Fig. 2.16 (a) for a signal impinging from $\varphi_{az} = 30^\circ$, $\vartheta_{el} = 30^\circ$.

(2.45). However, it could have an advantage on systems with limited memory, as the LUT size for the grid-based method can range from a few hundred kB to several MB depending on the chosen grid fineness.

The Gauss-Newton method can also have an advantage when it is sufficient to only track a target and not execute a complete search after every measurement. In this case, it is assumed, that the target only moves slightly between measurements, so that the result from the last measurement can be taken as a starting point for the Gauss-Newton method in the next measurement. This greatly reduces the number of searched points. A second search at a random point can be started each time to ensure that the tracked peak is indeed the correct one. Performing a grid search in the area of the last result is of course also an option for tracking.

Another possible solution could be to use particle swarm optimization as demonstrated in [80]. Because the grid-based solution had a runtime of 0.3 ms on a more powerful platform used in later experiments, no further methods were studied.

2.4.4 CRLB

In contrast to distance estimation, where phase noise played an important role, it has almost no effect on DOA, because it acts as an additive phase term which is equal in all channels. The dominant noise source here is the AWGN term $N_n(t)$ from Eq. (2.30).

The CRLB for 2D angle estimation for an array with arbitrary geometry and a signal impinging from a given direction is derived in [81] and can be applied to the arrays used in this work with slight adaptation for the angles definition from Fig. 2.14 like also defined in [82]. The lower bound for the azimuth $\sigma_{\varphi_{az}}$ and the elevation $\sigma_{\vartheta_{el}}$ angles estimation standard deviation is

$$\begin{aligned}\sigma_{\varphi_{az}} &\geq \sqrt{\frac{1}{J_{11}} \cdot \frac{1}{1 - \rho^2}}, \\ \sigma_{\vartheta_{el}} &\geq \sqrt{\frac{1}{J_{22}} \cdot \frac{1}{1 - \rho^2}},\end{aligned}\quad (2.47)$$

where ρ describes the degradation in angle estimation due to the simultaneous estimation of both the azimuth and elevation angles given by

$$\rho = \frac{J_{12}^2}{J_{11} J_{22}}. \quad (2.48)$$

The variables J_{ij} represent the elements of the Fisher information matrix \mathbf{J} given by

$$\begin{aligned}J_{11} &= 2NG \sum_{n=1}^N (-x_n \sin \varphi_{az} \cos \vartheta_{el} + y_n \cos \varphi_{az} \cos \vartheta_{el})^2, \\ J_{22} &= 2NG \sum_{n=1}^N (-x_n \cos \varphi_{az} \sin \vartheta_{el} - y_n \sin \varphi_{az} \sin \vartheta_{el} + z_n \cos \vartheta_{el})^2, \\ J_{12} &= 2NG \sum_{n=1}^N (-x_n \sin \varphi_{az} \cos \vartheta_{el} + y_n \cos \varphi_{az} \cos \vartheta_{el}) \cdot \\ &\quad (-x_n \cos \varphi_{az} \sin \vartheta_{el} - y_n \sin \varphi_{az} \sin \vartheta_{el} + z_n \cos \vartheta_{el}),\end{aligned}\quad (2.49)$$

with

$$G = \left(\frac{2\pi}{\lambda}\right)^2 \cdot \frac{\eta_{lin}^2}{1 + N \cdot \eta_{lin}}. \quad (2.50)$$

x_n , y_n , and z_n are the coordinates of the N antenna elements in the array coordinate system. The SNR η_{lin} is defined as in Eq. (2.31).

A MC simulation was performed to analyze the performance of the delay-and-

sum beamformer. The planar array from Fig. 2.16 (a) and a signal impinging from $\varphi_{az} = 30^\circ$, $\vartheta_{el} = 30^\circ$ were assumed. The result in Fig. 2.19 shows that the CRLB is attained for both angles. The worse result for elevation is due to the smaller aperture in this direction.

2.4.5 Calibration

2.4.5.1 Signal Model

In order to account for some further effects present in real systems, the phase term ϕ_n of the signal model from Eq. (2.33) needs to be extended to

$$\begin{aligned}\phi_n &= \mathbf{k}^T(\varphi_{az}, \vartheta_{el}) \cdot (\mathbf{r}_{Rx,n} + \mathbf{p}_{Rx,n} + \mathbf{p}_{Rx,PC,n}(\varphi_{az}, \vartheta_{el})) + \phi_{err,n} \\ &= \phi_{g,n}(\varphi_{az}, \vartheta_{el}) + \phi_{p,n}(\varphi_{az}, \vartheta_{el}) + \phi_{PM,n} + \phi_{MC,n} + \phi_0\end{aligned}\quad (2.51)$$

The term $\phi_{g,n}(\varphi_{az}, \vartheta_{el}) = \mathbf{k}^T(\varphi_{az}, \vartheta_{el}) \cdot \mathbf{r}_{Rx,n}$ is the difference in the received phases in antennas $n = 1 \dots N$ due to the problem geometry. It is the term which contains the information on the DOA and the only one which was considered so far. The term

$$\phi_{p,n}(\varphi_{az}, \vartheta_{el}) = \mathbf{k}^T(\varphi_{az}, \vartheta_{el}) \cdot (\mathbf{p}_{Rx,n} + \mathbf{p}_{Rx,PC,n}(\varphi_{az}, \vartheta_{el})) \quad (2.52)$$

accounts for the 3D deviation $\mathbf{p}_{Rx,n}$ of the location of the antenna phase centers from the ideal values due to imperfections in production and mechanical assembly (antenna position errors) as well as the angle-dependent variation in the phase center position $\mathbf{p}_{Rx,PC,n}$ due to coupling effects as mentioned in [83]. These are effects, which change the antenna radiation pattern and phase center position depending on the neighboring antennas. Due to the complexity of modeling and calibrating such effects and their relatively small impact on the performance, $\mathbf{p}_{Rx,PC,n}$ is not considered in this work. Angle-dependent (also referred to as “local”) calibration which attempts to solve this problem is discussed e.g. in [84] for a dense and in [85] for a sparse calibration grid.

The term $\phi_{MC,n}$ accounts for the mutual coupling between the Rx channels (on the RF board as well as between the antennas). The mutual coupling can be modeled as a complex constant, i.e. the signal from one channel is superimposed on another with a certain attenuation and phase shift, but the radiation pattern and the phase center do not change [83]. $\phi_{MC,n}$ is thus angle-independent.

The term $\phi_{PM,n}$ models the channel-to-channel phase mismatch, caused by the different electrical length of the flexible cables connecting the antennas to the front-end and further non-idealities in the system. The variation in the electrical length of the cables comes from manufacturing tolerances and from the different bending states of the cables. A measurement with a network analyzer showed a

difference of approximately 9° of the phase of the S_{21} parameter between straight and bent state, probably because the bending locally changes the thickness of the insulating layer.

Terms $\phi_{MC,n}$ and $\phi_{PM,n}$ are angle-independent. The phase term ϕ_0 is the same for all channels but different in every measurement cycle due to the unknown initial phase of the ramps. Due to ϕ_0 , no absolute phase information is available and thus only relative phase differences between the channels can be evaluated. The term ϕ_0 can be removed by norming all phases to one of the array elements. This approach, however, can cause further problems due to the phase error of the channel used for norming. These showed to be very small in practice. An alternative solution is to use the phase differences between all permutations of pairs of channels during calibration and beamforming. This mitigates the issue with the phase error in the channel used for norming, but makes it impossible to obtain a closed-form solution to the calibration problem.

If a corner reflector is used instead of a radar node during calibration, ϕ_0 would not be an issue. However, the Tx antenna of the radar node presents a better defined and easier to reference point target which is important for the calibration procedure.

2.4.5.2 Simulation

In order to evaluate the effect of the different error sources, a number of MC simulations was conducted. The simulations are based on the signal processing chain and the error model presented in Sections 2.4.3 and 2.4.5.1.

AWGN A series of simulations was conducted to evaluate the precision depending on the SNR for different DOA similar to Section 2.4.4. 100 simulations were performed every 5° on a grid in the range $\pm 60^\circ$ in both azimuth and elevation directions. The resulting standard deviations of the azimuth and elevation DOA errors are summarized in Fig. 2.20. As expected, the error distribution stays approximately the same and only the value changes from 0.3° at $\eta = -20\text{ dB}$ to 0.003° at $\eta = 20\text{ dB}$ in azimuth (0.4° to 0.004° in elevation, respectively). It is also evident that the precision deteriorates when moving away from boresight direction due to the broadening of the beamwidth.

Phase Mismatch and Mutual Coupling As shown in [86], the effect of the phase mismatch and mutual coupling $\phi_{PM,n}$ and $\phi_{MC,n}$ can be modeled by

$$\mathbf{x} = \mathbf{Cs} + \mathbf{n}. \quad (2.53)$$

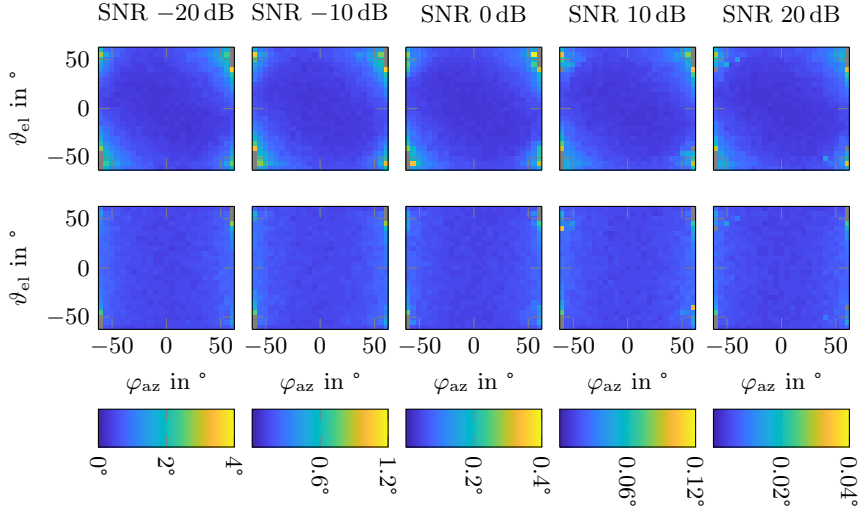


Fig. 2.20: Simulation of DOA estimation error depending on SNR. The color of every pixel denotes the standard deviation of the error in the estimation at the corresponding angles φ_{az} and ϑ_{el} . Upper row: Azimuth error in $^{\circ}$. Lower row: Elevation error in $^{\circ}$. Note the different colormap scales below the plots. Gray denotes azimuth/elevation combinations where DOA estimation fails due to a high sidelobe.

The $N \times 1$ signal vector $\mathbf{s} = [S_1(2d_0), \dots, S_N(2d_0)]^T$ denotes the ideal signal in all N channels as given by Eq. (2.33). The $N \times N$ complex matrix \mathbf{C} models the error terms $\phi_{PM,n}$ and $\phi_{MC,n}$ from Eq. (2.51). The diagonal elements represent the gain and phase mismatch errors in every channel and the non-diagonal elements model the coupling between the channels. The $N \times 1$ vector \mathbf{x} describes the extended signal model with the phase errors ϕ_{err} from Eq. (2.51) and the AWGN vector \mathbf{n} . In order to compensate for the errors, the signal \mathbf{x} can be premultiplied by the complex calibration matrix $\mathbf{T} = \mathbf{C}^{-1}$, assuming \mathbf{C} is invertible.

As proposed in [86] and [87], an estimate for the calibration matrix \mathbf{T} can be obtained using $M \geq N$ measurements at known angles $\varphi_{az,m}$, $\vartheta_{el,m}$ with $m = 1 \dots M$. These measurements are combined in the $N \times M$ matrix $\tilde{\mathbf{X}}$. The elements of the corresponding $N \times M$ matrix $\tilde{\mathbf{S}}$ with the ideally expected signals at the known measurement angles can be calculated according to the

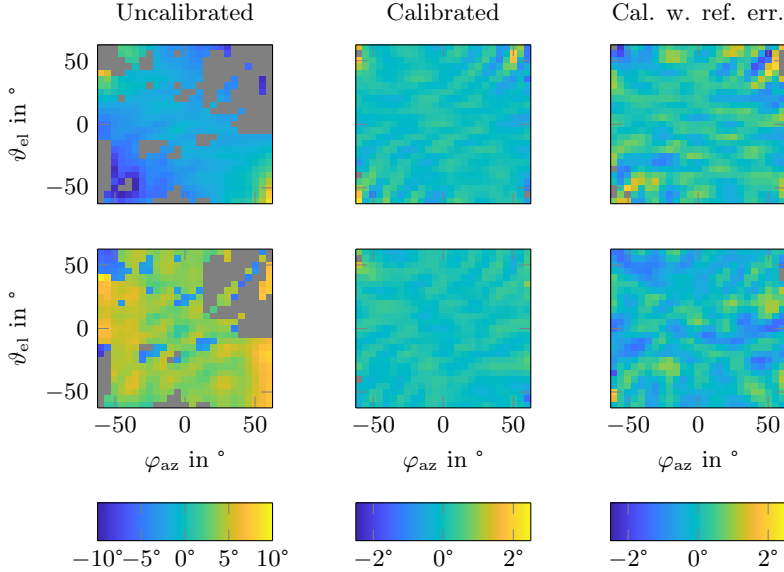


Fig. 2.21: DOA estimation error before and after phase mismatch and mutual coupling calibration. Upper row: Azimuth error in $^{\circ}$. Lower row: Elevation error in $^{\circ}$. Left column: Before calibration. Middle column: After calibration assuming ideal reference measurements. Right column: After calibration assuming errors in reference measurements. Gray denotes azimuth/elevation combinations where DOA estimation fails due to a high sidelobe.

signal model

$$\tilde{s}_{n,m} = s_n(\varphi_{az,m}, \vartheta_{el,m}) = \exp(j\mathbf{k}^T(\varphi_{az,m}, \vartheta_{el,m}) \cdot \mathbf{r}_{Rx,n}), \quad (2.54)$$

with the wave vector \mathbf{k} from Eq. (2.39). The complex value $\tilde{s}_{n,m}$ thus represents the expected phase in each channel n in every measurement m assuming unity amplitude.

The calibration matrix \mathbf{T} can then be found as the least-squares solution of

$$\mathbf{T} = \arg \min_{\mathbf{T}} \|\tilde{\mathbf{S}} - \mathbf{T}\tilde{\mathbf{X}}\|_F, \quad (2.55)$$

where $\|\cdot\|_F$ denotes the Frobenius norm. As shown in [88], Eq. (2.55) has a

closed-form solution given by

$$\mathbf{T} = \tilde{\mathbf{S}} \tilde{\mathbf{X}}^H (\tilde{\mathbf{X}} \tilde{\mathbf{X}}^H)^{-1}, \quad (2.56)$$

with the matrix conjugate transpose operator $|\cdot|^H$ (Hermitian transpose).

Based on this error and calibration model, a series of simulations were conducted to evaluate the effect of phase mismatch and mutual coupling on the DOA estimation accuracy. The parameters for the simulation were SNR $\eta = 0$ dB; a normal distribution with a standard deviation of 60° and zero mean for the phase mismatch and mutual coupling phases; a uniform distribution from 0 (linear) to -7.5 dB for the mutual coupling magnitude.

The DOA estimation result for a realization of the error sources is shown in Fig. 2.21. As evident from the error plots before calibration, there is an error of $> 20^\circ$ for many azimuth / elevation combinations caused by a side lobe, which becomes higher than the main lobe due to the error terms. By applying the calibration method from Eq. (2.56), assuming ideal reference measurement data $\varphi_{az,m}$, $\vartheta_{el,m}$, the mean absolute error in both azimuth and elevation directions could be reduced to approximately 0.2° for an angle range of $\sqrt{\varphi_{az}^2 + \vartheta_{el}^2} < 60^\circ$ as shown in the middle of Fig. 2.21.

To test the stability of the calibration procedure, a normally distributed angle error in both azimuth and elevation with a standard deviation of 2° and zero mean was added to the reference measurement angles $\varphi_{az,m}$, $\vartheta_{el,m}$ in another simulation. As evident from the plots on the right-hand side of Fig. 2.21, this only slightly increased the error to about 0.35° since the reference error contributions approximately cancel out. A bias in the reference causes a bias in the result of roughly the same magnitude.

3D Position and Phase Center Errors The procedure from the previous sections was repeated, but this time 3D position errors $\mathbf{p}_{Rx,n}$ as described in Eq. (2.52) were also added to the simulation. While the calibration matrix \mathbf{T} is angle independent, the phase term $\phi_{p,n}$ caused by the antenna position errors depends on the DOA and cannot be removed by \mathbf{T} . In order to compensate it, the 3D antenna position errors \mathbf{p}_{Rx} need to be determined. This can also be accomplished by means of a least-squares fit by extending (2.55) to

$$\{\mathbf{T}, \mathbf{p}_{Rx}\} = \arg \min_{\mathbf{T}, \mathbf{p}_{Rx}} \|\tilde{\mathbf{S}}(\mathbf{p}_{Rx}) - \mathbf{T} \tilde{\mathbf{X}}\|_F. \quad (2.57)$$

This is a nonlinear least-squares problem which does not have a closed-form solution. It is, however, separable into a linear problem with respect to \mathbf{T} and a nonlinear with respect to \mathbf{p}_{Rx} [89]. The damped Newton method was used to solve it in [89]. A computationally more effective approach is presented in [90],

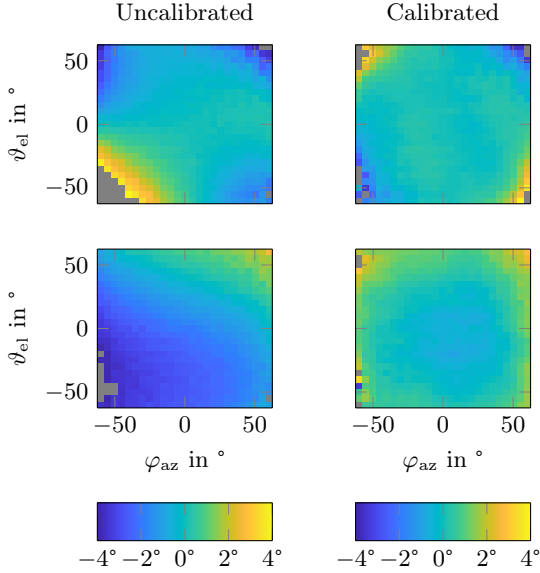


Fig. 2.22: DOA estimation error before and after position error calibration. Upper row: Azimuth error in °. Lower row: Elevation error in °. Left column: Before calibration. Right column: After calibration. Gray denotes errors beyond $\pm 4^\circ$ and azimuth/elevation combinations where DOA estimation fails due to a high sidelobe.

which, however, cannot be applied to the system at hand, since no absolute, but only relative signal phases are known.

The approach taken here, was to first find \mathbf{T} as in Eq. (2.56) and then use the Gauss-Newton method as described in Section 2.4.3 to estimate the position error \mathbf{p}_{Rx} . Similar to (2.42), the cost function is defined as

$$\begin{aligned} \mathbf{F}_x &= \begin{bmatrix} \Re\{\tilde{\mathbf{S}}(\mathbf{p}_{\text{Rx}})\} - \Re\{\mathbf{T}\tilde{\mathbf{X}}\} \\ \Im\{\tilde{\mathbf{S}}(\mathbf{p}_{\text{Rx}})\} - \Im\{\mathbf{T}\tilde{\mathbf{X}}\} \end{bmatrix} \\ &= \begin{bmatrix} \cos(\mathbf{k}^T(\varphi_{az,m}, \vartheta_{el,m})(\mathbf{r}_{\text{Rx}} + \mathbf{p}_{\text{Rx}}))^T - \Re\{\mathbf{T}\tilde{\mathbf{X}}\} \\ \sin(\mathbf{k}^T(\varphi_{az,m}, \vartheta_{el,m})(\mathbf{r}_{\text{Rx}} + \mathbf{p}_{\text{Rx}}))^T - \Im\{\mathbf{T}\tilde{\mathbf{X}}\} \end{bmatrix}, \end{aligned} \quad (2.58)$$

with the $3N$ unknowns \mathbf{p}_{Rx} (x, y, z for every channel N) and M equations (number of measurements at known directions $\varphi_{az,m}, \vartheta_{el,m}$). The algorithm is started

with initial guess $\mathbf{p}_{\text{Rx}} = \mathbf{0}$, which is assumed to be close to the searched result. If the position error is large, the algorithm is likely to converge to a local minimum.

The effect of 3D position errors with normal distribution, zero mean and a standard deviation of 1 mm ($\approx 0.1\lambda$) and its calibration is illustrated in Fig. 2.22. In another simulation, the same error was also added to the errors from the previous section. The proposed calibration approach could successfully simultaneously estimate the position errors and the mutual coupling. The mean absolute error was 0.4° for ideal reference and 0.8° for reference with errors as in the previous section. The position errors could be estimated with a mean absolute accuracy of 0.3 mm.

2.4.5.3 Measurement Results

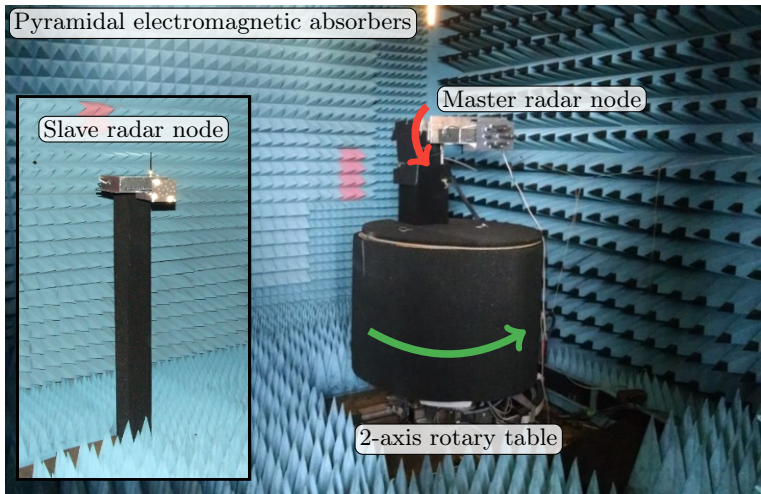


Fig. 2.23: Radar on 2-axis rotary table in anechoic chamber. The arrows denote the rotation axes.

To verify the developed calibration procedure, a series of 2000 measurements was conducted in an anechoic chamber and processed offline. The slave radar node was stationary and the master node was fixed on a programmable 2-axis rotary table as shown in Fig. 2.23. The master node was rotated in both azimuth and elevation directions in such a manner, that an angle range of $\sqrt{\varphi_{\text{az}}^2 + \vartheta_{\text{el}}^2} < 70^\circ$ was covered. A total station Leica TS30 was used to determine the rotation

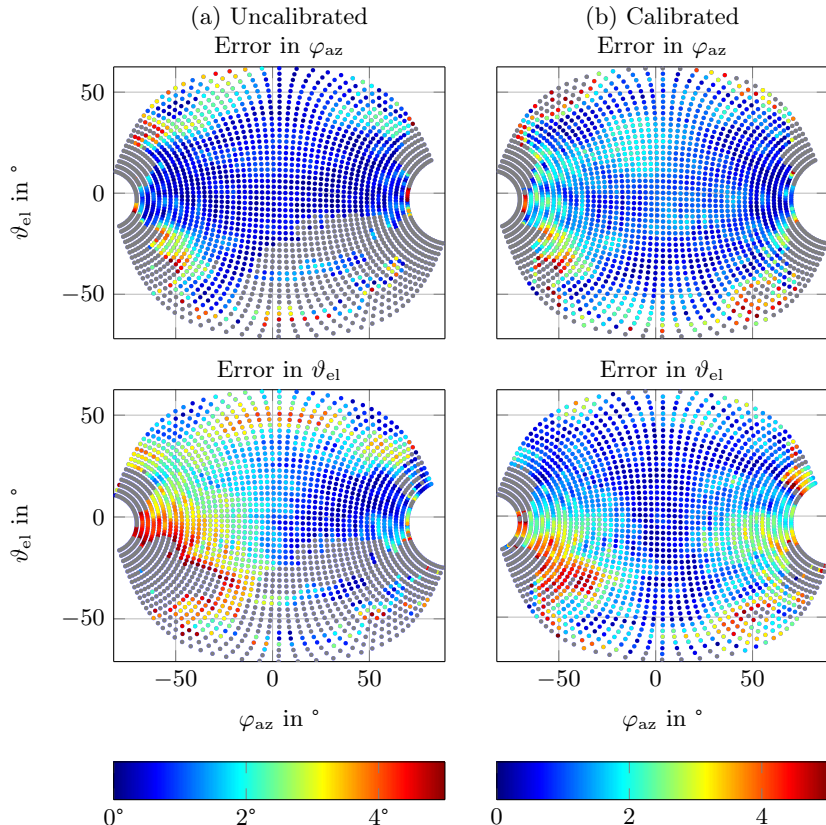


Fig. 2.24: Each dot denotes a DOA measurement. The absolute error in each measurement is color-coded corresponding to the colormap. Gray dots denote measurements with an absolute error $> 5^\circ$. a) Before calibration. b) After calibration.

axes of the rotary table in order to calculate the ideal signal matrix $\tilde{\mathbf{S}}$.

The absolute measurement error before and after applying the calibration procedure from the previous section is shown in Fig. 2.24. Each dot in the graphs represents a measurement at the corresponding azimuth and elevation angles and the color represents the absolute error in the estimation of the azimuth and

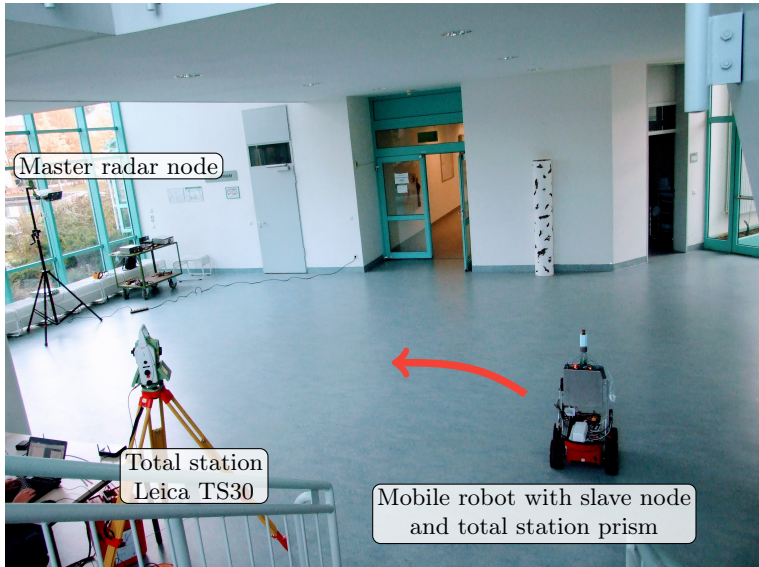


Fig. 2.25: Measurement environment: Foyer in Cauerstr. 6, FAU Erlangen-Nürnberg. The red arrow denotes the robot movement direction.

elevation angles. It is evident from the uncalibrated results that large errors occur for positive azimuth and negative elevation angles of the impinging signal. The reason is the rise of a high side lobe caused mostly by phase mismatch. Calibrating the system extends the unambiguous angular range to approximately $\sqrt{\varphi_{az}^2 + \vartheta_{el}^2} < 60^\circ$. The mean absolute angle error was approximately 1° in both azimuth and elevation directions. As shown in Fig. 2.17 b), before calibration the SLL is -2.2 dB and the main peak is shifted by about 1° in both azimuth and elevation. A more detailed study on the effect of mutual coupling on the beam pattern shape can be found in [91]. The result in Fig. 2.17 c) after calibration demonstrates the decrease of the SLL to the close-to-ideal value of -3.2 dB and the correct position of the main beam.

While the measurement in the anechoic chamber provides a very good overview of the performance of the system over the entire angular measurement range it is very arduous and time-consuming. The reference signal had to be determined by measuring the orientation of the master node with the Leica TS30 total station, which was inaccurate due to the problem geometry. The orientation of the

radar node was calculated directly from the total station measurements. A typical 3D error of the total station of 1 mm over the length of the antenna array of 7 cm results in an angle error of 0.8°. Furthermore, the two rotation axes of the rotary table had to be determined from the total station measurements, which was a further error source.

An alternative measurement procedure is shown in Fig. 2.25. A relatively large area with little multipath reflections is chosen. The master node, which is to be calibrated, was stationary and mounted on a tripod. The slave node was mounted on a mobile robot and driven in the area in front of the master node. The reference signal matrix $\tilde{\mathbf{S}}$ was obtained by tracking a prism on the mobile robot by the total station. This procedure has the advantage, that the direction to the calibration source and thus $\tilde{\mathbf{S}}$ can be determined more accurately as it is calculated by converting the prism position tracked by the total station to the local polar coordinate system of the master node's antenna array. A typical 3D error of the total station of 1 mm at a distance of 3 m results in an angle error of 0.02°. The complete pose of the master node needs to be measured precisely only once. This makes this procedure suitable for on-site calibrations.

Multiple test runs consisting of about 500 DOA measurements each were made on 2 different days and rearranging the scenario to test the stability of the calibration. The test run trajectories are shown in Fig. 2.26. The resulting accuracy (RMSE) in azimuth and elevation after separately calibrating each error source is listed in Table 2.2 (cf. Appendix B.3 regarding accuracy metrics). The calibration matrix \mathbf{T} and the position errors \mathbf{p}_{Rx} estimated from test run "call1" were used to evaluate all measurements.

As evident from the results, the phase mismatch is the dominant error source and compensating it is sufficient for reliable DOA estimation. Contrary to expectation, additionally calibrating mutual coupling slightly deteriorates the result in some of the measurements. The reason is probably multipath causing strong variations of the magnitude across the array, unstable amplification in the Rx path, or the unmodeled and uncompensated angle-dependent coupling.

An analysis of the calibration matrix illustrated in Fig. 2.27 shows a maximum coupling of -7.5 dB between channels 1 and 5. This result is reasonable as the corresponding antennas are spatially close to each other as illustrated in Fig. 2.16 a) and the on-board coupling is better than -30 dB. It can also be seen, that the diagonal elements describing the channel gain mismatch are all much larger and close to 0 dB.

By also calibrating the phase center position errors \mathbf{p}_{Rx} , the result is consistently improved in all measurements demonstrating the efficiency of the proposed calibration procedure. A combination of only phase mismatch and position errors calibration was also tested, but did not lead to any consistent improvement.

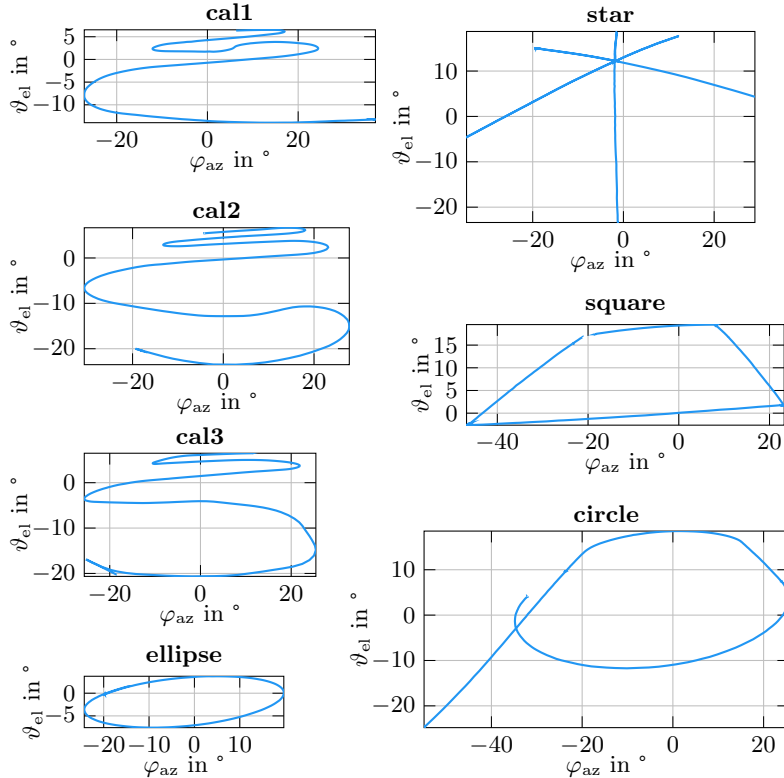


Fig. 2.26: Test runs used for calibration and testing.

Table 2.2: DOA estimation accuracy (RMSE) with calibration of different error sources. PM: phase mismatch; MC: mutual coupling; PE: position errors.

Test run	PM		PM + MC		PM + MC + PE	
	φ_{az}	ϑ_{el}	φ_{az}	ϑ_{el}	φ_{az}	ϑ_{el}
cal1	0.60°	0.77°	0.59°	0.75°	0.34°	0.69°
cal2	0.67°	1.04°	0.67°	1.03°	0.46°	0.97°
cal3	0.58°	0.92°	0.59°	0.89°	0.38°	0.87°
ellipse	0.83°	1.59°	0.92°	1.68°	0.72°	1.38°
star	0.60°	1.68°	0.67°	1.77°	0.45°	1.47°
square	0.63°	1.32°	0.74°	1.33°	0.52°	1.09°
circle	0.72°	0.88°	0.73°	0.90°	0.52°	0.77°

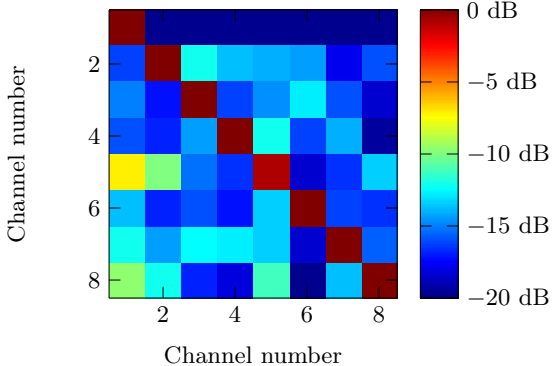


Fig. 2.27: Absolute value of phase mismatch and mutual coupling calibration matrix \mathbf{T} in dB.

The estimated 3D phase center position errors were within the range of ± 2 mm. This is a realistic value in line with the research on the position of the mean electrical phase center (MEPC) of patch antennas for GPS applications [92], [93]. A closer study and modeling of the angle-dependent phase center position of the antennas in an array could help to further improve the DOA estimation accuracy. An alternative approach would be a sector-based calibration where the angle search range is divided into sectors and a separate calibration matrix \mathbf{T}_{sec} is determined for each sector. Utilizing neural networks as mentioned in [83] is another viable possibility.

2.4.6 Ring Array

The amplitude A_n in Eq. (2.33) is not of much use for the DOA estimation with the planar array as all antennas look in the same direction and ideally receive equal signal power (assuming a single target, no multipath and equal radiation pattern and receive path characteristics). However, for the ring arrays in Fig. 2.16 b) and c), the Rx signal amplitude information can be used additionally to aid the DOA estimation in a manner similar to the classic amplitude-comparison monopulse technique in [94]. An extension also incorporating phase information and named “complex monopulse” (CMP) as a combination of amplitude-comparison monopulse and phase-comparison monopulse was presented in [95] and [96]. Instead of calculating pairwise complex ratios as in the CMP algo-

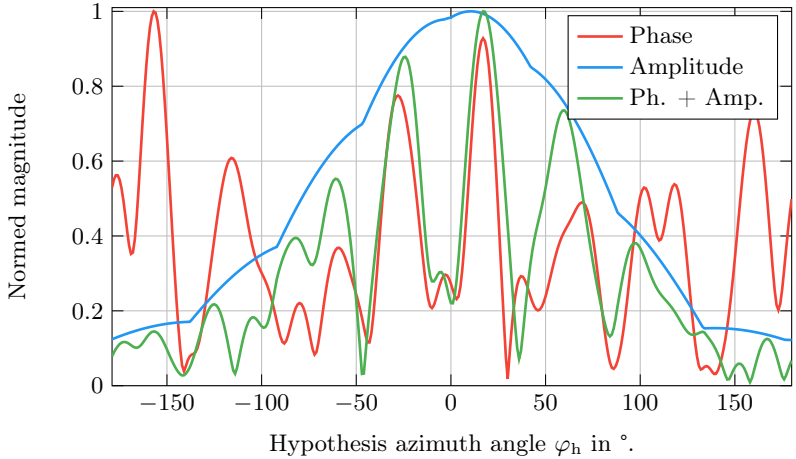


Fig. 2.28: Measurement result for DOA estimation with the ring array using only phase information, only amplitude information, and using both. A side lobe at -157.2° is present, which is higher than the main lobe at 18.1° when only the phase is used. The amplitude is used to resolve this ambiguity.

rithm, in this work the delay-and-sum digital beamformer from Eq. (2.38) was extended by amplitude hypothesis information as

$$H_{2D,\text{amp},n}(\varphi_h, \vartheta_h) = A_{\text{hyp},n}(\varphi_h, \vartheta_h) \exp(-j\mathbf{k}^T(\varphi_h, \vartheta_h)\mathbf{r}_{\text{Rx},n}), \quad (2.59)$$

with the hypothesis for the signal amplitude $A_{\text{hyp},n}$ in channel n given by

$$A_{\text{hyp},n}(\varphi_h, \vartheta_h) = f_{\text{RP}}(\varphi_h - \varphi_{\text{ant},n}, \vartheta_h - \vartheta_{\text{ant},n}). \quad (2.60)$$

The function f_{RP} describes the radiation pattern of the antenna elements. It can be implemented either as a LUT or as an analytic expression (e.g. a cardioid in the case of patch antennas [97]). In this work the equations from [98] for the radiation expression of a patch antenna were used. The angles $\varphi_{\text{ant},n}$ and $\vartheta_{\text{ant},n}$ denote the orientation of the antenna element n in the azimuth, respectively in the elevation plane in the array coordinate system (corresponding to yaw and pitch in Tait–Bryan angles). The effect of the antenna orientation in the third dimension (roll) was neglected as it only leads to an approximately equal variation of the amplitude in all antennas due to polarization mismatch. This

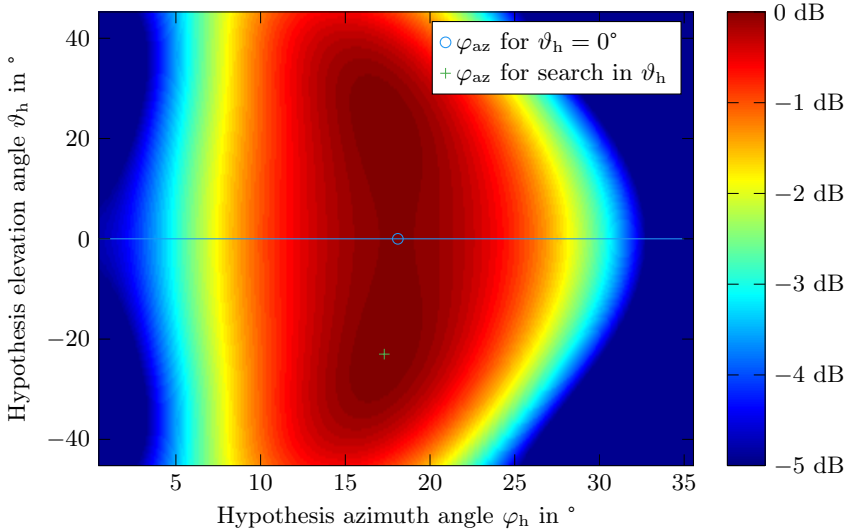


Fig. 2.29: 2D angle-estimation search.

would have no effect on the DOA algorithm, as only relative amplitudes are evaluated. Eq. (2.59) can readily be applied to 3D arrays, for example with antenna elements on the surface of a hemisphere (dome array), or within the volume of a sphere (crow's nest array).

Naturally, calibrating the ring array is very important to get reliable and accurate DOA measurements. In general, the models and procedures from Section 2.4.5 can also be applied to the ring array. However, care has to be taken to only use antennas with LOS path to the calibration target. The remaining channels contain noise or multipath reflections. Choosing the channels to use is possible by applying the hypothesis for the element radiation pattern f_{RP} for the calibration measurement direction.

The resulting pseudo-spectrum after calibration applied to real measured data when using only the signal phase, only the signal amplitude or both is depicted in Fig. 2.28. As evident, using only the signal phase as in Eq. (2.38) results in a “side lobe” at $\varphi_{az} = -157.2^\circ$ which is higher than the “main lobe” at 18.1° . Using only the amplitude, a very broad MBW results and the DOA is estimated to $\varphi_{az} = 10.3^\circ$ which is a coarse, but stable result. Combining the phase and amplitude information, the correct result $\varphi_{az} = 18.1^\circ$ is found.

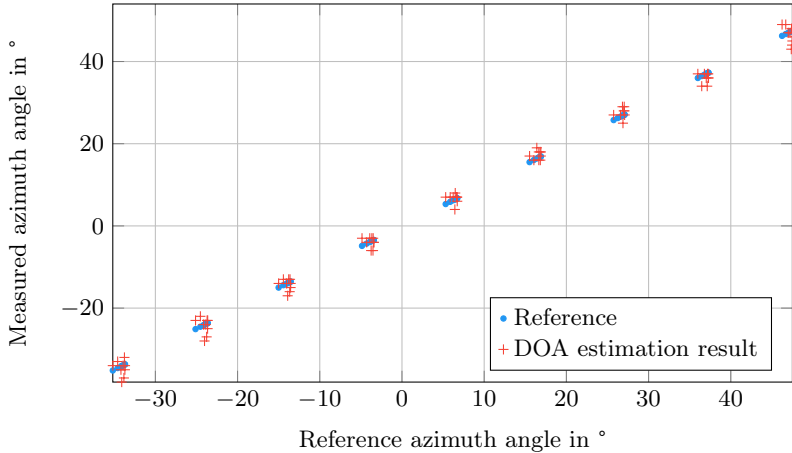


Fig. 2.30: Measurement result of azimuth DOA estimation using an 8-channel ring array in an anechoic chamber for an azimuth range of $-35^\circ \dots 50^\circ$ and elevation range of $-40^\circ \dots 40^\circ$.

Although all antenna elements lie in one plane, it is not sufficient to only perform a 1D search in azimuth direction. This is illustrated in Fig. 2.29 for a signal impinging from $\varphi_{az} = 16.7^\circ$ and $\vartheta_{el} = -43.9^\circ$. A search in both azimuth and elevation is performed as given by Eq. (2.59) and (2.40). If a search over φ_h for $\vartheta_h = 0^\circ$ is performed, the result is $\varphi_{az} = 18.1^\circ$ (the search and the result are denoted as a blue line and circle in Fig. 2.29). As can be seen, if a search over the elevation range is also performed, a better match is found at $\varphi_{az} = 17.3^\circ$ and $\vartheta_{el} = -23^\circ$ (denoted as a green plus), which is the correct result. The reason for this effect is, that the DOA estimation problem is 1D (all elements and the target lie in a plane) only when looked at from $\vartheta_{el} = 0^\circ$. When looked at from above or below, the problem becomes 3D and a 2D search is necessary for accurate DOA estimation. However, due to the very small aperture in elevation direction, no reliable elevation angle estimation is possible.

The performance of the ring array was evaluated in an anechoic chamber using the proposed algorithms. The setup was similar to Fig. 2.23. The master radar node with the ring array was fixed on a 2-axis rotary table and the slave node was stationary. Measurements in the range $-35^\circ \dots 50^\circ$ in azimuth and $-40^\circ \dots 40^\circ$ in elevation were done. The Leica total station TS30 was used as a reference. As can be seen from the result shown in Fig. 2.30, the radar

DOA measurement closely matches the reference, even for large variations in the elevation angle. Using both amplitude and phase information and a 2D search resulted in an RMSE in azimuth of 1.69° . The resulting RMSE was 4.5° when using only the amplitude information. When using both the amplitude and the phase information and performing a search only over φ_h for $\vartheta_h = 0^\circ$, the RMSE was 2.92° .

2.5 3D RTOF + DOA Positioning

In order to obtain a 3D position estimate from the combination of RTOF and DOA based on the techniques discussed in the previous sections, the measurement needs to be transformed from the polar representation $\mathbf{z} = [d \quad \varphi_{az} \quad \vartheta_{el}]^T$ to the Cartesian $\mathbf{x} = [x \quad y \quad z]^T$. This can be achieved using the basic geometric considerations

$$\mathbf{x}(\mathbf{z}) = \begin{bmatrix} x \\ y \\ z \end{bmatrix} = \begin{bmatrix} d \cos \vartheta_{el} \cos \varphi_{az} \\ d \cos \vartheta_{el} \sin \varphi_{az} \\ d \sin \vartheta_{el} \end{bmatrix}. \quad (2.61)$$

The result is given in the array coordinate system with origin in the geometric center of the array.

2.5.1 Unbiased Estimator

As shown in the previous sections, the errors in both range and angles can typically be described as Gaussian distributions. However, due to the nonlinear conversion caused by the trigonometric terms, the resulting probability distribution for the Cartesian position is in general not Gaussian anymore as shown in Fig. 2.31 (a) on the example of a 2D conversion. Furthermore, as first demonstrated in [100] and later further studied in [101], [102], [103], and [104] in the context of Converted Measurements Kalman Filter (CMKF), the estimator in Eq. (2.61) is not unbiased. This can be shown by representing the measurement \mathbf{z} as

$$\mathbf{z} = \begin{bmatrix} d \\ \varphi_{az} \\ \vartheta_{el} \end{bmatrix} = \begin{bmatrix} \bar{d} + \tilde{d} \\ \bar{\varphi}_{az} + \tilde{\varphi} \\ \bar{\vartheta}_{el} + \tilde{\vartheta} \end{bmatrix}, \quad (2.62)$$

where \bar{d} , $\bar{\varphi}_{az}$, and $\bar{\vartheta}_{el}$ denote the true values and \tilde{d} , $\tilde{\varphi}$, and $\tilde{\vartheta}$ are additive white Gaussian noise terms with zero mean and variances σ_d^2 , σ_φ^2 , and σ_ϑ^2 . Inserting

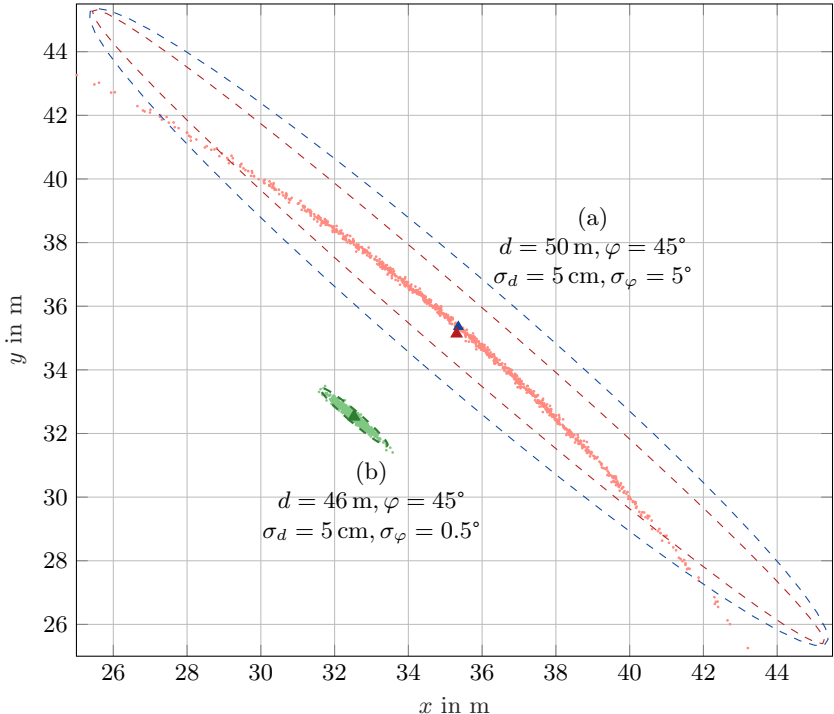


Fig. 2.31: Monte-Carlo simulation of 2D RTOF + DOA measurements converted to Cartesian coordinates (each MC run is denoted by a dot). The radar is in the origin of the coordinate system. In (a) a target was simulated at a distance $d = 50 \text{ m}$ and angle $\varphi = 45^\circ$ with a relatively large angular standard deviation of $\sigma_\varphi = 5^\circ$. The red ellipse illustrates the covariance assuming a Gaussian distribution. The ellipse corresponds to a Mahalanobis distance of 3.2 encompassing 99.5 % of the data [99]. The blue ellipse illustrates the covariance calculated by Eq. (2.67). The red triangle is the mean obtained by Eq. (2.61). The blue triangle is the unbiased mean given by Eq. (2.65). In (b), the target is 4 m closer to the radar with a relatively low angular standard deviation of $\sigma_\varphi = 0.5^\circ$. The green ellipse illustrates the covariance assuming a 2D Gaussian distribution and the green triangle denotes the mean.

Eq. (2.62) in (2.61) and taking the expectation of z yields

$$\mathbb{E}\{z\} = \mathbb{E}\left\{(\bar{d} + \tilde{d}) \sin(\bar{\vartheta}_{\text{el}} + \tilde{\vartheta})\right\} = \dots = \lambda_{\vartheta} \bar{d} \sin \bar{\vartheta}_{\text{el}}, \quad (2.63)$$

using trigonometric identities and assuming mutual independence of the range and angle noise. The bias factor is $\lambda_{\vartheta} = \mathbb{E}\{\cos \tilde{\vartheta}\} = \exp(\sigma_{\vartheta}^2/2)$. The estimator of z from Eq. (2.61) thus has a bias given by

$$b_z = \mathbb{E}\{d \sin \vartheta_{\text{el}} - \bar{d} \sin \bar{\vartheta}_{\text{el}}\} = (\lambda_{\vartheta} - 1)\bar{d} \sin \bar{\vartheta}_{\text{el}}. \quad (2.64)$$

It increases with the standard deviation of the angular noise, as well as with the distance to the target. It is also dependent on the angle to the target.

As shown in [101], the bias can be removed by pre-multiplying the estimator from Eq. (2.63) with λ_{ϑ}^{-1} , assuming the variance of the angular measurement σ_{ϑ}^2 is known. The complete unbiased estimator \mathbf{x}_u is hence given by

$$\mathbf{x}_u(z) = \begin{bmatrix} \lambda_{\vartheta}^{-1} \lambda_{\varphi}^{-1} d \cos \vartheta_{\text{el}} \cos \varphi_{\text{az}} \\ \lambda_{\vartheta}^{-1} \lambda_{\varphi}^{-1} d \cos \vartheta_{\text{el}} \sin \varphi_{\text{az}} \\ \lambda_{\vartheta}^{-1} d \sin \vartheta_{\text{el}} \end{bmatrix}. \quad (2.65)$$

The mean obtained by the standard conversion from (2.61) is shown as a red triangle in Fig. 2.31 (a) and has an error of approximately 13 cm in both x and y directions. The correct mean obtained by the unbiased estimator is shown as a blue triangle.

The entries of the corresponding covariance matrix $\mathbf{R}_{\mathbf{x}\mathbf{x},u}$ can be calculated by

$$R_{\mathbf{x}\mathbf{x},u,i,j} = \mathbb{E}\{(x_i - \mathbb{E}\{x_i\})(x_j - \mathbb{E}\{x_j\}) | \bar{d}, \bar{\varphi}_{\text{az}}, \bar{\vartheta}_{\text{el}}\}, \quad (2.66)$$

where x_i denotes the i -th entry of \mathbf{x}_u . However, the expectation in Eq. (2.66) is conditioned on the true values. Since they are unknown in practice, [101] proposes to approximate it by conditioning it on the measurements instead

$$R_{\mathbf{x}\mathbf{x},u,i,j} = \mathbb{E}\{(x_i - \mathbb{E}\{x_i\})(x_j - \mathbb{E}\{x_j\}) | d, \varphi_{\text{az}}, \vartheta_{\text{el}}\}. \quad (2.67)$$

The covariance matrix calculated based on the standard conversion from Eq. (2.61) is illustrated as a red ellipse in Fig. 2.31 (a); the result of Eq. (2.67) is shown in blue. As evident from the plot, the resulting probability distribution can only roughly be approximated by a Gaussian distribution.

2.5.2 CRLB for 3D RTOF + DOA Positioning

In the opposite case when the angular measurement variances σ_{φ}^2 and σ_{ϑ}^2 are relatively small or the distance to the target is relatively short, the resulting

probability distribution after conversion to Cartesian coordinates can be well approximated by a Gaussian distribution and the bias of the estimator in Eq. (2.61) can be neglected. This is illustrated by the green distribution, ellipse and mean in Fig. 2.31 (b). Then, based on the range and angular CRLB calculated in Sections 2.3.1 and 2.4.4, a CRLB for the 3D position can be derived [105], [106]. With the vector to be estimated $\mathbf{x} = [x \ y \ z]^T$, the measurement vector \mathbf{z} conditioned on \mathbf{x} is given by the standard conversion from Cartesian to polar coordinates

$$\mathbf{z}(\mathbf{x}) = \begin{bmatrix} d \\ \varphi_{\text{az}} \\ \vartheta_{\text{el}} \end{bmatrix} = \begin{bmatrix} \sqrt{x^2 + y^2 + z^2} \\ \text{atan2}(y, x) \\ \text{atan2}(z, \sqrt{x^2 + y^2}) \end{bmatrix}, \quad (2.68)$$

where $\text{atan2}(\cdot)$ is the four-quadrant extension of the arcus tangens defined in Appendix A.2.

The corresponding likelihood function to obtain the polar representation \mathbf{z} given the Cartesian \mathbf{x} can then be approximated by a multivariate Gaussian distribution given by

$$p(\mathbf{z}|\mathbf{x}) = \frac{1}{\sqrt{\det(2\pi\mathbf{Q})}} \exp\left(-\frac{1}{2}(\mathbf{z} - \mathbb{E}\{\mathbf{z}(\mathbf{x})\})^T \mathbf{Q}^{-1} (\mathbf{z} - \mathbb{E}\{\mathbf{z}(\mathbf{x})\})\right), \quad (2.69)$$

where \mathbf{Q} denotes the covariance matrix of the measurement

$$\mathbf{Q} = \begin{bmatrix} \sigma_d^2 & 0 & 0 \\ 0 & \sigma_{\varphi_{\text{az}}}^2 & 0 \\ 0 & 0 & \sigma_{\vartheta_{\text{el}}}^2 \end{bmatrix}. \quad (2.70)$$

The Fisher Information Matrix (FIM)

$$\mathbf{J}_{\mathbf{x}} = \mathbb{E}_{\mathbf{x}} \left\{ \left(\frac{\partial \ln p(\mathbf{z}|\mathbf{x})}{\partial \mathbf{x}} \right) \cdot \left(\frac{\partial \ln p(\mathbf{z}|\mathbf{x})}{\partial \mathbf{x}} \right)^T \right\}. \quad (2.71)$$

is then the expectation conditioned on \mathbf{x} of the squared log-likelihood of $p(\mathbf{z}|\mathbf{x})$ [57]. As shown in [57], Chapter 3.9 and in [106], inserting Eq. (2.69) in (2.71) yields

$$\mathbf{J}_{\mathbf{x}} = \mathbf{G}^T \mathbf{Q}^{-1} \mathbf{G}, \quad (2.72)$$

with the observation matrix \mathbf{G} , which is the Jacobian

$$\mathbf{G} = \frac{\partial \mathbf{z}(\mathbf{x})}{\partial \mathbf{x}}. \quad (2.73)$$

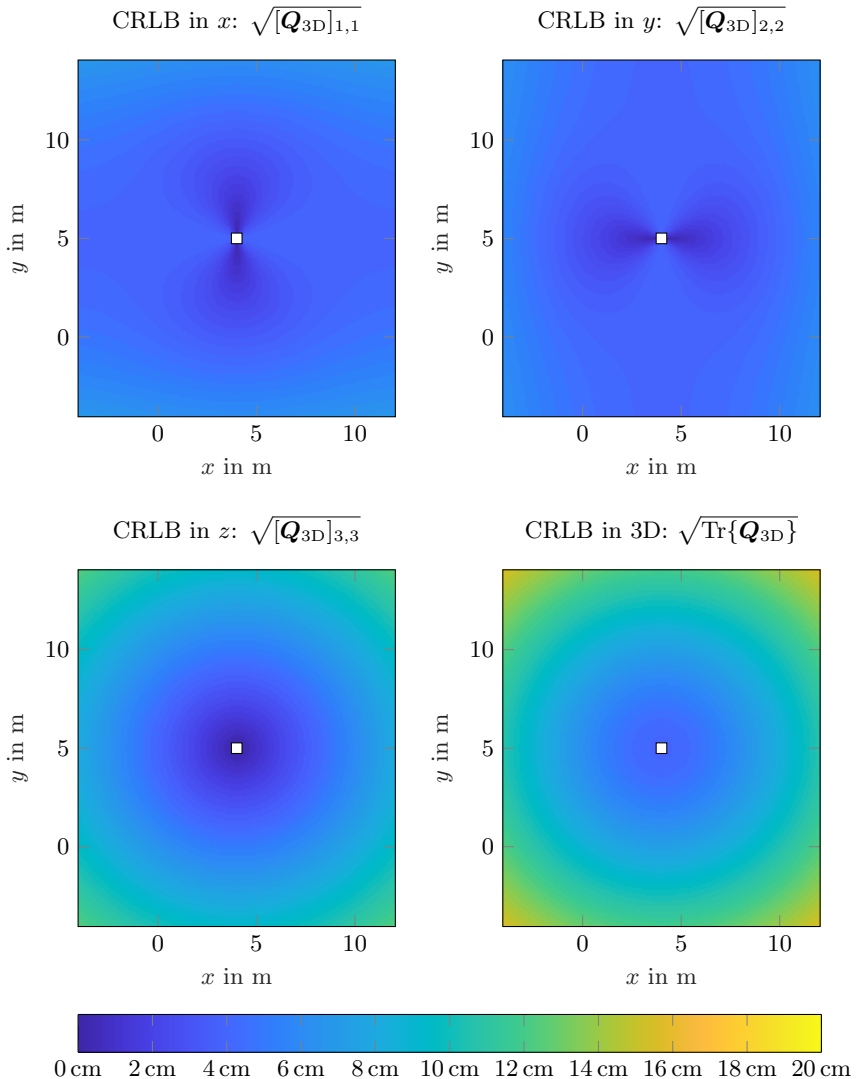


Fig. 2.32: The result for the CRLB in x , y , z direction and in 3D using a combination of RTOF and DOA with one static radar node denoted by a white square.

The CRLB \mathbf{Q}_{3D} is then the inverse of \mathbf{J}_x from Eq. (2.72)

$$\mathbf{Q}_{3D} = \mathbf{J}_x^{-1} = (\mathbf{G}^T \mathbf{Q}^{-1} \mathbf{G})^{-1}. \quad (2.74)$$

This means that given a measurement in polar coordinates \mathbf{z} with a covariance matrix \mathbf{Q} which is converted to Cartesian \mathbf{x} with a covariance matrix \mathbf{Q}_x ,

$$Q_{x,i,i} \geq [\mathbf{J}_x^{-1}]_{i,i}, \quad (2.75)$$

applies for $i = 1, 2, 3$.

If the estimator from Eq. (2.68) is approximated by the first-order Taylor expansion around the expectation of the measurement

$$\mathbf{x}(\mathbf{z}) \approx \mathbf{x}(\mathbb{E}\{\mathbf{z}\}) + \frac{\partial \mathbf{x}(\mathbf{z})}{\partial \mathbf{z}}(\mathbf{z} - \mathbb{E}\{\mathbf{z}\}), \quad (2.76)$$

the covariance matrix \mathbf{Q}_x becomes

$$\begin{aligned} \mathbf{Q}_x &= \mathbb{E}_{\mathbf{z}} \left\{ (\mathbf{x} - \mathbb{E}\{\mathbf{x}\})(\mathbf{x} - \mathbb{E}\{\mathbf{x}\})^T \right\} \\ &= \frac{\partial \mathbf{x}(\mathbf{z})}{\partial \mathbf{z}} \mathbb{E}_{\mathbf{z}} \left\{ (\mathbf{z} - \mathbb{E}\{\mathbf{z}\})(\mathbf{z} - \mathbb{E}\{\mathbf{z}\})^T \right\} \frac{\partial \mathbf{x}(\mathbf{z})}{\partial \mathbf{z}}^T \\ &= \mathbf{G}^{-1} \mathbf{Q} \mathbf{G}^{-T} = \mathbf{J}_x^{-1}. \end{aligned} \quad (2.77)$$

The estimator from Eq. (2.62) thus attains the CRLB (2.74), if the Taylor approximation in Eq. (2.76) is accurate, i.e. if the conversion is linear.

The components of the CRLB \mathbf{Q}_{3D} were evaluated on a grid of 10 cm in 2D in the area around the radar node as shown in Fig. 2.32 (cf. Appendix B.4 regarding CRLB and position dilution of precision (PDOP)). The values $\sigma_d = 8$ cm, $\sigma_{\varphi_{az}} = 0.8^\circ$, and $\sigma_{\vartheta_{el}} = 1.2^\circ$ were assumed for the range, azimuth, and elevation standard deviations. For simplicity, omnidirectional antenna coverage was assumed. As evident, a single radar node combining the RTOF and DOA measurement principles is sufficient for 3D positioning with an accuracy < 15 cm within a range of 12 m.

2.5.3 Measurement Results

A series of indoor tests was conducted to evaluate the system. In order to get an estimate for the intrinsic performance, an environment with few multipath reflections was needed. The relatively large foyer of the FAU Erlangen-Nürnberg building at Cauerstr. 6 from Fig. 2.25 was chosen. One radar node equipped with the 2D planar antenna array from Fig. 2.16 (a) was fixed on a tripod at a height of approximately 2 m (depicted as a dark red square in Fig. 2.33). A

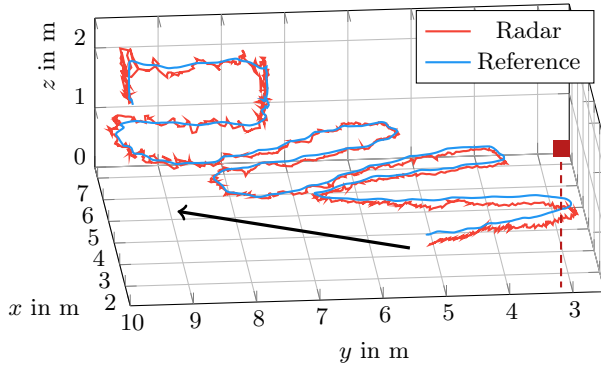


Fig. 2.33: 3D positioning result. One radar node (denoted by the dark red square) was stationary. A second node was carried by a person (the black arrow denotes the movement direction).

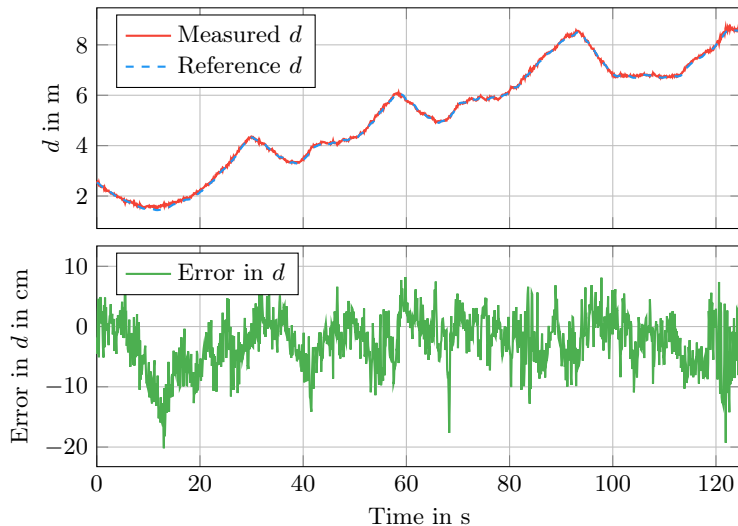


Fig. 2.34: Distance measurement result and error.

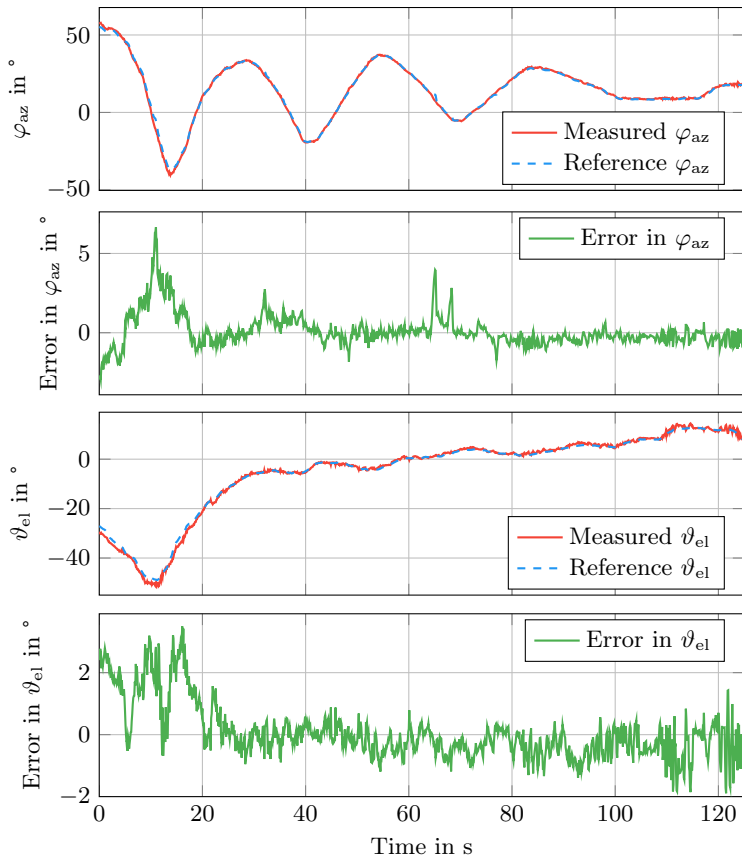


Fig. 2.35: Azimuth and elevation angles measurement result and error.

second node was carried by a person in his hands and moved in normal walking speed in the area in front of the stationary node. A total station Leica TS30 was used as a 3D ground-truth reference.

The walked trajectory as measured by the radar and the total station is shown in Fig. 2.33, demonstrating a very good correspondence of the radar to the ground truth. The 3D positioning result of the total station was converted from the global Cartesian to the local radar polar coordinate system. The measurements were recorded in a common time basis and the total station results were linearly interpolated to the measurement times of the radar in order to estimate its accuracy. The result of the distance measurement and the corresponding error is shown in Fig. 2.34. The error was mostly within the bounds of ± 10 cm and the root-mean-square error (RMSE) was 5.12 cm. The angle error depicted in Fig. 2.35 was mostly less than $\pm 2^\circ$; RMSE was 1.03° in azimuth and 0.91° in elevation.

Although this presents a very good positioning result, it is worse than the CRLB calculated in the previous chapters. There are several reasons for that discrepancy. There exist a number of multipath components caused by signal reflections on the floor, ceiling and walls distorting the LOS signal. The DOA

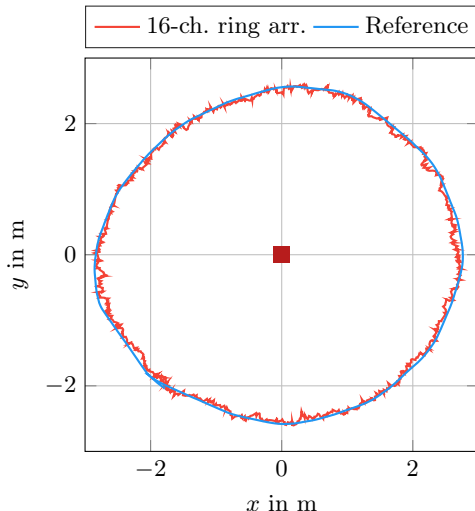


Fig. 2.36: 2D positioning result using 16-channel ring array. The dark red square denotes the position of the master radar node.

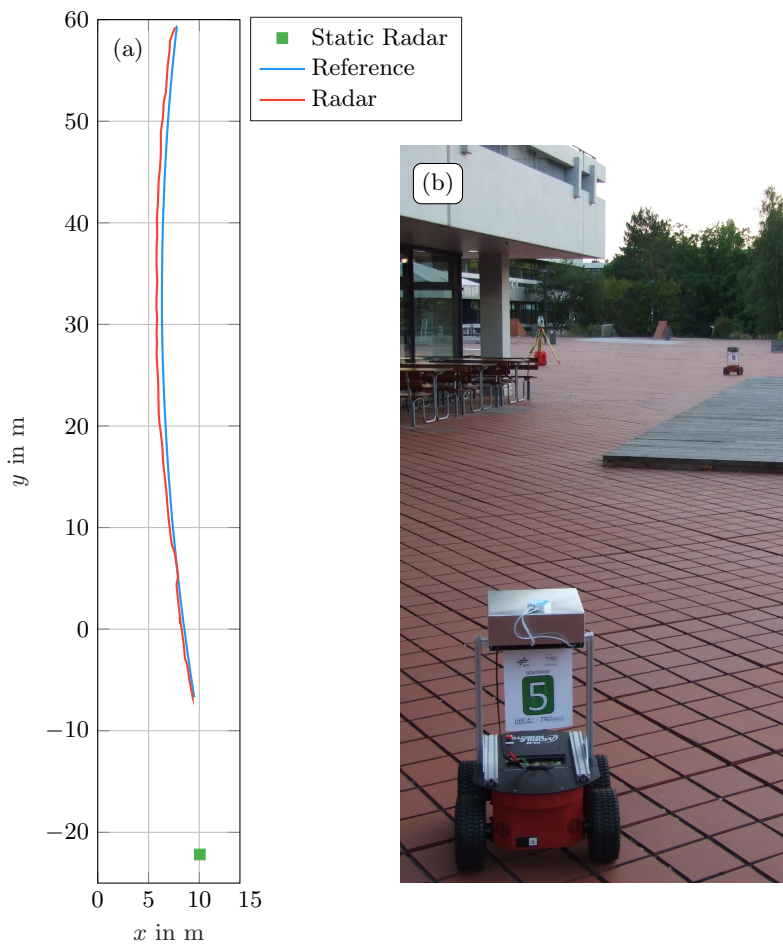


Fig. 2.37: Localization result (a) in outdoor scenario (b) at a range of up to 80 m.

estimation is also affected by imperfect calibration. Although care was taken to obtain accurate ground-truth data in space and time, residual synchronization errors between the radar and the total station are still present. Furthermore, not the same point in space was tracked by the total station (tracking a prism) and the radar (tracking the Tx antenna of mobile radar node). This was manually compensated after the measurement, but still leaves room for some additional error.

Another test run in an equivalent scenario was performed using the 16-channel ring antenna array from Fig. 2.16 (c). The master node with the ring array was stationary at a height of approximately 1 m in the middle of the foyer and a mobile robot carrying the slave node went in circles around it. The result in Fig. 2.36 shows a very good match between the radar result and the reference and demonstrates the omnidirectional coverage in azimuth. The range RMSE was 4.03 cm and the azimuth RMSE was 1.17°.

In order to verify the system performance at larger distances, an outdoor measurement was also performed as shown in Fig. 2.37. Unfortunately, due to test site limitations the maximum measured distance was 80 m. As can be seen, the measurement result was very stable with an RMSE of 6 cm in distance, 0.72° in azimuth, and 0.65° in elevation. Based on this measurement, the result in Fig. 2.6, and the FSPL equation, the maximum measurement range of the system was calculated to 250 m for the estimator “sumabs” and 150 m for “1 channel” from Section 2.3.1.2.

3 Probabilistic Sensor Fusion for Mobile Robot Localization Applications

As no model can reflect reality perfectly and no sensor can provide ideal measurements, the result of any mobile robot localization algorithm inevitably contains a certain amount of error. In order to take this into account, algorithms based on the probabilistic paradigm were developed. They consider states and measurements not as single values, but as probability distributions. This allows to represent the corresponding uncertainties in a mathematically correct manner and weight them in such a way as to obtain an optimal estimate of the true pose of the mobile robot operating in a noisy world [107].

3.1 Bayes Filter

The state can be divided in static and dynamic. In the context of the discussed applications, the static state consists of the map of the environment and the poses of the radar nodes. The dynamic state represents the mobile robot pose. For 3D localization problems, the pose is six-dimensional (position x, y, z and orientation yaw, pitch, roll); for 2D problems – three-dimensional (position x, y and orientation yaw, resp. heading).

The mobile robot can influence the state by executing a control action such as moving for a given time with a certain velocity. The control data thus represents the change of state. The mobile robot can also gather information about the state by doing measurements like estimating the distance to a static radar node. The measurement data conveys information about the current state. In this work, the state will be represented by the vector \mathbf{x}_t , the measurements by \mathbf{z}_t , and the control by \mathbf{u}_t , where the index t denotes the discrete time step.

The state is said to be complete, if it reflects all aspects that carry any information useful to predict the next state so that no past measurements and controls would improve the prediction. This is equivalent to assuming that the state transition probability can be modeled as a one-dimensional Markov chain:

$$p(\mathbf{x}_t | \mathbf{x}_{0:t-1}, \mathbf{z}_{1:t-1}, \mathbf{u}_{1:t}) = p(\mathbf{x}_t | \mathbf{x}_{t-1}, \mathbf{u}_t), \quad (3.1)$$

where the function $p(\cdot|\cdot)$ denotes the conditional probability of its first argument on the second argument. The complete state assumption means that it is pos-

sible to estimate the state recursively based only on the previous estimate and the last control. The current state is conditionally independent of the previous states, measurements, and controls. This greatly reduces the computational cost of the algorithm.

The complete-state assumption applied to the measurement probability implies

$$p(\mathbf{z}_t | \mathbf{x}_{0:t}, \mathbf{z}_{1:t-1}, \mathbf{u}_{1:t}) = p(\mathbf{z}_t | \mathbf{x}_t). \quad (3.2)$$

This means that the result of a measurement can be predicted based only on the current state and no previous states, measurements, or controls improve this prediction.

However, discrepancies between the models and the real world violate the complete-state assumption. In the case of a WLPS, these are e.g. non-idealities in the motion and measurement models, but also systematic measurement errors caused, for example, by multipath reflections and static or mobile objects obstructing the LOS path between the secondary radar nodes. Multipath errors, however, tend to have a close-to-random behavior when viewed over a range of positions and can be roughly modeled as a stochastic error source (cf. Section 2.3.2). In general, probabilistic algorithms are relatively robust to a mismatch between model and reality.

As the true ideal state \mathbf{x}_t is unknown and cannot be directly measured, probabilistic algorithms instead calculate and maintain a belief bel for the state \mathbf{x}_t . The belief after executing a control is given by

$$\overline{\text{bel}}(\mathbf{x}_t) = p(\mathbf{x}_t | \mathbf{z}_{1:t-1}, \mathbf{u}_{1:t}). \quad (3.3)$$

The bar $\overline{\cdot}$ denotes a prediction, i.e. an estimate for the state based on all controls and past measurements. By also including the last measurement in the update step, the belief becomes

$$\text{bel}(\mathbf{x}_t) = p(\mathbf{x}_t | \mathbf{z}_{1:t}, \mathbf{u}_{1:t}). \quad (3.4)$$

Executing a control (the prediction step) always increases the uncertainty and integrating the measurement (update step) always decreases the uncertainty of the belief (except for the extreme cases of ideal controls or infinitely inaccurate measurements).

Eq. (3.3) and (3.4) provide the foundation for the Bayes filter. Given an initial state \mathbf{x}_0 with a belief $\text{bel}(\mathbf{x}_0)$, it recursively incorporates the control and calculates a state prediction using the theorem of total probability:

$$\overline{\text{bel}}(\mathbf{x}_t) = \int p(\mathbf{x}_t | \mathbf{u}_t, \mathbf{x}_{t-1}) \text{bel}(\mathbf{x}_{t-1}) d\mathbf{x}_{t-1}. \quad (3.5)$$

Then it updates it with the measurement:

$$\text{bel}(\mathbf{x}_t) = \eta p(\mathbf{z}_t | \mathbf{x}_t) \overline{\text{bel}}(\mathbf{x}_t), \quad (3.6)$$

with the normalization constant η . As the Bayes filter can only be directly applied to very simple problems, it will not be further discussed here. However, it is the basis of many other probabilistic algorithms [107].

3.2 Kalman Filter

The Kalman filter implements the Bayes filter for the case of linear Gaussian systems. It represents the belief by the moments representation, i.e. by the mean μ and the covariance Σ . On top of the complete-state assumption, the Kalman filter also requires that the initial belief $\text{bel}(x_0)$ is Gaussian and that the motion and measurement models are linear. This ensures that the distribution of the posteriors will always remain Gaussian.

The state transition from state \mathbf{x}_{t-1} to state \mathbf{x}_t with the control \mathbf{u}_t is expressed by

$$\mathbf{x}_t = \mathbf{A}_t \mathbf{x}_{t-1} + \mathbf{B}_t \mathbf{u}_t + \boldsymbol{\varepsilon}_t. \quad (3.7)$$

The noise vector $\boldsymbol{\varepsilon}_t \sim \mathcal{N}(\mathbf{0}, \mathbf{R}_t)$ models the increase in uncertainty caused by the state transition as a multivariate Gaussian distribution with zero mean and covariance matrix \mathbf{R}_t . The state, the control, and the noise are column vectors. The square matrix \mathbf{A}_t models the change of state to the next time step when no control is present. The matrix \mathbf{B}_t transforms the control into a state change.

The state transition probability from Eq. (3.1) then becomes

$$p(\mathbf{x}_t | \mathbf{x}_{t-1}, \mathbf{u}_t) = \frac{1}{\sqrt{\det(2\pi \mathbf{R}_t)}} \exp \left(-\frac{1}{2} (\mathbf{x}_t - \mathbb{E}\{\mathbf{x}_t\})^T \mathbf{R}_t^{-1} (\mathbf{x}_t - \mathbb{E}\{\mathbf{x}_t\}) \right), \quad (3.8)$$

with the expectation $\mathbb{E}\{\mathbf{x}_t\} = \mathbf{A}_t \mathbf{x}_{t-1} + \mathbf{B}_t \mathbf{u}_t$.

Similarly, the measurement \mathbf{z}_t is obtained by

$$\mathbf{z}_t = \mathbf{C}_t \mathbf{x}_t + \boldsymbol{\delta}_t, \quad (3.9)$$

with the measurement noise term $\boldsymbol{\delta}_t \sim \mathcal{N}(\mathbf{0}, \mathbf{Q}_t)$ and the matrix \mathbf{C}_t implementing the linear measurement model. The measurement probability from Eq. (3.2) is then given by

$$p(\mathbf{z}_t | \mathbf{x}_t) = \frac{1}{\sqrt{\det(2\pi \mathbf{Q}_t)}} \exp \left(-\frac{1}{2} (\mathbf{z}_t - \mathbb{E}\{\mathbf{z}_t\})^T \mathbf{Q}_t^{-1} (\mathbf{z}_t - \mathbb{E}\{\mathbf{z}_t\}) \right), \quad (3.10)$$

where $\mathbb{E}\{\mathbf{z}_t\} = \mathbf{C}_t \mathbf{x}_t$.

By inserting Eq. (3.8) into (3.5) and after some manipulations which can be found e.g. in [57] or [107], the predicted belief $\bar{\text{bel}}(\mathbf{x}_t)$ at time step t represented by the mean $\bar{\boldsymbol{\mu}}_t$ and the covariance $\bar{\boldsymbol{\Sigma}}_t$ is

$$\begin{aligned}\bar{\boldsymbol{\mu}}_t &= \mathbf{A}_t \boldsymbol{\mu}_{t-1} + \mathbf{B}_t \mathbf{u}_t, \\ \bar{\boldsymbol{\Sigma}}_t &= \mathbf{A}_t \boldsymbol{\Sigma}_{t-1} \mathbf{A}_t^T + \mathbf{R}_t.\end{aligned}\quad (3.11)$$

Similarly, inserting Eq. (3.10) and (3.11) in (3.6), the updated belief $\text{bel}(\mathbf{x}_t)$ at time step t given by the mean $\boldsymbol{\mu}_t$ and the covariance $\boldsymbol{\Sigma}_t$ is

$$\begin{aligned}\boldsymbol{\mu}_t &= \bar{\boldsymbol{\mu}}_t + \mathbf{K}_t \Delta \mathbf{z}, \\ \boldsymbol{\Sigma}_t &= (\mathbf{I} - \mathbf{K}_t \mathbf{C}_t) \bar{\boldsymbol{\Sigma}}_t,\end{aligned}\quad (3.12)$$

with

$$\begin{aligned}\Delta \mathbf{z} &= \mathbf{z}_t - \mathbf{C}_t \bar{\boldsymbol{\mu}}_t = \mathbf{z}_t - \hat{\mathbf{z}}_t, \\ \mathbf{K}_t &= \bar{\boldsymbol{\Sigma}}_t \mathbf{C}_t^T \mathbf{S}_t^{-1}, \\ \mathbf{S}_t &= \mathbf{C}_t \bar{\boldsymbol{\Sigma}}_t \mathbf{C}_t^T + \mathbf{Q}_t.\end{aligned}\quad (3.13)$$

\mathbf{I} denotes an identity matrix the size of $\boldsymbol{\Sigma}_t$. The innovation vector $\Delta \mathbf{z}$ is the difference between the measurement \mathbf{z}_t and the predicted measurement $\hat{\mathbf{z}}_t = \mathbf{C}_t \bar{\boldsymbol{\mu}}_t$. The innovation covariance matrix \mathbf{S}_t is given by the addition of the uncertainty after the prediction step converted from state space to measurement space $\mathbf{C}_t \bar{\boldsymbol{\Sigma}}_t \mathbf{C}_t^T$ and the measurement uncertainty \mathbf{Q}_t . It is used to calculate the Kalman gain \mathbf{K}_t , which can be interpreted as a weighting factor for the measurement represented by the innovation vector $\Delta \mathbf{z}$. When the measurement uncertainty \mathbf{Q}_t is small, \mathbf{K}_t is large and the measurement is trusted more – the mean is changed to match the measurement and the covariance is decreased as shown in Eq. (3.12). In fact, for $\mathbf{Q}_t = \mathbf{0}$ we obtain $\boldsymbol{\Sigma}_t = \mathbf{0}$, i.e. for ideal measurements, there is no uncertainty in the state estimation. For $\mathbf{Q}_t \rightarrow \infty$, the update step does not change the belief $\text{bel}(\mathbf{x}_t)$, since the measurement is infinitely inaccurate.

3.3 Extended Kalman Filter (EKF)

If the motion and/or measurement model is not linear – which is frequently the case for real systems – the Kalman filter from Chapter 3.2 is not applicable. Instead, the extended Kalman filter (EKF) can be used. It represents the state transition and the measurement by the nonlinear functions \mathbf{g} and \mathbf{h} :

$$\begin{aligned}\mathbf{x}_t &= \mathbf{g}(\mathbf{u}_t, \mathbf{x}_{t-1}) + \boldsymbol{\varepsilon}_t, \\ \mathbf{z}_t &= \mathbf{h}(\mathbf{x}_t) + \boldsymbol{\delta}_t\end{aligned}\quad (3.14)$$

(compare with Eq. (3.7) and (3.9)). Due to the nonlinearity of the models, the posterior uncertainty distributions are no longer Gaussian. The core concept of the EKF consists in using a linear approximation of the nonlinear model obtained from the first-order Taylor expansion of \mathbf{g} and \mathbf{h} around the most likely state estimate. It is given by the Jacobian matrices \mathbf{G}_t and \mathbf{H}_t :

$$\begin{aligned}\mathbf{G}_t &= \left. \frac{\partial \mathbf{g}}{\partial \mathbf{x}} \right|_{\mathbf{u}_t, \bar{\mu}_t}, \\ \mathbf{H}_t &= \left. \frac{\partial \mathbf{h}}{\partial \mathbf{x}} \right|_{\bar{\mu}_t}.\end{aligned}\quad (3.15)$$

Using these Jacobians to replace the matrices \mathbf{A}_t and \mathbf{C}_t from Chapter 3.2 guarantees that the state uncertainty will always be approximated by a Gaussian distribution.

Similar to Eq. (3.11) the EKF prediction step is then given by

$$\begin{aligned}\bar{\mu}_t &= \mathbf{g}(\mathbf{u}_t, \mu_{t-1}) \\ \bar{\Sigma}_t &= \mathbf{G}_t \Sigma_{t-1} \mathbf{G}_t^T + \mathbf{R}_t.\end{aligned}\quad (3.16)$$

The update step becomes (cf. Eq. (3.12) and (3.13))

$$\begin{aligned}\mu_t &= \bar{\mu}_t + \mathbf{K}_t (\mathbf{z}_t - \mathbf{h}(\bar{\mu}_t)), \\ \Sigma_t &= (\mathbf{I} - \mathbf{K}_t \mathbf{H}_t) \bar{\Sigma}_t,\end{aligned}\quad (3.17)$$

with

$$\begin{aligned}\mathbf{S}_t &= \mathbf{H}_t \bar{\Sigma}_t \mathbf{H}_t^T + \mathbf{Q}_t, \\ \mathbf{K}_t &= \bar{\Sigma}_t \mathbf{H}_t^T \mathbf{S}_t^{-1}.\end{aligned}\quad (3.18)$$

The EKF provides a method to handle weakly nonlinear systems by approximating the unknown underlying probability density function by a unimodal multivariate Gaussian distribution. While this improves the computational efficiency, the linear approximation given by the Taylor expansion is not always accurate. This is the case for large uncertainties and for locally highly nonlinear functions, since the resulting probability distributions can only poorly be approximated by a Gaussian. Nevertheless, in practical applications the EKF is robust even in cases when the underlying assumptions are somewhat violated.

Further algorithms such as the unscented Kalman filter (UKF) and the particle filter (PF) were developed to tackle non-linear problems. However, as shown in [108] and [109], these algorithms are more computationally expensive and do not outperform the EKF in the case of landmark-based positioning which is observed here. Therefore, they will not be discussed further in this work.

3.4 Geometric Interpretation of the Covariance Matrix

In order to facilitate the description of the sensor fusion algorithms used, a brief overview of the geometric properties of the covariance matrix used to describe the state and measurement uncertainty is given here following [110], [111], and [99]. The covariance matrix Σ for the 2D case is

$$\Sigma = \begin{bmatrix} \sigma(x, x) & \sigma(x, y) \\ \sigma(y, x) & \sigma(y, y) \end{bmatrix}, \quad (3.19)$$

with the data covariance

$$\sigma(x, y) = \sigma(y, x) = \mathbb{E}\{(x - \mathbb{E}(x))(y - \mathbb{E}(y))\}. \quad (3.20)$$

The Mahalanobis distance

$$D_M(\mathbf{u}) = \sqrt{(\mathbf{u} - \boldsymbol{\mu})^T \Sigma^{-1} (\mathbf{u} - \boldsymbol{\mu})}. \quad (3.21)$$

is a measure of how far away in terms of “standard deviations” a point \mathbf{u} is from the mean $\boldsymbol{\mu} = [\mathbb{E}(x) \quad \mathbb{E}(y)]^T$. Using the Mahalanobis distance, a 2D covariance matrix can be visualized as an ellipse on which D_M is constant. The uncertainty ellipse is given by the set of points

$$E(l) = \{\mathbf{u} \in \mathbb{R}^2 \mid D_M(\mathbf{u}) = l_D\}, \quad (3.22)$$

where l_D is a parameter determining the percentage of the values lying within the ellipse.

Fig. 3.1 (a) illustrates the Gaussian distribution corresponding to a covariance matrix for the case $\sigma(x, y) = 0$ with zero mean as an uncertainty ellipse with $D_M = 3$. As evident, the axes of the resulting uncertainty ellipse are parallel to the x and y axes. In the illustrated case, the uncertainty is high along the y axis and lower along the x axis. If the eigendecomposition of Σ

$$\Sigma = \mathbf{V} \mathbf{L} \mathbf{V}^{-1} \quad (3.23)$$

is analyzed, the matrix \mathbf{V} whose columns are the eigenvectors of Σ is

$$\mathbf{V} = \begin{bmatrix} 1 & 0 \\ 0 & 1 \end{bmatrix}. \quad (3.24)$$

The matrix \mathbf{L} whose diagonal elements are the corresponding eigenvalues is

$$\mathbf{L} = \begin{bmatrix} \sigma(x, x) & 0 \\ 0 & \sigma(y, y) \end{bmatrix}. \quad (3.25)$$

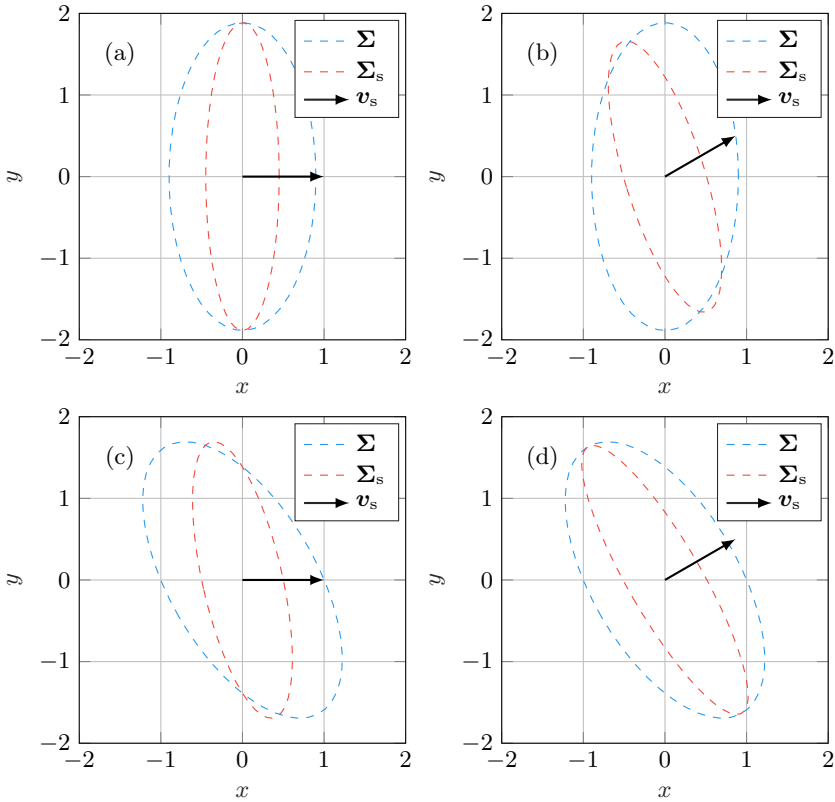


Fig. 3.1: Geometry-dependent reduction of uncertainty.

Analyzing the covariance matrix Σ illustrated in Fig. 3.1 (c) with $\sigma(x, y) \neq 0$, which is merely a rotated version of the matrix in (a), shows that it has unchanged eigenvalue matrix L , but its eigenvectors now point in the direction of the largest variance. The covariance elements $\sigma(x, y)$ have the effect of changing the orientation of the ellipse since they express the correlation in uncertainty in the x and y direction. The variances determine the length of the main axes of the ellipse.

The covariance matrix Σ can thus be interpreted as an identity matrix I scaled by the scaling matrix $S = \sqrt{L}$ and subsequently rotated by the rotation

matrix $\mathbf{R} = \mathbf{V}$:

$$\boldsymbol{\Sigma} = \mathbf{RSISR}^T. \quad (3.26)$$

Since \mathbf{R} is orthogonal $\mathbf{R}^{-1} = \mathbf{R}^T$ applies. Because \mathbf{S} is diagonal $\mathbf{S}^T = \mathbf{S}$ is valid.

If a sensor provides measurement data along a direction \mathbf{v}_s , this would reduce the position uncertainty along this direction. If the direction of \mathbf{v}_s coincides with the x direction, the resulting covariance matrix $\boldsymbol{\Sigma}_s$ can be calculated by stretching (resp. shrinking) by a scaling factor of $l_s < 1$:

$$\boldsymbol{\Sigma}_s = \begin{bmatrix} l_s & 0 \\ 0 & 1 \end{bmatrix} \boldsymbol{\Sigma} \begin{bmatrix} l_s & 0 \\ 0 & 1 \end{bmatrix}^T = \mathbf{L}_s \boldsymbol{\Sigma} \mathbf{L}_s^T. \quad (3.27)$$

This case is illustrated in Fig. 3.1 (a) and (c). If \mathbf{v}_s is not parallel to the x axis as in Fig. 3.1 (b) and (d), the covariance matrix needs to be stretched along the direction given by the vector \mathbf{v}_s . This is accomplished by the rotation matrix $\mathbf{V}_{\text{rot}}^{-1}$ which rotates \mathbf{v}_s in direction of the x axis. The covariance matrix is first rotated by $\mathbf{V}_{\text{rot}}^{-1}$, stretched and rotated back:

$$\boldsymbol{\Sigma}_s = (\mathbf{V}_{\text{rot}} \mathbf{L}_s \mathbf{V}_{\text{rot}}^{-1}) \boldsymbol{\Sigma} (\mathbf{V}_{\text{rot}} \mathbf{L}_s \mathbf{V}_{\text{rot}}^{-1})^T. \quad (3.28)$$

The form of Eq. (3.28) is identical to the error propagation law, which interprets it as the transformation of an uncertainty by a linear system [112].

4 iserveU: Health-Care Service Robot Indoor Positioning

¹ Recently, robotic systems have been experiencing a strong growth and have started becoming an integral part of everyday life [113]. One of the prime reasons for this process is the continuously falling cost of processing power which allows for complex algorithms to be executed. This leads to a reduction in the price of robot labor, which makes using robots as a substitute for human jobs financially more attractive. While most of the currently employed robots are industrial robots (e.g. car assembly robots or automated ground vehicles (AGV) for logistic applications), the segment of service robots is expected to experience a significant development in the near future [114], [115] with an annual growth of approximately 30 % [116].

A service robot is defined as a “robot that performs useful tasks for humans or equipment excluding industrial automation applications” in the ISO standard 8373:2012. Service robots are usually employed among humans and could interact with people. Typically, a distinction is made between professional and consumer service robots. While professional service robots serve as human workforce replacement (e.g. transportation robots in the logistics), personal service robots are aimed at aiding people in their daily lives (e.g. robotic vacuum cleaners) [116]. Healthcare service robots pose an important type of robots, which are expected to grow in significance in the near future.

4.1 Motivation

Due to the quickly aging population, especially in highly developed countries, the demand for hospital workers will continue to grow in the next decades. As recognized in [117], a large portion of hospital expenses (30 % ... 46 %) is spent for hospital logistics. This includes simple, but tiring and repetitive assignments, such as transportation or patient guiding tasks. The hospital expenses could be reduced and the quality of service improved, if an autonomous robotic system assumed these tasks. The nursing staff could then take more time for important tasks such as patient care.

¹Large portions of this chapter have been submitted in the form of two journal papers to IEEE Access [51] and IEEE Transactions on Microwave Theory and Techniques.

Several commercial hospital logistics service robot systems are already available. Probably the earliest one is HelpMate (1994) [118], which initially used ultrasound and structured light vision for localization and collision avoidance, which was later replaced by a laser scanner [119]. Another early system is CSS Robotics' SpeciMinder (2008) [120], created to help technicians in hospital laboratories by transporting specimens. Its localization and navigation is also based on a laser rangefinder. Two more recent systems show the continuing interest in the area: Aethon's TUG (2007) [121] and TransCar (2011) from Swisslog (part of KUKA) [122] automatic healthcare service robot systems. They are both capable of towing carts with food or medical supplies while autonomously navigating using a laser scanner and ultrasound for additional safety.

This short overview of the state-of-the-art of healthcare service robotics shows the importance of such systems, which will only be growing in the future. It is also evident that basically all available systems use laser scanners for navigation and localization. As outlined in Chapter 1.1 while powerful, such systems can quickly become unreliable in dynamic situations or in the presence of objects invisible for the laser scanner (e.g. glass, bars, objects like tables and chairs which have almost no parts in the 2D scan plane of the lasers scanner). Since laser-scanner-based positioning relies on matching the sensor readings to a map, such systems can become unstable, when the robot position is lost, e.g. due to a severe disturbance and it needs to be reinitialized, as many areas of the map frequently look very similar. The kidnapped robot case (when the robot is manually moved, but it doesn't realize this) is also a problem for the same reason. Therefore, an alternative to laser scanners is necessary. In this chapter, one such alternative – a WLPS for healthcare service robots – will be presented. It was developed within the scope of the research project iserveU².

The main aim of the project was to create a healthcare service robot called an intelligent transport assistant (ITA) to relief nursing staff in hospitals by taking over logistic tasks. Several use cases were defined. The mobile robot is supposed to navigate autonomously through the hospital building and transport clinical materials, meals, and laundry. In addition, it should be able to guide patients through hospital facilities and follow nursing staff while carrying a payload. One of the main challenges for the development of this system was to provide real-time accurate and reliable positioning, which is a prerequisite for successful navigation. In order to enable guidance and following tasks, the robot should also be able to locate a person carrying a hand-held transponder.

²The project iserveU (Intelligente modulare Serviceroboter-Funktionalitäten im menschlichen Umfeld am Beispiel von Krankenhäusern / Intelligent modular service robot functionalities in the environment of humans at the example of hospitals) had a run-time of 3 years and was funded by the Federal Ministry of Education and Research of Germany (BMBF), registration no. 01IM12008F. Project partners were Robert Bosch GmbH, RWTH Aachen, TU Clausthal, Symeo GmbH, HS Ulm, REC GmbH.



Fig. 4.1: Service robot for transportation tasks in hospitals developed in the project iserveU. A static radar node can be seen in the background of the picture on the right.

4.2 WLPS for Healthcare Service Robots

Indoor operation poses a very difficult scenario for wireless positioning systems, because of the strong and numerous multipath reflections and the high accuracy requirements due to the relatively small dimensions of the environment [123]. As summarized in [47], [48], and [124], a large number of various indoor positioning system concepts have been presented in the past. However, thus far, no company or device has managed to attain a widespread commercial adoption. Indoor localization systems have remained a niche product, although multiple systems could demonstrate very good performance [125]. Microsoft has been annually organizing its Indoor Localization Competition³ (see also Chapter 6.1) trying to give a fair overview of the state-of-the-art of indoor positioning. As detailed in [126], the competition has shown an improvement in system performance every year, demonstrating the active research ongoing in the area of indoor positioning. There is also an indoor localization competition finding place as part of the

³<https://www.microsoft.com/en-us/research/event/microsoft-indoor-localization-competition>

Indoor Positioning and Indoor Navigation Conference (IPIN) [127]. Research in the area of indoor positioning systems (IPS) was also defined as one of the main three goals in AGV research by Kiva Systems (now Amazon Robotics) in [128].

In order to fulfill the positioning requirements for the system in Chapter 4.1, a WLPS was developed. As outlined in Section 1.2, since the most widely used indoor positioning techniques – laser scanners and multilateration-based systems – both suffer from some inherent drawbacks, an alternative localization system was developed to overcome these drawbacks. The secondary radar system described in Chapter 2 combining RTOF and DOA was used as an absolute reference. Thanks to the employed measurement concept, a single radar node was sufficient to provide positioning coverage in a room. For long corridors, two radar nodes were used. To support the positioning in lateral corridor direction, an ultrasonic wall-detection device was additionally employed. A multi-modal⁴ sensor fusion algorithm was developed to fuse the sensor measurements with the odometry readings. An odometer measures the revolution of the robot’s wheels using wheel-encoders and optionally gyroscope data. Additionally, a portable radar node (“follow-me-beacon”) was used for personnel positioning relative to the service robot. This enables the robot to execute tasks like following nursing staff or guiding patients. The prototype of the mobile robot with the positioning technology is shown in Fig. 4.1.

4.3 System Overview and Prerequisites

Fig. 4.2 shows an overview of the developed WLPS. Essentially, it consists of stationary infrastructure and a mobile robot equipped with sensors. The infrastructure comprises one or more reference radar nodes equipped with a 2D planar antenna array presented in Chapter 2. The stationary reference node ① performs bilateral measurements with the mobile radar node ② on the robot ④ (i.e. operates interchangeably as master or slave). The ultrasonic system ③ measures the distance and orientation relative to the wall.

Several coordinate systems and transformations need to be determined in advance during the system setup. The global coordinate system f_{glo} shown in yellow in Fig. 4.2 is the one in which the map M_{og} of the scenario is available and in which the mobile robot pose is estimated. The map M_{og} is a binary occupancy grid map denoting whether a point on a grid of 5 cm is occupied (wall or object) or free (corridor or room). The map is manually generated using a total station or a laser scanner. The stationary radar coordinate frame $f_{\text{rad,st}}$ (in green in Fig. 4.2) is determined based on total station measurements

⁴Disambiguation: Here “multi-modal” refers to the usage of different sensor types (sensing modalities) and not to multimodal probability distributions [129].

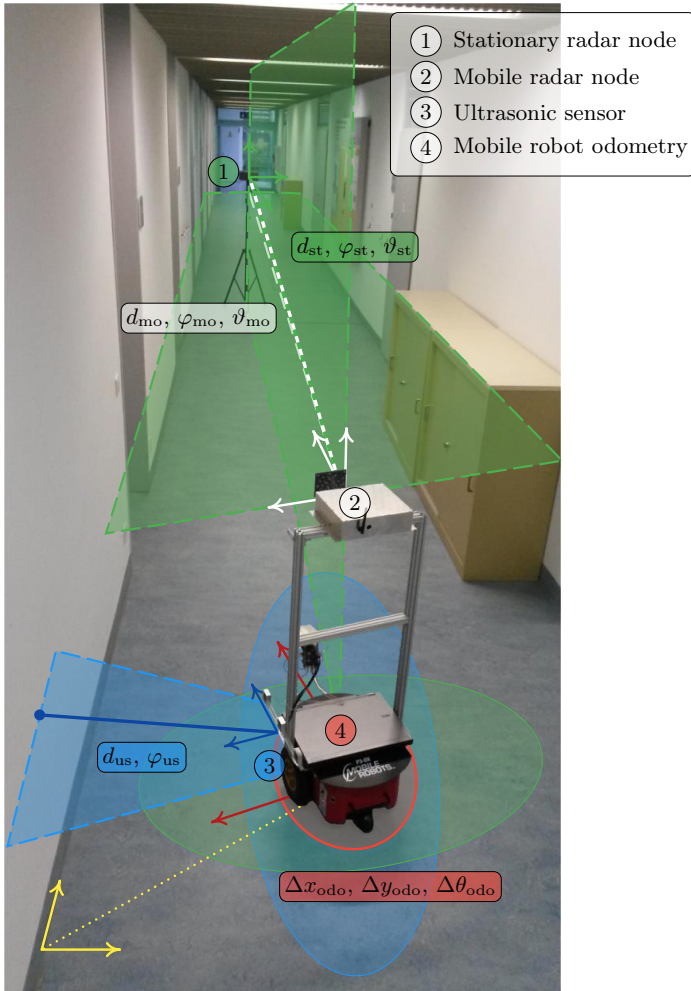


Fig. 4.2: Localization scenario “Corridor in Cauerstr. 6” and WLPS concept (adapted from [51] and [130]). The dashed planes and the arrows illustrate the coordinate frames and the planes in which each sensor operates and provides measurement results. The ellipses denote qualitatively the corresponding measurement uncertainties. See description in text.

relative to \mathbf{f}_{glo} . The mobile robot coordinate system \mathbf{f}_{rob} (in red) is set to the center of the robot and is the frame in which the odometry data is provided. The aim of the localization system is to determine the 2D position and orientation of \mathbf{f}_{rob} defined by the robot position x_{rob} , y_{rob} and the robot orientation around the global z -axis θ_{rob} (heading) relative to \mathbf{f}_{glo} . The mobile radar node and ultrasonic sensor frames $\mathbf{f}_{\text{rad,mo}}$ and \mathbf{f}_{us} in white, resp. blue, are determined relative to \mathbf{f}_{rob} .

When the static node is in master mode, it measures the distance to the mobile node d_{st} and both azimuth and elevation angles φ_{st} and ϑ_{st} in $\mathbf{f}_{\text{rad,st}}$ with a measurement uncertainty described by the covariance matrix $\mathbf{Q}_{\text{rad,st}}$. By transforming this measurement result to Cartesian coordinates in \mathbf{f}_{glo} , the 3D position of the mobile robot can be determined⁵. As the robot only operates in a 2D plane, the determined 3D position is projected to the floor plane. The corresponding measurement uncertainty is illustrated as a green ellipse in Fig. 4.2 (size and orientation not to scale).

When the mobile node assumes the master role, it determines the distance and angles to the reference node d_{mo} , φ_{mo} , and ϑ_{mo} in $\mathbf{f}_{\text{rad,mo}}$ with a measurement uncertainty $\mathbf{Q}_{\text{rad,mo}}$. These are then transformed to \mathbf{f}_{rob} . The previously determined 2D position can be improved with d_{mo} and ϑ_{mo} relative to the known reference node position. Additionally, the mobile robot heading can be determined using φ_{mo} . Thus, a single bilateral measurement and only one reference node is sufficient for complete 2D pose estimation.

While this approach works well in typical office rooms and foyers, where multipath components can be resolved from the LOS path, the angle estimation is disturbed and cannot provide sufficient accuracy in long narrow corridors, where the multipath length is similar to the LOS length and the angle error is in the order of magnitude of the corridor width. To support the positioning in cross-range corridor direction in such environments, an ultrasonic sensor array is additionally employed. It provides the distance d_{us} and angle φ_{us} to the wall in \mathbf{f}_{us} with a measurement uncertainty \mathbf{Q}_{us} . Given an estimate of the mobile robot pose and a map of the scenario, d_{us} and φ_{us} can be used to update the robot orientation and the position in a direction perpendicular to the wall resulting in a measurement uncertainty similar to the blue ellipse in Fig. 4.2.

Finally, the robot odometer provides a measure for the 2D relative motion of the robot (translation and rotation) Δx_{odo} , Δy_{odo} , and $\Delta \theta_{\text{odo}}$ in \mathbf{f}_{rob} . While very stable and accurate over a short course, odometry is a relative sensor and needs to be initialized with a correct absolute position. Furthermore, it tends

⁵This conversion assumes that an estimate for the robot orientation is available, since the radar node is not in the origin of the mobile robot coordinate system. As no orientation information is available during initialization, this leads to a relatively small error, which is corrected by subsequent measurements.

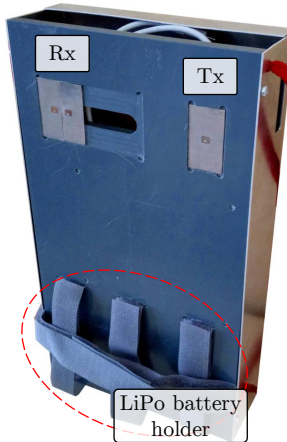


Fig. 4.3: The portable radar node (“follow-me beacon”) has a size of size $20 \times 15 \times 5$ cm and weighs 500 g with a LiPo battery enabling more than 2 hours of continuous operation.

to drift away on the long run due to error accumulation caused among others by slippage of the wheels and drift of the gyroscope. The corresponding uncertainty is illustrated as a red ellipse in Fig. 4.2. It can be fused with the other sensor measurements to improve the short-term stability of the localization.

As mentioned in Chapter 4.1, the service robot should not only be able to navigate autonomously through the hospital premises, but also to guide patients or follow nursing staff while carrying a payload. Both tasks require knowledge of the position of a person relative to the mobile robot. This was accomplished using the portable radar node (“follow-me beacon”) shown in Fig. 4.3, which is to be carried by the person on their back or front as shown. The follow-me beacon implements the same measurement technique as described in Chapter 2.1. It is based on the same DSP and RF chips as the other radar nodes (cf. Chapter 2.2), but has only 1 Tx and 2 Rx channels to minimize size and energy consumption. It can thus measure range and only coarsely the angle of arrival.

When in “follow” or “lead” mode the mobile robot performs consecutive radar measurements to the static nodes and to the follow-me beacon in order to determine its own position in the map and the relative position of the person. The range and azimuth / elevation angle measurements from the mobile robot to the

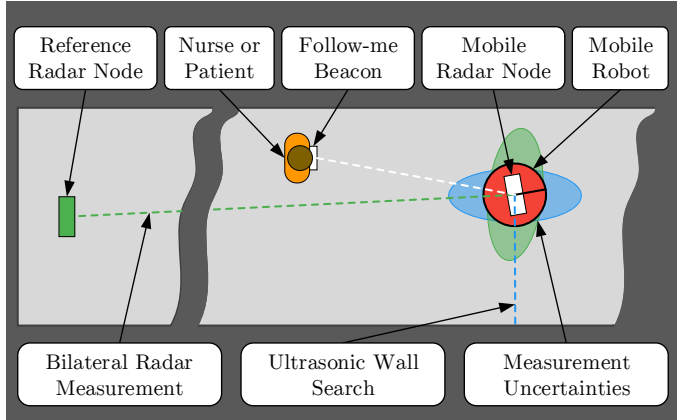


Fig. 4.4: Schematic illustration of indoor mobile robot and person localization concept (adapted from [46]).

follow-me beacon will be denoted as d_{fb} , φ_{fb} , and ϑ_{fb} . They are available in the coordinate system $\mathbf{f}_{rad,mo}$ with a measurement uncertainty $\mathbf{Q}_{rad,mo}$.

The complete localization concept is summarized in Fig. 4.4. The following sections will describe the EKF-based sensor fusion and localization approach.

4.4 State Vector and Motion Model

The state vector $\mathbf{x}_{rob,t}$ describes the sought mobile robot pose (2D position and heading) at the discrete point in time t and is defined as

$$\mathbf{x}_{rob,t} = \begin{bmatrix} x_{rob,t} \\ y_{rob,t} \\ \theta_{rob,t} \end{bmatrix}. \quad (4.1)$$

In the EKF used, it is represented by the belief consisting of the mean $\boldsymbol{\mu}_{rob,t}$ and the corresponding covariance matrix (pose uncertainty)

$$\boldsymbol{\Sigma}_{rob,t} = \begin{bmatrix} \sigma_{x,rob}^2 & \sigma_{xy,rob} & \sigma_{x\theta,rob} \\ \sigma_{xy,rob} & \sigma_{y,rob}^2 & \sigma_{y\theta,rob} \\ \sigma_{x\theta,rob} & \sigma_{y\theta,rob} & \sigma_{\theta,rob}^2 \end{bmatrix}. \quad (4.2)$$

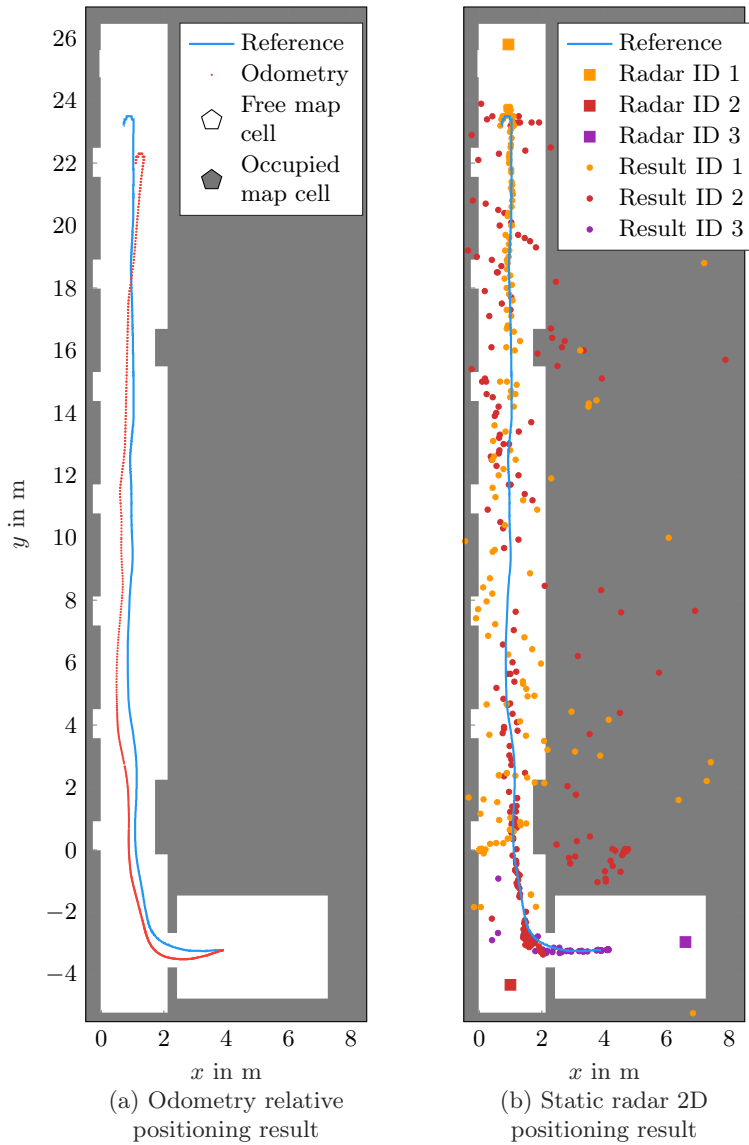


Fig. 4.5: Typical measurement result of the robot odometry (a) and 3 static radars (b) in the office building from Fig. 4.25 (c). A Leica TS30 total station was used as a reference (adapted from [51]).

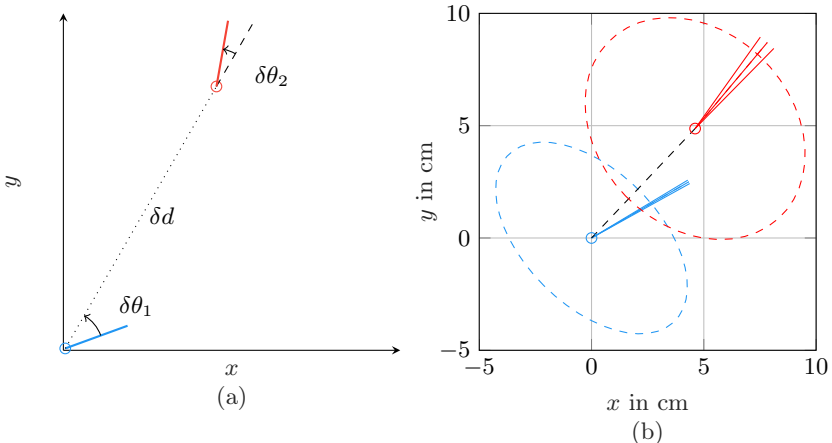


Fig. 4.6: (a) Geometric representation of the prediction step using odometry.
(b) Simulation of prediction step. The \circ symbol / dashed ellipse signify the position and uncertainty of the mobile robot (blue before and red after the prediction step); the solid lines denote the mobile robot heading and the stretch between them is proportional to the heading uncertainty (adapted from [51]).

The EKF prediction step is realized by an odometry motion model. Instead of using the control velocities, it uses the sensor readings of the odometer. Even though not a control, but a sensor measurement, odometry carries the same information, but tends to be more accurate, since it measures the result of applying the control to the physical system (Chapter 5.4 in [107]).

Odometry provides the relative change of the mobile robot pose in the coordinate system $\mathbf{f}_{\text{rob},t}$ during the time step δt_{odo} moving from $x_{t-1}, y_{t-1}, \theta_{t-1}$ to x_t, y_t, θ_t . A typical dead-reckoning positioning result given by the mobile robot odometry is shown in Fig. 4.5 (a). The robot started at $[x, y] \approx [4 \text{ m}, -3 \text{ m}]$ and moved out of the room and along the corridor with speed of up to 1 m/s. The odometry result was shifted and rotated in post-processing to roughly match the reference. As evident, although very stable on the short run, there is a significant drift in both range and orientation during the test with a length of approximately 30 m. The drift was most significant when the robot was turning as wheel slippage is maximal in this situation. The accuracy in translation and

rotation is approximately 2 cm/m and 0.016° ⁶.

As shown in Fig. 4.6 (a), the motion can be represented by an initial turn by $\delta\theta_{1,t}$, a translation of δd_t and a final rotation by $\delta\theta_{2,t}$ given by [107]

$$\begin{aligned}\delta\theta_{1,t} &= \text{wrap}(\text{atan}2(y_t - y_{t-1}, x_t - x_{t-1}) - \theta_{t-1}), \\ \delta d_t &= \sqrt{(x_t - x_{t-1})^2 + (y_t - y_{t-1})^2}, \\ \delta\theta_{2,t} &= \text{wrap}(\theta_t - \theta_{t-1} - \delta\theta_{1,t}).\end{aligned}\quad (4.3)$$

The control vector \mathbf{u}_t then becomes

$$\mathbf{u}_t = \begin{bmatrix} \delta\theta_{1,t} \\ \delta d_t \\ \delta\theta_{2,t} \end{bmatrix}. \quad (4.4)$$

The function $\text{wrap}(\cdot)$ limits its argument to the range $\pm\pi$ as defined in Section A.3. The model assumes a linear motion by δd_t in the direction $\delta\theta_{1,t}$. The second rotation $\delta\theta_{2,t}$ is added to the model to account for the fact, that the real motion trajectory might not be linear. Otherwise, the three-dimensional state vector $[x \ y \ \theta]^T$ would be incompletely described by a two-dimensional model $[\delta d \ \delta\theta_1]^T$. The corresponding covariance matrix \mathbf{M}_t in control space is

$$\mathbf{M}_t = \begin{bmatrix} \alpha_{\theta,\theta} |\delta\theta_{1,t}| + \alpha_{\theta,d} \delta d_t & 0 & 0 \\ 0 & \alpha_{d,d} \delta d_t + \alpha_{d,\theta} (|\delta\theta_{1,t}| + |\delta\theta_{2,t}|) & 0 \\ 0 & 0 & \alpha_{\theta,\theta} |\delta\theta_{2,t}| + \alpha_{\theta,d} \delta d_t \end{bmatrix}^2. \quad (4.5)$$

The parameters $\alpha_{\theta,\theta}$, $\alpha_{\theta,d}$, $\alpha_{d,\theta}$, and $\alpha_{d,d}$ describe the accumulated error during the motion.

The prediction step and the state transition function \mathbf{g}_{odo} then take the form (compare also with Eq. (3.16))

$$\bar{\mathbf{x}}_{\text{rob},t} = \mathbf{x}_{\text{rob},t-1} + \underbrace{\begin{bmatrix} \delta d_t \cos(\theta_{\text{rob},t} + \delta\theta_{1,t}) \\ \delta d_t \sin(\theta_{\text{rob},t} + \delta\theta_{1,t}) \\ \delta\theta_{1,t} + \delta\theta_{2,t} \end{bmatrix}}_{\mathbf{g}_{\text{odo}}} + \mathcal{N}(\mathbf{0}, \mathbf{M}_{xy\theta,t}), \quad (4.6)$$

where the noise term describes the influence of the odometry noise on the state vector with the noise covariance in state space $\mathbf{M}_{xy\theta,t}$.

The prediction for the robot pose $\bar{\mu}_{\text{rob},t}$ is then governed by the nonlinear

⁶The accuracy for a particular test run depends on many factors such as the trajectory driven, the velocity, the floor material, the tyres pressure, etc.

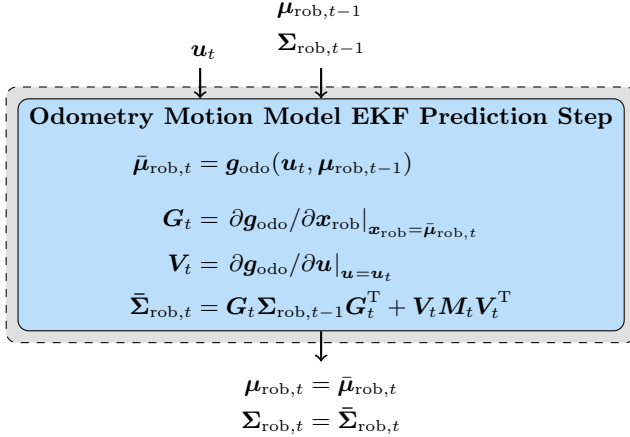


Fig. 4.7: Simplified block diagram of the odometry-based EKF prediction step.

state transition function \mathbf{g}_{odo} (cf. Eq. (3.16)):

$$\bar{\boldsymbol{\mu}}_{\text{rob},t} = \mathbf{g}_{\text{odo}}(\boldsymbol{u}_t, \boldsymbol{\mu}_{\text{rob},t-1}) = \boldsymbol{\mu}_{\text{rob},t-1} + \begin{bmatrix} \delta d_t \cos(\theta_{\text{rob},t} + \delta\theta_{1,t}) \\ \delta d_t \sin(\theta_{\text{rob},t} + \delta\theta_{1,t}) \\ \delta\theta_{1,t} + \delta\theta_{2,t} \end{bmatrix}. \quad (4.7)$$

The state transition Jacobian \mathbf{G}_t used to linearize \mathbf{g}_{odo} for the EKF prediction step is then

$$\mathbf{G}_t = \frac{\partial \mathbf{g}_{\text{odo}}}{\partial \boldsymbol{x}_{\text{rob}}} \Big|_{\boldsymbol{x}_{\text{rob}}=\bar{\boldsymbol{\mu}}_{\text{rob},t}} = \begin{bmatrix} 1 & 0 & -\delta d_t \sin(\bar{\theta}_{\text{rob},t} + \delta\theta_{1,t}) \\ 0 & 1 & \delta d_t \cos(\bar{\theta}_{\text{rob},t} + \delta\theta_{1,t}) \\ 0 & 0 & 1 \end{bmatrix}. \quad (4.8)$$

The Jacobian \mathbf{V}_t to transform the control covariance \mathbf{M}_t to state space $\mathbf{M}_{xy\theta,t} = \mathbf{V}_t \mathbf{M}_t \mathbf{V}_t^T$ is

$$\mathbf{V}_t = \frac{\partial \mathbf{g}_{\text{odo}}}{\partial \boldsymbol{u}} \Big|_{\boldsymbol{u}=\boldsymbol{u}_t} = \begin{bmatrix} -\delta d_t \sin(\bar{\theta}_{\text{rob},t} + \delta\theta_{1,t}) & \cos(\bar{\theta}_{\text{rob},t} + \delta\theta_{1,t}) & 0 \\ \delta d_t \cos(\bar{\theta}_{\text{rob},t} + \delta\theta_{1,t}) & \sin(\bar{\theta}_{\text{rob},t} + \delta\theta_{1,t}) & 0 \\ 1 & 0 & 1 \end{bmatrix}. \quad (4.9)$$

The resulting state covariance prediction is then given by

$$\bar{\boldsymbol{\Sigma}}_{\text{rob},t} = \mathbf{G}_t \boldsymbol{\Sigma}_{\text{rob},t-1} \mathbf{G}_t^T + \mathbf{V}_t \mathbf{M}_t \mathbf{V}_t^T. \quad (4.10)$$

The first term on the right-hand side models the uncertainty propagation after the motion. The second term accounts for the added uncertainty due to the noisy odometry readings. The prediction step always increases the state uncertainty. The algorithm is summarized in Fig. 4.7.

4.5 Fusing Static Radar Node Measurements

As illustrated in Fig. 4.2, one or more static radar nodes are mounted at the test site. A typical measurement result is shown in Fig. 4.5 (b). The 3 static radar nodes with ID 1, 2, and 3 measured the distance d_{st} and angles φ_{st} and ϑ_{st} to the radar node on the mobile robot which was moving as described in Section 4.4. As evident, the radars provide a very accurate 2D position measurement at a close range ($\lesssim 10$ m) with standard deviation of approximately 1° in both azimuth and elevation. However, the angle estimation is severely distorted at longer distances due to multipath, which renders it unreliable. The distance standard deviation is approximately constant 7 cm.

In order to fuse this measurement in the mobile robot position estimate it is converted from static radar measurement space $[d_{st}, \varphi_{st}, \vartheta_{st}]$ to state space $[x_{rob}, y_{rob}]$. Using a conversion from polar to Cartesian coordinates, the measured 3D position of the Tx antenna of the mobile radar node in $f_{rad,st}$ is

$$\mathbf{p}_{rad,st, f_{rad,st}} = \begin{bmatrix} d_{st} \cos \vartheta_{st} \cos \varphi_{st} \\ d_{st} \cos \vartheta_{st} \sin \varphi_{st} \\ d_{st} \sin \vartheta_{st} \end{bmatrix}. \quad (4.11)$$

$\mathbf{p}_{rad,st, f_{rad,st}}$ is then converted to global coordinates to obtain the absolute 3D position of the static radar node measurement

$$\mathbf{p}_{rad,st} = b_{tran}(f_{rad,st}, f_{glo}, \mathbf{p}_{rad,st, f_{rad,st}}). \quad (4.12)$$

The function $\mathbf{p}_d = b_{tran}(f_s, f_d, \mathbf{p}_s)$ converts a point \mathbf{p}_s from a source coordinate system f_s to a point \mathbf{p}_d in a destination coordinate system f_d and is defined in Appendix A.4. The resulting point $\mathbf{p}_{rad,st}$ is used to determine the 2D position of the mobile robot in global coordinates. The problem geometry is depicted in Fig. 4.8 and 4.12.

The resulting measurement model is given by the transformation of the position of the measured point (which is the array centroid of the mobile radar node

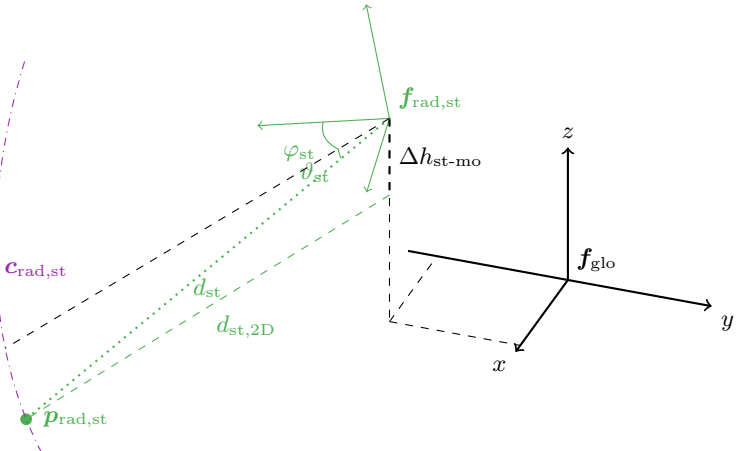


Fig. 4.8: Geometry of static radar node measurement. \mathbf{f}_{glo} denotes the global coordinate system; $\mathbf{f}_{\text{rad},\text{st}}$ is the static radar coordinate system. The radar locates the mobile robot at the 3D position $\mathbf{p}_{\text{rad},\text{st}}$ in global coordinates. $d_{\text{st},2\text{D}}$ is the projection of the 3D distance measurement to the 2D positioning problem. The constant and known height difference between mobile radar node and stationary node mounting height is $\Delta h_{\text{st-mo}}$ (adapted from [51]).

$\mathbf{p}_{\text{rad},\text{mo},\mathbf{f}_{\text{rob}}}$) to global coordinates:

$$\begin{aligned} \mathbf{h}_{\text{rad},\text{st}}(\mathbf{x}_{\text{rob}}) &= \text{btran}(\mathbf{f}_{\text{rob}}, \mathbf{f}_{\text{glo}}, \mathbf{p}_{\text{rad},\text{mo},\mathbf{f}_{\text{rob}}}) \\ &\approx \begin{bmatrix} x_{\text{rob}} + d_{\Delta 2\text{D}} \cos(\theta_{\text{rob}} - \theta_{\Delta 2\text{D}}) \\ y_{\text{rob}} + d_{\Delta 2\text{D}} \sin(\theta_{\text{rob}} - \theta_{\Delta 2\text{D}}) \end{bmatrix}. \end{aligned} \quad (4.13)$$

$d_{\Delta 2\text{D}}$ and $\theta_{\Delta 2\text{D}}$ are the 2D projections of the known distance and angle from the origin of the robot coordinate system to the mobile radar (see Fig. 4.12). If the mobile robot heading θ_{rob} is not known yet (which is the case during the initializing procedure), the measurement model in Eq. (4.13) leads to a relatively small error (this is discussed in Section 4.9).

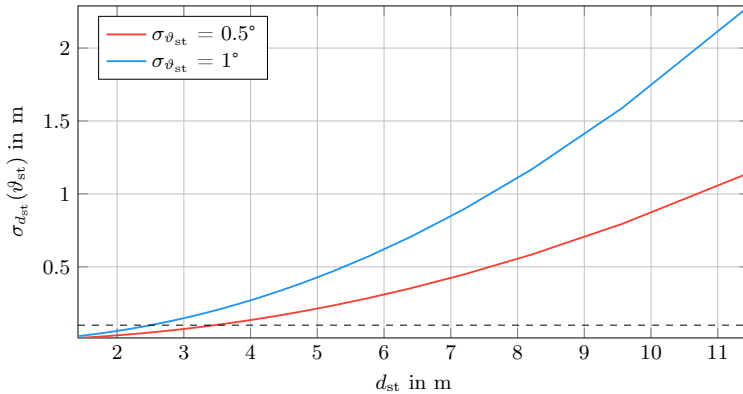


Fig. 4.9: Standard deviation of distance estimation based on elevation angle measurement for 2 different elevation measurement uncertainties. The dashed line denotes a standard deviation $\sigma_{d_{st}} = 10 \text{ cm}$.

4.5.1 Using Elevation to Support Distance Estimation

Since the mobile robot operates in 2D only and both the mobile and the static radar nodes are mounted at known constant heights, only a distance and an azimuth angle measurement are sufficient to determine the 2D position of the robot. However, as the elevation angle measurement is supported by the radar devices used, the problem is overdetermined as 3 measurements are available (d_{st} , φ_{st} , and ϑ_{st}) to determine 2 unknowns (x_{rob} and y_{rob}). The additional knowledge of the elevation angle can, however, be potentially used to improve the distance estimation using

$$d_{st}(\vartheta_{st}) = \frac{\Delta h_{\text{st-mo}}}{\sin(\vartheta_{st})} \quad (4.14)$$

with the mounting point height difference of the static and mobile radar nodes

$$\Delta h_{\text{st-mo}} = h_{\text{rad,st}} - h_{\text{rad,mo}}. \quad (4.15)$$

The standard deviation of the elevation-based distance estimation $\sigma_{d_{st}}$ is then

$$\sigma_{d_{st}}(\vartheta_{st}) = \sqrt{\left(\frac{\partial d_{st}(\vartheta_{st})}{\partial \vartheta_{st}} \right)^2 \sigma_{\vartheta_{st}}^2} = \left| -\frac{\cos(\vartheta_{st}) \Delta h_{\text{st-mo}}}{\sin(\vartheta_{st})^2} \right| \sigma_{\vartheta_{st}}, \quad (4.16)$$

where $\sigma_{\vartheta_{st}}$ denotes the standard deviation of the elevation measurement. For typical values of $\Delta h_{st-mo} = 1 \text{ m}$ and $\sigma_{\vartheta_{st}} = 0.5^\circ$ resp. $\sigma_{\vartheta_{st}} = 1^\circ$ the distance estimation uncertainty based on the elevation angle for a range of distances is given in Fig. 4.9. As can be seen, the distance estimation error remains below 10 cm for $d_{st} \lesssim 2.5 \text{ m}$ and $\lesssim 3 \text{ m}$, respectively. It is thus sensible to use the elevation angle up to this distance, as it causes uncertainty in the order of magnitude of the distance estimation. For larger distances, the error grows due to geometric dilution of precision and multipath interference and the elevation measurement hardly conveys any useful information to the distance estimation.

4.5.2 2D EKF for Static Radar Node Measurements

As previously mentioned, the elevation measurement is not reliable at large distances and therefore it can cause a large error in the position of $\mathbf{p}_{rad,st}$. Changing ϑ_{st} while keeping d_{st} and φ_{st} constant would move the measured position $\mathbf{p}_{rad,st}$ along the dash-dotted purple arc (circle) $\mathbf{c}_{rad,st}$ in Fig. 4.8. Depending on the roll orientation of $\mathbf{f}_{rad,st}$, the circle is not necessarily orthogonal to the global xy plane. This means that an error in ϑ_{st} changes not only the z but also the x and y coordinates of $\mathbf{p}_{rad,st}$.

As the mobile robot operates in 2D, its position can be described by $\mathbf{p}_{rad,st,2D}$, which is the 2D component of $\mathbf{p}_{rad,st}$. One possible solution to find $\mathbf{p}_{rad,st,2D}$ without using the elevation angle is to find the intersection point of the circle $\mathbf{c}_{rad,st}$ with the plane in which the mobile radar node moves, which is parallel to the global xy plane at height $h_{rad,mo}$. The circle $\mathbf{c}_{rad,st}$ can be described by its center $\mathbf{m}_{rad,st}$ (which is the position of the static radar array centroid and the origin of $\mathbf{f}_{rad,st}$), its radius d_{st} , and a vector $\mathbf{n}_{c_{rad,st}}$ normal to its plane. The normal vector $\mathbf{n}_{c_{rad,st}}$ converted from $\mathbf{f}_{rad,st}$ to global coordinates is given by

$$\mathbf{n}_{c_{rad,st}} = \mathbf{b}_{tran} \left(\mathbf{f}_{rad,st}, \mathbf{f}_{glo}, \begin{bmatrix} d_{st} \cos \varphi_{st} \\ d_{st} \sin \varphi_{st} \end{bmatrix} \times \mathbf{n}_{z,rad,st} \right), \quad (4.17)$$

where \times denotes the cross product. $\mathbf{n}_{z,rad,st}$ is the unit vector in z -direction of $\mathbf{f}_{rad,st}$. The sought intersection point $\mathbf{p}_{rad,st,2D}$ must fulfill 3 conditions:

1. Its z -coordinate is $h_{rad,mo}$.
2. It lies in the plane of the circle $\mathbf{c}_{rad,st}$. In general, the scalar product of the plane normal and any vector from a given point to a point in the plane is equal. Since $\mathbf{m}_{rad,st}$ is a known point in the plane, it can be used to

construct a second condition for $\mathbf{p}_{\text{rad,st},2D}$:

$$\begin{bmatrix} x_{\mathbf{p}_{\text{rad,st},2D}} \\ y_{\mathbf{p}_{\text{rad,st},2D}} \\ h_{\text{rad,mo}} \end{bmatrix} \cdot \mathbf{n}_{\mathbf{c}_{\text{rad,st}}} = \mathbf{m}_{\text{rad,st}} \cdot \mathbf{n}_{\mathbf{c}_{\text{rad,st}}}, \quad (4.18)$$

where \cdot denotes the scalar product.

3. The distance of the sought point to the center of the circle equals the circle radius:

$$\|\mathbf{p}_{\text{rad,st}} - \mathbf{m}_{\text{rad,st}}\| = d_{\text{st}}. \quad (4.19)$$

The resulting equations have a closed-form solution, which is not given here for the sake of brevity. As they are quadratic, there are 2 possible solutions. However, one of them can be easily dismissed, as it lies behind the radar.

The measurement vector in state space then becomes

$$\begin{aligned} \mathbf{z}_{\text{rad,st},t} &= \mathbf{h}_{\text{rad,st}}(\mathbf{x}_{\text{rob}}) + \mathcal{N}(\mathbf{0}, \mathbf{Q}_{\text{rad,st},xy}) \\ &= \mathbf{p}_{\text{rad,st},2D,t} = \mathbf{m}_{\text{rad,st},xy} + \begin{bmatrix} \hat{d}_{2D,t} \cos \hat{\varphi}_{\text{st},2D,t} \\ \hat{d}_{2D,t} \sin \hat{\varphi}_{\text{st},2D,t} \end{bmatrix}. \end{aligned} \quad (4.20)$$

$\mathbf{Q}_{\text{rad,st},xy}$ is the measurement covariance matrix of the static radar converted to xy state space. The distance and angle from the static to the mobile radar node $\hat{d}_{2D,t}$ and $\hat{\varphi}_{\text{st},2D,t}$ in the xy plane are

$$\begin{aligned} \hat{d}_{2D,t} &= \|\mathbf{p}_{\text{rad,st},2D,t} - \mathbf{m}_{\text{rad,st},xy}\|_{[x,y]}, \\ \hat{\varphi}_{\text{st},2D,t} &= \angle(\mathbf{p}_{\text{rad,st},2D,t}, \mathbf{m}_{\text{rad,st},xy})_{[x,y]}. \end{aligned} \quad (4.21)$$

The subscript $[x,y]$ signifies that the corresponding operation is executed in the xy plane (cf. also Appendix A.1 and A.2).

Using Eq. (4.13) the measurement prediction $\hat{\mathbf{z}}_{\text{rad,st},t}$ becomes

$$\hat{\mathbf{z}}_{\text{rad,st},t} = \mathbf{h}_{\text{rad,st}}(\bar{\mathbf{p}}_{\text{rob},t}) = \begin{bmatrix} \bar{x}_{\text{rob},t} + d_{\Delta 2D} \cos(\bar{\theta}_{\text{rob},t} - \theta_{\Delta 2D}) \\ \bar{y}_{\text{rob},t} + d_{\Delta 2D} \sin(\bar{\theta}_{\text{rob},t} - \theta_{\Delta 2D}) \end{bmatrix}. \quad (4.22)$$

Since the EKF update step is performed in state space, the static radar measurement covariance matrix

$$\mathbf{Q}_{\text{rad,st}} = \begin{bmatrix} \sigma_{d_{\text{st}}}^2 & 0 \\ 0 & \sigma_{\varphi_{\text{st}}}^2 \end{bmatrix} \quad (4.23)$$

needs to be converted from measurement space to state space to obtain the

measurement covariance in state space

$$\mathbf{Q}_{\text{rad,st},xy,t} = \mathbf{G}_t \mathbf{Q}_{\text{rad,st}} \mathbf{G}_t^T. \quad (4.24)$$

This is accomplished using the Jacobian

$$\mathbf{G}_t = \frac{\partial \mathbf{z}_{\text{rad,st}}}{\partial \begin{bmatrix} \hat{d}_{2D} \\ \hat{\varphi}_{\text{st},2D} \end{bmatrix}} \left|_{\begin{bmatrix} \hat{d}_{2D} \\ \hat{\varphi}_{\text{st},2D} \end{bmatrix} = \begin{bmatrix} \hat{d}_{2D,t} \\ \hat{\varphi}_{\text{st},2D,t} \end{bmatrix}}\right. = \begin{bmatrix} \cos \hat{\varphi}_{\text{st},2D,t} & -\hat{d}_{2D,t} \sin \hat{\varphi}_{\text{st},2D,t} \\ \sin \hat{\varphi}_{\text{st},2D,t} & \hat{d}_{2D,t} \cos \hat{\varphi}_{\text{st},2D,t} \end{bmatrix}. \quad (4.25)$$

The conversion from Eq. (4.24) using the Jacobian in (4.25) is an approximation to the real problem assuming $\hat{d}_{2D} \approx d_{\text{st}}$ and $\hat{\varphi}_{\text{st},2D} \approx \varphi_{\text{st}}$. It is accurate for small roll and pitch angles of $\mathbf{f}_{\text{rad,st}}$, which is valid for the problems discussed here.

The EKF innovation covariance \mathbf{S}_t then becomes (compare with Eq. (3.18))

$$\mathbf{S}_t = \mathbf{H}_t \boldsymbol{\Sigma}_{\text{rob},t} \mathbf{H}_t^T + \mathbf{G}_t \mathbf{Q}_{\text{rad,st}} \mathbf{G}_t^T, \quad (4.26)$$

where the measurement matrix \mathbf{H}_t is the Jacobian

$$\mathbf{H}_t = \frac{\partial \mathbf{h}_{\text{rad,st}}}{\partial \mathbf{x}_{\text{rob}}} \Big|_{\mathbf{x}_{\text{rob}} = \bar{\mu}_{\text{rob},t}} = \begin{bmatrix} 1 & 0 & -d_{\Delta 2D} \sin(\bar{\theta}_{\text{rob},t} - \theta_{\Delta 2D}) \\ 0 & 1 & d_{\Delta 2D} \cos(\bar{\theta}_{\text{rob},t} - \theta_{\Delta 2D}) \end{bmatrix}. \quad (4.27)$$

With the innovation vector

$$\Delta \mathbf{z}_t = \mathbf{z}_{\text{rad,st},t} - \hat{\mathbf{z}}_{\text{rad,st},t}, \quad (4.28)$$

the remaining EKF equations become:

$$\begin{aligned} \mathbf{K}_t &= \boldsymbol{\Sigma}_{\text{rob},t} \mathbf{H}_t^T \mathbf{S}_t^{-1}, \\ \bar{\mu}_{\text{rob},t} &= \mu_{\text{rob},t} + \mathbf{K}_t \Delta \mathbf{z}_t, \\ \bar{\Sigma}_{\text{rob},t} &= (\mathbf{I} - \mathbf{K}_t \mathbf{H}_t) \boldsymbol{\Sigma}_{\text{rob},t}. \end{aligned} \quad (4.29)$$

Even though only the 2D position of the mobile robot is measured by the static radar, the 3rd column of the matrix \mathbf{H}_t in Eq. (4.27) also contains a dependence on the orientation θ_{rob} . This reflects the fact that the position of the mobile robot is not measured directly; the position of the mobile radar array centroid is measured instead. The ramification of this is that the filter will not only change the position, but also the orientation of the robot, even though the latter is not measured directly. This behavior is correct, as the uncertainty in the position of

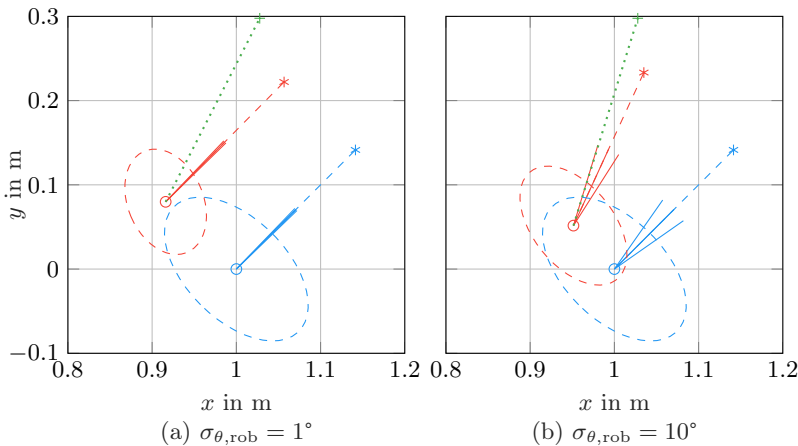
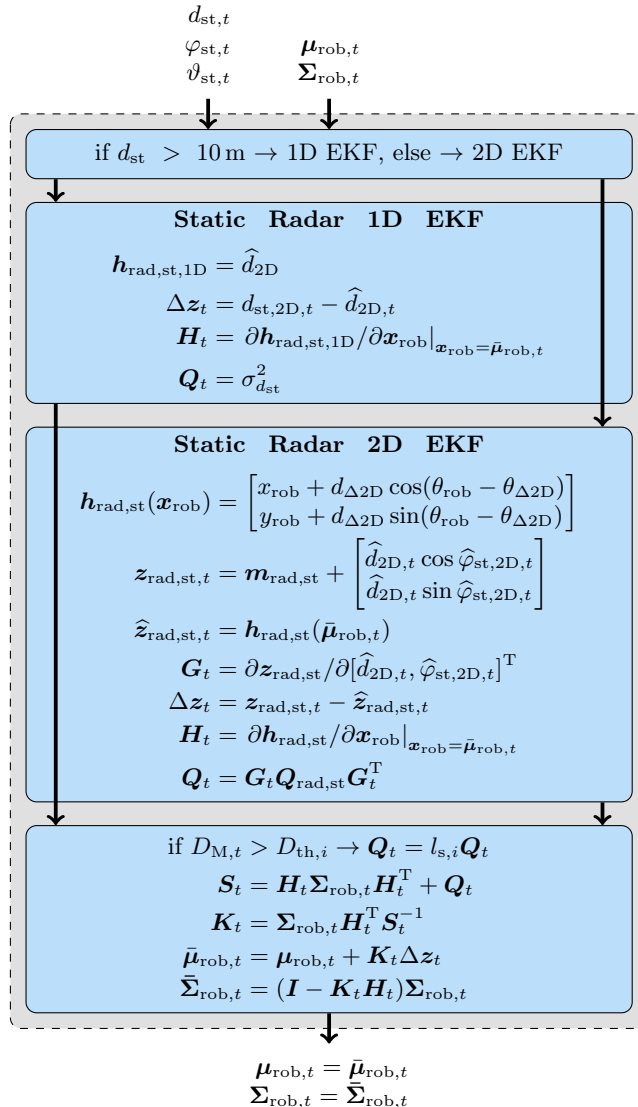


Fig. 4.10: Simulation of the behavior of the 2D EKF for fusing the static radar node measurements. The \circ symbol and the dashed ellipse signify the position and position uncertainty of the mobile robot (blue before the update; red after the update); the $*$ symbol denotes the position of the mobile radar node array centroid; the $+$ symbol is the 2D position measured by the static radar; the solid lines denote the mobile robot heading and the stretch between them is proportional to the heading uncertainty. The mobile robot heading uncertainty is (a) $\sigma_{\theta,\text{rob}} = 1^\circ$ and (b) $\sigma_{\theta,\text{rob}} = 10^\circ$. All other parameters are equal in both subfigures.

the mobile radar array centroid results from the uncertainty of both the position and the orientation of the mobile robot. The change in the orientation depends on the proportion of the position and orientation uncertainty – if the position uncertainty is low and the orientation uncertainty is high the filter will rotate the robot more and translate it less; in the opposite case, the filter with translate more and rotate less.

This is exemplified in Fig. 4.10. In both Fig. 4.10 (a) and (b) a pose with a corresponding uncertainty was assumed for the robot (shown in blue). A measurement was then fused using the proposed filter (shown in green). The result is shown in red. The only difference between both simulations is that $\sigma_{\theta,\text{rob}} = 1^\circ$ in (a) and $\sigma_{\theta,\text{rob}} = 10^\circ$ in (b) for the heading uncertainty was assumed. As evident from (a), for small $\sigma_{\theta,\text{rob}}$, the filter performs almost pure

**Fig. 4.11:** Simplified block diagram of the static radar EKF correction step.

translation. It reduces the position uncertainty and leaves the heading and heading uncertainty almost untouched. For large $\sigma_{\theta,\text{rob}}$ as in (b), the filter performs a translation and a rotation. In this case the position uncertainty is reduced less than in (a). The orientation uncertainty is also reduced here, as denoted by the stretch between the solid lines.

The filter update will be a pure translation if the mobile radar node is placed in the middle of the mobile robot coordinate system ($d_{\Delta 2D} = 0 \text{ m}$) as the measurement matrix in this case becomes

$$\mathbf{H}_t = \begin{bmatrix} 1 & 0 & 0 \\ 0 & 1 & 0 \end{bmatrix}. \quad (4.30)$$

This simplifies the computations and makes the performance of the filter more predictable and stable since the position and the orientation are decoupled. Unfortunately, it is not always possible to position the mobile radar node array centroid above the origin of the robot coordinate system, especially when more than one mobile node is mounted on the robot.

4.5.3 1D EKF for Static Radar Node Measurements

While the 2D approach in Section 4.5.2 works well for relatively small distances ($d_{\text{st}} \lesssim 10 \text{ m}$), it fails to handle adequately the large angular error caused by multipath distortions at long distances. Therefore, for $d_{\text{st}} > 10 \text{ m}$ a modified 1D version of the filter is used, which relies only on the measured distance and discards the estimated angles. The sensor fusion is performed in measurement space.

The measurement function $\mathbf{h}_{\text{rad,st},1D}$ is

$$\mathbf{h}_{\text{rad,st},1D} = \sqrt{\hat{d}_{2D,x}^2 + \hat{d}_{2D,y}^2} = \hat{d}_{2D}, \quad (4.31)$$

where the x and y components of \hat{d}_{2D} from Eq. (4.21) are

$$\begin{aligned} \hat{d}_{2D,x,t} &= \bar{x}_{\text{rob},t} + d_{\Delta 2D} \cos(\bar{\theta}_{\text{rob},t} - \theta_{\Delta 2D}) - m_{\text{rad,st},x}, \\ \hat{d}_{2D,y,t} &= \bar{y}_{\text{rob},t} + d_{\Delta 2D} \sin(\bar{\theta}_{\text{rob},t} - \theta_{\Delta 2D}) - m_{\text{rad,st},y}. \end{aligned} \quad (4.32)$$

As the correction is now performed in measurement space, the innovation vector is redefined to

$$\Delta \mathbf{z}_t = d_{\text{st},2D,t} - \hat{d}_{2D,t}. \quad (4.33)$$

The measurement Jacobian \mathbf{H}_t becomes

$$\mathbf{H}_t = \frac{\partial \mathbf{h}_{\text{rad,st},1D}}{\partial \mathbf{x}_{\text{rob}}} \Big|_{\mathbf{x}_{\text{rob}}=\bar{\mu}_{\text{rob},t}} = \begin{bmatrix} \frac{\partial \hat{d}_{2D,x,t}}{\partial d_{2D,t}} & \frac{\partial \hat{d}_{2D,y,t}}{\partial d_{2D,t}} & \frac{\partial \mathbf{h}_{\text{rad,st},1D}}{\partial \theta_{\text{rob}}} \Big|_{\bar{\theta}_{\text{rob},t}} \end{bmatrix}. \quad (4.34)$$

The complete expression for $\frac{\partial \mathbf{h}_{\text{rad,st},1D}}{\partial \theta_{\text{rob}}}$ in Eq. (4.34) is omitted here for the sake of brevity. The innovation covariance is then

$$\mathbf{S}_t = \mathbf{H}_t \Sigma_{\text{rob},t} \mathbf{H}_t^T + \sigma_{d_{\text{st}}}^2. \quad (4.35)$$

The remaining filter equations remain the same as in Eq. (4.29). The processing of the static radar measurements is summarized in Fig. 4.11.

4.6 Fusing Mobile Radar Node Measurements

As the radar system used allows for bilateral measurements, the radar node on the mobile robot estimates the distance d_{mo} to the static node. If the 2D planar antenna array from Fig. 2.16 (a) is used, both angles φ_{mo} and ϑ_{mo} are measured as well. If the ring antenna array from Fig. 2.16 (b) or (c) is used, only the horizontal angle φ_{mo} is determined. All measurements are given in the mobile node coordinate system $\mathbf{f}_{\text{rad,mo}}$ as illustrated in Fig. 4.12.

The result of the mobile radar measurement for a test run in an office building is shown in Fig. 4.13 (a). As evident, even for relatively short distances, the angle estimation accuracy is not very high (standard deviation 15°)⁷. This is due to the ring array used, as it has a very small aperture and only 3 to 4 antennas per direction. Its performance in the presence of multipath is therefore limited. As discussed in this section, having a coarse absolute orientation estimate is very important for the application at hand.

Using the 2D projection of the measurement in the same way as in Eq. (4.32), the measurement function $\mathbf{h}_{\text{rad,mo}}$ is defined as

$$\mathbf{h}_{\text{rad,mo}} = \begin{bmatrix} \sqrt{\hat{d}_{2D,x}^2 + \hat{d}_{2D,y}^2} \\ \text{atan}2(\hat{d}_{2D,y}, \hat{d}_{2D,x}) \end{bmatrix} = \begin{bmatrix} \hat{d}_{2D} \\ \hat{\varphi}_{\text{mo},2D} \end{bmatrix}, \quad (4.36)$$

where \hat{d}_{2D} and $\hat{\varphi}_{\text{mo},2D}$ denote the 2D distance and angle between the mobile and static radar nodes viewed from the mobile node.

As the same measurement principle as in the static radar is used, the considerations regarding the elevation angle measurements from Section 4.5 are valid

⁷It should be noted, that this error also includes the error in the mobile robot orientation as no reference for it was available.

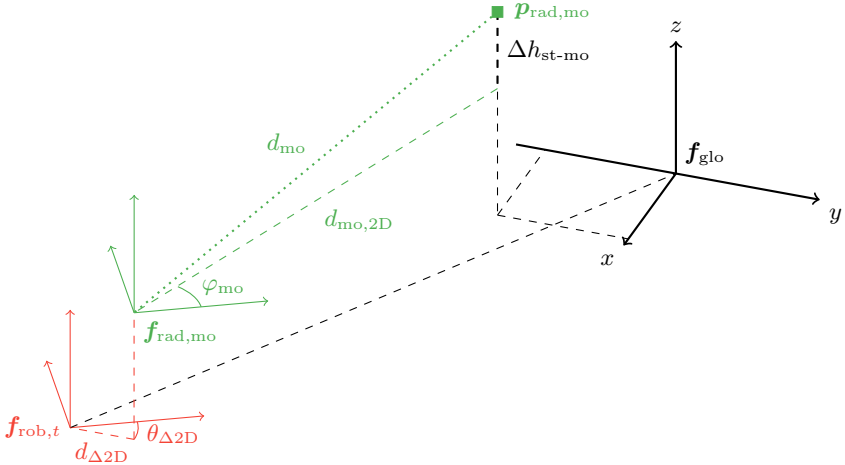


Fig. 4.12: Geometry of mobile radar node measurement. \mathbf{f}_{glo} denotes the global coordinate system; $\mathbf{f}_{\text{rob},t}$ is the mobile robot coordinate system at time t ; $\mathbf{f}_{\text{rad},\text{mo}}$ is the mobile radar node coordinate system. The radar locates the static node at 3D position $\mathbf{p}_{\text{rad},\text{mo}}$ in global coordinates. $d_{\text{mo},2\text{D}}$ is the projection of the 3D distance measurement to the 2D positioning problem. The constant and known height difference between mobile radar node and stationary node mounting height is $\Delta h_{\text{st-mo}}$ (adapted from [51]).

here as well. Applying the circle-plane intersection approach from Eq. (4.18) and (4.19), the projections $d_{\text{mo},2\text{D}}$ of the measured distance and $\varphi_{\text{mo},2\text{D}}$ of the measured azimuth angle on the xy plane are determined. The measurement vector $\mathbf{z}_{\text{rad},\text{mo},t}$ at time step t becomes

$$\mathbf{z}_{\text{rad},\text{mo},t} = \begin{bmatrix} d_{\text{mo},2\text{D},t} \\ \varphi_{\text{mo},2\text{D},t} \end{bmatrix}. \quad (4.37)$$

The measurement prediction vector $\hat{\mathbf{z}}_{\text{rad},\text{mo},t}$ and innovation vector $\Delta \mathbf{z}_t$ are obtained analogously to Eq. (4.22) resp. (4.28).

Using the derivative of the $\text{atan}2(\cdot)$ function shown in Appendix A.2, the

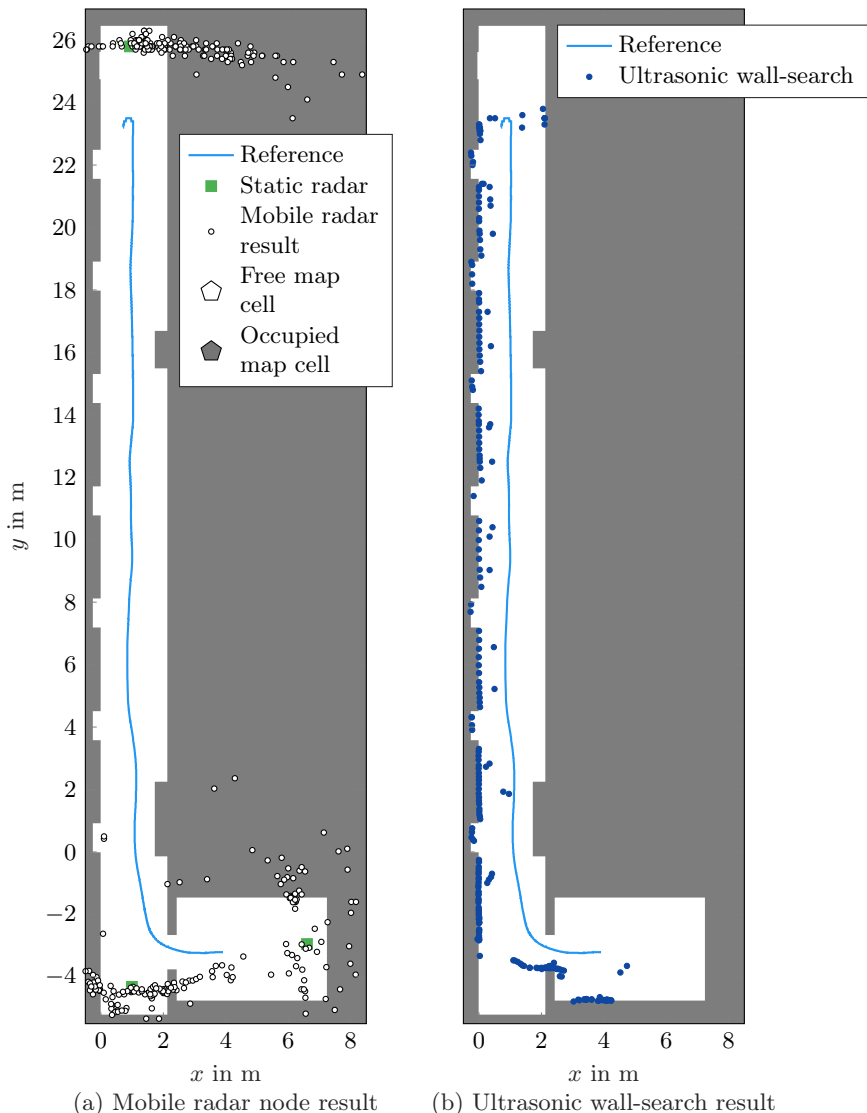


Fig. 4.13: Typical measurement result of the mobile radar node (a) and ultrasonic wall-search system (b) in the corridor shown in Fig. 4.25 (c). A Leica total station was used as a reference (adapted from [51]).

measurement matrix \mathbf{H}_t which is the Jacobian of $\mathbf{h}_{\text{rad,mo}}$ is derived:

$$\begin{aligned} \mathbf{H}_t &= \frac{\partial \mathbf{h}_{\text{rad,mo}}}{\partial \mathbf{x}_{\text{rob}}} \Big|_{\mathbf{x}_{\text{rob}} = \bar{\mathbf{x}}_{\text{rob}}} \\ &= \begin{bmatrix} -\frac{\hat{d}_{2D,x,t}}{\hat{d}_{2D,t}} & -\frac{\hat{d}_{2D,y,t}}{\hat{d}_{2D,t}} & \frac{d_{\Delta 2D}(\hat{d}_{2D,x,t} \sin \theta_{\Delta 2D} - \hat{d}_{2D,y,t} \cos \theta_{\Delta 2D})}{\hat{d}_{2D,t}} \\ \frac{\hat{d}_{2D,y,t}}{\hat{d}_{2D,t}} & -\frac{\hat{d}_{2D,x,t}}{\hat{d}_{2D,t}} & -\frac{d_{\Delta 2D}(\hat{d}_{2D,y,t} \sin \theta_{\Delta 2D} + \hat{d}_{2D,x,t} \cos \theta_{\Delta 2D})}{\hat{d}_{2D,t}^2} - 1 \\ \frac{\hat{d}_{2D,t}^2}{\hat{d}_{2D,t}} & \frac{\hat{d}_{2D,t}^2}{\hat{d}_{2D,t}} & \end{bmatrix}. \end{aligned} \quad (4.38)$$

The EKF update is then performed as given in Eq. (4.29).

Fig. 4.14 illustrates the behavior of the filter depending on the heading uncertainty of the mobile robot. As seen in Fig. 4.14 (a), for relatively low heading uncertainty, the filter performs a translation and almost no rotation. Assuming a higher heading uncertainty and keeping the remaining simulation parameters unchanged, the filter performs almost pure rotation and almost no translation as shown in Fig. 4.14 (b).

If the mobile radar node is positioned above the origin of the robot coordinate system, i.e. $d_{\Delta 2D} = 0$, the equation for \mathbf{H}_t simplifies to

$$\mathbf{H}_t = \begin{bmatrix} -\frac{\hat{d}_{2D,x,t}}{\hat{d}_{2D,t}} & -\frac{\hat{d}_{2D,y,t}}{\hat{d}_{2D,t}} & 0 \\ \frac{\hat{d}_{2D,y,t}}{\hat{d}_{2D,t}} & -\frac{\hat{d}_{2D,x,t}}{\hat{d}_{2D,t}} & -1 \\ \frac{\hat{d}_{2D,t}^2}{\hat{d}_{2D,t}} & \frac{\hat{d}_{2D,t}^2}{\hat{d}_{2D,t}} & \end{bmatrix}. \quad (4.39)$$

In contrast to the static radar node measurement, the position and orientation estimate do not decouple for the mobile radar node. The reason is that even though the mobile robot heading in this case does not influence the range measurement, a change of the mobile robot position does have an effect on the angle measurement. This is modeled by the first two elements in the second row of \mathbf{H}_t in Eq. (4.39).

Even though the static radar node measures the distance to the robot and the mobile radar node measures the distance to the static unit, the physical quantity measured – the distance between two points \hat{d}_{2D} – is the same, the problem is reciprocal. Thus, the distance measurement of the mobile radar node conveys no qualitatively new information, but can only be used to improve the current estimate. As the path is not entirely reciprocal due to the motion of the robot, some multipath resistance is gained due to diversity.

This is not the case for the measured angle. While the angle measurement φ_{st} of the static radar node carries information about the 2D position of the robot, the information contained in the mobile node measurement φ_{mo} is about

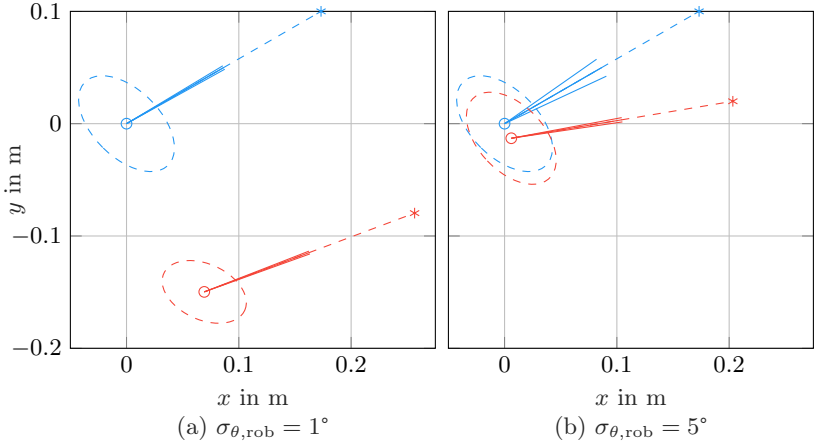


Fig. 4.14: Simulation of the behavior of the 2D EKF for fusing the mobile radar node measurements. The \circ symbol and the dashed ellipse signify the position and uncertainty of the mobile robot (blue before the update; red after the update); the $*$ symbol denotes the position of the mobile radar node; the solid lines denote the mobile robot heading and the stretch between them is proportional to the heading uncertainty. The mobile robot heading uncertainty is (a) $\sigma_{\theta,\text{rob}} = 1^\circ$ and (b) $\sigma_{\theta,\text{rob}} = 5^\circ$. All other parameters are equal in both subfigures.

the robot heading. The mobile radar node can thus be categorized as a range and bearing sensor [107]. Each radar measurement provides only 2 constraints in the three-dimensional mobile robot pose space and is thus not sufficient for complete pose estimation. However, one bilateral radar measurement is enough to determine the complete 2D pose of the mobile robot.

As already mentioned, the angle measurement with the antenna arrays used is not reliable in the envisaged environment for large distances. Therefore, for $d_{\text{mo}} \gtrsim 10 \text{ m}$ the filter was divided in two 1D filters similar to Section 4.5.3. As their derivation is very similar to the filters already shown, it will not be discussed here in detail.

Even though the angle estimation for $d_{\text{mo}} \gtrsim 10 \text{ m}$ is not very accurate, it is very useful especially during the initialization procedure and when the filter loses the robot position and needs to recover. In these cases, the coarse absolute orientation is very important, as it is necessary to fuse the odometry readings

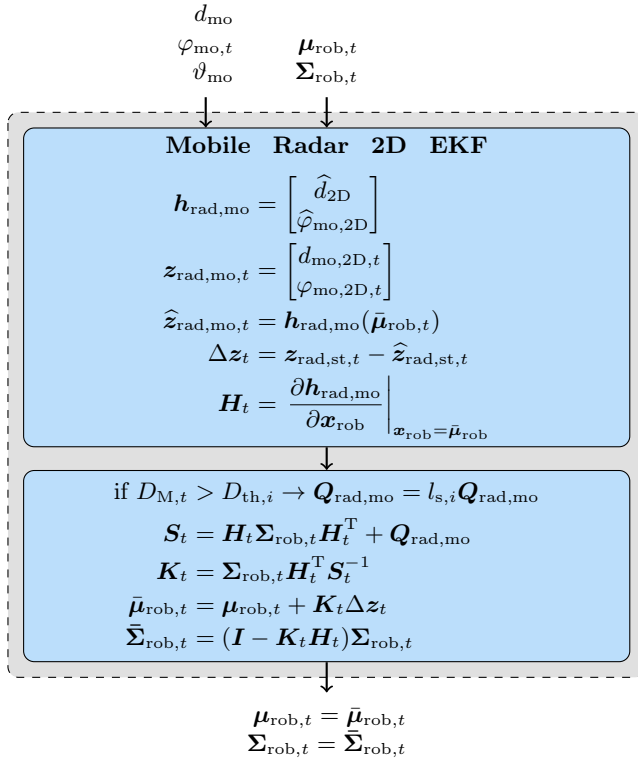


Fig. 4.15: Simplified block diagram of the mobile radar EKF correction step.

correctly. Otherwise, the filter would not know if the robot is driving up or down the corridor or towards the wall. Of course, estimating the driving direction is possible using only the range data, but this assumes that the robot is moving for a certain time. Using the mobile radar node angle, only a single measurement is sufficient even when the robot is not moving. Thus, a high reliability is achieved. The EKF for the mobile radar measurements is summarized in Fig. 4.15.

4.7 Fusing Ultrasonic Measurements

To increase the position and orientation estimation accuracy for larger distances between the robot and the static radar, an ultrasonic sensor was additionally employed to measure the relative orientation and distance of the robot to the walls.

4.7.1 Wall-Finding Ultrasonic Sensor

The ultrasonic device used consists of 3 air-coupled piezoelectric ultrasonic transducers, which are arranged in a linear array [131]. They are operated as transmitters and receivers in immediate succession obtaining 3 echo reflections from the wall. The Hough transform is then used to convert the digitized echoes to the distance-angle parameter space. A subsequent peak search yields the sought distance d_{us} and angle φ_{us} to the wall in \mathbf{f}_{us} . This system can detect a wall up to a distance of 3 m and within an angle of $\pm 40^\circ$.

The performance of the ultrasonic system in a typical indoor office scenario is illustrated in Fig. 4.13 (b). As evident, the sensor mostly successfully manages to find the wall. It only fails at the door frames, where more than a single unambiguous wall hypothesis exists. Apart from that, the sensor has a standard deviation of 1 cm in range and 2.5° in angle.

4.7.2 Ultrasonic Virtual Tag

In order to fuse the ultrasonic measurement into the robot pose estimate, the concept of a “virtual tag” was introduced. The virtual tag is defined as the point in the map, which corresponds to the ultrasonic measurement and relative to which the robot pose can be determined. For an ideal measurement this is the point on the wall closest to the robot.

Given the ultrasonic measurement d_{us} and φ_{us} , the virtual tag position $\mathbf{m}_{\text{us}, \mathbf{f}_{\text{us}}}$ in the ultrasonic coordinate frame \mathbf{f}_{us} can be calculated with simple geometric considerations to

$$\mathbf{m}_{\text{us}, \mathbf{f}_{\text{us}}} = \begin{bmatrix} d_{\text{us}} \cos \varphi_{\text{us}} \\ d_{\text{us}} \sin \varphi_{\text{us}} \end{bmatrix}. \quad (4.40)$$

$\mathbf{m}_{\text{us}, \mathbf{f}_{\text{us}}}$ is then transformed to the robot coordinate system $\mathbf{f}_{\text{rob}, t}$ using the static known transformation and then to the global coordinate system \mathbf{f}_{glo} to obtain the virtual tag position in global coordinates \mathbf{m}_{us} (shown as a blue square in Fig. 4.16).

To update the robot orientation estimate, the angle measured by the ultrasonic sensor needs to be converted to global coordinates. The angle ϕ_{us} between the origin of the coordinate system of the ultrasonic sensor $\mathbf{o}_{\mathbf{f}_{\text{us}}}$ and the virtual

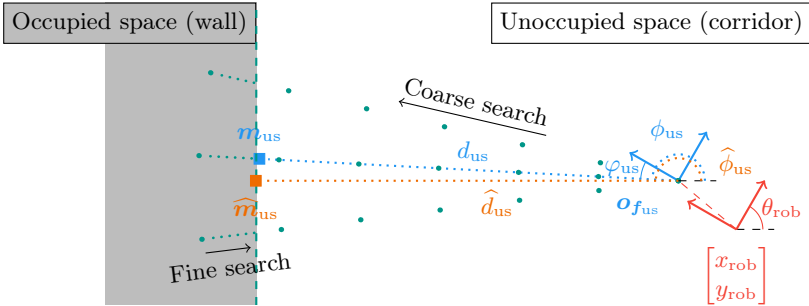


Fig. 4.16: Ultrasonic virtual tag measurement and estimation given a robot pose estimate and a binary occupancy grid map (adapted from [51]).

tag is calculated by

$$\phi_{\text{us}} = \angle(o_f_{\text{us}}, m_{\text{us}}) \approx \theta_{\text{rob}} + \varphi_{\text{us}} + \pi/2. \quad (4.41)$$

The measurement function \mathbf{h}_{us} is then defined as

$$\mathbf{h}_{\text{us}} = \begin{bmatrix} d_{\text{us}} \\ \theta_{\text{rob}} + \varphi_{\text{us}} + \pi/2 \end{bmatrix}. \quad (4.42)$$

and the measurement vector is

$$\mathbf{z}_{\text{us},t} = \mathbf{h}_{\text{us}}(\mathbf{x}_{\text{rob},t}) + \mathcal{N}(\mathbf{0}, \mathbf{Q}_{\text{us}}) = \begin{bmatrix} d_{\text{us},t} \\ \phi_{\text{us},t} \end{bmatrix}. \quad (4.43)$$

\mathbf{Q}_{us} denotes the measurement covariance matrix of the ultrasonic sensor.

The estimate for the 2D position of the virtual tag \hat{m}_{us} is defined by

$$\hat{\mathbf{m}}_{\text{us}} = \begin{bmatrix} \hat{x}_{\hat{\mathbf{m}}_{\text{us}}} \\ \hat{y}_{\hat{\mathbf{m}}_{\text{us}}} \end{bmatrix}. \quad (4.44)$$

It needs to be calculated by finding the point on the wall closest to the current position estimate.

Since the map of the scenario is only available as a raster binary occupancy-grid map and not as geometric primitives, the problem cannot be solved analytically. Instead, ray casting is used. A ray is shot from the estimate for the ultrasonic sensor coordinate system origin o_f_{us} in the direction of the current ultrasonic angle measurement ϕ_{us} from Eq. (4.41), as this is a good guess at where the wall is located relative to the mobile robot as shown in Fig. 4.16. The

values of the points in the map are probed until an occupied point is found.

In order to efficiently find the intersection point with the wall, a coarse search with an interval Δd_{coarse} is first performed starting from $\mathbf{o}_{f_{\text{us}}}$ in wall direction. The points belonging to this ray are given by

$$\mathbf{p}_{\text{probe},n} = \text{round}_{\text{map}} \left(\mathbf{o}_{f_{\text{us}}} + \begin{bmatrix} \Delta d_{\text{coarse}} \cos \phi_{\text{us}} \\ \Delta d_{\text{coarse}} \sin \phi_{\text{us}} \end{bmatrix} n \right), \quad (4.45)$$

where n denotes the consecutive point number and the function $\text{round}_{\text{map}}(\cdot)$ rounds the continuous $[x, y]$ coordinates to a discrete point on the map (thick teal points in Fig. 4.16). Starting at $n = 1$, the state of the point $\mathbf{p}_{\text{probe},n}$ in the map $\mathbf{M}_{\text{og}}[\mathbf{p}_{\text{probe},n}]$ is checked. If the point is unoccupied, this means that the point lies inside the corridor / room and the search continues with $n = n + 1$. This is repeated until an occupied point is found, which lies inside the wall. The sought point on the surface of the wall is then somewhere on the line between the last 2 points. It should be noted, that this method assumes the wall is thicker than Δd_{coarse} . Otherwise, it might not be detected, as it could lie between two consecutive points.

In order to accurately find the point on the surface of the wall, a fine search in backward direction is performed with

$$\mathbf{p}_{\text{probe},m} = \text{round}_{\text{map}} \left(\mathbf{p}_{\text{probe},n} - \begin{bmatrix} \Delta d_{\text{fine}} \cos \phi_{\text{us}} \\ \Delta d_{\text{fine}} \sin \phi_{\text{us}} \end{bmatrix} m \right). \quad (4.46)$$

These points are illustrated as thin teal points in Fig. 4.16. Again, the state of the map point $\mathbf{M}_{\text{og}}[\mathbf{p}_{\text{probe},m}]$ is checked for growing m until an unoccupied point $\mathbf{p}_{\text{wall}}(\phi_{\text{us}})$ is found. It lies on the wall with an accuracy given by the resolution of the raster map Δd_{map} . This is valid for $\Delta d_{\text{fine}} \leq \Delta d_{\text{map}}$.

To find the position of the virtual tag, the ray casting procedure is repeated two more times at angles $\phi_{\text{us}} \pm \Delta\phi_{\text{wall}}$ to additionally obtain the points $\mathbf{p}_{\text{wall}}(\phi_{\text{us}} + \Delta\phi_{\text{wall}})$ and $\mathbf{p}_{\text{wall}}(\phi_{\text{us}} - \Delta\phi_{\text{wall}})$. If the mobile robot is close to an ideal wall in the map, all 3 points would lie on a line, which describes the wall in global coordinates. If it is close to a corner, the points lie on both sides of the corner and not on a line. In this case an error is returned, as the sensor would fail to find a wall and a virtual tag cannot be defined unambiguously.

A hypothesis for the wall is given by the line through the points $\mathbf{p}_{\text{wall}}(\phi_{\text{us}} + \Delta\phi_{\text{wall}})$ and $\mathbf{p}_{\text{wall}}(\phi_{\text{us}} - \Delta\phi_{\text{wall}})$. To determine whether a wall or a corner is

found, the distance d_{pt} from $\mathbf{p}_{\text{wall}}(\phi_{\text{us}})$ to the wall hypothesis is examined:

$$\begin{aligned} \mathbf{v}_{n,\text{wall}} &= \frac{\mathbf{p}_{\text{wall}}(\phi_{\text{us}} + \Delta\phi_{\text{wall}}) - \mathbf{p}_{\text{wall}}(\phi_{\text{us}} - \Delta\phi_{\text{wall}})}{\|\mathbf{p}_{\text{wall}}(\phi_{\text{us}} + \Delta\phi_{\text{wall}}) - \mathbf{p}_{\text{wall}}(\phi_{\text{us}} - \Delta\phi_{\text{wall}})\|}, \\ \mathbf{v}_{p,\text{wall}} &= \mathbf{p}_{\text{wall}}(\phi_{\text{us}} - \Delta\phi_{\text{wall}}) + ((\mathbf{p}_{\text{wall}}(\phi_{\text{us}}) - \mathbf{p}_{\text{wall}}(\phi_{\text{us}} - \Delta\phi_{\text{wall}})) \cdot \mathbf{v}_{n,\text{wall}}) \mathbf{v}_{n,\text{wall}}, \\ d_{\text{pt}} &= \|\mathbf{p}_{\text{wall}}(\phi_{\text{us}}) - \mathbf{v}_{p,\text{wall}}\|, \end{aligned} \quad (4.47)$$

In Eq. (4.47), $\mathbf{v}_{n,\text{wall}}$ describes the unit vector starting at $\mathbf{p}_{\text{wall}}(\phi_{\text{us}} - \Delta\phi_{\text{wall}})$ in direction of the wall hypothesis. d_{pt} is the distance between $\mathbf{p}_{\text{wall}}(\phi_{\text{us}})$ and its projection $\mathbf{v}_{p,\text{wall}}$ on $\mathbf{v}_{n,\text{wall}}$. For $d_{\text{pt}} < \Delta d_{\text{map}}$ the 3 points are assumed to approximately lie on a line taking into account the map discretization (in the ideal case $d_{\text{pt}} = 0$ is valid, as the projection of a point from the line on the line is the point itself). Otherwise, a corner is detected and the ultrasonic measurement is dismissed as unreliable.

Assuming a wall was found, the virtual tag position estimate $\widehat{\mathbf{m}}_{\text{us}}$ is the projection of $\mathbf{o}_{f_{\text{us}}}$ on the line describing the wall [132]:

$$\widehat{\mathbf{m}}_{\text{us}} = \mathbf{p}_{\text{wall}}(\phi_{\text{us}} - \Delta\phi_{\text{wall}}) + ((\mathbf{o}_{f_{\text{us}}} - \mathbf{p}_{\text{wall}}(\phi_{\text{us}} - \Delta\phi_{\text{wall}})) \cdot \mathbf{v}_{n,\text{wall}}) \mathbf{v}_{n,\text{wall}}. \quad (4.48)$$

$\widehat{\mathbf{m}}_{\text{us}}$ is depicted as an orange square in Fig. 4.16.

The measurement prediction vector $\widehat{\mathbf{z}}_{\text{us},t}$ is then

$$\widehat{\mathbf{z}}_{\text{us},t} = \mathbf{h}_{\text{us}}(\bar{\mu}_{\text{rob},t}) = \begin{bmatrix} \|\mathbf{o}_{f_{\text{us}}} - \widehat{\mathbf{m}}_{\text{us}}\| \\ \bar{\theta}_{\text{rob}} + \varphi_{\text{us}} + \pi/2 \end{bmatrix} \approx \begin{bmatrix} \widehat{d}_{\text{us},t} \\ \widehat{\phi}_{\text{us},t} \end{bmatrix}. \quad (4.49)$$

4.7.3 EKF for Ultrasonic Sensor

Given the measurement $\mathbf{z}_{\text{us},t}$ with the corresponding covariance

$$\mathbf{Q}_{\text{us}} = \begin{bmatrix} \sigma_{d_{\text{us}}}^2 & 0 \\ 0 & \sigma_{\varphi_{\text{us}}}^2 \end{bmatrix} \quad (4.50)$$

and the prediction $\widehat{\mathbf{z}}_{\text{us},t}$ at time step t , an EKF was derived to update the mobile robot pose estimate. An important fact is seen by comparing Eq. (4.1) with (4.43) – while the state is 3D (2D position and orientation), the measurement is only 2D (distance and angle). Thus, the complete pose cannot be determined using only $\mathbf{z}_{\text{us},t}$. Even though the exact 2D position of the virtual tag was calculated by the ray casting procedure, in fact it is only known that it lies on the line describing the wall (its lateral position); its exact position along the line (longitudinal position) is unknown. It is only determined relative to the current position estimate. Therefore, using the 2D position of the virtual tag in the

EKF would erroneously reduce the uncertainty of the estimate in longitudinal direction. Thus, the 2D EKF for the mobile radar from Section 4.6 cannot be used here. Instead, two 1D EKFs were used – one for the distance to the wall and one for the orientation.

1D EKF for Orientation Based on the ultrasonic angle measurement, the mobile robot orientation is estimated relative to the wall. Since the wall coordinates in the map are known, this gives the global orientation. The innovation vector Δz_t is given by

$$\Delta z_t = \text{wrap}(\hat{\phi}_{\text{us},t} - \phi_{\text{us},t}). \quad (4.51)$$

The measurement matrix is $H_t = 1$ and the innovation covariance S_t is

$$S_t = H_t \sigma_{\theta,\text{rob},t}^2 H_t^T + \sigma_{\varphi_{\text{us}}}^2, \quad (4.52)$$

with the robot orientation variance $\sigma_{\theta,\text{rob},t}^2$ from Eq. (4.2) and the ultrasonic sensor angle measurement variance $\sigma_{\varphi_{\text{us}}}^2$ from Eq. (4.50). The Kalman gain K_t and updated estimate for the robot orientation $\bar{\theta}_{\text{rob},t}$ and uncertainty $\sigma_{\theta,\text{rob},t}$ follow from the EKF equations:

$$\begin{aligned} K_t &= \sigma_{\theta,\text{rob},t}^2 H_t^T S_t^{-1}, \\ \bar{\theta}_{\text{rob},t} &= \bar{\theta}_{\text{rob},t} + K_t \Delta z_t. \end{aligned} \quad (4.53)$$

As described in Section 3.4, Eq. (3.27), the effect of this filter on the covariance matrix is a scaling by a matrix $V_{s,t}$:

$$\begin{aligned} V_{s,t} &= \begin{bmatrix} 1 & 0 & 0 \\ 0 & 1 & 0 \\ 0 & 0 & \sqrt{1 - K_t H_t} \end{bmatrix}, \\ \Sigma_{\text{rob},t} &= V_{s,t} \bar{\Sigma}_{\text{rob},t} V_{s,t}^T. \end{aligned} \quad (4.54)$$

This ensures that the variance $\sigma_{\theta,\text{rob},t}^2$ as well as the covariances $\sigma_{x\theta,\text{rob},t}$ and $\sigma_{y\theta,\text{rob},t}$ in $\Sigma_{\text{rob},t}$ are correctly updated.

1D EKF for Distance to Wall The 1D distance EKF operates along the axis connecting the virtual tag and the position estimate (the orange dotted line in Fig. 4.16). The unit vector describing this axis is given by

$$v_{\text{us},t} = \begin{bmatrix} \cos \hat{\phi}_{\text{us},t} \\ \sin \hat{\phi}_{\text{us},t} \\ 0 \end{bmatrix}. \quad (4.55)$$

The position variance along this axis $\sigma_{v_{us,t}}^2$ is described by the projection of the robot pose uncertainty $\Sigma_{rob,t}$ from Eq. (4.2) on $v_{us,t}$:

$$\sigma_{v_{us,t}}^2 = v_{us,t}^T \Sigma_{rob,t} v_{us,t}. \quad (4.56)$$

The innovation vector Δz_t for the resulting 1D EKF is in this case a scalar given by

$$\Delta z_t = d_{us,t} - \hat{d}_{us,t}. \quad (4.57)$$

The measurement Jacobian $H_t = 1$ is a scalar as well. The innovation covariance S_t results from the uncertainty in the position of the robot plus the measurement uncertainty

$$S_t = H_t \sigma_{v_{us,t}}^2 H_t^T + \sigma_{d_{us,t}}^2. \quad (4.58)$$

The Kalman gain K_t and the corrected estimate $\bar{d}_{z,us,t}$ follow from the EKF equations:

$$\begin{aligned} K_t &= \sigma_{v_{us,t}}^2 H_t^T S_t^{-1}, \\ \bar{d}_{z,us,t} &= \hat{d}_{us,t} + K_t \Delta z_t, \end{aligned} \quad (4.59)$$

The updated 2D estimate for the robot position from the 1D EKF result is then

$$\begin{bmatrix} \bar{x}_{rob} \\ \bar{y}_{rob} \end{bmatrix} = \hat{\mathbf{m}}_{us} - \begin{bmatrix} \bar{d}_{z,us} \cos \hat{\phi}_{us} \\ \bar{d}_{z,us} \sin \hat{\phi}_{us} \end{bmatrix}. \quad (4.60)$$

It should be noted, that only $\bar{d}_{z,us}$ is measured by the sensor and changed by the filter. The direction $\hat{\phi}_{us}$ is determined by the wall geometry in the close vicinity of the current position estimate; its value is not directly measured by the sensor and therefore is not updated.

The EKF derivation above updates the position of the origin of the ultrasonic sensor coordinate system $\mathbf{o}_{f_{us}}$. However, its result is directly applied to the mobile robot position in Eq. (4.60). This is valid, since both coordinate systems f_{us} and $f_{rob,t}$ are connected by a known and constant transformation. Eq. (4.60) can be interpreted as shifting the mobile robot (and herewith both coordinate systems) along v_{us} from Eq. (4.55) without changing its orientation.

In order to incorporate the 1D distance measurement in the 2D pose estimate, its uncertainty also has to be fused correctly. The uncertainty reduction factor $l_{s,t}$ along $v_{us,t}$ is

$$l_{s,t} = \sqrt{1 - K_t H_t} \leq 1. \quad (4.61)$$

The robot covariance matrix $\Sigma_{rob,t}$ is updated by scaling it with $l_{s,t}$ along $v_{us,t}$. This is accomplished by first rotating $\Sigma_{rob,t}$ by $-\hat{\phi}_{us,t}$, scaling it with $l_{s,t}$ and rotating it back by $\hat{\phi}_{us,t}$ as described in Section 3.4. The corresponding

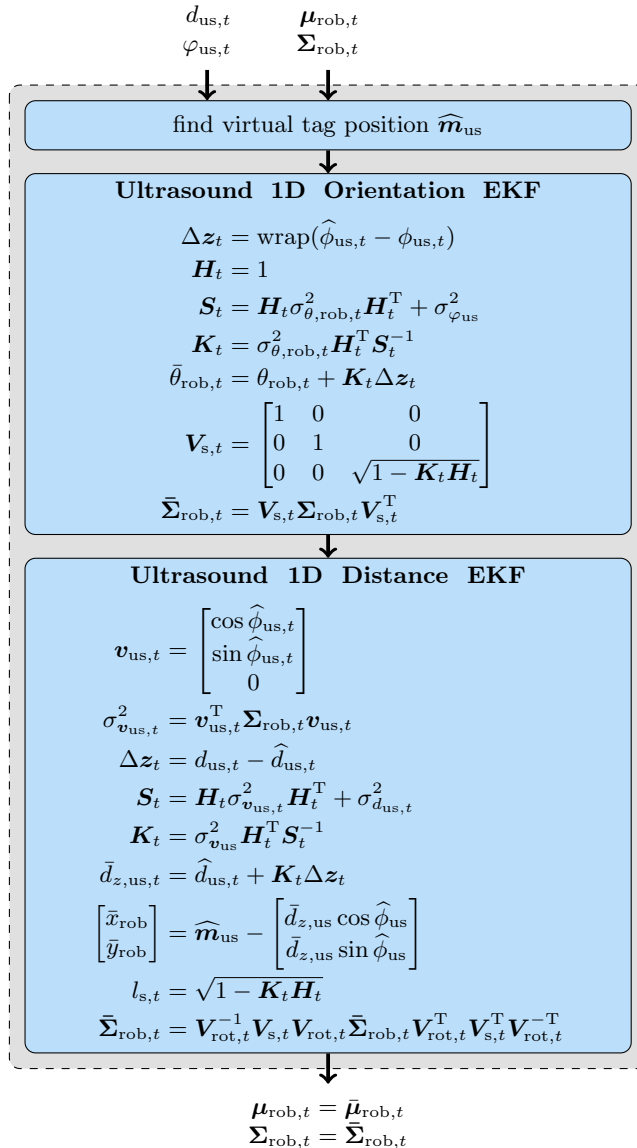


Fig. 4.17: Simplified block diagram of the ultrasonic wall-search EKF correction step.

rotation matrix is given by

$$\mathbf{V}_{\text{rot},t} = \begin{bmatrix} \cos(-\hat{\phi}_{\text{us},t}) & -\sin(-\hat{\phi}_{\text{us},t}) & 0 \\ \sin(-\hat{\phi}_{\text{us},t}) & \cos(-\hat{\phi}_{\text{us},t}) & 0 \\ 0 & 0 & 1 \end{bmatrix} \quad (4.62)$$

and the scaling matrix is

$$\mathbf{V}_{\text{s},t} = \begin{bmatrix} l_{\text{s},t} & 0 & 0 \\ 0 & 1 & 0 \\ 0 & 0 & 1 \end{bmatrix}. \quad (4.63)$$

The update of the robot pose covariance matrix is then performed by

$$\boldsymbol{\Sigma}_{\text{rob},t} = \mathbf{V}_{\text{rot},t}^{-1} \mathbf{V}_{\text{s},t} \mathbf{V}_{\text{rot},t} \bar{\boldsymbol{\Sigma}}_{\text{rob},t} \mathbf{V}_{\text{rot},t}^T \mathbf{V}_{\text{s},t}^T \mathbf{V}_{\text{rot},t}^{-T}. \quad (4.64)$$

Although the ultrasonic range measurement only updates the mobile robot position estimate, it is important to apply the stretching step (4.64) to the complete uncertainty matrix $\bar{\boldsymbol{\Sigma}}_{\text{rob},t}$ in order to also correctly update the covariances $\sigma_{x\theta,\text{rob},t}$ and $\sigma_{y\theta,\text{rob},t}$. The EKF for the ultrasonic wall-search is summarized in Fig. 4.17.

The ultrasonic sensor provides very accurate results at short distances and when its view is unobstructed. This is normally the case in hospital and office building corridors, which is the main envisioned scenario for the system. However, even in this case, it is unable to give an absolute estimate of the mobile robot orientation as it measures it relative to the wall. Due to the symmetry of typical corridors, the orientation result thus has an ambiguity of 180°. This ambiguity can be resolved with the help of the mobile radar node. As the angular measurement range of the sensor is limited to ±40° due to the radiation characteristic of the ultrasonic transducers, the sensor provides erroneous measurement for larger angles. This means that the sensor is blind when the robot is facing the wall (the sensor is mounted on the side of the robot). A possible solution would be to use multiple sensors on all sides of the robot.

Another use-case when the ultrasonic sensor fails, is when the mobile robot operates in an office / hospital room, as rooms tend to be filled with objects, which frequently obstruct the wall-measurement and the wall-detection works unreliable in such cluttered environments. Large foyers are also a problematic scenario due to the limited measurement range of the ultrasonic sensor. Such situations can be covered by a purely radar-based localization, as in these cases it can provide both accurate range and angle measurements due to the lower number of available multipath components.

4.8 Using Mahalanobis Distance to Improve Reliability and Integrity

Although the performance of the EKF is optimal for normally distributed statistical measurement errors, it can quickly deteriorate when systematic errors are present. For the ultrasonic sensor such errors can occur, when the wall detection fails, for example when the robot is passing by a corner or there are objects between the robot and the wall. Systematic errors for the radar can be caused by objects blocking the LOS path or by multipath interference. This manifests as measurements with very wrong distance and angles. Since such cases cannot be modeled, the EKF would try to treat them as normal measurements. This is a violation of the complete state assumption defined in Section 3.1 and causes an error in the position estimate.

A simulation of a 1D positioning system is shown in Fig. 4.18 (a) to exemplify this. The system consists of an odometer and a range-measuring radar. As evident from the figure, using only odometry (the blue curve), the estimate drifts away with time from the correct result (the black curve). Fusing the odometry data with the radar data (in green) using an EKF leads to the result in red which follows the ideal curve much better.

However, the outliers in the radar measurements during time $t \approx 1 \dots 2$ s cause a significant error in the EKF result as they pose unmodeled systematic error and violate the Markov assumption (Chapter 2.4.4 in [107]). A kidnapping as present at $t = 7.5$ s also leads to a large error. Kidnapping means that the robot is “teleported”, i.e. it gets moved to a new location while still believing it’s at the old location as the motion was not measured by the odometer (Chapter 7.1 in [107]).

In order to improve the stability of the EKF and enable outlier detection, the Mahalanobis distance D_M presented in Section 3.4 is used [133]. It is calculated during the EKF correction step and is given by

$$D_{M,t} = \sqrt{\Delta z_t^T S_t^{-1} \Delta z_t}. \quad (4.65)$$

When applied to positioning problems, for the same Euclidean distance between a measurement and a prediction (i.e. length of the innovation vector Δz), the Mahalanobis distance is shorter when the position uncertainty is larger (equivalently, it can be said that it’s equal to “fewer standard deviations” from that distribution). D_M can thus be used as a benchmark for the plausibility of a measurement, when a belief for the position is available.

As shown in Listing 4.1, an outlier detection can be achieved by thresholding. If $D_{M,t}$ is above a certain value, the measurement is marked as erroneous. It can either be discarded completely, or its measurement uncertainty can be in-

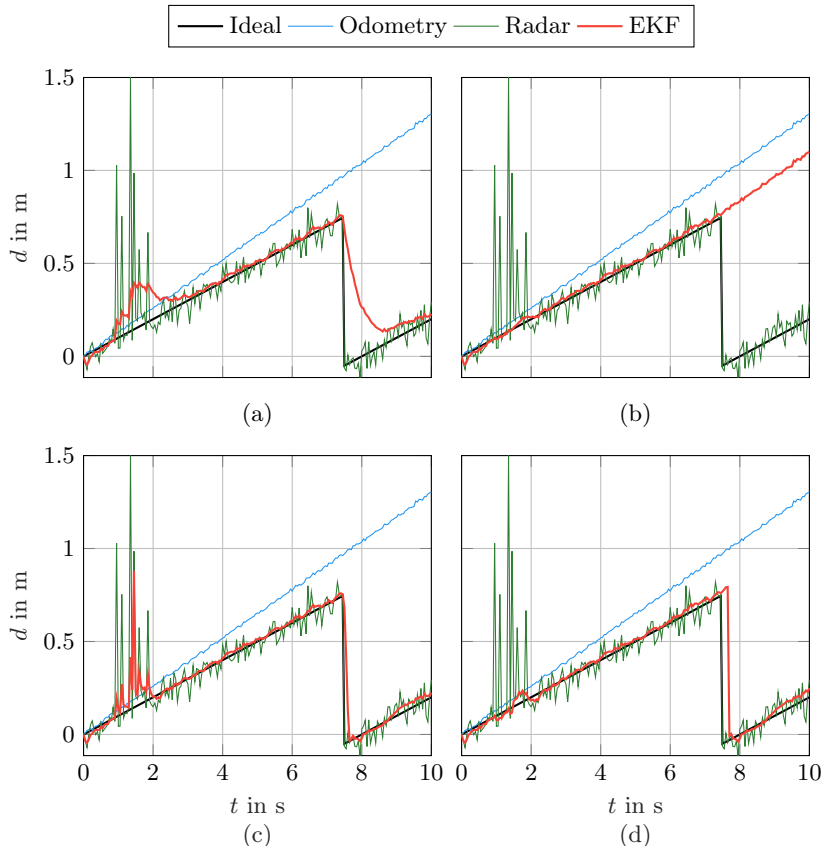


Fig. 4.18: 1D simulation demonstrating the usage of the Mahalanobis distance D_M for outlier detection and self-recovery: (a) Not using D_M ; (b) Using D_M for outlier detection only (Listing 4.1); (c) Using D_M for self-recovery only (Listing 4.2); (d) Using D_M for outlier detection and self-recovery (Listing 4.1 and 4.2).

Listing 4.1: Usage of Mahalanobis distance D_M for outlier detection (simplified).

```
if  $D_{M,t} > D_{\text{th1}}$ 
    % increase measurement covariance by  $l_{s1}$  if  $D_M > D_{\text{th1}}$ 
     $\mathbf{Q} = l_{s1} \mathbf{Q}$ 
end
```

Listing 4.2: Usage of Mahalanobis distance D_M for self-recovery (simplified).

```
if  $D_{M,t} > D_{\text{th2}}$ 
    % increase state covariance by  $l_{s2}$  if  $D_M > D_{\text{th2}}$ 
     $\Sigma_{\text{rob},t} = l_{s2} \Sigma_{\text{rob},t}$ 
end
```

creased. This lowers the weighting of the measurement and thus its effect on the pose. This is illustrated in Fig. 4.18 (b). While this approach can successfully filter out outliers when the position estimate is accurate, it also discards correct measurements when the position estimate is wrong thus preventing self-recovery as evident for the jump at $t = 7.5$ s.

This problem can be solved by the approach in Listing 4.2. When a measurement with large D_M is detected, the covariance matrix $\Sigma_{\text{rob},t}$ describing the mobile robot position uncertainty is manually scaled by a certain factor. If many consecutive measurements have large D_M , this frequently means, that the current position estimate is wrong. Using this technique, the filter successfully and quickly recovers from “kidnapping” as shown in Fig. 4.18 (c). However, the performance when outliers are present also deteriorates, as the filter now reacts more sensitively to large changes due to the increased covariance.

When both techniques are combined, if there are only a few measurements with large D_M which is typically the case for outliers, there is almost no impact on the positioning, as the position uncertainty is reduced by the subsequent correct measurements. In the case of a sudden position change, the position covariance is increased until it becomes so big, that D_M falls below the threshold and the measurement is used to update the position estimate. This enables self-recovery for the case of a lost or kidnapped robot as visible in Fig. 4.18 (d). However, it should be noted, that in general the outlier-resistance is slightly reduced and the reaction time to sudden changes is slower as can be seen by comparing (d) with (b) and with (c).

Typical values used in this work for the parameters in Listing 4.1 and 4.2 are $D_{\text{th1}} = 2$, $D_{\text{th2}} = 5$, $l_{s1} = 100$, and $l_{s2} = 1.1$. These values are independent of

the absolute values of the measurement covariances.

Using these techniques improves the reliability (how often localization fails) as well as the integrity (how well the localization can recover from failure or at least can detect it) of the system [134].

4.9 Initialization / Kidnapped-Robot Case

One of the main advantages of the proposed mobile robot localization concept is that it uses an absolute reference (the static radar node) to estimate the robot pose. When the system is started, the pose is initialized to some coordinates (e.g. the origin of the global coordinate system facing in positive y direction) and the state uncertainty is set to a very high value. A single bilateral radar measurement is then sufficient to obtain an initial coarse estimate for the complete mobile robot pose. The estimate is then refined with subsequent ultrasonic measurements. Compared to relative localization techniques, e.g. based on a laser scanner and map matching, this enables a quick, easy, and unambiguous initialization without any prior knowledge about the mobile robot pose.

The absolute reference also enables reliable self-recovery for the case when the sensor fusion result is implausible, e.g. when the estimate is on an occupied point (inside a wall). If such an implausible situation occurs, the state uncertainty of the mobile robot is set to a very large value. The subsequent sensor measurements are then used to recover the state as during the initialization procedure described in the previous paragraph.

The concept used also makes it possible to detect when the robot is kidnapped. If it is suddenly displaced to a new position without its knowledge, there will be a big discrepancy between the predicted and the measured position and the Mahalanobis distance will be large. Thanks to the absolute reference, the techniques from Section 4.8 can reliably handle this case.

4.10 Relative Positioning of a Person

As described in Chapter 4.3, in the envisioned application, the mobile robot should be capable of autonomously following or leading a person. This is possible by estimating the person's position in 2D relative to the robot. For the application at hand this was realized by radar measurements from the radar node on the robot to the portable radar node shown in Fig. 4.3 (follow-me beacon) carried by the person.

Based on the range d_{fb} , azimuth φ_{fb} , and elevation ϑ_{fb} measurements from the mobile radar to the follow-me beacon, its 3D position in the Cartesian mobile

radar coordinate system $\mathbf{f}_{\text{rad},\text{mo}}$ is

$$\mathbf{p}_{\text{fb},\mathbf{f}_{\text{rad},\text{mo}}} = \begin{bmatrix} d_{\text{fb}} \cos \vartheta_{\text{fb}} \cos \varphi_{\text{fb}} \\ d_{\text{fb}} \cos \vartheta_{\text{fb}} \sin \varphi_{\text{fb}} \\ d_{\text{fb}} \sin \vartheta_{\text{fb}} \end{bmatrix}. \quad (4.66)$$

On the assumption that an estimate for the mobile robot pose exists, $\mathbf{p}_{\text{fb},\mathbf{f}_{\text{rad},\text{mo}}}$ can be converted to the global coordinate system by

$$\mathbf{p}_{\text{fb}} = \mathbf{b}_{\text{tran}}(\mathbf{f}_{\text{rad},\text{mo}}, \mathbf{f}_{\text{glo}}, \mathbf{p}_{\text{fb},\mathbf{f}_{\text{rad},\text{mo}}}). \quad (4.67)$$

In contrast to the measurements to or from the static radar nodes described in Chapter 4.5 and 4.6, the height difference between the mobile radar node and the follow-me beacon is not constant due to the unknown height of the person and the variation during a stride. Therefore, the elevation angle measurement ϑ_{fb} is used to improve the estimation of the distance between the robot and the person in the xy plane.

In order to improve the accuracy and stability of the radar-based localization, an EKF based on a 2D discrete white noise acceleration (DWNA) model was used [38], Chapter 6.2.2 in [135]. The state vector \mathbf{x}_{fb} contains the 2D position $[x_{\text{fb}} \ y_{\text{fb}}]^T$ and 2D velocity $[v_{\text{fb},x} \ v_{\text{fb},y}]^T$ of the follow-me beacon carried by the tracked person:

$$\mathbf{x}_{\text{fb}} = \begin{bmatrix} x_{\text{fb}} \\ y_{\text{fb}} \\ v_{\text{fb},x} \\ v_{\text{fb},y} \end{bmatrix}. \quad (4.68)$$

The model is based on the assumption, that during one time step, the person moves with a constant acceleration vector $\mathbf{a}_{\text{fb}} = [a_{\text{fb},x} \ a_{\text{fb},y}]^T$. The acceleration terms are not measured and are thus unknown. Their mean is 0 as in general people start at standstill, accelerate, move, decelerate and stop. Therefore, the accelerations are modeled as mutually independent zero-mean and normally distributed noise terms with a covariance matrix $\mathbf{Q}_a = \sigma_a^2 \mathbf{I}$: $\mathbf{a}_{\text{fb}} \sim \mathcal{N}(\mathbf{0}, \mathbf{Q}_a)$.

The state prediction for the time step t is then given by the standard linear motion equations

$$\begin{aligned} \begin{bmatrix} x_{\text{fb},t} \\ y_{\text{fb},t} \end{bmatrix} &= \begin{bmatrix} x_{\text{fb},t-1} \\ y_{\text{fb},t-1} \end{bmatrix} + \begin{bmatrix} v_{\text{fb},x,t-1} \\ v_{\text{fb},y,t-1} \end{bmatrix} \Delta t + \begin{bmatrix} a_{\text{fb},x,t-1} \\ a_{\text{fb},y,t-1} \end{bmatrix} \frac{\Delta t^2}{2}, \\ \begin{bmatrix} v_{\text{fb},x,t} \\ v_{\text{fb},y,t} \end{bmatrix} &= \begin{bmatrix} v_{\text{fb},x,t-1} \\ v_{\text{fb},y,t-1} \end{bmatrix} + \begin{bmatrix} a_{\text{fb},x,t-1} \\ a_{\text{fb},y,t-1} \end{bmatrix} \Delta t, \end{aligned} \quad (4.69)$$

where Δt denotes the time between two consecutive EKF prediction steps. This

can be written in a more compact form as

$$\mathbf{x}_{\text{fb},t} = \mathbf{A}\mathbf{x}_{\text{fb},t-1} + \mathbf{B}\mathbf{a}_{\text{fb},t-1}, \quad (4.70)$$

with the state transition matrices

$$\mathbf{A} = \begin{bmatrix} 1 & 0 & \Delta t & 0 \\ 0 & 1 & 0 & \Delta t \\ 0 & 0 & 1 & 0 \\ 0 & 0 & 0 & 1 \end{bmatrix} \quad (4.71)$$

and

$$\mathbf{B} = \begin{bmatrix} 0.5\Delta t^2 & 0 \\ 0 & 0.5\Delta t^2 \\ \Delta t & 0 \\ 0 & \Delta t \end{bmatrix}. \quad (4.72)$$

Keeping in mind that the acceleration is modeled as zero-mean ($\mathbb{E}\{\mathbf{a}_{\text{fb}}\} = \mathbf{0}$), the EKF prediction step becomes

$$\begin{aligned} \bar{\mu}_{\text{fb},t} &= \mathbf{A}\mu_{\text{fb},t-1}, \\ \bar{\Sigma}_{\text{fb},t} &= \mathbf{A}\Sigma_{\text{fb},t-1}\mathbf{A}^T + \mathbf{B}Q_a\mathbf{B}^T. \end{aligned} \quad (4.73)$$

As evident from Eq. (4.67), the radar measures the position of the follow-me beacon directly. Hence, the measurement vector and measurement prediction vector are

$$\begin{aligned} \mathbf{z}_t &= \begin{bmatrix} p_{\text{fb},x,t} \\ p_{\text{fb},y,t} \end{bmatrix}, \\ \hat{\mathbf{z}}_t &= \begin{bmatrix} \bar{\mu}_{\text{fb},x,t} \\ \bar{\mu}_{\text{fb},y,t} \end{bmatrix} = \underbrace{\begin{bmatrix} x_{\text{fb},t} \\ y_{\text{fb},t} \end{bmatrix}}_{\mathbf{h}_{\text{fb}}} + \mathcal{N}(\mathbf{0}, \mathbf{R}_t). \end{aligned} \quad (4.74)$$

$p_{\text{fb},x,t}$ and $p_{\text{fb},y,t}$ denote the x and y components of \mathbf{p}_{fb} from Eq. (4.67) and \mathbf{R}_t the measurement noise in $[x, y]$ space. $\hat{\mathbf{z}}$ is derived directly from $\bar{\mu}_{\text{fb}}$ in Eq. (4.73). This leads to the innovation vector

$$\Delta\mathbf{z}_t = \mathbf{z}_t - \hat{\mathbf{z}}_t = \begin{bmatrix} p_{\text{fb},x,t} \\ p_{\text{fb},y,t} \end{bmatrix} - \begin{bmatrix} \bar{\mu}_{\text{fb},x,t} \\ \bar{\mu}_{\text{fb},y,t} \end{bmatrix} \quad (4.75)$$

and the measurement matrix

$$\mathbf{H} = \left. \frac{\partial \mathbf{h}_{\text{fb}}}{\partial \mathbf{x}_{\text{fb}}} \right|_{\mathbf{x}_{\text{fb}}=\bar{\mu}_{\text{fb}}} = \begin{bmatrix} 1 & 0 & 0 & 0 \\ 0 & 1 & 0 & 0 \end{bmatrix}. \quad (4.76)$$

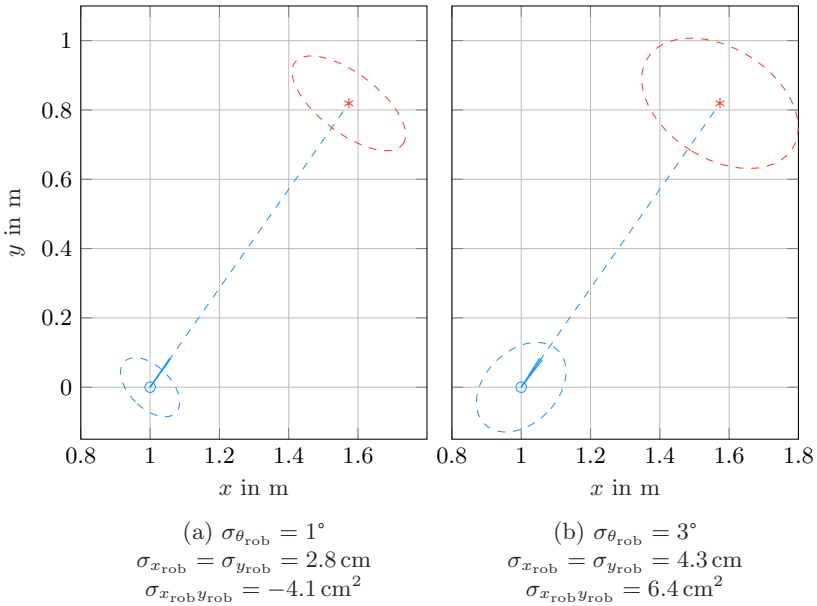


Fig. 4.19: Resulting follow-me beacon position uncertainty (in red) depending on the pose uncertainty of the mobile robot (in blue). Identical radar measurement uncertainties were used; the robot position and orientation uncertainty in (a) is lower than in (b).

Since the position of the follow-me beacon is measured relative to the mobile robot, the absolute measurement uncertainty results from the addition of the pose uncertainty of the robot and the radar measurement uncertainty. This is illustrated in Fig. 4.19. The case of a relatively low robot position and orientation error is shown in (a). As evident from (b), while keeping the measurement covariance matrix unchanged, increasing the position uncertainty has additive impact on the absolute position error of the follow-me beacon; increasing the orientation uncertainty causes a widening of the covariance ellipse in cross-range direction.

This can be expressed as a linear conversion of the covariance matrix

$$\mathbf{Q}_t = \begin{bmatrix} & 0 & 0 \\ \Sigma_{\text{rob},t} & 0 & 0 \\ & 0 & 0 \\ 0 & 0 & 0 \\ 0 & 0 & 0 \end{bmatrix} \quad (4.77)$$

from state space / radar measurement space $\mathbf{p}_x = [x_{\text{rob}} \ y_{\text{rob}} \ \theta_{\text{rob}} \ d_{\text{fb}} \ \phi_{\text{fb}}]^T$ to measurement space $\mathbf{p}_z = [x_{\text{fb}} \ y_{\text{fb}}]^T$ described by the Jacobian

$$\mathbf{G}_t = \frac{\partial \mathbf{p}_z}{\partial \mathbf{p}_x} = \begin{bmatrix} 1 & 0 & -d_{\text{fb},t} \sin \phi_{\text{fb},t} & \cos \phi_{\text{fb},t} & -d_{\text{fb},t} \sin \phi_{\text{fb},t} \\ 0 & 1 & d_{\text{fb},t} \cos \phi_{\text{fb},t} & \sin \phi_{\text{fb},t} & d_{\text{fb},t} \cos \phi_{\text{fb},t} \end{bmatrix}. \quad (4.78)$$

The 2D projection of \mathbf{p}_{fb} from Eq. (4.66) was used to obtain the polar representation

$$\begin{bmatrix} d_{\text{fb}} \\ \phi_{\text{fb}} \end{bmatrix} = \begin{bmatrix} \|\bar{\mu}_{\text{fb},xy} - \mu_{\text{rob},xy}\| \\ \angle(\bar{\mu}_{\text{fb},xy}, \mu_{\text{rob},xy}) \end{bmatrix} \approx \begin{bmatrix} d_{\text{fb}} \\ \varphi_{\text{fb}} + \theta_{\text{rob}} \end{bmatrix} \quad (4.79)$$

and

$$\begin{bmatrix} x_{\text{fb}} \\ y_{\text{fb}} \end{bmatrix} = \mu_{\text{rob},xy} + \begin{bmatrix} d_{\text{fb}} \cos \phi_{\text{fb}} \\ d_{\text{fb}} \sin \phi_{\text{fb}} \end{bmatrix}. \quad (4.80)$$

The approximation in Eq. (4.79) allows for an easier conversion of the covariance. It is accurate when the height of the mobile radar node and of the follow-me beacon are approximately equal and when the mobile radar node is placed in the center of the robot. Both conditions are fulfilled relatively well for the system at hand.

The innovation covariance then becomes

$$\mathbf{S}_t = \mathbf{H}_t \bar{\Sigma}_{\text{fb},t} \mathbf{H}_t^T + \mathbf{G}_t \mathbf{Q}_t \mathbf{G}_t^T. \quad (4.81)$$

The belief is then updated by

$$\begin{aligned} \mathbf{K}_t &= \bar{\Sigma}_{\text{fb},t} \mathbf{H}_t^T \mathbf{S}_t^{-1}, \\ \boldsymbol{\mu}_{\text{fb},t} &= \bar{\mu}_{\text{fb},t} + \mathbf{K}_t \Delta \mathbf{z}_t, \\ \Sigma_{\text{fb},t} &= (\mathbf{I} - \mathbf{K}_t \mathbf{H}_t) \bar{\Sigma}_{\text{fb},t}. \end{aligned} \quad (4.82)$$

From the equations above, it is not directly evident how the velocity is estimated. This can be seen by assuming a known initial state with $\Sigma_{\text{fb},t} = \mathbf{0}$ and a perfect measurement $\mathbf{z}_t = [x_{\text{fb}} \ y_{\text{fb}}]^T$ with $\mathbf{Q} = \mathbf{0}$. Under these assumptions, the state covariance from Eq. (4.73) simplifies to $\bar{\Sigma}_{\text{fb},t} = \mathbf{B} \mathbf{Q}_{\text{a}} \mathbf{B}^T$ and the in-

novation covariance from Eq. (4.81) to $\mathbf{S}_t = \mathbf{H}_t \bar{\Sigma}_{\text{fb},t} \mathbf{H}_t^T$. Inserting these into the Kalman gain equation yields

$$\mathbf{K}_t = \begin{bmatrix} 1 & 0 \\ 0 & 1 \\ \frac{2}{\Delta t} & 0 \\ 0 & \frac{2}{\Delta t} \end{bmatrix}. \quad (4.83)$$

The state update equation using the Kalman gain from Eq. (4.83) and using the above mentioned assumptions becomes

$$\boldsymbol{\mu}_{\text{fb},t} = \begin{bmatrix} x_{\text{fb},t} \\ y_{\text{fb},t} \\ 2 \frac{x_{\text{fb},t} - x_{\text{fb},t-1}}{\Delta t} - v_{\text{fb},x,t-1} \\ 2 \frac{y_{\text{fb},t} - y_{\text{fb},t-1}}{\Delta t} - v_{\text{fb},y,t-1} \end{bmatrix}. \quad (4.84)$$

The standard linear motion equations can be explicitly recognized in Eq. (4.84). In the common case of non-zero state covariance and non-ideal measurements, the state update is a weighted version of Eq. (4.84). The EKF for the follow-me beacon relative positioning is summarized in Fig. 4.20.

To execute follow or lead tasks, only the relative position of the follow-me beacon to the robot is necessary. Implementing the sensor fusion in absolute coordinates, however, has the advantage, that the mobile robot localization uncertainty can be correctly considered. When the robot pose is known with high certainty, the measurement of the follow-me beacon position should be weighted more than in the opposite case. This ensures the consistent performance of the filter. The techniques using the Mahalanobis distance to filter outliers from Chapter 4.8 and the comments about initialization and self-recovery from Chapter 4.9 are valid here as well.

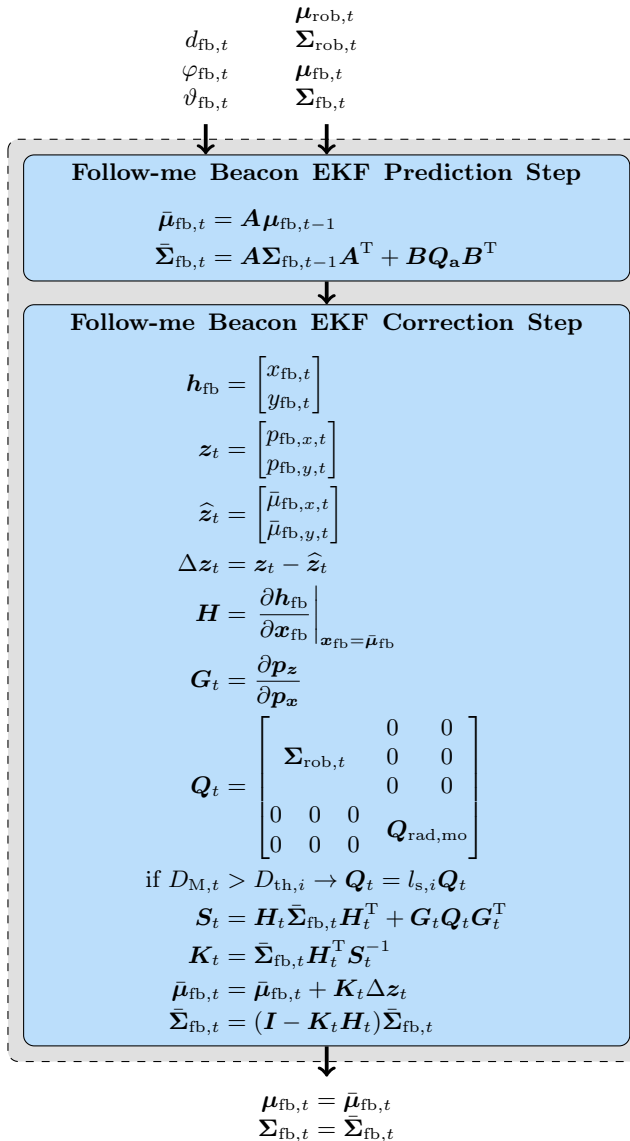


Fig. 4.20: Simplified block diagram of the follow-me beacon relative positioning EKF.

4.11 System Implementation

In order to verify the effectiveness of the proposed localization concept and algorithms, a mobile robot was equipped with the sensors presented in the previous chapters. All algorithms were implemented on embedded hardware to enable real-time⁸ processing for a realistic evaluation of the system.

A simplified block diagram of the implementation is given in Fig. 4.21. The two dashed rounded rectangles represent the two main processing units from the point of view of the localization system. The grey one is the robot with the main robot computer carrying the mobile radar with its DSP board which is shown in green.

Three software frameworks (shown as red rounded rectangles) were used to streamline the development, implementation, integration, and testing process: Symeo FusionEngine [44], SmartSoft [136], and ROS [137]. All three frameworks are based on the same basic principle – divide the processing in nodes (software modules), which communicate internally and externally using messages (data packets formatted according to certain rules). The radar signal processing was implemented in the programming language C on the DSP board of the mobile radar (the FFT and low level synchronization routines were implemented in an FPGA by Symeo). The algorithms described in this chapter were also implemented in C as nodes for the Symeo FusionEngine as it is light-weight, stable, and platform agnostic. Corresponding SmartSoft wrapper nodes were written to enable interoperability and integration with nodes and services in SmartSoft and in ROS contributed by other project partners.

The blue rectangles in Fig. 4.21 denote sensors and the black arrows inputs and outputs. The sensors “odometry” and “wall detection” provide their measurement data \mathbf{z}_{odo} and \mathbf{z}_{us} directly to the SmartSoft framework. It then forwards them as a message (SmartSoft communication pattern / object) to the FusionEngine.

On start, the framework FusionEngine reads in the binary 2D occupancy-grid map of the scenario \mathbf{M}_{og} and the poses of the static radar nodes $\mathbf{m}_{rad,st}$ in it. It then begins sending command messages \mathbf{c}_{meas} to the mobile radar node software coordinating the measurement procedure.

Based on the information in \mathbf{c}_{meas} , the mobile radar node performs measurements to one of the multiple available static radar nodes or the follow-me beacon. \mathbf{c}_{meas} contains the ID number of the radar node to measure to and

⁸The term “real-time” is commonly used in computer science to denote whether a processing operation is always executed within a deadline (hard real-time) or can take longer on cost of degrading the system performance (soft real-time). The definition used here, common in digital signal processing, is similar. It states that the input data (from the sensors) is processed at a faster rate than it arrives, thus enabling continuous operation (localization output), albeit with a certain latency.

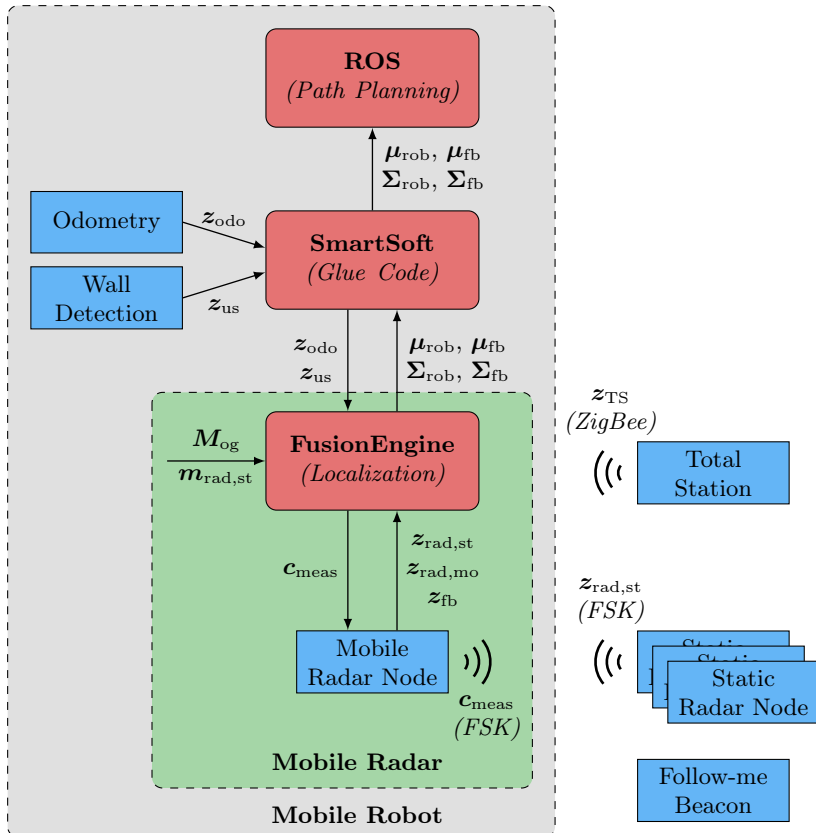


Fig. 4.21: Simplified block diagram of implemented system. See description in text (adapted from [51]).

the measurement mode. The mode can be unilateral (mobile radar is master, the other node is slave) or bilateral (as in unilateral with a subsequent second measurement with swapped roles). The measurement result of the static radars is transmitted back to the mobile radar over an FSK link in the 24 GHz band. The mobile radar software transmits the radar measurement result from and to the static radar $z_{\text{rad,st}}$ and $z_{\text{rad,mo}}$ and to the follow-me beacon z_{fb} to the FusionEngine.

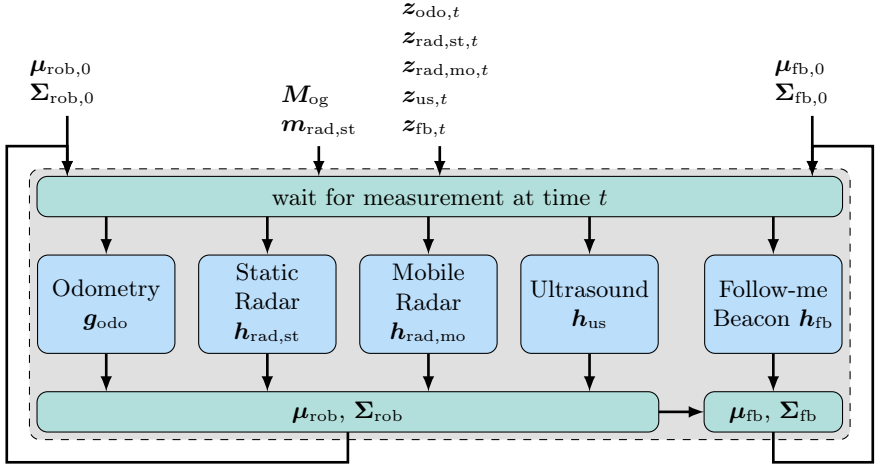


Fig. 4.22: Simplified block diagram of the EKFs implemented in C in the software framework Symeo FusionEngine.

The sensor fusion is distributed across multiple FusionEngine nodes. There are nodes preprocessing the sensor data and filtering out outliers based on thresholding of the Rx signal power, beamformer magnitude, and measurement sample variance. Other nodes coordinate the radar measurements and implement the EKFs presented in the previous chapters. Finally, there is a main node which maintains the state vector, the coordinate transformations and fuses the results of all EKFs. As the measurements from the different sensors are conditionally independent, i.e. $p(\mathbf{x}|\mathbf{z}_{odo}, \mathbf{z}_{us}, \mathbf{z}_{rad}) = p(\mathbf{x}|\mathbf{z}_{odo})p(\mathbf{x}|\mathbf{z}_{us})p(\mathbf{x}|\mathbf{z}_{rad})$, they do not need to be processed simultaneously, but can be fused sequentially in the order they are obtained (Chapter 7.4.3 in [107]). An overview of the implementation of the EKFs is given in Fig. 4.22.

However, care needs to be taken about the correct processing order, since the sensors used have different processing latencies Δt_{proc} and the time of reception and timestamping in the software t_{rec} does not necessarily correspond to the time t_{meas} at which the respective physical effects were measured. This problem is known as “out-of-sequence measurements”, because it leads to an incorrect temporal order of the measurements [138]. In the presented system, this problem was solved by introducing a so-called “delay window” (a.k.a. “time sequencer” in ROS). It is basically a FIFO buffer ordering the measurements not by the

time they are received by the system, but by the estimated time the respective physical effect was measured $\hat{t}_{\text{meas}} = t_{\text{rec}} - \Delta t_{\text{proc}}$, assuming the latency of the corresponding sensor is known and constant. While this ensures the correct fusion order of the measurements and thus increases the accuracy, it also causes a delay in the availability of the final result. Due to the relatively low latency of the sensors ($\lesssim 100$ ms) and the relatively slow robot motion ($\lesssim 1$ m/s), this did not have any significant impact on the performance.

4.12 Results

In order to verify the effectiveness of the proposed concept, it was thoroughly tested in three different real-life scenarios: a university building, a hospital, and a company office building. Three robot platforms were used: A Festo Robotino [139] (Fig. 4.23 (a) and (b)), a Pioneer P3-DX (Fig. 4.2), and a Pioneer P3-AT [140] (Fig. 4.23 (c)). Thanks to the modularity of the employed frameworks, only minimal configuration changes in software were necessary to switch between the platforms.

During the tests, several configurations of the system were used. On the robots, there were either two radar nodes equipped with the planar 2D arrays from Fig. 2.16 (a) as shown in Fig. 4.23 (a) or one single radar node equipped with the ring antenna array from Fig. 2.16 (b) or (c) as in Fig. 4.23 (b) and (c). Although both configurations yielded very good results in terms of accuracy, the ring-array featured better reliability, since it offered a 360° coverage in azimuth (see lower part of Fig. 4.23).

The 2-radar configuration is virtually blind when the robot stands or moves transversely in the corridor, as no LOS connection to the static nodes is present. Detecting this condition in the sensor data fusion is challenging, as both radars supply coarsely correct results over multipath reflections. The range sample variance can be successfully employed to detect and filter out such situations (the variance of the range measurement is in general much lower for LOS than for MP during robot motion). Synchronizing and coordinating the measurement cycles of the two mobile radars is a further complication.

The ring array configuration is not affected by the orientation of the robot, uses less hardware and the measurement cycle coordination is simpler. However, as fewer antennas are available per angle, the angular accuracy and multipath resistance is lower. This does not have any significant impact on the system performance, as the robot orientation is estimated mainly by the wall-detection system. The two configurations in the test scenarios are shown in Fig. 4.24.

Two versions of the wall-detection system were used as well. The one used in the configurations in Fig. 4.2 and 4.23 (c) relies on 3 ultrasonic sensors and can

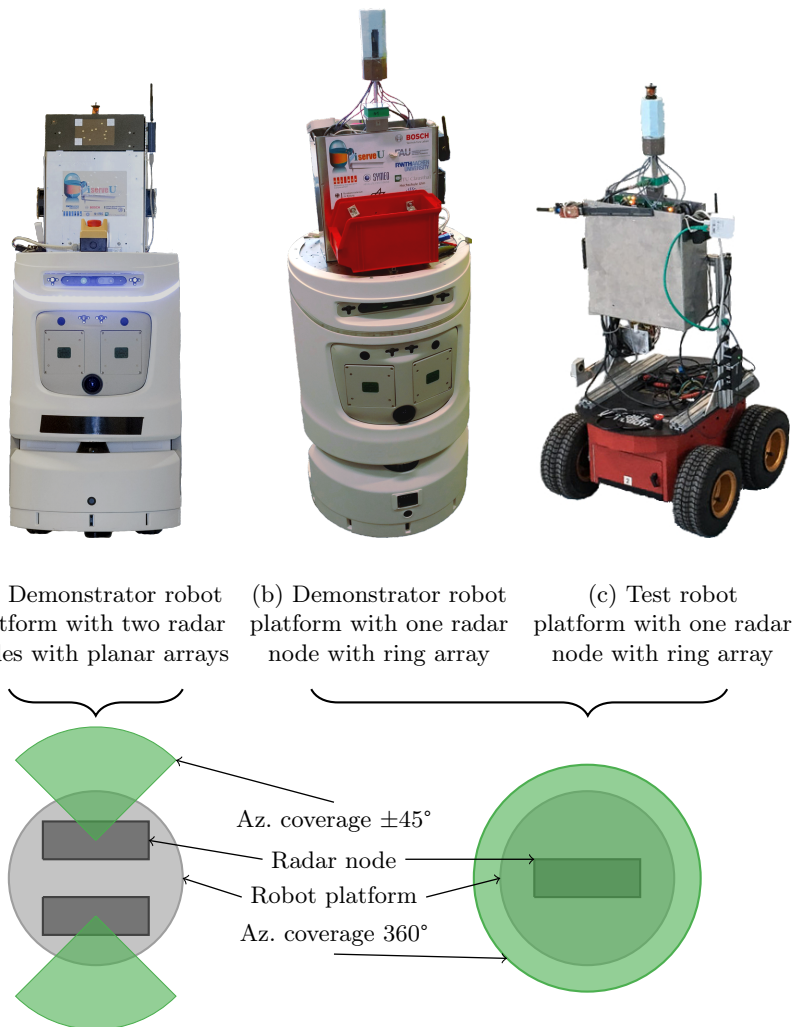


Fig. 4.23: Robot platforms and sensor configurations used during development and verification. See description in text (adapted from [51]).

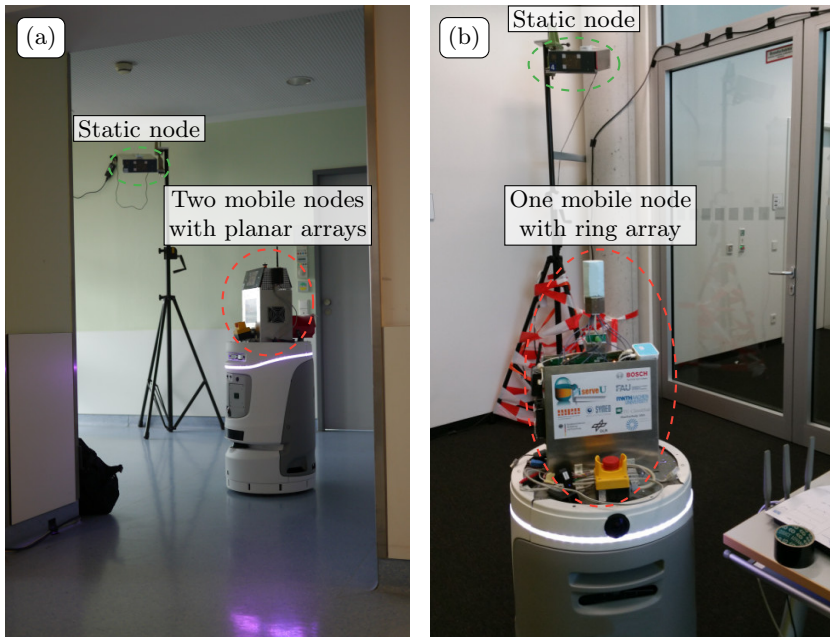


Fig. 4.24: Mobile robot equipped with radar node in the Katharinenhospital (a) and office building (b) scenarios (adapted from [51]).

detect the wall on one side of the robot. The platform in Fig. 4.23 (a) and (b) is equipped with an ultrasonic camera (comprising two 2D ultrasonic arrays) and a laser scanner and can detect the walls on both sides. Again, thanks to the modularity of the frameworks used, only minor configuration changes were required to switch between the different hardware devices.

Cauerstr. 6 The first test scenario, where the system was mainly developed and tested, was the FAU Erlangen-Nürnberg university building in Cauerstr. 6, Erlangen, Germany. The scenario consisted of an office room with a size of 4.5×3.5 m and a relatively narrow corridor sized 2.1×32 m as shown in Fig. 4.25 (c). Two metal cabinets were also present in the corridor. During the test run, the robot started at position $[4\text{ m}, -3\text{ m}]$, moved out of the room and along the corridor to its destination $[0.7\text{ m}, 23.3\text{ m}]$, where it turned around. The test robot platform was remotely controlled manually and moved with a speed

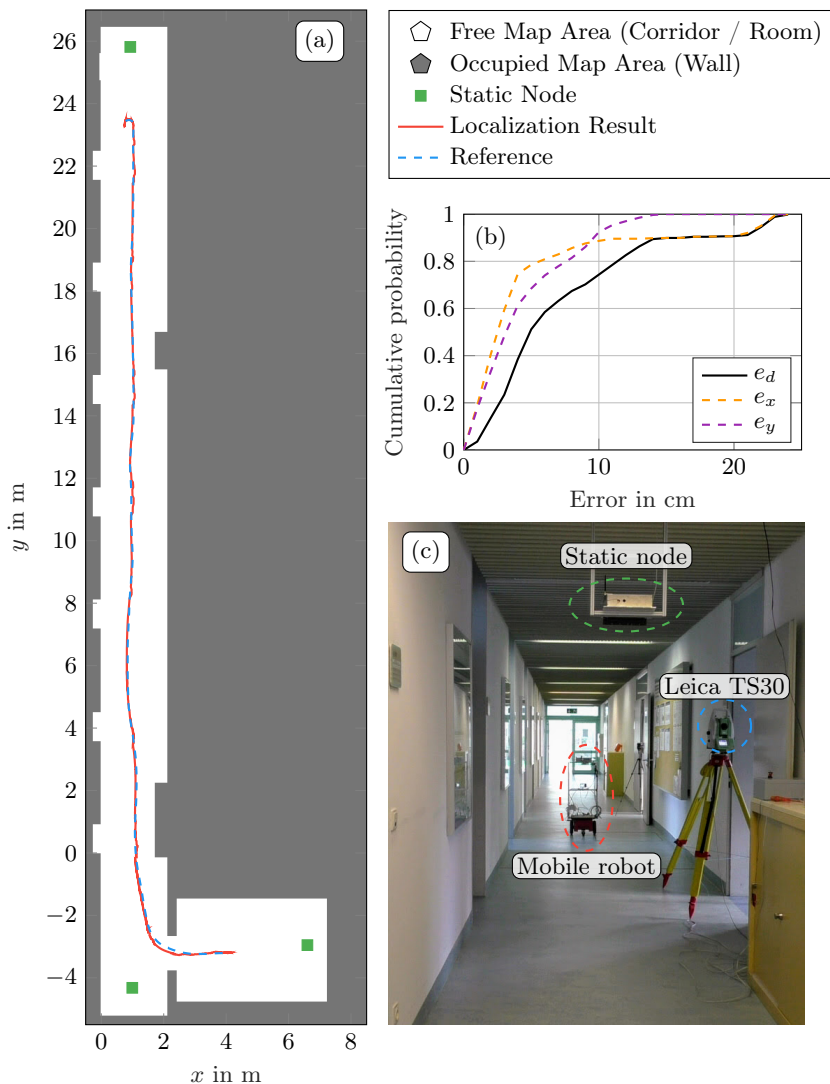


Fig. 4.25: Measurement result in test scenario “Corridor in Cauerstr. 6, FAU Erlangen-Nürnberg” with test robot platform, 1 mobile radar with an 8-channel ring array and ultrasonic array for wall detection (adapted from [51]).

between 0.5 m/s and 1 m/s. The robot platform from Fig. 4.23 was used.

The room (visible as a white rectangle to the lower right of Fig. 4.25 (a)) was cluttered with furniture such as tables, chairs, and cabinets, which decreased the performance of the wall-detection system. To enable positioning in the room, a static radar node was placed in it (shown as a green square at coordinates [6.6 m, -3 m]). Bilateral radar measurements were used to initialize and track the mobile robot pose.

In the corridor, the mobile robot was located based on 2 static radar nodes (shown as green squares) and the wall-detection system. Simultaneously, it was tracked by a high-precision total station Leica TS30 whose result was used as a reference.

The localization result of a typical test-run of the multi-modal sensor fusion described in the previous sections is shown as a red curve in Fig. 4.25 (a). The reference is shown as a blue dashed line. It can clearly be seen, that the localization result accurately matches the reference which proves the effectiveness of the proposed concept.

The resulting 2D positioning error was calculated from the logged data by linearly interpolating the reference measurements to the points of time when the localization estimates were obtained. This approximation was assumed to be valid, as the measurement rate is relatively high compared to the robot motion speed. The resulting cumulative probability distributions for the error in x -direction e_x , in y -direction e_y , and the absolute 2D error e_d are shown in Fig. 4.25 (b). The results are summarized in Table 4.1 in the column “Cauerstr. 6”. The maximum error is 24.2 cm.

Unfortunately, no reference for the heading was available (cf. Appendix B.2). Assuming that the mobile robot orientation coincides with the motion direction, a rough estimate can be derived from the position reference measurements using trigonometry and applying a smoothing operation. Compared to this, the orientation RMS error is 1.92°. Although this error estimate is not very accurate (especially when the mobile robot rotates around its axis with almost zero translation), it shows unequivocally that the proposed local positioning system is capable of providing orientation estimate with relatively high accuracy.

The shape of the cumulative probability distributions resembles, but does not completely match a Gaussian. The reason for this are the different underlying error sources. While the e_x in the room is relatively large due to imperfect initialization, it becomes much smaller in the corridor, where the wall-detection system is used. There is also a relatively large error in the area where the robot exits the room, as the radar measurements there are strongly influenced by multipath reflections from the door frame.

As uncertainty is a major aspect of probabilistic algorithms, it is interesting to analyze the accuracy of the estimated covariance matrix. This was done by

evaluating the squared Mahalanobis distance D_M^2 of the measurements

$$D_M^2 = [e_x \ e_y] \Sigma_{xy}^{-1} [e_x \ e_y]^T, \quad (4.85)$$

where Σ_{xy} denotes the position covariance matrix. The mean of D_M^2 for the shown test run was 5.85. For an ideal zero-mean Gaussian 2D covariance matrix, the expectation is $E\{D_M^2\} = 2$. This means that the filter provided a too optimistic estimate for the position uncertainty. Nevertheless, it can be used in further processing steps (e.g., navigation).

As already mentioned, narrow corridors represent a very difficult scenario for microwave-based localization systems, as multipath reflections from the walls, floor, ceiling, and objects in the scenario interfere with the LOS signal and significantly increase the measurement error. Thanks to the fusion with complementary sensors, accurate and robust localization is possible even under these challenging circumstances.

Katharinenhospital A second measurement campaign was conducted in the Katharinenhospital, Stuttgart, Germany shown in Fig. 4.26 (c) with the demonstrator robot platform from Fig. 4.23 (a). The laser scanner was used for wall detection. The measurement scenario consisted of a main corridor of size 2.5×65 m and multiple side corridors. As the tests were performed during a normal work day, multiple patients, visitors, and nursing staff moving around hospital meal delivery carts and wheeled beds were present. All these objects caused multipath reflections and partially obstructed the LOS path between the static and the mobile radar stations and hindered wall detection. Nevertheless, the localization system could provide reliable positioning service with sufficient accuracy for autonomous transportation tasks. The localization could be initialized and recovered automatically in case of failure.

The trajectory of a typical run with the total station measurements as a reference and the corresponding cumulative error probability distributions are shown in Fig. 4.26 (a) and (b). The results are summarized in Table 4.1 in the column “Katharinenhosp.”. The largest error was 39.4 cm. Again, an estimate for the heading error was derived from the total station position data as no dedicated orientation reference system was available. The resulting heading RMS error was 1.56° . This is an excellent result, especially given the fact that only 2 static radar nodes were used to provide coverage for the entire corridor of length 65 m.

Office Building The third measurement campaign was performed in a corridor in an office building shown in Fig. 4.27 (c) with the robot configuration from Fig. 4.23 (b). The laser scanner was used for wall detection. The scenario comprised

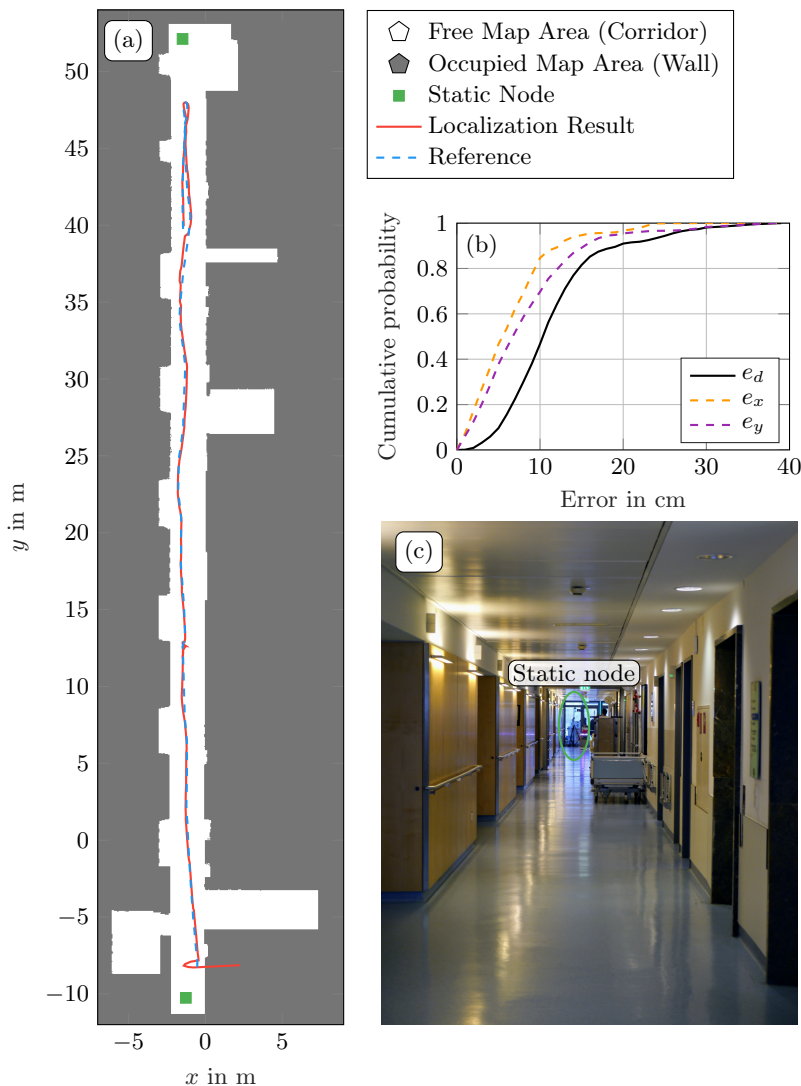


Fig. 4.26: Measurement result in test scenario “Corridor in Katharinenhospital Stuttgart” with demonstrator robot platform, two mobile radar nodes with 2D planar arrays and laser scanner for wall detection (adapted from [51]).

a corridor of the size of 2.25×30 m, two side corridors and a wider part furnished as a waiting room of the size of 5.3×3.4 m connected to the main corridor without a door (as seen at the bottom of Fig. 4.27 (a)). The whole scenario could be covered using only 2 static radar nodes. As the waiting room was cluttered with furniture and other objects, the performance of the wall-detection system was strongly reduced. To enable localization in the waiting room, the lower static radar node (depicted as a green square in Fig. 4.27) was placed to also cover this area. Using bilateral radar measurements, a simultaneous 2D position and orientation estimation was possible.

A typical autonomous test run is shown in the figure using the total station as a reference. Due to the large angular velocity of the robot relative to the total station, tracking failed in the beginning and no reference data was available. This segment was not used during further analysis. The resulting cumulative error probability distribution is shown in Fig. 4.27 (b). The results are summarized in Table 4.1 in the Column “Office”. The largest error was 37.9 cm.

A very interesting comparison was conducted during this measurement campaign. For two test runs, the mobile robot was localized with the presented wireless positioning system and simultaneously with a SICK laser scanner using the ROS adaptive Monte Carlo localization (AMCL) node. While the performance of both systems was equal in the corridor (with a difference of less than 0.5 cm for any of the systems depending on the trajectory segment chosen), the laser scanner localization had an error of up to 30 cm at the end of the corridor where a glass door was located (at [1 m, 26.5 m]) as can be also seen in the photo in Fig. 4.27 (a) and (c).

The laser scanner measurement also presented an opportunity to evaluate the quality of the mobile robot orientation estimation. Taking the laser scanner localization as ground truth, the RMS error was 1.48° . Albeit not obtained by a highly accurate reference, this value gives a feeling of the achieved orientation estimation accuracy.

Table 4.1: iserveU localization accuracy results expressed as 68 %, resp. 95 % of the measurement errors being below a certain threshold value as given by the cumulative error distribution.

σ ($\hat{=} 68\%$) / 2σ ($\hat{=} 95\%$)	Cauerstr. 6	Katharinenhosp.	Office
σ_x	4.97 cm	7.88 cm	2.44 cm
σ_y	4.90 cm	9.74 cm	10.08 cm
σ_{2D}	8.32 cm	12.8 cm	10.73 cm
$2\sigma_x$	22.08 cm	15.96 cm	6.76 cm
$2\sigma_y$	11.02 cm	19.92 cm	22.53 cm
$2\sigma_{2D}$	24.22 cm	28.81 cm	22.54 cm

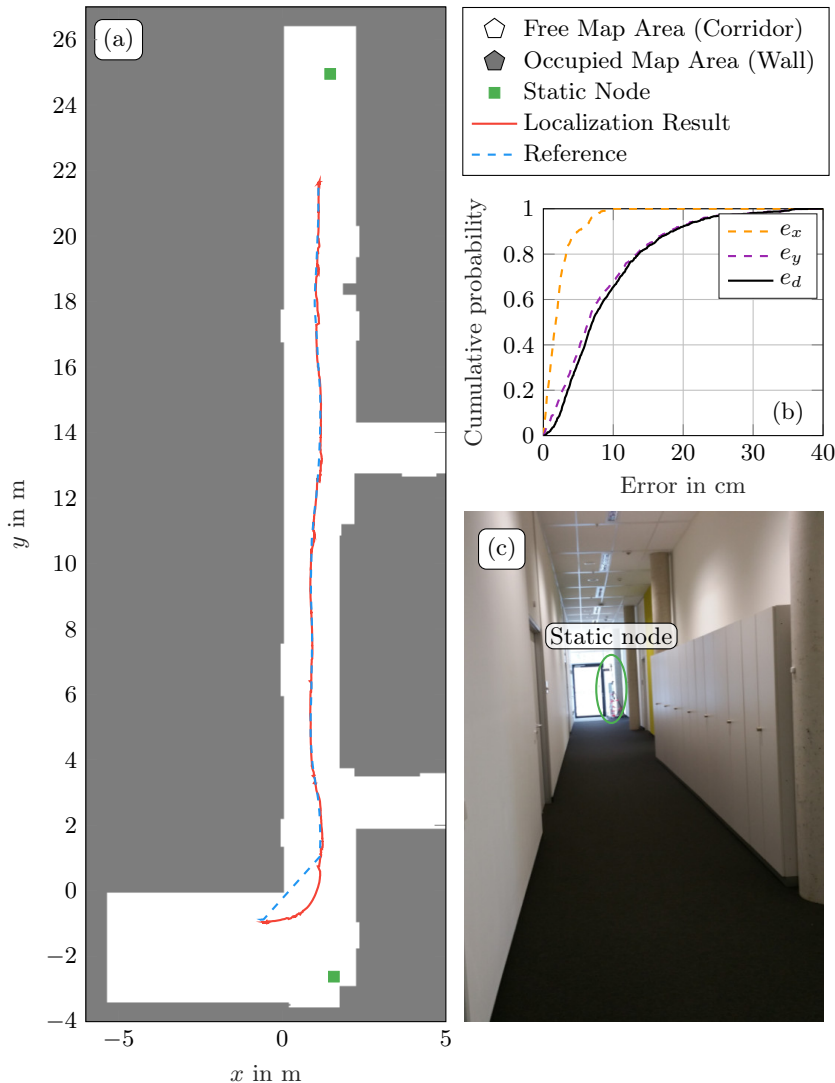


Fig. 4.27: Measurement result in test scenario “Corridor in office building” with demonstrator robot platform, 1 mobile radar with an 8-channel ring array and laser scanner for wall detection (adapted from [51]).

This shows that the proposed approach has approximately equal performance in terms of accuracy compared to the laser-scanner based localization, which can be assumed as the state-of-the-art for indoor mobile robot localization. The radar-based approach, however, has better reliability in cases when transparent surfaces are present in the scenario. Although not explicitly tested, the reliability in the presence of bars, reflective surfaces, and dust should also be improved as these pose a similar problem for laser scanners.

Follow-me Beacon Localization The positioning of a person carrying the follow-me beacon relative to the mobile robot was also verified as shown in Fig. 4.28. The mobile robot was manually controlled and the person followed it in the scenario in Fig. 4.25 (c). The total station was used as a reference for the person position. No reference for the robot position was available. The resulting trajectory in Fig. 4.28 (a) shows a close match between the estimated person position obtained with the techniques presented in this chapter and the reference. As can be seen from the cumulative error distribution in Fig. 4.28 (b), 68 % of the

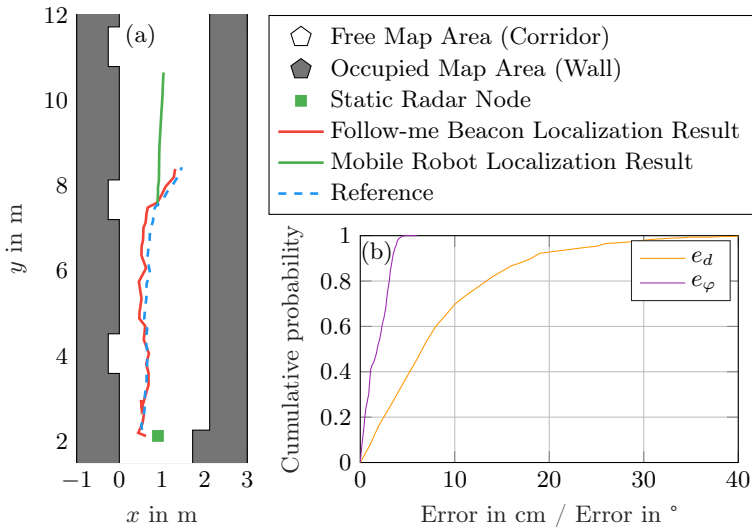


Fig. 4.28: Follow-me beacon localization in test scenario “Corridor in Cauerstr. 6, FAU Erlangen-Nürnberg” with test robot platform, 1 mobile radar with planar 2D array and ultrasonic array for wall detection.

errors of the distance between the robot and the person are below 9.7 cm and 95 % below 24.3 cm. The largest error was 44.3 cm. 68 % of the errors of the angle between the robot and the person are below 2.7° and 95 % below 3.7°. The largest error was 4.7°. It should be noted that the unknown error in the mobile robot pose is also part of this error.

4.13 Hybrid Localization

The radar device used offers an interesting possibility. Although it was designed and mainly used as a secondary radar, it can also be utilized as a primary radar. This can be particularly useful to replace the ultrasonic sensor for wall detection in order to reduce the complexity of the system. If the ring antenna array is used, this would enable the robot to detect walls and obstacles in 360°.

A test was performed to investigate the suitability of the radar and ring array for wall-detection. As the distance to the wall was quite small ($\lesssim 1.5$ m) and the bandwidth used was relatively low, the Rx/Tx coupling on the PCB as well as between the antennas was a serious problem, as the wall reflection was indistinguishable from the coupling. This was solved by using a 3 m long coaxial cable between the board and the Tx antenna and an RF amplifier to compensate the

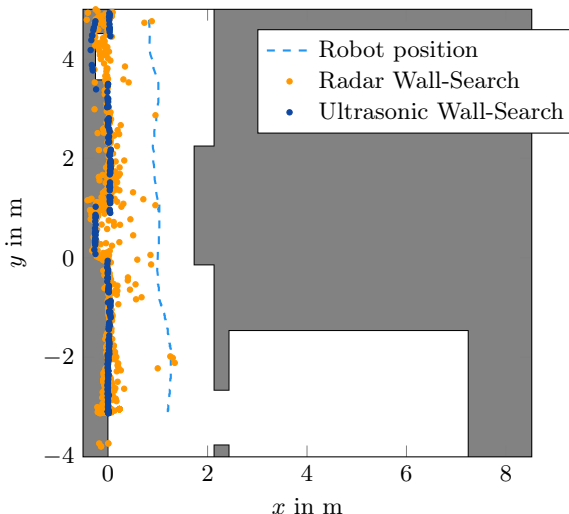


Fig. 4.29: Wall-search using radar as primary radar.

losses in the cable. This made the coupling peak resolvable from the reflection peak in the FFT spectrum. The coupling between the antennas was reduced by using RF absorbers and a more directional Tx antenna. Unfortunately, this reduced the 360° measurement range to about $\pm 45^\circ$.

The result of a measurement in the scenario from Fig. 4.25 (a) is shown in Fig. 4.29. The ultrasonic wall-searching sensor was used together with the radar in primary mode to compare the performance of both systems. As can be seen from the picture, despite the limitations described in the previous paragraph, the radar manages to successfully find the wall using a combination of range and DOA measurements as described in Chapter 2 assuming specular reflection from the wall. The obtained accuracy expressed as the measurement error standard deviation was 5.8 cm in range and 3.1° in angle. Although worse than the performance of the ultrasonic sensor, this is in general enough for accurate and reliable indoor mobile robot positioning.

One reason for the superior performance of the ultrasonic device is the better resolution. The resolution in range Δd for a primary radar / sonar is in general given by

$$\Delta d = \frac{c}{2B}. \quad (4.86)$$

This equates to $\frac{343 \text{ m/s}}{2 \cdot 2.4 \text{ kHz}} = 7.15 \text{ cm}$ for the ultrasonic sensor used and $\frac{3 \times 10^8 \text{ m/s}}{2 \cdot 250 \text{ MHz}} = 60 \text{ cm}$ for the radar. Due to the long coaxial cable used to resolve the signal from the coupling, the SNR was poor and as shown in Section 2.3.1.2 this also impairs the accuracy.

This simple experiment shows that a hybrid primary-secondary radar approach is viable and can be successfully used for indoor mobile robot localization. Employing optimized hardware and more advanced signal processing techniques such as range-Doppler processing, synthetic aperture radar (SAR), SLAM, and occupancy-grid mapping, a powerful radar-based system for indoor localization, navigation, and collision avoidance can be developed.

4.14 Conclusion

The proposed concept of fusing secondary radar combining range and angle radar measurements with further complementary sensors could be successfully verified in three realistic challenging scenarios. The comparison to the laser scanner localization also demonstrated the advantage of using an absolute reference.

The localization can be improved by using a higher RF bandwidth and more Rx channels. This is both feasible with modern highly integrated radar chips. This would also reduce the size of the system and improve its acceptance.

5 TransTerrA: 6 DOF Mobile Robot Localization for Planetary Exploration

Another class of service robots is represented by mobile robots for space exploration missions on foreign planets like the Rover SherpaTT shown in Fig. 5.1. While GNSS is the state-of-the-art technology for outdoor localization on Earth, such systems are not present on other planets and an alternative is needed.

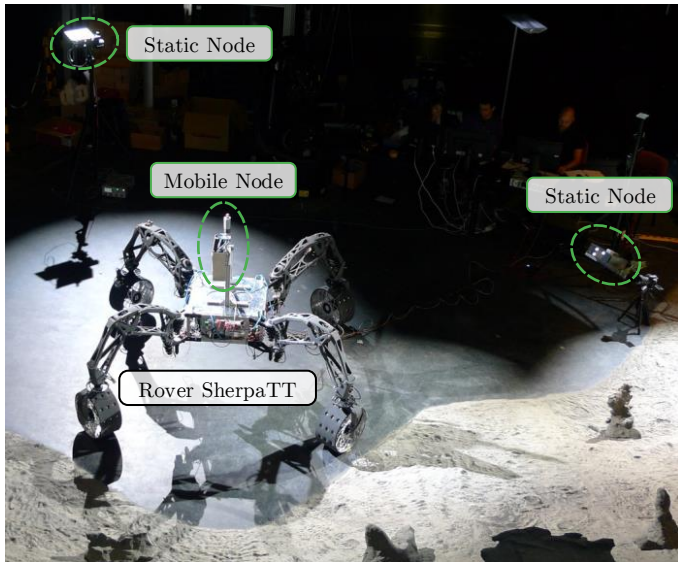


Fig. 5.1: The rover SherpaTT [141] with radar-based wireless localization positioning system (WLPS) in the space exploration hall of the Deutsches Forschungszentrum für künstliche Intelligenz / German Research Center for Artificial Intelligence (DFKI) in Bremen, Germany [142] (adapted from [143]).

5.1 Motivation

As is the case e.g. on Mars, the environmental conditions are very harsh. The temperature and lighting frequently vary in large intervals, the environment is dusty, and an atmosphere is not always present. This is a serious challenge for localization systems based on cameras, laser scanners, and sound/ultrasound.

An overview of currently used techniques based on relative sensors such as wheel encoders or visual odometry is given in [144]. Since such approaches inherently suffer from error accumulation, the position estimate deteriorates as the mobile robot moves. A common exploration scenario includes driving around a crater and mapping it by taking a series of images as described in [144]. The images are combined to an integrated map. Points of interest (POI) are identified in the map for closer study after a (manual) compensation of the localization error. This is an arduous and time-consuming process. The mobile robot then returns to the POI locations for investigation. Accurately driving back to a POI is, however, only possible if both the mobile robot and the target location are known.

In this chapter a wireless local positioning system for 6 degrees of freedom (DOF) pose estimation of mobile robots using sparse infrastructure is presented. It consists of at least one static node installed at the test site and another node on the mobile robot, as depicted in Fig. 5.1. As the static nodes serve as an absolute reference, error accumulation is no more an issue. Varying lighting, the presence of dust, and the absence of atmosphere is not a problem as well due to the robustness of radar in such conditions. The proposed WLPS can improve and speed up the process of mapping and target finding in planetary exploration missions.

Although the proposed system was developed for space exploration, it can also be used in terrestrial applications where GNSS is not available (e.g. indoors, in warehouses, under large structures outdoors), when its coverage and accuracy is insufficient or when 3D orientation estimation with a small baseline is required. The necessity for a localization alternative / supplement to GNSS is also emphasized in [134]: “After many years of operation, we have concluded that the physics of GPS precludes it ever being made sufficiently reliable to be used as a stand-alone autonomous navigation system.”

In the past, most positioning systems have been used for tracking and logging of the vehicle position, as a navigation aid and for collision avoidance. Current research, however, focuses on fully autonomous systems. One example are automated guided vehicles (AGVs) which are currently employed in warehouse logistics. State-of-the-art positioning solutions use inductive guide paths [145], magnetic point sequences [146], optical guide paths [147], [148], laser triangulation based on reflective markers or transponders embedded into the ground

[149]. All of these positioning methods rely on complex infrastructure, require significant installation and maintenance effort, and are not very flexible.

The WLPS presented in this chapter, is an interesting alternative. It was developed as part of the project TransTerra¹, which builds upon the project SOKOROB². The aim of SOKOROB was to develop a self-organizing wireless positioning network, consisting of 5 mobile robots, operating in 3D. By performing bilateral secondary RTOF+DOA measurements using the system presented in Chapter 2, the relative poses of all robots to each other are determined in 3D. This was accomplished using a breadth-first search algorithm as demonstrated in SOKOROB and presented in [150] and can be improved by a probabilistic approach. In TransTerrA it was assumed that 4 of the mobile robots are static and their poses are known. The fifth is located relative to them while executing an exploration mission as presented in this chapter.

5.2 Comparison of Positioning Techniques

The scenario investigated here is shown in Fig. 5.2. It consists of 4 static radar nodes with known poses in 3D space (3D position and 3D orientation) and a mobile robot equipped with a radar node moving in the area between them with 6 degrees of freedom (3 translational and 3 rotational). The goal is to determine its complete pose relative to the static nodes.

Given this setup and the radar hardware from Chapter 2, the following positioning techniques can be applied to determine the 3D position of the mobile robot (see also Fig. 1.2):

- Multilateration – The sought target position is determined based on the measured distances (RTOF) to nodes at known positions.
- Multiangulation – The sought target position is determined based on the measured angles (DOA) to nodes at known positions and with known orientations.

¹The project TransTerrA (Semi-autonome kooperative Exploration planetarer Oberflächen mit Errichtung einer logistischen Kette sowie Betrachtung terrestrischer Anwendbarkeit einzelner Aspekte / Semi-autonomous cooperative exploration of planetary surfaces including the installation of a logistic chain as well as consideration of the terrestrial applicability of individual aspects) had a runtime of 1 year and was funded by the German Aerospace Center (DLR), registration no. 50RA1301. The project was conducted in collaboration with the Robotics Innovation Center (RIC) belonging to DFKI GmbH in Bremen, Germany.

²The project SOKOROB (Selbstorganisierendes ad-hoc Ortungsnetzwerk für extraterrestrische Explorationssysteme basierend auf kooperativen mobilen Roboter-Schwärmen / Self-organizing ad-hoc Positioning Network for Extraterrestrial Exploration Systems Based on Cooperative Mobile Robot Swarms) had a runtime of 3 years and was funded by the German Aerospace Center (DLR), registration no. 50RA1205.

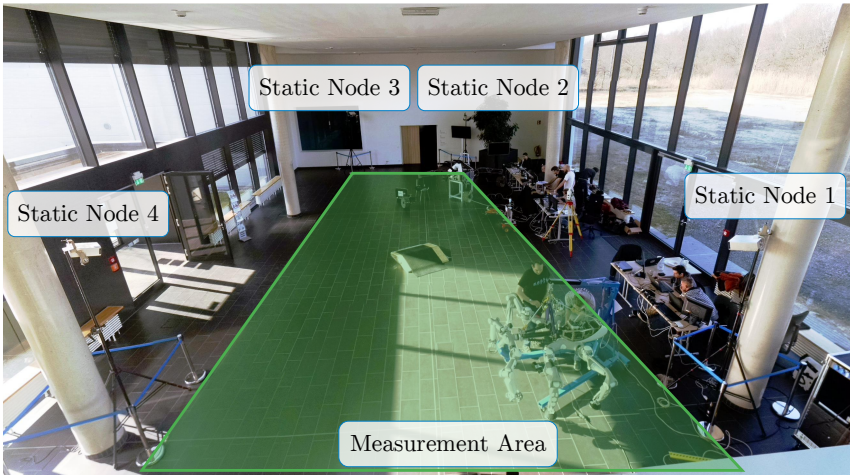


Fig. 5.2: Measurement scenario in the entrance hall of the DFKI building at Robert-Hooke-Straße 1, Bremen, Germany.

- RTOF+DOA – The sought target position is determined using a combination of measured distances (RTOF) and measured angles (DOA) to nodes at known positions and with known orientations.

In the following sections, these techniques will be compared regarding the achievable positioning accuracy for the geometry of the given scenario.

5.2.1 Multilateration

Given N static nodes at known positions $\mathbf{p}_{s,n} = [x_n \ y_n \ z_n]^T$, $n = 1 \dots N$, the distance d_n from the target $\mathbf{p}_t = [x \ y \ z]^T$ to node n is given by

$$d_n = \|\mathbf{p}_{s,n} - \mathbf{p}_t\| = \sqrt{(x - x_n)^2 + (y - y_n)^2 + (z - z_n)^2}. \quad (5.1)$$

The range d_1 constrains the target position on the surface of a sphere around node 1 with a radius equal to the measured distance. When the measurement uncertainty is also considered, the position constraint becomes a spherical shell with a thickness corresponding to the measurement variance. An additional measurement d_2 from a second static node results in the general case in a constraint with the shape of a circle in 3D or roughly a torus, when measurement uncertainty is considered. A third range d_3 to a third node limits the

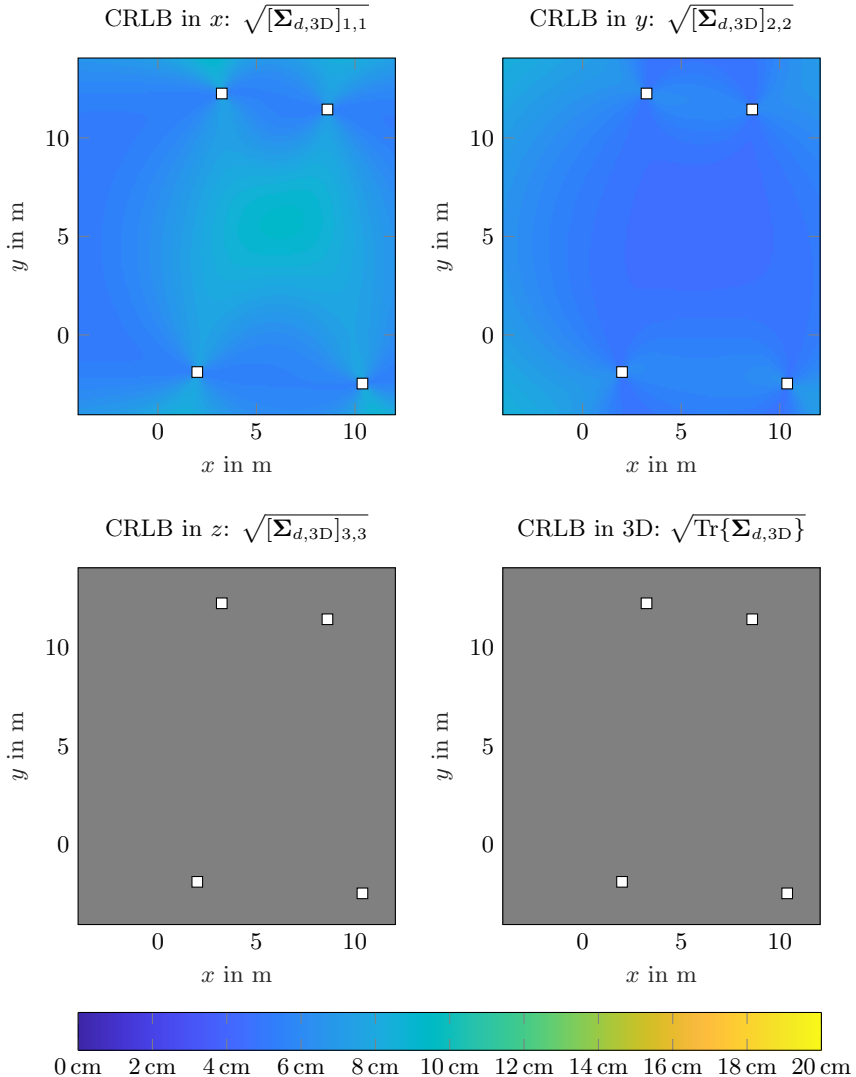


Fig. 5.3: The result for the CRLB in x , y , z direction and in 3D using multiilateration with 4 static radar nodes $p_{s,n}$, denoted by white squares. Gray denotes areas where positioning fails (see explanation in text).

sought position to two points, resp. two approximately spherical distributions. A fourth range d_4 is then necessary to determine the target position unambiguously. These considerations assume non-degenerate geometry, i.e. the static nodes do not all lie in the same point, on a straight line or in a plane.

Two algebraic solutions to the multilateration problem are presented in [50] and [151]. The main idea is to formulate an equation system from the nonlinear range equations in Eq. (5.1) and solve it in the least-squares sense. The attainable accuracy for a given localization scenario geometry and target position can be theoretically derived using the CRLB as shown in [49], [152], and Section 2.5.2. Given the measurement model in Eq. (5.1), the measurement Jacobian \mathbf{G}_d is

$$\mathbf{G}_d(\mathbf{p}_s, \mathbf{p}_t) = \frac{\partial \mathbf{d}(\mathbf{p}_s, \mathbf{p}_t)}{\partial \mathbf{p}_t} = \begin{bmatrix} \frac{x-x_1}{d_1} & \frac{y-y_1}{d_1} & \frac{z-z_1}{d_1} \\ \frac{x-x_2}{d_2} & \frac{y-y_2}{d_2} & \frac{z-z_2}{d_2} \\ \frac{x-x_3}{d_3} & \frac{y-y_3}{d_3} & \frac{z-z_3}{d_3} \\ \frac{x-x_4}{d_4} & \frac{y-y_4}{d_4} & \frac{z-z_4}{d_4} \end{bmatrix}, \quad (5.2)$$

where $\mathbf{d} = [d_1 \ d_2 \ d_3 \ d_4]^T$ is a vector containing all measured ranges with $N = 4$ for the problem at hand. Assuming independent and identically distributed Gaussian noise with standard deviation σ_d in all sensors, the measurement noise matrix is the 4×4 diagonal $\mathbf{Q}_d = \sigma_d^2 \mathbf{I}$. The derivation from Section 2.5.2 applies here as well and the resulting 3D position covariance matrix is

$$\Sigma_{d,3D}(\mathbf{p}_s, \mathbf{p}_t) = \mathbf{J}_d^{-1} = \left(\mathbf{G}_d^T \mathbf{Q}_d^{-1} \mathbf{G}_d \right)^{-1}. \quad (5.3)$$

The CRLB for the measurement scenario shown in Fig. 5.2 was calculated. The known positions of the static nodes $\mathbf{p}_{s,n}$ from the picture and the realistic value for the distance measurement standard deviation $\sigma_d = 8$ cm were assumed. The result for the CRLB in x , y , z direction and in 3D is shown in Fig. 5.3. The values of the covariance matrix $\Sigma_{d,3D}$ were calculated for \mathbf{p}_t on a 10 cm grid in the area surrounding the static nodes $\mathbf{p}_{s,n}$ at the height of the nodes. As apparent from the plots, for the given geometry and measurement accuracy, multilateration is capable of providing a position estimate in x and y with an accuracy of less than 10 cm in the area between the nodes. However, localization in z and thus in 3D completely fails, as the target and all nodes are in the same plane or very close to it. Therefore, the last column of \mathbf{G}_d becomes 0 and \mathbf{J}_d is not invertible. For the plots, only the 2D problem was considered. The 3D case where the target position also varies in z is examined in Section 6.2.

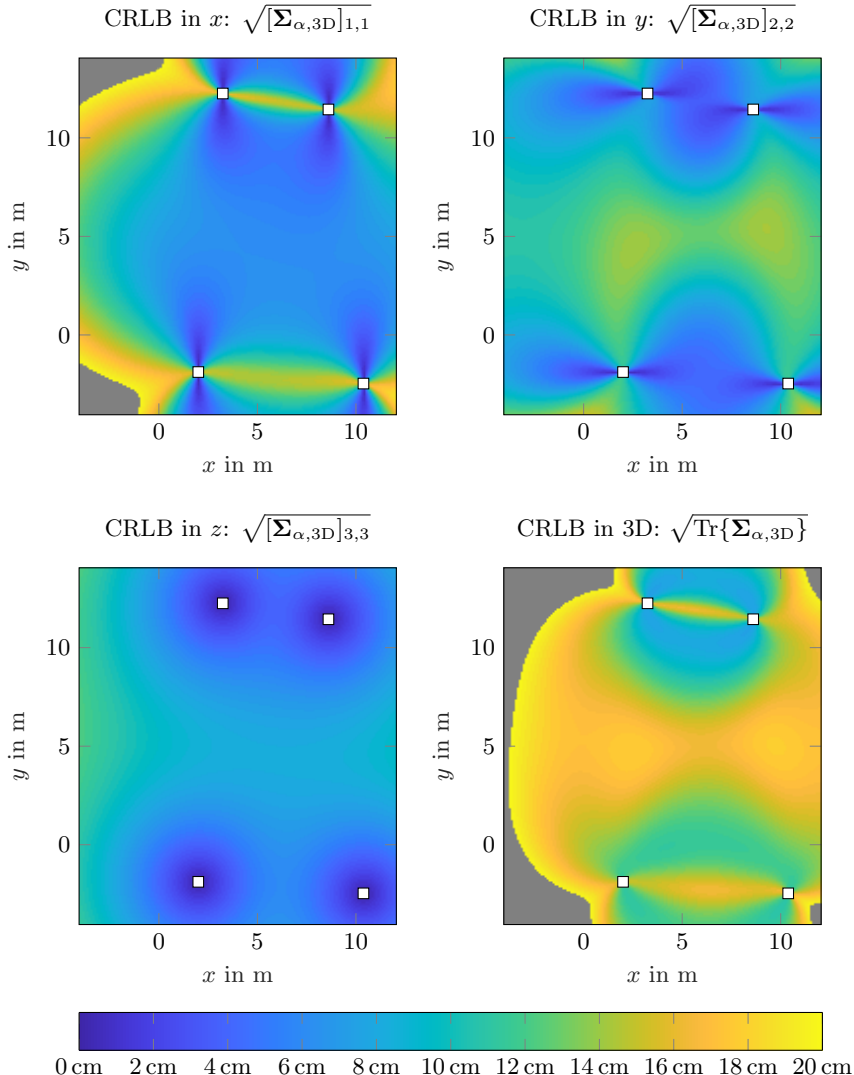


Fig. 5.4: The result for the CRLB in x, y, z direction and in 3D using multiangulation with 4 static radar nodes $p_{s,n}$, denoted by white squares. Gray denotes areas with an error > 20 cm.

5.2.2 Multiangulation

Again we consider $N = 4$ static nodes at known positions $\mathbf{p}_{s,n}$ and with known orientation. For simplicity, the nodes are considered to have omnidirectional coverage with angle-independent accuracy. The nodes measure the azimuth $\varphi_{az,n}$ and elevation $\vartheta_{el,n}$ angles to the target \mathbf{p}_t :

$$\begin{aligned}\varphi_{az,n} &= \text{atan2}(y - y_n, x - x_n), \\ \vartheta_{el,n} &= \text{asin} \left(\frac{z - z_n}{d_n} \right).\end{aligned}\quad (5.4)$$

Given a 2D angular measurement from one node, the target position is constrained on a ray starting from the node and pointing in direction of the measured angles. Considering measurement errors, the ray becomes roughly a pyramid with the apex at the node and base lengths proportional to the measurement accuracy in azimuth and elevation and growing with distance. A second node is then sufficient to estimate the position of the target as the intersection point of two rays. When the measurement error is taken into account, the rays don't intersect and the point between them where their distance to each other is minimal is taken. When more than two nodes are present, the least-squares solution for the intersection of the rays is sought [132].

Similar to the CRLB for multilateration and as shown in [106], [153], and [154], the measurement Jacobian \mathbf{G}_α for multiangulation is

$$\mathbf{G}_\alpha(\mathbf{p}_s, \mathbf{p}_t) = \frac{\partial \boldsymbol{\alpha}(\mathbf{p}_s, \mathbf{p}_t)}{\partial \mathbf{p}_t} = \begin{bmatrix} \frac{y_1 - y}{d_{xy,1}^2} & \frac{x - x_1}{d_{xy,1}^2} & 0 \\ \frac{y_2 - y}{d_{xy,2}^2} & \frac{x - x_2}{d_{xy,2}^2} & 0 \\ \frac{y_3 - y}{d_{xy,3}^2} & \frac{x - x_3}{d_{xy,3}^2} & 0 \\ \frac{y_4 - y}{d_{xy,4}^2} & \frac{x - x_4}{d_{xy,4}^2} & 0 \\ -\frac{(x - x_1)(z - z_1)}{d_{xy,1}^2 d_{xy,1}} & -\frac{(y - y_1)(z - z_1)}{d_{xy,1}^2 d_{xy,1}} & \frac{d_{xy,1}}{d_{xy,1}^2} \\ -\frac{(x - x_2)(z - z_2)}{d_{xy,2}^2 d_{xy,2}} & -\frac{(y - y_2)(z - z_2)}{d_{xy,2}^2 d_{xy,2}} & \frac{d_{xy,2}}{d_{xy,2}^2} \\ -\frac{(x - x_3)(z - z_3)}{d_{xy,3}^2 d_{xy,3}} & -\frac{(y - y_3)(z - z_3)}{d_{xy,3}^2 d_{xy,3}} & \frac{d_{xy,3}}{d_{xy,3}^2} \\ -\frac{(x - x_4)(z - z_4)}{d_{xy,4}^2 d_{xy,4}} & -\frac{(y - y_4)(z - z_4)}{d_{xy,4}^2 d_{xy,4}} & \frac{d_{xy,4}}{d_{xy,4}^2} \end{bmatrix}. \quad (5.5)$$

The vector containing all azimuth and elevation measurements is denoted as $\boldsymbol{\alpha} = [\varphi_{az,1} \ \varphi_{az,2} \ \varphi_{az,3} \ \varphi_{az,4} \ \vartheta_{el,1} \ \vartheta_{el,2} \ \vartheta_{el,3} \ \vartheta_{el,4}]^T$. The distance $d_{xy,n}$ is the projection of d_n on the xy plane. Using the 4×4 identity matrix $\mathbf{I}_{4 \times 4}$, assuming independent and identically distributed Gaussian noise on the DOA with standard deviation $\sigma_{\varphi_{az}}$, respectively $\sigma_{\vartheta_{el}}$, the measurement noise

matrix is

$$\mathbf{Q}_\alpha = \begin{bmatrix} \sigma_{\varphi_{\text{az}}}^2 \mathbf{I}_{4 \times 4} & \mathbf{0} \\ \mathbf{0} & \sigma_{\vartheta_{\text{el}}}^2 \mathbf{I}_{4 \times 4} \end{bmatrix}. \quad (5.6)$$

Analogously to Eq. (5.3), the 3D position covariance matrix is

$$\Sigma_{\alpha,3\text{D}}(\mathbf{p}_s, \mathbf{p}_t) = \mathbf{J}_\alpha^{-1} = \left(\mathbf{G}_\alpha^T \mathbf{Q}_\alpha^{-1} \mathbf{G}_\alpha \right)^{-1}. \quad (5.7)$$

The result of evaluating Eq. (5.7) on a 10 cm grid in the measurement area with $\sigma_{\varphi_{\text{az}}} = 0.8^\circ$ and $\sigma_{\vartheta_{\text{el}}} = 1.2^\circ$ is shown in Fig. 5.4. As evident, multiangulation with four nodes measuring both angles is capable of providing a 3D position estimate in the measurement area. However, a strong accuracy deterioration can be observed in several areas due to unfavorable uncertainty intersection of the measurements (dilution of precision).

5.2.3 RTOF+DOA

The CRLB for the combination of RTOF and DOA for a single node was derived in Section 2.5.2. Assuming unbiased measurements $\mathbf{z}_n = \mathcal{N}(\bar{\mathbf{z}}_n(\mathbf{x}), \mathbf{Q}_n)$ with independent and identically distributed Gaussian noise as defined in Eq. (2.70), the probability density function for the combination of nodes $n = 1, \dots, N$ is

$$\begin{aligned} p(\mathbf{z}_1, \dots, \mathbf{z}_N | \mathbf{x}) &= \\ &= \prod_{n=1}^N \frac{1}{\sqrt{\det(2\pi\mathbf{Q}_n)}} \exp\left(-\frac{1}{2}(\mathbf{z}_n - \bar{\mathbf{z}}_n(\mathbf{x}))^T \mathbf{Q}_n^{-1} (\mathbf{z}_n - \bar{\mathbf{z}}_n(\mathbf{x}))\right). \end{aligned} \quad (5.8)$$

Eq. (5.8) can be interpreted as the likelihood to obtain the measurements $\mathbf{z}_1, \dots, \mathbf{z}_N$ when the target is at position \mathbf{x} . Geometrically, it corresponds to the intersection of the uncertainty ellipsoids as demonstrated in [155]. Analogously to Eq. (2.71), the FIM is obtained by

$$\mathbf{J}_x = E_{\mathbf{x}} \left\{ \left(\frac{\partial \ln p(\mathbf{z}_1, \dots, \mathbf{z}_N | \mathbf{x})}{\partial \mathbf{x}} \right) \cdot \left(\frac{\partial \ln p(\mathbf{z}_1, \dots, \mathbf{z}_N | \mathbf{x})}{\partial \mathbf{x}} \right)^T \right\}. \quad (5.9)$$

Similar to Eq. (2.74) we obtain

$$\Sigma_{d\alpha,3\text{D}} = \mathbf{J}_x^{-1} = \left(\sum_{n=1}^N \mathbf{G}_n^T \mathbf{Q}_n^{-1} \mathbf{G}_n \right)^{-1} \quad (5.10)$$

for the CRLB for 3D localization with N nodes using a combination of RTOF and DOA measurements. \mathbf{G}_n is the Jacobian $\mathbf{G}_n = \partial \bar{\mathbf{z}}_n(\mathbf{x}) / \partial \mathbf{x}$.

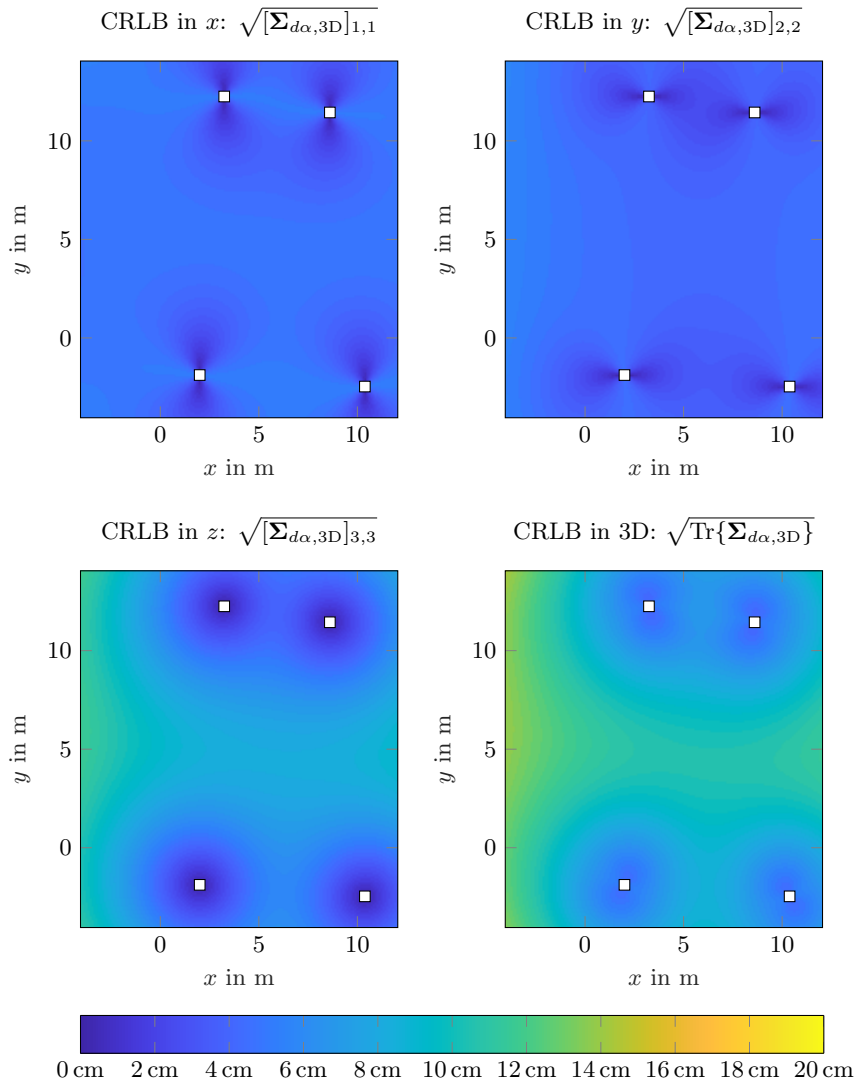


Fig. 5.5: The result for the CRLB in x , y , z direction and in 3D using a combination of RTOF and DOA with 4 static radar nodes $p_{s,n}$, denoted by white squares.

The result of evaluating $\Sigma_{d\alpha,3D}$ on a grid of 10 cm at a constant height for the scenario in Fig. 5.2 with $N = 4$ is shown in Fig. 5.5. As evident, the combination of RTOF and DOA enables a consistently high 3D positioning accuracy in the measurement area.

Estimator EKF Assuming that an EKF is used to fuse the measurements of the N nodes, an initial estimate for the 3D position of the target can be obtained by the measurement of node 1. Assuming no prior knowledge of the target location, the state covariance Σ_0 is very large. The update of the covariance matrix is then:

$$\mathbf{S} = \mathbf{H}\Sigma_0\mathbf{H}^T + \mathbf{Q}_1 \quad (5.11a)$$

$$\mathbf{K} = \Sigma_0\mathbf{H}^T\mathbf{S}^{-1} \quad (5.11b)$$

$$\Sigma_1 = (\mathbf{I} - \mathbf{K}\mathbf{H})\Sigma_0. \quad (5.11c)$$

Using the identity for the inverse of the sum of invertible matrices

$$(\mathbf{A} + \mathbf{B})^{-1} = \mathbf{A}^{-1} - \mathbf{A}^{-1}\mathbf{B}(\mathbf{I} + \mathbf{A}^{-1}\mathbf{B})^{-1}\mathbf{A}^{-1} \quad (5.12)$$

from [156], the Kalman gain \mathbf{K} can be rewritten as

$$\mathbf{K} = \mathbf{H}^{-1} - \mathbf{H}^{-1}\mathbf{Q}_1(\mathbf{I} + \mathbf{H}^{-T}\Sigma^{-1}\mathbf{H}^{-1}\mathbf{Q}_1)\mathbf{H}^{-T}\Sigma_0^{-1}\mathbf{H}^{-1}. \quad (5.13)$$

Inserting Eq. (5.13) in (5.11c) yields

$$\Sigma_1 = (\mathbf{H}_1^T\mathbf{Q}_1^{-1}\mathbf{H}_1 + \Sigma_0^{-1})^{-1} \approx (\mathbf{H}_1^T\mathbf{Q}_1^{-1}\mathbf{H}_1)^{-1}. \quad (5.14)$$

The approximation is valid, since the initial state covariance Σ_0 is very large. Fusing the measurement of a second node with the same considerations yields

$$\Sigma_2 = (\mathbf{H}_2^T\mathbf{Q}_2^{-1}\mathbf{H}_2 + \Sigma_1^{-1})^{-1} = (\mathbf{H}_2^T\mathbf{Q}_2^{-1}\mathbf{H}_2 + \mathbf{H}_1^T\mathbf{Q}_1^{-1}\mathbf{H}_1)^{-1}. \quad (5.15)$$

The extension to N nodes can be done analogously. The result of Eq. (5.15) matches (5.10). Hence, for the assumptions made, the EKF attains the CRLB.

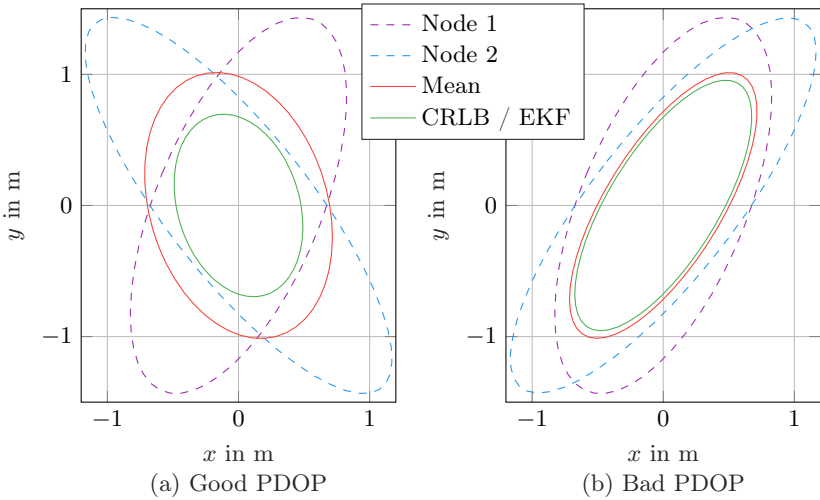


Fig. 5.6: Geometric illustration of resulting covariance ellipses of the fusion of RTOF+DOA measurements from two nodes depending on problem geometry and estimator used.

Estimator “mean” If instead of the EKF, a simple mean is used disregarding the information about the measurement uncertainty, we obtain

$$\boldsymbol{x}(\boldsymbol{z}) = \frac{1}{N} \sum_{n=1}^N \boldsymbol{x}(\boldsymbol{z}_n) \quad (5.16a)$$

$$\boldsymbol{\Sigma}_{d\alpha,3D} = E \left\{ (\boldsymbol{x}(\boldsymbol{z}) - \bar{\boldsymbol{x}})(\boldsymbol{x}(\boldsymbol{z}) - \bar{\boldsymbol{x}})^T \right\} = \frac{1}{N^2} \sum_{n=1}^N \boldsymbol{H}_n^T \boldsymbol{Q}_n \boldsymbol{H}_n \quad (5.16b)$$

A comparison of the estimators EKF from Eq. (5.15) corresponding to the CRLB and the mean from Eq. (5.16) is shown in Fig. 5.6 for two different problem geometries. As visible, the EKF results in a smaller covariance.

Optimal Node Placement Assuming the 2D case for simplicity, the measurement matrix \boldsymbol{H}_n takes the form

$$\boldsymbol{H}_n = \begin{bmatrix} \cos \varphi_{az,n} & \sin \varphi_{az,n} \\ -\sin \varphi_{az,n}/d & \cos \varphi_{az,n}/d \end{bmatrix}, \quad (5.17)$$

where $\varphi_{az,n}$ is the angle between the radar node n and the target. We also assume two nodes with equal distance d to the target and use the EKF as an estimator. The optimal position of the nodes can then be determined by minimizing the trace of Σ_2 from Eq. (5.15)

$$\varphi_{az,1}, \varphi_{az,2} = \underset{\varphi_{az,1}, \varphi_{az,2}}{\arg \min} \text{Tr}\{\Sigma_2\}. \quad (5.18)$$

The minimum can be found by taking the derivative of the trace with respect to one of the angles and setting it to zero:

$$\frac{\partial \text{Tr}\{\Sigma_2\}}{\partial \varphi_{az,1}} = \dots = \cos(\varphi_{az,2} - \varphi_{az,1}) \stackrel{!}{=} 0. \quad (5.19)$$

The solution is $\varphi_{az,2} = \varphi_{az,1} + (2n + 1)\pi/2, n = 0, \pm 1, \pm 2, \pm 3, \dots$. Inserting this in the second derivative proves that this is a local minimum. The effect of the problem geometry on the expected accuracy is also evident from Fig. 5.6. When the static nodes are placed in such a way, that the covariance matrices are geometrically orthogonal ($\varphi_{az,2} = \varphi_{az,1} + (2n + 1)\pi/2$), the resulting positioning uncertainty is small and a good position dilution of precision (PDOP) is attained

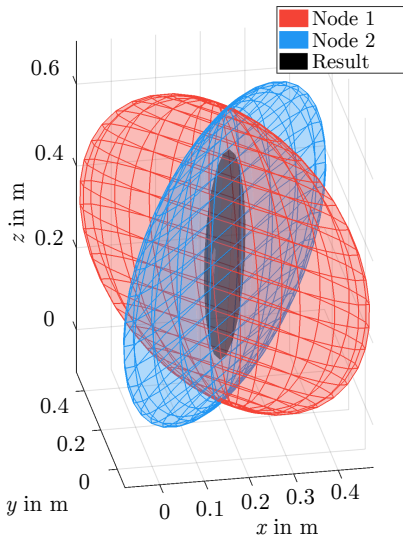


Fig. 5.7: CRLB of the intersection of two measurements in 3D.

as shown in (a). This is the case for most positions between the nodes from the scenario in Fig. 5.2. When both covariance matrices are geometrically parallel to each other ($\varphi_{az,2} = \varphi_{az,1} + n\pi$), the resulting uncertainty is higher due to bad PDOP as can be seen in (b). This is the case when the target is far away from the static radar nodes.

These results can easily be transferred to the 3D case as shown in Fig. 5.7. In the given scenario the covariance intersection in the xy plane is approximately orthogonal and therefore a good accuracy in horizontal direction is achieved. As the covariance ellipsoids in z are approximately parallel, the vertical accuracy is worse.

5.3 EKF for 6 DOF Positioning

Based on four static and one mobile radar nodes, an EKF was constructed to achieve 3D position and 3D orientation localization. Each measurement from a static node equipped with the planar 2D antenna array from Fig. 2.16 (a) directly provides a 3D position estimate with a corresponding uncertainty. The mobile node was fitted with the ring antenna array from Fig. 2.16 (b), which was used to support the estimation of its yaw orientation. A 0.1°-accurate dual-axis inclinometer Posital Fraba ACS-080 was additionally employed to measure the pitch and roll orientation of the robot. Deliberately, no further inertial measurement unit (IMU) was used, in order to keep the developed positioning system generically applicable for wheeled as well as legged robots.

The state vector \mathbf{x} is defined as

$$\mathbf{x} = \begin{bmatrix} \mathbf{p}_{xyz} \\ \mathbf{v}_{xyz} \\ \boldsymbol{\theta}_{\alpha\beta\gamma} \\ \boldsymbol{\omega}_{\alpha\beta\gamma} \end{bmatrix}, \quad (5.20)$$

with the 3D position $\mathbf{p}_{xyz} = [x \ y \ z]^T$, the 3D translational velocity $\mathbf{v}_{xyz} = [v_x \ v_y \ v_z]^T$, the 3D orientation $\boldsymbol{\theta}_{\alpha\beta\gamma} = [\alpha \ \beta \ \gamma]^T$, and the 3D angular velocity $\boldsymbol{\omega}_{\alpha\beta\gamma} = [\omega_\alpha \ \omega_\beta \ \omega_\gamma]^T$.

5.3.1 Motion Model

As no IMU was available, a DWNA motion model similar to the one described in Section 4.10 was used. To also account for the additional DOF of motion in z and rotation in pitch and roll, the state transition matrices \mathbf{A} from Eq. (4.71)

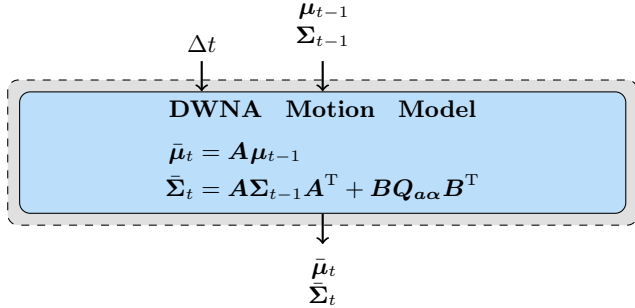


Fig. 5.8: Simplified block diagram of the EKF prediction step.

and B from (4.72) are extended to

$$A = \begin{bmatrix} I & \Delta t I & 0 & 0 \\ 0 & I & 0 & 0 \\ 0 & 0 & I & \Delta t I \\ 0 & 0 & 0 & I \end{bmatrix}, \quad (5.21a)$$

$$B = \begin{bmatrix} 0.5\Delta t^2 I & 0 \\ I\Delta t & 0 \\ 0 & 0.5\Delta t^2 I \\ 0 & I\Delta t \end{bmatrix}. \quad (5.21b)$$

I denotes the 3×3 identity and 0 the 3×3 zero matrices. Δt is the time between two successive EKF prediction steps.

The prediction equations remain unchanged as in (4.73)

$$\begin{aligned} \bar{\mu}_t &= A\mu_{t-1}, \\ \bar{\Sigma}_t &= A\Sigma_{t-1}A^T + BQ_{a\alpha}B^T, \end{aligned} \quad (5.22)$$

with the matrix $Q_{a\alpha}$ describing the translational a and angular α accelerations as white Gaussian noise with covariance matrix

$$Q_{a\alpha} = \begin{bmatrix} \sigma_a^2 I & 0 \\ 0 & \sigma_\alpha^2 I \end{bmatrix}. \quad (5.23)$$

The prediction step is summarized in Fig. 5.8.

5.3.2 EKF for 3D Position

The EKF for estimating the 3D position is also very similar to the one used in Section 4.10. The measurement vector $\mathbf{z}_{n,t}$ for node n is given by the conversion from polar to Cartesian coordinates

$$\mathbf{z}_{n,t} = \begin{bmatrix} d_{\text{st},n,t} \cos \vartheta_{\text{st},n,t} \cos \varphi_{\text{st},n,t} \\ d_{\text{st},n,t} \cos \vartheta_{\text{st},n,t} \sin \varphi_{\text{st},n,t} \\ d_{\text{st},n,t} \sin \vartheta_{\text{st},n,t} \end{bmatrix}, \quad (5.24)$$

with the distance $d_{\text{st},n,t}$, azimuth $\varphi_{\text{st},n,t}$, and elevation $\vartheta_{\text{st},n,t}$ angles measured by static node n at time step t . The measurement prediction vector is given by the current estimate of the mobile robot 3D position

$$\hat{\mathbf{z}}_{n,t} = \begin{bmatrix} \bar{\mu}_{x,t} \\ \bar{\mu}_{y,t} \\ \bar{\mu}_{z,t} \end{bmatrix} = \underbrace{\begin{bmatrix} x \\ y \\ z \end{bmatrix}}_{\mathbf{h}_{\text{pos}}} + \mathcal{N}(\mathbf{0}, \mathbf{R}_t). \quad (5.25)$$

The measurement matrix \mathbf{H}_t is

$$\mathbf{H}_t = \frac{\partial \mathbf{h}_{\text{pos}}}{\partial \mathbf{x}} \Big|_{\mathbf{x}=\bar{\mu}_t} = \begin{bmatrix} 1 & 0 & 0 \\ 0 & 1 & 0 \\ 0 & 0 & 1 \end{bmatrix} \mathbf{0}_{3 \times 9}. \quad (5.26)$$

The Jacobian \mathbf{G}_t to convert the measurement covariance matrix $\mathbf{Q}_{\text{rad,st}}$

$$\mathbf{Q}_{\text{rad,st}} = \begin{bmatrix} \sigma_{d_{\text{st}}}^2 & 0 & 0 \\ 0 & \sigma_{\varphi_{\text{st}}}^2 & 0 \\ 0 & 0 & \sigma_{\vartheta_{\text{st}}}^2 \end{bmatrix} \quad (5.27)$$

to state space $\mathbf{R}_t = \mathbf{G}_t \mathbf{Q}_{\text{rad,st}} \mathbf{G}_t^T$ is derived analogously to Eq. (4.78) and is given by

$$\mathbf{G}_t = \begin{bmatrix} \cos \varphi_{\text{st},n,t} \cos \vartheta_{\text{st},n,t} & -d_{\text{st},n,t} \sin \varphi_{\text{st},n,t} \cos \vartheta_{\text{st},n,t} & -d_{\text{st},n,t} \cos \varphi_{\text{st},n,t} \sin \vartheta_{\text{st},n,t} \\ \sin \varphi_{\text{st},n,t} \cos \vartheta_{\text{st},n,t} & d_{\text{st},n,t} \cos \varphi_{\text{st},n,t} \cos \vartheta_{\text{st},n,t} & -d_{\text{st},n,t} \sin \varphi_{\text{st},n,t} \sin \vartheta_{\text{st},n,t} \\ \sin \vartheta_{\text{st},n,t} & 0 & d_{\text{st},n,t} \cos \vartheta_{\text{st},n,t} \end{bmatrix}. \quad (5.28)$$

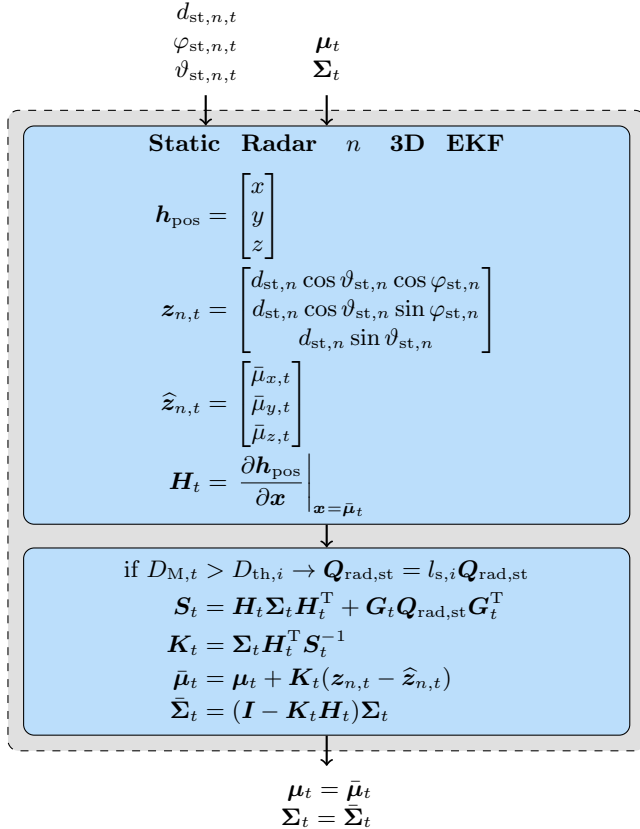


Fig. 5.9: Simplified block diagram of the EKF 3D position estimation step.

The update step is then

$$\begin{aligned} \mathbf{S}_t &= \mathbf{H}_t \mathbf{\Sigma}_t \mathbf{H}_t^T + \mathbf{G}_t \mathbf{Q}_{\text{rad,st}} \mathbf{G}_t^T, \\ \mathbf{K}_t &= \mathbf{\Sigma}_t \mathbf{H}_t^T \mathbf{S}_t^{-1}, \\ \bar{\mu}_t &= \mu_t + \mathbf{K}_t (\mathbf{z}_{n,t} - \hat{\mathbf{z}}_{n,t}), \\ \bar{\mathbf{\Sigma}}_t &= (\mathbf{I} - \mathbf{K}_t \mathbf{H}_t) \mathbf{\Sigma}_t. \end{aligned} \tag{5.29}$$

As the measurements of all static nodes are conditionally independent, i.e. $p(\mathbf{x}|\mathbf{z}_1, \dots, \mathbf{z}_N) = \prod_{n=1}^N p(\mathbf{x}|\mathbf{z}_n)$, they are fused sequentially in the order they are obtained. The propagation step from Section 5.3.1 with the time difference to the previous update is performed before fusing the current measurement. The EKF for 3D position estimation is summarized in Fig. 5.9.

5.3.3 EKF for 3D Orientation

As already mentioned, a dual-axis inclinometer and the azimuth angle measurement of the mobile radar node were used to estimate the 3D orientation of the mobile robot.

Inclinometer The inclinometer measures the angles θ_x and θ_y between its x and y axes $\mathbf{v}_{x,\text{inc}}$ and $\mathbf{v}_{y,\text{inc}}$ and the global xy plane, respectively. The global coordinate system is defined with its z axis anti-parallel to the gravity vector. The problem geometry is illustrated in Fig. 5.10.

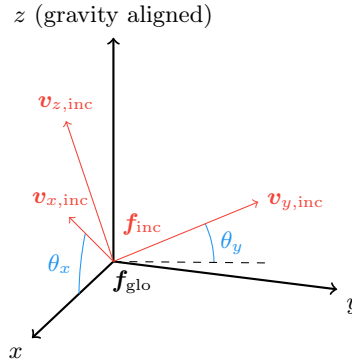


Fig. 5.10: Global coordinate system \mathbf{f}_{glo} , dual-axis inclinometer coordinate system \mathbf{f}_{inc} and measured angles θ_x and θ_y .

In order to fuse the inclinometer data to the current orientation estimate, they need to be converted to Tait-Bryan angles. This can be achieved by calculating the rotation matrix $\mathbf{R}_{\text{inc}} = [\mathbf{v}_{x,\text{inc}} \quad \mathbf{v}_{y,\text{inc}} \quad \mathbf{v}_{z,\text{inc}}]$, which describes the orientation of \mathbf{f}_{inc} . Since the inclinometer does not measure the yaw (heading) angle, it can be assumed without loss of generality that the $\mathbf{v}_{x,\text{inc}}$ vector lies in the global xz plane for the derivation of \mathbf{R}_{inc} . From geometric considerations,

$\mathbf{v}_{x,\text{inc}}$ is

$$\mathbf{v}_{x,\text{inc}} = \begin{bmatrix} \cos \theta_x \\ 0 \\ \sin \theta_x \end{bmatrix}. \quad (5.30)$$

$\mathbf{v}_{y,\text{inc}}$ is the vector which fulfills the following three conditions:

1. $\mathbf{v}_{y,\text{inc}}$ is orthogonal to $\mathbf{v}_{x,\text{inc}}$: $\mathbf{v}_{y,\text{inc}} \cdot \mathbf{v}_{x,\text{inc}} = 0$.
2. $\mathbf{v}_{y,\text{inc}}$ is a unit vector: $\|\mathbf{v}_{y,\text{inc}}\| = 1$.
3. The projections of $\mathbf{v}_{y,\text{inc}}$ on the z axis has the length $\sin \theta_y$: $\mathbf{v}_{y,\text{inc}} \cdot [0 \ 0 \ 1] = \sin \theta_y$.

The resulting equations have the closed-form solution

$$\mathbf{v}_{y,\text{inc}} = \begin{bmatrix} -\tan \theta_x \sin \theta_y \\ \cos \theta_y \sqrt{1 - (\tan \theta_x \tan \theta_y)^2} \\ \sin \theta_y \end{bmatrix}. \quad (5.31)$$

The z -axis vector is then given by the cross product $\mathbf{v}_{z,\text{inc}} = \mathbf{v}_{x,\text{inc}} \times \mathbf{v}_{y,\text{inc}}$. This completely defines the orientation matrix \mathbf{R}_{inc} .

The robot orientation matrix \mathbf{R}_{rob} is then obtained by rotating the constant matrix $\mathbf{R}_{\text{inc2rob}}$ by \mathbf{R}_{inc} :

$$\mathbf{R}_{\text{rob}} = \mathbf{R}_{\text{inc}} \mathbf{R}_{\text{inc2rob}}. \quad (5.32)$$

$\mathbf{R}_{\text{inc2rob}}$ describes the relative 3D orientation of the mobile robot and the inclinometer coordinate systems and needs to be determined during the assembly of the system. Using the conversion from rotation matrix to pitch β and roll γ angles from [157], the measurement vector $\mathbf{z}_{\text{inc},t}$ at time t is given by

$$\mathbf{z}_{\text{inc},t} = \begin{bmatrix} \beta(\mathbf{R}_{\text{rob}}) \\ \gamma(\mathbf{R}_{\text{rob}}) \end{bmatrix} = \begin{bmatrix} \text{atan2}\left(-[\mathbf{R}_{\text{rob}}]_{3,1}, \sqrt{[\mathbf{R}_{\text{rob}}]_{3,2}^2 + [\mathbf{R}_{\text{rob}}]_{3,3}^2}\right) \\ \text{atan2}\left(-[\mathbf{R}_{\text{rob}}]_{3,2}, [\mathbf{R}_{\text{rob}}]_{3,3}\right) \end{bmatrix}. \quad (5.33)$$

The measurement prediction vector is

$$\hat{\mathbf{z}}_{\text{inc},t} = \begin{bmatrix} \bar{\mu}_{\beta,t} \\ \bar{\mu}_{\gamma,t} \end{bmatrix} = \underbrace{\begin{bmatrix} \beta \\ \gamma \end{bmatrix}}_{\mathbf{h}_{\text{inc}}} + \mathcal{N}(\mathbf{0}, \mathbf{R}_t). \quad (5.34)$$

Again, the covariance matrix \mathbf{R}_t which describes the noise in state space is given by the conversion $\mathbf{R}_t = \mathbf{G}_t \mathbf{Q}_{\text{inc}} \mathbf{G}_t^T$ of the 2×2 inclinometer covariance matrix $\mathbf{Q}_{\text{inc}} = \sigma_{\text{inc}}^2 \mathbf{I}$ with the Jacobian $\mathbf{G}_t = \partial \mathbf{z}_{\text{inc}} / \partial [\theta_x \ \theta_y]$. With the measurement

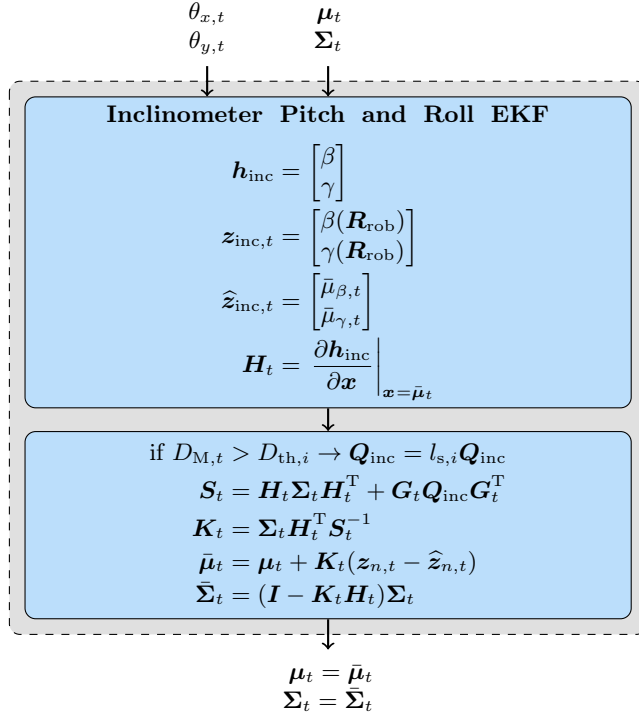


Fig. 5.11: Simplified block diagram of the inclinometer-based EKF for mobile robot pitch and roll estimation.

matrix \mathbf{H}_t

$$\mathbf{H}_t = \frac{\partial \mathbf{h}_{\text{inc}}}{\partial \mathbf{x}} \Big|_{\mathbf{x}=\bar{\mu}_t} = \begin{bmatrix} \mathbf{0}_{2 \times 7} & 1 & 0 & \mathbf{0}_{2 \times 3} \end{bmatrix}, \quad (5.35)$$

the pitch β and roll γ angles can be updated using the standard EKF equations as in Eq. (5.29). This is summarized in Fig. 5.11.

Mobile Radar Node The radar node on the mobile robot is equipped with the ring antenna array from Fig. 2.16 (b) and is capable of measuring the distance and the azimuth angle $\varphi_{\text{mo},n}$ to the static radar nodes at positions $\mathbf{m}_{\text{rad,st},n}$, $n = 1 \dots 4$. It is used to determine the yaw orientation α of the mobile robot.

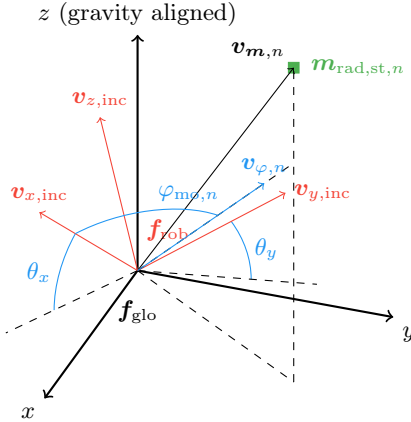


Fig. 5.12: Robot coordinate frame f_{rob} with mobile radar azimuth angle measurement φ_{mo} .

The result of the azimuth measurement is the vector

$$\mathbf{v}_{\varphi,n} = \mathbf{v}_{x,\text{inc}} \cos \varphi_{\text{mo}} + \mathbf{v}_{y,\text{inc}} \sin \varphi_{\text{mo}}, \quad (5.36)$$

which is the projection of the static node position $\mathbf{m}_{\text{rad},\text{st},n}$ on the plane spanned by $\mathbf{v}_{x,\text{inc}}$ and $\mathbf{v}_{y,\text{inc}}$.

If the mobile radar node is parallel to gravity ($\beta = \gamma = 0^\circ$), the measured azimuth angle corresponds to the yaw orientation of the mobile robot up to a constant offset given by the relative orientation of the mobile radar node to the robot coordinate system. This is in general not the case at non-zero pitch or roll angles as can be seen in Fig. 5.12.

An alternative interpretation is to say that the azimuth measurement constrains the static node position to the plane spanned by $\mathbf{v}_{\varphi,n}$ and $\mathbf{v}_{z,\text{inc}}$. It should be noted, that this plane is only known from the combination of the inclinometer and azimuth DOA measurements. If the roll or pitch angles are non-zero and are unknown, no accurate yaw estimation is possible using only azimuth DOA. Additionally, an estimate for the mobile robot 3D position should be available.

The mobile robot yaw orientation $\alpha(\varphi_{\text{mo}})$ can thus be determined as the angle

corresponding to the rotation

$$\mathbf{R}_z(\alpha(\varphi_{\text{mo}})) = \begin{bmatrix} \cos \alpha(\varphi_{\text{mo}}) & \sin \alpha(\varphi_{\text{mo}}) & 0 \\ -\sin \alpha(\varphi_{\text{mo}}) & \cos \alpha(\varphi_{\text{mo}}) & 0 \\ 0 & 0 & 1 \end{bmatrix}. \quad (5.37)$$

$\mathbf{R}_z(\alpha(\varphi_{\text{mo}}))$ rotates \mathbf{f}_{rob} around the global z axis so that $\mathbf{m}_{\text{rad,st},n}$ lies in the plane spanned by $\mathbf{v}_{\varphi,n}$ and $\mathbf{v}_{z,\text{inc}}$. The sought yaw angle $\alpha(\varphi_{\text{mo}})$ has to satisfy two conditions:

1. The plane normal $\mathbf{v}_{\varphi,n} \times \mathbf{v}_{z,\text{inc}}$ is orthogonal to the vector $\mathbf{v}_{\mathbf{m},n}$ pointing at $\mathbf{m}_{\text{rad,st},n}$: $(\mathbf{R}_z(\alpha(\varphi_{\text{mo}}))(\mathbf{v}_{\varphi,n} \times \mathbf{v}_{z,\text{inc}})) \cdot \mathbf{v}_{\mathbf{m},n} \stackrel{!}{=} 0$. There are two angles $\alpha(\varphi_{\text{mo}})_1$ and $\alpha(\varphi_{\text{mo}})_2 = \alpha(\varphi_{\text{mo}})_1 + \pi$ which satisfy this condition and there exists a rather long closed-form solution, which is not given here for the sake of brevity.
2. The projections of the rotated $\mathbf{v}_{\varphi,n}$ on $\mathbf{v}_{\mathbf{m},n}$ is positive, i.e. they point roughly in the same direction (the second result in the first condition points in the opposite direction): $(\mathbf{R}_z(\alpha(\varphi_{\text{mo}}))\mathbf{v}_{\varphi,n}) \cdot \mathbf{v}_{\mathbf{m},n} > 0$.

The measurement vector \mathbf{z}_{mo} is then

$$\mathbf{z}_{\text{mo},n,t} = \alpha(\varphi_{\text{mo},n,t}) \quad (5.38)$$

and the measurement prediction

$$\widehat{\mathbf{z}}_{\text{mo}} = \bar{\mu}_{\alpha,t} = \underbrace{\alpha}_{\mathbf{h}_{\text{mo}}} + \mathcal{N}(\mathbf{0}, \mathbf{R}_t). \quad (5.39)$$

\mathbf{R}_t is the measurement covariance matrix in state space given by the conversion $\mathbf{R}_t = \mathbf{G}_t \sigma_{\varphi_{\text{mo}}}^2 \mathbf{G}_t^T$, where $\sigma_{\varphi_{\text{mo}}}^2$ is the variance of the azimuth measurement of the mobile radar node. Due to the very long expressions involved, the Jacobian \mathbf{G}_t was implemented as numeric instead of analytic differentiation:

$$\mathbf{G}_t = \frac{\partial \mathbf{z}_{\text{mo}}}{\partial \varphi_{\text{mo}}} \approx \frac{\Delta \mathbf{z}_{\text{mo}}}{\Delta \varphi_{\text{mo}}}. \quad (5.40)$$

The measurement matrix \mathbf{H}_t is again given by the differentiation of the measurement function:

$$\mathbf{H}_t = \left. \frac{\partial \mathbf{h}_{\text{mo}}}{\partial \mathbf{x}} \right|_{\mathbf{x}=\bar{\mu}_t} = [\mathbf{0}_{1 \times 6} \quad 1 \quad \mathbf{0}_{1 \times 5}]. \quad (5.41)$$

The standard EKF equations can then be used to estimate the yaw orientation of the mobile robot. This is summarized in Fig. 5.13.

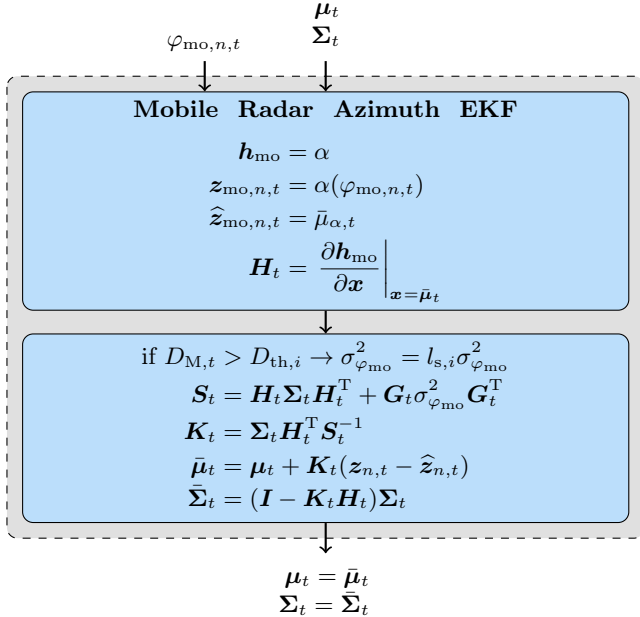


Fig. 5.13: Simplified block diagram of the mobile radar-based EKF for mobile robot yaw estimation.

5.3.4 System Implementation

The architecture of the realized system is very similar to the one shown in Fig. 4.21 and will not be repeated here. All algorithms were implemented in C on an embedded platform and the sensor fusion framework Symeo FusionEngine was used. Due to the modularity of the framework, some of the functionality implemented in Chapter 4 could be reused. The radar measurement rate was 30 Hz. This was also the rate with which the state was updated. The comments regarding initialization, recovery, and outlier detection from Sections 4.8 and 4.9 apply here as well.

5.3.5 Results

The complete system was tested in three scenarios: the study hall Tentoria at the FAU Erlangen-Nürnberg (Fig. 5.14 (a)), the DFKI space exploration hall

in Bremen (Fig. 5.1), and the entrance hall of the DFKI building at Robert-Hooke-Straße 1, Bremen (Fig. 5.2).

Tentoria The measurements were performed as part of the SOKOROB project, where the relative 3D positions and 3D orientations of 5 mobile robots Pioneer P3-AT (cf. Fig. 4.23 (c)) had to be determined. Using this hardware, the TransTerra scenario could be mimicked by keeping the outer four robots static, measuring their poses precisely with the total station and driving around with the fifth mobile robot. The robot started on the platform in the middle, drove down the ramp and then around it. During the run, its 3D position was tracked by the total station, which served as ground-truth reference and by the EKF described in Section 5.3. The result is shown in Fig. 5.14 (b). The red dots denote the estimated 3D position of the mobile robot and the red lines its 3D orientation. As can be seen, the EKF result matches the reference trajectory accurately. Due to software limitations, the measurement rate in this campaign was restricted to approximately 1 Hz, so that only a few measurement points were obtained while the robot was driving relatively fast around the ramp. Unfortunately, no reference for the orientation was available. However, one can see that it mostly matches the driven trajectory. The cumulative error distribution is shown in Fig. 5.14 (c). The exact attained measurement accuracy in x , y , z , and in 3D is given in the column “Tentoria” in Table 5.1.

DFKI Space Exploration Hall (DFKI SEH) A second measurement campaign was performed in the DFKI space exploration hall in Bremen. As visible from Fig. 5.1, two static radar nodes were used. The mobile radar node was carried by the space exploration rover SherpaTT. As stated in [143] “SherpaTT is a hybrid wheeled-leg rover with an active suspension system composed of four limbs with a wheel mounted at the end of each limb. A total of 20 active degrees of freedom (DOF) allow the robot to adapt to rough terrain while at the same time maintaining a desired body height and/or attitude of the central body.” The measurement results of a triangle-like trajectory are shown in Fig. 5.15 (a). Again, the measurement trajectory closely matches the reference. As can be seen, the estimated orientation is approximately constant, which corresponds to the reality, as the mobile robot was moved sideways demonstrating its ability to move in any direction. The cumulative error distribution is shown in Fig. 5.15 (b) and the attained accuracy is given in Table 5.1 in the column “DFKI SEH”.

DFKI Entrance Hall (DFKI EH) A third measurement campaign was conducted in the entrance hall of the DFKI shown in Fig. 5.2. Four static radar nodes equipped with 2D planar antennas were installed on tripod stands and their

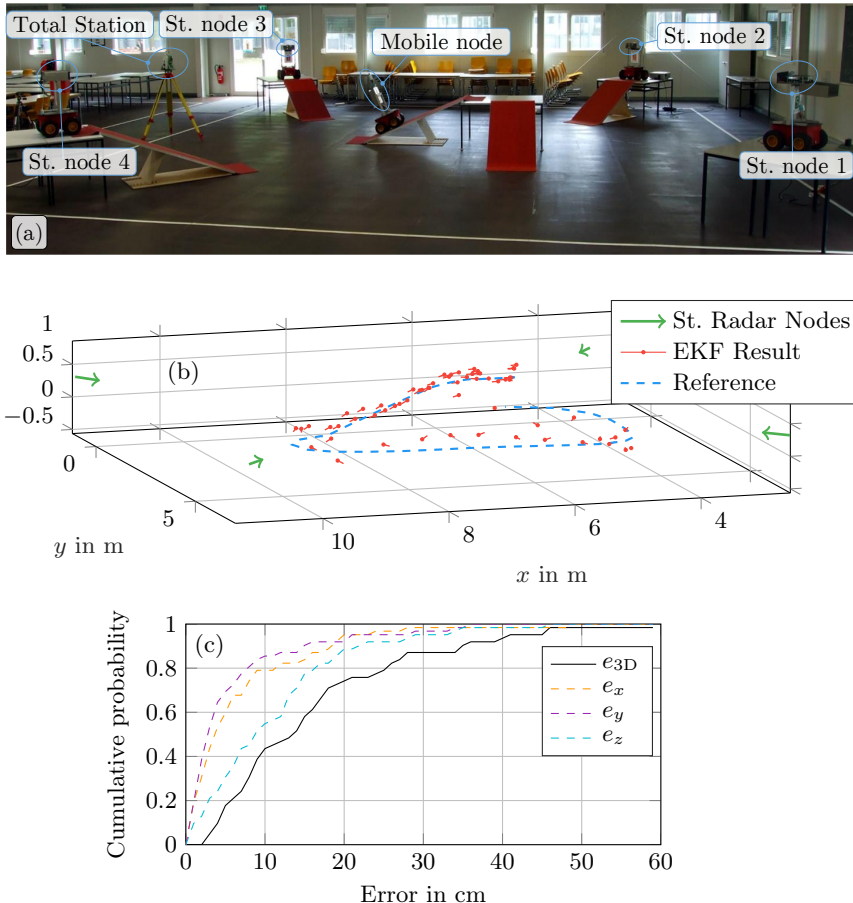


Fig. 5.14: Measurement result in test scenario “Tentoria, FAU Erlangen-Nürnberg” (a) with mobile node with an 8-channel ring array and 4 static nodes with 2D planar arrays (adapted from [150] and [158]). Localization result and reference (b) and cumulative error probability (c).

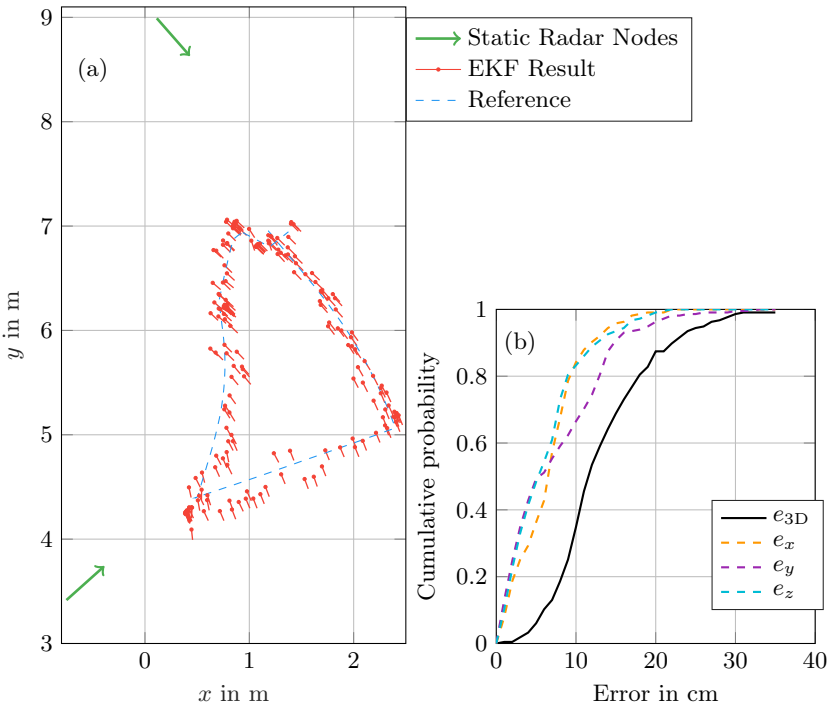


Fig. 5.15: Localization result with reference in DFKI space exploration hall (a) and cumulative error distribution (b).

poses were precisely measured with the total station. The measurement area had the size of 8×14 m. The rover SherpaTT was equipped with the radar with the ring antenna array and the dual-axis inclinometer as shown in Fig. 5.16. The result of a typical test run is shown in Fig. 5.17 (a). During the experiment, the height of the rover was changed at multiple times to also demonstrate the localization capability in z -direction as shown in Fig. 5.17 (c). The cumulative error distribution is shown in Fig. 5.17 (b) and the attained accuracy is summarized in Table 5.1 in the column “DFKI EH”.

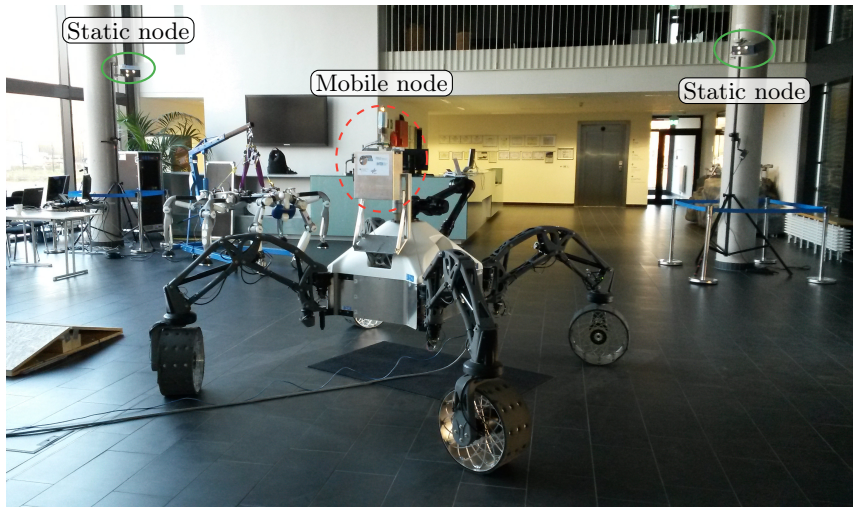


Fig. 5.16: Rover SherpaTT equipped with mobile radar node and static nodes in the background.

Table 5.1: TransTerrA localization accuracy results expressed as 68 %, resp. 95 % of the measurement errors being below a certain threshold value as given by the cumulative error distribution.

σ ($\hat{=} 68\%$) / 2σ ($\hat{=} 95\%$)	Tentoria	DFKI SEH	DFKI EH
σ_x	7.3 cm	8.1 cm	3.8 cm
σ_y	4.9 cm	10.9 cm	3.5 cm
σ_z	13.2 cm	7.6 cm	4.7 cm
σ_{3D}	17.4 cm	14.9 cm	7.3 cm
$2\sigma_x$	19.4 cm	14.5 cm	7.4 cm
$2\sigma_y$	20.6 cm	19.6 cm	7.1 cm
$2\sigma_z$	28.9 cm	16.5 cm	9.7 cm
$2\sigma_{3D}$	40.6 cm	26.2 cm	12.1 cm

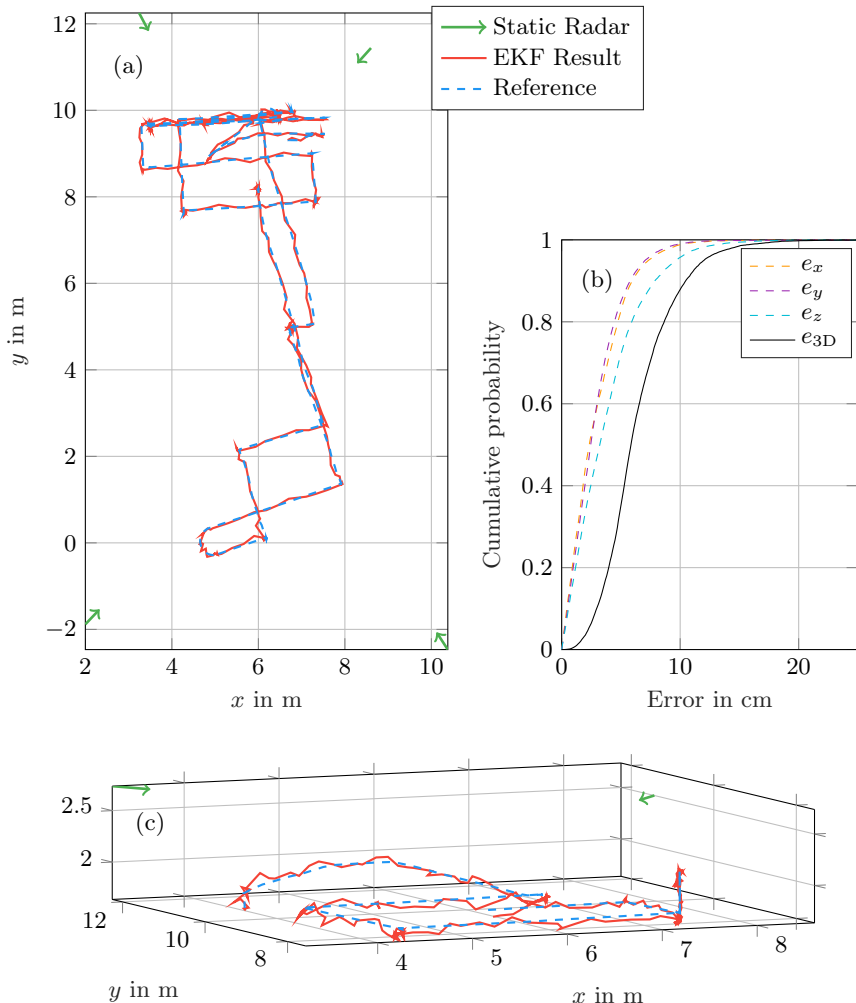


Fig. 5.17: Localization result with reference in DFKI building entrance hall (a) and cumulative error probability (b). A zoom-in demonstrating the localization capability in z -direction (c).

5.4 Conclusion

In this chapter the accurate 6 DOF localization of a mobile robot with 4 static radar nodes combining range and angle measurements was verified. The results in three different scenarios showed a gradual improvement, as the measurement rate of the system was increased and the array calibration improved.

Similar to Section 4.14, this application would also profit from modern radar chips, offering higher bandwidth and more Rx channels. Additionally, employing algorithms which can resolve (e.g. SAGE) and utilize the ground multipath reflections [70] could improve the localization accuracy in z direction. Phase-tracking approaches as in [159] can also lead to accuracy improvements, but may be more susceptible to interference.

6 Further Applications

6.1 Microsoft Indoor Localization Competition

Although initially developed for planetary exploration applications, the system presented in Chapter 5 fulfilled all requirements to participate in the Microsoft Indoor Localization Competition 2016 [126], [160], [161]. The aim of this event is to obtain a fair comparison of the performance of different localization systems under equal real-life conditions. The competition took place in the Dachoyer hall of the Hofburg building (former imperial palace) in Vienna, Austria shown in Fig. 6.1 and 6.4. The evaluation area contained two floors and a staircase (see also the simplified geometry 3D plot in Fig. 6.2 and 6.3). As can be seen, numerous objects and persons were present on-site and even more during the evaluation of the systems. This made the task particularly challenging.

Since the maximum number of static nodes allowed by the rules was five, the system from Chapter 5 was extended by one further node. As the map of the scenario was known in advance, a CRLB simulation was performed to obtain an initial estimate of the achievable accuracy and to choose optimal positions for the static nodes. The result is shown in Fig. 6.2. As evident, 5 static nodes combining RTOF and DOA with a field of view of $\pm 60^\circ$ are sufficient to cover the whole evaluation area. A 3D accuracy of 10-20 cm can be expected in the absence of systematic errors.

During the evaluation it turned out, that it was impossible to place the static nodes as planned due to various limitations. Therefore, they were placed as shown in Fig. 6.3. The mobile node was carried by hand to the evaluation points chosen by the organizers and an IMU was additionally used as a standstill detector to be able to automatically provide a constant and stable result as required by the rules. NLOS paths between the mobile and the static nodes were filtered out by a threshold on the sample variance of the measurements. The evaluation points and the result of the proposed system are also shown in Fig. 6.3.

The achieved result is given in Table 6.1. As can be seen, the accuracy in x and y direction was much better than in z which stands in line with the theoretical result. A major source of error in z were the points on the staircase (shown as a darker brown rectangle in the figures), where the metal railings visible in Fig. 6.4 caused multipath reflections and partially obstructed the LOS path.

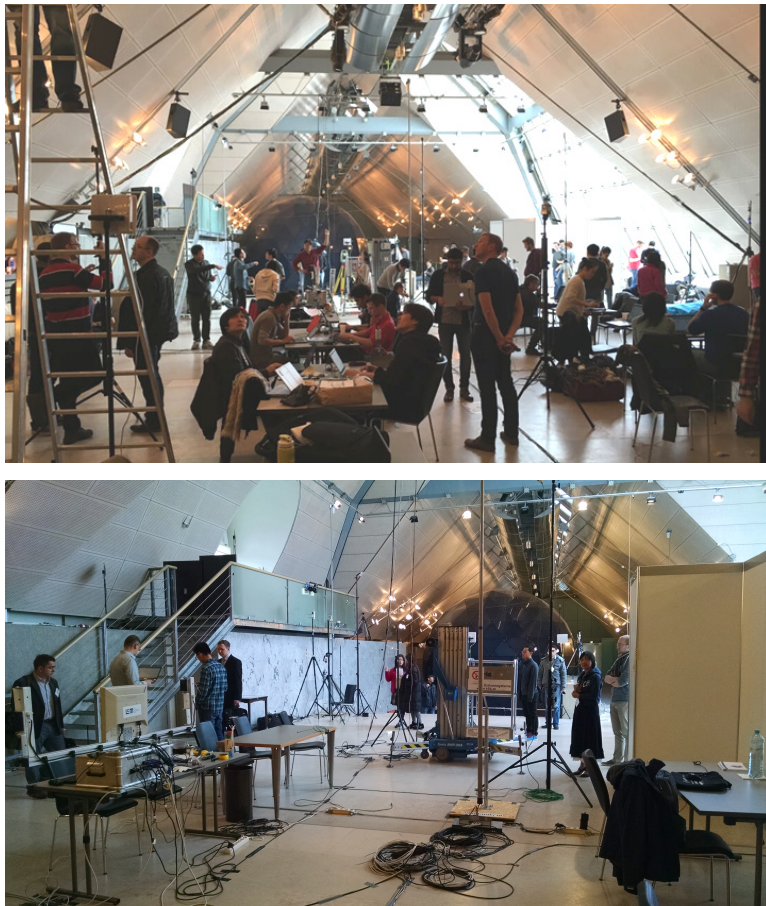


Fig. 6.1: Microsoft Indoor Localization Competition 2016 evaluation area in the Dachfoyer hall of the Hofburg building (former imperial palace) in Vienna, Austria.

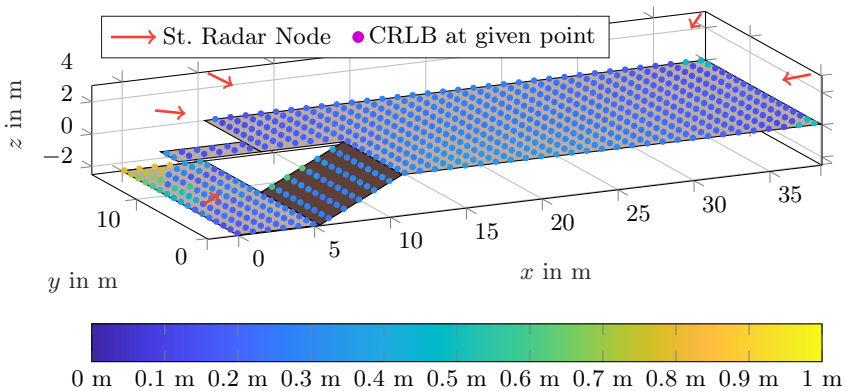


Fig. 6.2: 3D plan of evaluation area with poses of static radar nodes. Each color-coded point denotes a position at which the CRLB was calculated.

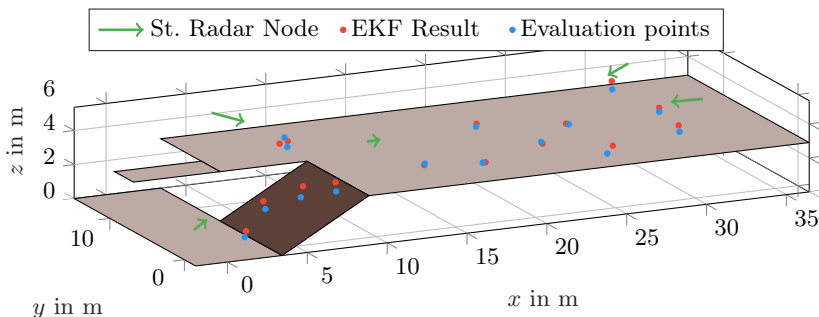


Fig. 6.3: Poses of static radar nodes used during the competition. Evaluation points and result.

Table 6.1: Localization accuracy in x , y , z , and in 3D in the evaluation phase at the Microsoft Indoor Localization Competition 2016. The accuracy metric used was the mean absolute error as chosen by the organizers.

mean($ e_x $)	mean($ e_y $)	mean($ e_z $)	mean($ e_{3D} $)
8.10 cm	10.35 cm	31.59 cm	37.23 cm

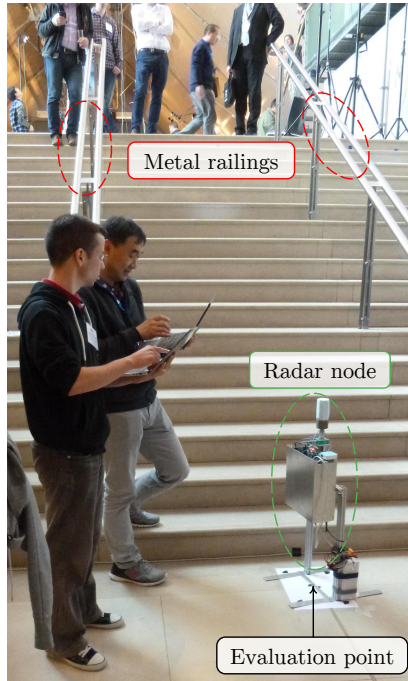


Fig. 6.4: The author and the participating system during the competition phase at an evaluation point at the staircase. There were three more evaluation points on the staircase.

With this result, the system was the fourth most accurate system in the competition out of 31 contestants (18 in the 3D and 13 in the 2D category; the complete official results can be seen in [160]). The most accurate system was based on laser scanners, which are not allowed to participate in the competition anymore as of 2018. Except for several sound/ultrasound devices, virtually all

other systems were based on the Decawave UWB boards with a bandwidth of up to 900 MHz and multilateration. This again shows the advantages of the proposed concept which yielded very similar (and compared to most contestants better) localization results with a much lower bandwidth of 250 MHz.

6.2 UAV Localization

Another interesting application which is expected to rapidly grow in importance in the years to come is unmanned aerial vehicles (UAV) localization. UAVs are poised to transform multiple industries in the next decades, like e.g. parcel delivery [162], [163], surveillance [164], and automated warehouse inventory [165]. GNSS/RTK is currently widely used for UAV localization and navigation as it offers 3D position and heading estimation with an accuracy in the range of 1 cm and 1°, respectively. However, it is not available indoors and its accuracy can be greatly reduced in urban canyons.

The most critical flight phases are during takeoff and landing. As applications relying on UAVs grow in popularity and acceptance, the risk of malicious jamming attacks of the GNSS satellite signals or the GNSS correction data streams increases. As the landing sites are static and in general known to the public (e.g. a parcel station), they are most vulnerable to attacks. Illegal, but commercially available jamming devices are freely available. The cheapest emit CW signals and cost as low as \$5. More advanced devices at prices of a few hundred dollars use sawtooth signals with bandwidth of up to 100 MHz. GNSS signals are very susceptible to such attacks, as their bandwidth is lower than 25 MHz and their power at Earth level is approximately -130 dBm. An overview of available GNSS jammers can be found in [166].

The jamming resistance of FMCW signals, on the other hand, is much higher due to the modulation scheme used and because they commonly use a much higher bandwidth [167]. A successful attack would require the jammer to estimate the signal parameters (sweep duration and bandwidth) and synchronize to them with sufficient accuracy. Therefore, the system presented in Chapter 2 is an interesting candidate for 3D UAV localization to increase the reliability during landing and takeoff, and also to enable indoor applications. Because the system is secondary, the signal power is relatively higher compared to GNSS: approximately -62 dBm at a distance of 100 m considering FSPL, simple patch antennas and legally limited Tx power of 13 dBm. This greatly improves the resistance to jamming.

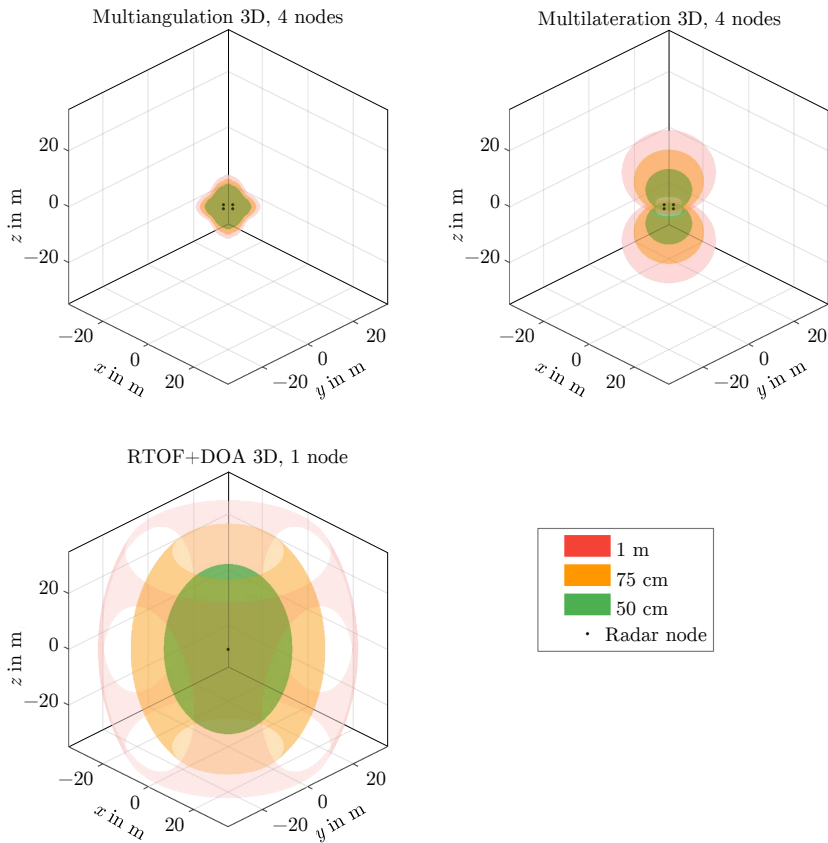


Fig. 6.5: CRLB for 3D positioning based on multiangulation, multilateration, and the combination of RTOF and DOA (extended and adapted from [168]).

6.2.1 CRLB

Based on the results from Section 5.2 multiangulation, multilateration, and the combination of RTOF and DOA were compared in terms of achievable accuracy using the CRLB for 3D positioning. The measurement variances $\sigma_d = 8\text{ cm}$ and $\sigma_{\varphi_{az}} = \sigma_{\vartheta_{el}} = 1^\circ$ for distance, azimuth, and elevation, respectively were assumed. Four nodes with omnidirectional coverage were simulated for multiangulation and multilateration, as this is the minimal number required for unambiguous localization. The nodes were placed equidistantly on a circle with a radius of 2 m. One omnidirectional node was assumed for the combination of RTOF and DOA.

The resulting CRLB in 3D is shown in Fig. 6.5. The colored bubbles denote iso-accuracy surfaces with a corresponding 3D positioning CRLB (e.g. the green surfaces denote 3D positions where the 3D position standard deviation is 50 cm). As can be seen, a single node using a combination of RTOF and DOA is capable of providing accurate localization at a much larger range compared to multiangulation and multilateration. The egg-like shape of the resulting iso-accuracy surfaces for RTOF+DOA is due to the fact that the positioning precision in z depends only on the ranging and the elevation error ($\sigma_z \propto [\sigma_d, \sigma_\vartheta]$) and in x and y also on the azimuth error ($\sigma_x, \sigma_y \propto [\sigma_d, \sigma_\varphi, \sigma_\theta]$). This can be considered during array design. The combination of RTOF and DOA is also much more compact, which is important, if application such as e.g. parcel delivery stations are considered.

6.2.2 Results

The suitability of the system presented in Chapter 2 for UAV localization was tested in a measurement campaign in collaboration with the Institute of Flight System Dynamics (FSD), RWTH Aachen University, Germany. A radar node with a 2D planar antenna was static on the ground and the UAV was equipped with the compact portable radar node from Fig. 4.3 as shown in Fig. 6.6 (a). The UAV used is the tiltwing Maverix, developed at FSD, Aachen. Being able to tilt the main wing in vertical as well as in horizontal position, it is capable of vertical takeoff/landing and wing-borne aerodynamic flight. It has a wing-span of approximately 1 m.

The results of three test flights performed with the described setup at a distance of up to 100 m are given in Table 6.2. The flight trajectory for flight #1 as measured by the radar and the RTK is shown in Fig. 6.6 (c). As can be seen, a single radar node is sufficient for accurate 3D positioning for UAV landing and takeoff. The segment with relatively large discrepancy between the radar result and the reference is due to problems with the antenna array calibration, as a

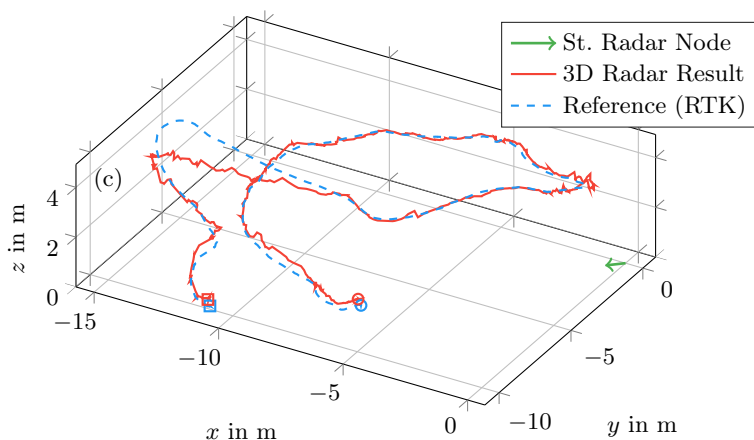
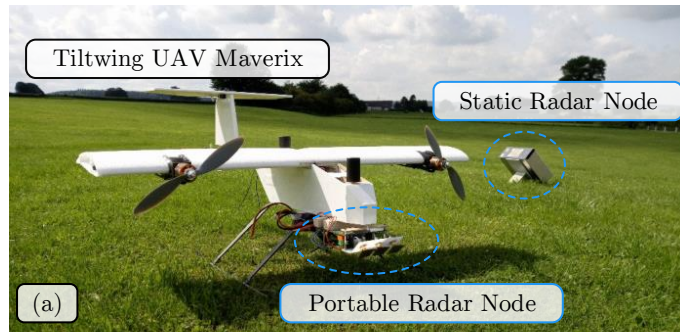


Fig. 6.6: Tiltwing UAV Maverix equipped with portable radar node (a); measurement during flight at the RC model airfield in Orsbach/Aachen, Germany (b); measured trajectory by radar with RTK as reference (c) (extended and adapted from [168]).

sidelobe was becoming higher than the mainlobe.

The initial theoretical derivations and test results prove the potential of the proposed system for UAV localization. In a next step, a Kalman filter can be used to improve the localization stability and reliability. An antenna array with hemispherical coverage used in the static radar node will ensure that the UAV can approach from any direction. A miniaturized portable radar node could make the system more attractive for smaller UAVs.

Table 6.2: Radar measurement errors in distance e_d , azimuth e_φ , elevation e_ϑ , and 3D distance e_{3D} for three test flights from a test campaign at the RC model airfield in Orsbach/Aachen, Germany shown in Fig. 6.6 (b). An RTK receiver was used as a reference.

Flight #	RMS(e_d)	RMS(e_φ)	RMS(e_ϑ)	mean(e_{3D})
1	8.25 cm	0.65°	0.97°	19.66 cm
2	7.91 cm	0.68°	0.94°	21.18 cm
3	11.61 cm	0.70°	1.04°	31.19 cm

7 Conclusion and Outlook

A wireless local positioning concept based on secondary radar combining RTOF with DOA measurements is presented in the thesis at hand. Using multi-modal sensor fusion with complementary sensors, its performance is demonstrated in several realistic applications.

The radar device used is a secondary FMCW radar with 8 Rx channels operating in the 24 GHz ISM band. Combining RTOF and DOA estimates, it was shown that 3D positioning is possible with only a single measurement from a static to a mobile radar node. This greatly reduces the complexity compared to state-of-the-art multilateration or multiangulation localization systems, where at least 4 static nodes are required. The error sources phase noise and AWGN and their effect on the ranging accuracy were studied. It was shown that a certain improvement can be achieved by combining all 8 Rx channels.

Compensating the phase noise typical for secondary radar as proposed in [169] can improve the localization precision.

The DOA estimation was also analyzed regarding the achievable accuracy, the efficient implementation on an embedded platform, and the effects of calibration. It was demonstrated that the phase mismatch between the Rx channels, the angle-independent mutual coupling, and the phase center position errors can be successfully calibrated.

A thorough analysis of angle-dependent phase errors and their compensation based on a signal model or a sector calibration could lead to further performance improvements.

Accurate and reliable 3D localization in outdoor and large indoor environments could be demonstrated in multiple experiments with only a single static radar node. RMSE of 5 cm in range and 1° in azimuth and elevation could be achieved. However, there were significant problems in long and narrow corridors, where multipath reflections severely interfered with the DOA estimation.

Employing a radar device with more Rx channels would lead to an array pattern with lower sidelobes and narrower beamwidths and increase the performance in such situations. Optimizing the antenna array for a certain scenario can also lead to improvements. Despite their high computational complexity, high-resolution algorithms such as Capon and MUSIC could also be employed to improve the angular resolution and reduce the negative impact of multipath signals.

Based on the presented radar concept, two wireless local positioning systems were developed and tested. The radar sensor was combined with an ultrasonic device and odometry in an EKF-based sensor fusion to provide robust localization of a healthcare service robot for autonomous navigation in a very challenging indoor environment. The complementary properties of the employed sensors ensured consistent localization quality. Only two static radar nodes were sufficient to provide coverage in an up to 60 m-long corridor. A 2D positioning accuracy of 10 cm and an orientation accuracy of 1.5° could be demonstrated in three real-life scenarios. A compact portable radar node carried by a human could also be located relative to the mobile robot to provide follow and lead functionality.

A multi-hypothesis Kalman filter could be used to increase the reliability even further in particularly difficult situations which can be described by multimodal distributions [107]. Additionally employing an IMU in the portable radar node can aid the relative localization of a person, especially in the case when no LOS path is available. A hybrid primary-secondary radar approach, as shortly demonstrated, also has great potential to create a powerful radar-based indoor positioning system.

Another system for 6 DOF mobile robot localization for planetary exploration applications was also presented. Using 4 static radar nodes, a mobile robot carrying a fifth node was located using an EKF on an area of 110 m². A 3D positioning accuracy in the range of 10 cm was achieved while simultaneously using a dual-axis inclinometer for roll and pitch and radar for yaw orientation estimation.

In such scenarios with relatively simple geometry, the multipath caused by the ground reflection can be used to improve the localization as shown e.g. in [70]. It could also be resolved with algorithms like SAGE. Phase-based approaches like the ones shown in [170] and [159] could lead to significant performance improvements, but will probably be more susceptible to interference.

The proposed system competed in the Microsoft Indoor Localization Competition 2016 and outperformed many of the contestants, even though a much lower bandwidth was used. Furthermore, the proposed approach was successfully tested for UAV localization.

Highly integrated 77 GHz FMCW radar chips with a higher bandwidth, multiple Rx / Tx channels as well as built-in mixing and signal digitization are becoming available from several manufacturers. These chips will enable radar devices with higher ranging and angular accuracy as well as a smaller form factor. This makes the concepts proposed in this work even more attractive for the aforementioned applications.

A Geometric Functions

A.1 Euclidean Distance

The Euclidean distance between two vectors $\|\mathbf{v}\| = \|\mathbf{v}_2 - \mathbf{v}_1\|$, resp. the Euclidean norm of a vector $\|\mathbf{v}\|$ is given by

$$\|\mathbf{v}\| = \sqrt{\sum_{n=1}^N v_n^2}, \quad (\text{A.1})$$

where N denotes the dimensionality of the vector \mathbf{v} .

A.2 Angle

The angle between two points \mathbf{p}_1 and \mathbf{p}_2 is

$$\angle(\mathbf{p}_1, \mathbf{p}_2) = \text{atan2}(p_{2,y} - p_{1,y}, p_{2,x} - p_{1,x}). \quad (\text{A.2})$$

The function $\text{atan2}(\cdot)$ is the four-quadrant extension of the arcus tangens commonly defined as

$$\text{atan2}(y, x) = \begin{cases} \text{atan}(\frac{y}{x}) & \text{if } x > 0 \\ \text{sign}(y)(\pi - \text{atan}(|\frac{y}{x}|)) & \text{if } x < 0 \\ 0 & \text{if } x = y = 0 \\ \text{sign}(y)\frac{\pi}{2} & \text{if } x = 0, y \neq 0. \end{cases} \quad (\text{A.3})$$

Using the identity $\frac{d \arctan x}{dx} = \frac{1}{1+x^2}$ and the chain rule, the partial derivatives can be shown to be

$$\frac{\partial \text{atan2}(y, x)}{\partial x} = \begin{cases} \frac{\partial}{\partial x} \text{atan}(\frac{y}{x}) = -\frac{y}{x^2+y^2} & \text{if } x > 0 \\ \cdots = -\frac{y}{x^2+y^2} & \text{if } x < 0 \\ 0 & \text{if } x = y = 0 \\ 0 & \text{if } x = 0, y \neq 0 \end{cases} \quad (\text{A.4})$$

and

$$\frac{\partial \text{atan}2(y, x)}{\partial y} = \begin{cases} \frac{\partial}{\partial y} \text{atan}\left(\frac{y}{x}\right) = \frac{x}{x^2+y^2} & \text{if } x > 0 \\ \cdots = \frac{x}{x^2+y^2} & \text{if } x < 0 \\ 0 & \text{if } x = y = 0 \\ 0 & \text{if } x = 0, y \neq 0. \end{cases} \quad (\text{A.5})$$

A.3 Wrap Angle

In order to wrap an arbitrary angle α to the range $\pm\pi$, i.e. to $\hat{\alpha} \in [-\pi, \pi)$, the function $\text{wrap}(\cdot)$ is defined as follows:

$$\hat{\alpha} = \text{wrap}(\alpha) = \text{mod}((\alpha + \pi), 2\pi) - \pi, \quad (\text{A.6})$$

with the modulo function $\text{mod}(\cdot, \cdot)$.

A.4 Basis Transformation

The function $\mathbf{p}_d = \text{b}_{\text{tran}}(\mathbf{f}_s, \mathbf{f}_d, \mathbf{p}_s)$ transforms the point \mathbf{p}_s from the source coordinate system \mathbf{f}_s into the point \mathbf{p}_d in the destination coordinate system \mathbf{f}_d (cf. Figure A.1). Although the following equations apply for the 3D case, they can easily be adapted for 2D.

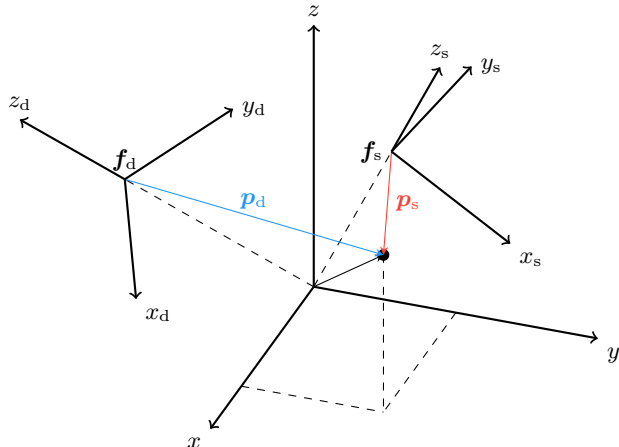


Fig. A.1: Transformation between coordinate systems.

The coordinate systems are given in the form

$$\begin{aligned}\mathbf{f} &= [\mathbf{p}_0^T \quad \mathbf{v}_x^T \quad \mathbf{v}_y^T] \\ &= [p_{0,x} \quad p_{0,y} \quad p_{0,z} \quad v_{x,x} \quad v_{x,y} \quad v_{x,z} \quad v_{y,x} \quad v_{y,y} \quad v_{y,z}]\end{aligned}\tag{A.7}$$

with the origin of the coordinate system \mathbf{p}_0 and the unit x -direction and y -direction vectors \mathbf{v}_x , resp. \mathbf{v}_y given in a certain “parent” coordinate system. The z -direction vector can be calculated to $\mathbf{v}_z = [v_{z,x} \quad v_{z,y} \quad v_{z,z}] = \mathbf{v}_x \times \mathbf{v}_y$ where \times denotes the cross product. \mathbf{f} can then be written in matrix form as

$$\mathbf{A}_f = \begin{bmatrix} v_{x,x} & v_{y,x} & v_{z,x} & p_{0,x} \\ v_{x,y} & v_{y,y} & v_{z,y} & p_{0,y} \\ v_{x,z} & v_{y,z} & v_{z,z} & p_{0,z} \\ 0 & 0 & 0 & 1 \end{bmatrix} = \begin{bmatrix} \mathbf{R}_f & & \mathbf{T}_f \\ 0 & 0 & 0 & 1 \end{bmatrix}.\tag{A.8}$$

The matrix \mathbf{A}_f can be interpreted as an affine transformation consisting of a rotation \mathbf{R}_f and a translation \mathbf{T}_f which converts a point \mathbf{p} from \mathbf{f} into its parent coordinate system. The point \mathbf{p} needs to be converted to homogeneous coordinates by appending a 1 to the Euclidean representation to obtain $\mathbf{p} = [p_x \quad p_y \quad p_z \quad 1]^T$.

The function $b_{\text{tran}}(\cdot, \cdot, \cdot)$ is then defined by

$$\begin{bmatrix} \mathbf{p}_d \\ 1 \end{bmatrix} = b_{\text{tran}}(\mathbf{f}_s, \mathbf{f}_d, \mathbf{p}_s) = \mathbf{A}_{f_d}^{-1} \mathbf{A}_{f_s} \begin{bmatrix} \mathbf{p}_s \\ 1 \end{bmatrix},\tag{A.9}$$

where \mathbf{A}_{f_d} and \mathbf{A}_{f_s} are the matrix representations of f_d and f_s derived analogously to Eq. (A.8).

B Evaluation of Positioning Systems

In order to verify the performance of a positioning system in a certain scenario, a ground truth obtained by a high-precision reference system is indispensable. One of the main requirements for a reference system is to feature an accuracy at least 10 times better than the tested system.

B.1 3D Position

The survey instrument used throughout this work as a 3D position reference is a total station TS30 from Leica Geosystems featuring mm-range accuracy [171]. The total station is usually mounted on a static tripod and needs to be manually aligned to gravity. A built-in dual-axis inclination sensor is used to correct for any errors in the instrument inclination. This ensures that the measured points will be provided in a coordinate system, which is aligned to gravity. A direct drive based on the converse piezoelectric effect in a ceramic material is used to precisely rotate the alidade and telescope of the device [171]. This enables the device to autonomously track a target or to be remotely controlled via an interface.

The 3D measurement comprises 1D ranging combined with a 2D angle measurement. The angle measurement is based on static line-coded glass circles at the alidade and the telescope which are read by a linear CCD array. As the code used is absolute, no device initialization procedure is necessary [171]. The 1D ranging is based on electronic distance measurement (EDM) using a modulated IR or visible-light signal. Some surveying systems use TOF measurements of laser pulses to determine the distance to the target. Others evaluate the phase difference between the emitted and received signal. In order to resolve the phase ambiguity, several measurements with different modulation frequencies are performed and the results are combined to obtain an accurate estimate at a long range [172] (similar to frequency-stepped continuous wave (FSCW) radar). Since the TOF measurement principle is better for long range measurements and the phase difference offers superior accuracy, Leica combines both in its PinPoint EDM technology [173]. 4 to 10 modulation frequencies in the range of 100 MHz are used. In order to enable high accuracy measurements, a calibration of some system parameters is necessary. This is done periodically (every several minutes) by switching the measurement laser beam to an internal reference light

path [173]. The total station Leica TS30 is also capable of measuring to a prism, a reflector or reflectorless. Prism tracking is also supported. The parameters of the instrument relevant to this work are summarized in Table B.1.

Although the TS30 is a very accurate and reliable device, it is important to understand and pay attention to its limitations. When used as a reference in calibration procedures its accuracy might turn out to be insufficient and cause additional errors. When tracking a moving target (e.g. prism on a mobile robot), it can easily lose it and require manual re-initialization if the LOS to the prism is blocked for example by a passing person or if the target moves too closely to the total station which would require angular velocities beyond the capability of the instrument. Furthermore, during the internal calibration procedure mentioned in the previous paragraph, the device does not provide any tracking data, which causes short interruptions in the reference data stream.

Table B.1: System parameters of total station Leica TS30 [174].

Parameter	Value
Angle accuracy (horizontal / vertical)	$0.5''$ (1.4×10^{-4})
Range accuracy (prism)	0.6 mm
Range accuracy (reflector)	1 mm
Range accuracy (reflectorless)	2 mm
Range accuracy (prism tracking)	3 mm
Tracking measurement rate	≈ 3 Hz

B.2 3D Orientation

Because the 3D orientation is also estimated by the systems developed in this work, a reference was required as well. Unfortunately, the total station could not be used, as it is incapable of simultaneously measuring the position of more than 1 point. Tracking multiple points on the target also has the disadvantage that when the target is far away, the orientation accuracy would deteriorate due to DOP.

One possible alternative which also supports 3D orientation measurements is the OptiTrack system mentioned in Section 1.1. However, it requires to install and calibrate a number of cameras to cover a certain test volume and has very high cost. This makes it unsuitable for on-site measurement campaigns.

An alternative camera-based solution was devised in this work. It consists of a low-cost camera mounted on the target (in this case the robot). A number of LEDs, which can be turned on or off via a radio link, are distributed across the test site at known coordinates. The LEDs are turned on sequentially (in time division multiplexing (TDM)) and the video sequence captured by the camera

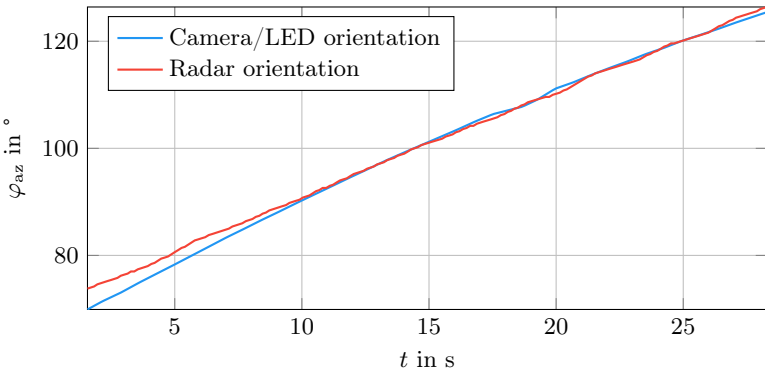


Fig. B.1: Mobile robot orientation measurement.

is processed using the computer vision library OpenCV [175]. After calibrating the intrinsic camera parameters, the azimuth and elevation angles to the LED can be estimated using the pinhole camera model [175]. As the camera's 3D position is tracked by the total station, two measurements to the static LEDs are sufficient to determine the 3D orientation of the camera and hence of the mobile robot. Unfortunately, the system development was started too late during this work. A very promising accuracy of 0.1° could be demonstrated with a low-cost webcam. Because the angle-measuring device is on the target, the DOP should also remain good at larger distances.

A test run was performed with the camera-based orientation reference system and the 16-channel ring array from Fig. 2.16 (c). Both systems were mounted on the mobile robot which was rotated around its axis and measured its orientation relative to a static LED and a static radar node. The result shown in Fig. B.1 demonstrates the feasibility of simultaneous 3D position and orientation estimation. The resulting radar heading RMSE was 1.32° .

B.3 Quantifying Positioning Quality

Describing the positioning quality of a given localization system is important in order to obtain an estimate for the expected performance. This is important for the design of higher levels of functionality, such as navigation, which rely on the localization. It also allows to compare the performance of different positioning systems and concepts.

At least two terms are commonly used to describe the localization quality and

system performance – “precision” and “accuracy”. While they are frequently used interchangeably, they carry different notions as defined by ISO 5725 [176].

The general definition of precision coincides with that of standard deviation (STD) and describes how close consecutive measurements are to each other in a static situation, i.e. how reproducible the result is. The measurement can be described by the random variable X having a stochastic component described by the precision σ and a mean $\bar{x} = E\{X\}$:

$$\sigma = \sqrt{E\{(X - E\{X\})^2\}}. \quad (\text{B.1})$$

When only N samples are available, the estimates for the precision $\hat{\sigma}$ (sample standard deviation) and the mean \hat{x} are

$$\hat{\sigma} = \sqrt{\frac{1}{N-1} \sum_{n=1}^N (x_n - \hat{x})^2}, \hat{x} = \frac{1}{N} \sum_{n=1}^N x_n. \quad (\text{B.2})$$

The term $N-1$ in the denominator makes sure that the estimator $\hat{\sigma}$ is unbiased for a finite number of samples N . No knowledge about the true value of the measurement is required to calculate the precision.

The trueness x_Δ of the measurement can be calculated only if the true value x_0 is known:

$$x_\Delta = x_0 - E\{X\}. \quad (\text{B.3})$$

When only N samples are available, the estimate for the trueness \hat{x}_Δ is

$$\hat{x}_\Delta = x_0 - \hat{x}. \quad (\text{B.4})$$

The trueness thus describes the bias (systematic error) of the measurement.

The accuracy (measurement uncertainty) describes both the stochastic and the systematic error. There are several metrics commonly used to describe it assuming N measurements with the true values $x_{0,n}$. The most straight-forward metric is the mean absolute error (MAE):

$$e_{\text{MAE}} = \frac{1}{N} \sum_{n=1}^N |x_n - x_{0,n}|. \quad (\text{B.5})$$

It describes the average absolute error of N measurements. The MAE was used by the organizers in Section 6.1 to compare the participating systems.

Another accuracy metric frequently used throughout this work is the root-

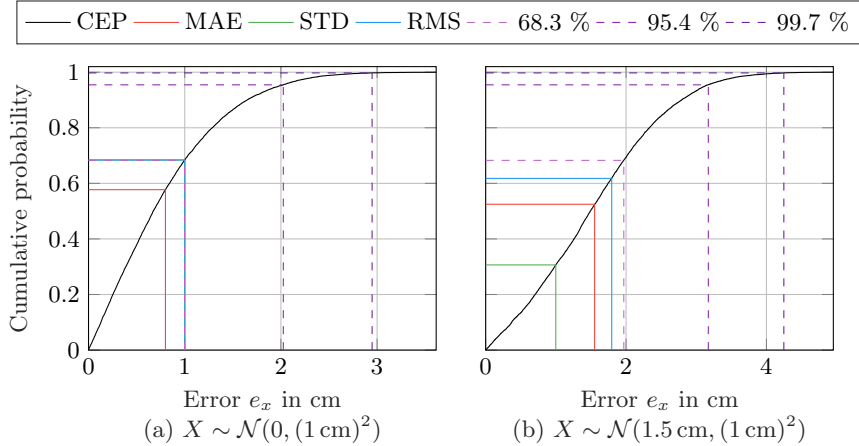


Fig. B.2: Cumulative error probability and error metrics for a bias-free Gaussian distribution with standard deviation of 1 cm (a) and the same distribution with a bias of 1.5 cm (b).

mean-square error (RMSE):

$$e_{\text{RMSE}} = \sqrt{\frac{1}{N} \sum_{n=1}^N (x_n - x_{0,n})^2}. \quad (\text{B.6})$$

As can be seen, the equation for the RMSE is very similar to both the standard deviation and the MAE. When the trueness is $\hat{x}_\Delta = 0$ (i.e. the measurement is bias-free), we have $e_{\text{RMSE}} = \hat{\sigma}$. Compared to the MAE, the RMSE weights large error stronger and is thus a more “pessimistic” metric.

The third and most objective accuracy metric which is used throughout this work is the cumulative error probability distribution (CEPD). It is defined as the relative number of measurements having an error lower than a certain threshold:

$$e_{\text{CEPD}}(e) = \frac{1}{N} \cdot \#(n \mid |x_n - x_{0,n}| < e), \quad (\text{B.7})$$

with the function $\#(n \mid C)$ which gives the number n of elements in a set fulfilling a certain condition C . It gives a more complete and general overview of the obtained error distribution and allows for different interpretations. Commonly, the error below which 68.27%, 95.45 %, and 99.74 % of the measurement sam-

ples lie are indicated, as these correspond to 1, 2, and 3 standard deviations, respectively (assuming the error has a Gaussian distribution).

The cumulative error probability and the other metrics of two error distributions are illustrated in Fig. B.2. While both distributions are Gaussian and have the same statistical component, the one shown in (a) is bias-free and the one in (b) has a bias of 1.5 cm. As can be seen from the equations in this section, when the measurement is bias-free, STD and RMS coincide. Additionally, if the error distribution is Gaussian, the 68.27 %-mark coincides with STD and RMS. This can be seen in Fig. B.2 (a), where we have $\text{STD} = \text{RMS} = e_{68.27\%} = 1 \text{ cm}$. This is not the case in (b), where $\text{STD} = 1 \text{ cm}$ is still valid, but RMS is larger, as it also describes the bias. This also applies for MAE.

B.4 CRLB and DOP

As shown e.g. in [177], the 3D position estimation covariance matrix Σ is in general given by

$$\Sigma = (\mathbf{G}^T \mathbf{Q}^{-1} \mathbf{G})^{-1}, \quad (\text{B.8})$$

where the matrix \mathbf{G} contains information about the problem geometry and \mathbf{Q} about the sensor measurement variance. As shown in Section 2.5.2, this definition coincides with the definition of the CRLB.

When the problem of position finding based on multilateration or multianulation is concerned, the measurement covariance is the scaled identity matrix $\mathbf{Q} = \mathbf{I}\sigma^2$, where σ^2 describes the standard deviation of the distance, resp. angle measurement. In this case Eq. (B.8) simplifies to

$$\Sigma = (\mathbf{G}^T \mathbf{G})^{-1} \sigma^2. \quad (\text{B.9})$$

Hence, the influence of the geometry $(\mathbf{G}^T \mathbf{G})^{-1}$ and of the sensor precision σ^2 can be separated. The position dilution of precision (PDOP) is then defined as

$$\text{PDOP} = \frac{\sqrt{\text{Tr}\{\Sigma\}}}{\sigma}. \quad (\text{B.10})$$

The XDOP, YDOP, ZDOP (=VDOP, vertical DOP), HDOP (horizontal DOP) are defined similarly. The advantage of this representation is that a metric is obtained, which is only dependent on the problem geometry and not on the sensor performance.

Unfortunately, for the combination of RTOF and DOA treated in this work, the covariance matrix \mathbf{Q} is diagonal, but not a scaled identity matrix as the variances of the range, azimuth, and elevation measurements are different (and even have different units). Hence, the simplification from Eq. (B.9) is not pos-

sible and no representation which is dependent only on the geometry can be obtained. Therefore, the CRLB is used to describe the error dependence on geometry for a given set of sensor parameters in this work.

List of Student Theses Supervised

- M. Müller, "Erprobung, Erweiterung und Verifizierung effizienter Algorithmen zur 2D-Winkelschätzung in Echtzeit mithilfe eines SIMO-Sekundärradar," Bachelorarbeit, 2015.
- C. Geitner, "Erprobung von Algorithmen zur Schritterkennung mithilfe von Inertialsensorik zur Stützung der Ortung eines tragbaren Transponders," Forschungspraktikum, 2015.
- C. Seidel, "Extension and test of an algorithm for distributed localisation in a positioning network using distance and angle measurement values," Bachelorarbeit, 2015.
- S. Kahrs, "Untersuchung und Kalibration ausgedünnter Antennenarrays," Forschungspraktikum, 2016.
- Y. Nie, "Untersuchung und effiziente FPGA-Implementierung hochauflösender Algorithmen zur Winkelschätzung mittels eines FMCW-Sekundärradar," Masterarbeit, 2016.
- K. Zhang, "Analyse hochauflösender Algorithmen zur Abstandsschätzung und Erweiterung einer FPGA-Implementierung zur Winkelschätzung für ein FMCW-Sekundärradar," Masterarbeit, 2016.
- T. Weidner, "Untersuchung des Algorithmus SAGE zur Abschätzung der Mehrwegeausbreitung," Forschungspraktikum, 2016.
- N. Winter, "Entwicklung eines Orientierungsreferenzsystems basierend auf Bildverarbeitung," Bachelorarbeit, 2016.
- S. Kahrs, "Untersuchung verschiedener Einflussgrößen auf die Genauigkeit der Winkelschätzung mittels eines FMCW Sekundärradar," Masterarbeit, 2016.
- J. Geiß, "Sensorfusion von Sekundärradar- und Inertialsensorikdaten zur Ortung eines tragbaren Transponders relativ zu einem mobilen Roboter," Masterarbeit, 2017.

Bibliography

- [1] P. Gao, H.-W. Kaas, D. Mohr, and D. Wee, “Automotive Revolution & Perspective Towards 2030,” *Auto Tech Rev.*, vol. 5, no. 4, pp. 20–25, Apr. 2016.
- [2] IFR, “Executive Summary WR Service Robots 2017,” IFR, Tech. Rep., 2017.
- [3] M. Heutger, “Self-Driving Vehicles in Logistics,” DHL, Tech. Rep., 2014.
- [4] G. Blewitt, “Basics of the GPS Technique : Observation Equations,” *Geod. Appl. GPS*, pp. 1–46, 1997.
- [5] I. Skog and P. Handel, “In-Car Positioning and Navigation Technologies - A Survey,” *IEEE Trans. Intell. Transp. Syst.*, vol. 10, no. 1, pp. 4–21, Mar. 2009.
- [6] P. Henkel and M. Iafrancesco, “Tightly coupled position and attitude determination with two low-cost GNSS receivers,” in *2014 11th Int. Symp. Wirel. Commun. Syst.* IEEE, Aug. 2014, pp. 895–900.
- [7] R. Mautz, “Combination of Indoor and Outdoor Positioning,” in *1st Int. Conf. Mach. Control Guid.*, 2008, pp. 79–87.
- [8] A. Harter, A. Hopper, P. Steggles, A. Ward, and P. Webster, “The anatomy of a context-aware application,” *Wirel. Networks*, vol. 8, no. 2-3, pp. 187–197, 2002.
- [9] N. B. Priyantha, “The Cricket Indoor Location System,” Ph.D. dissertation, Dept. Elect. Eng. and Comp. Sci., MIT, 2005.
- [10] A. Vladišauskas and L. Jakevičius, “Absorbtion of ultrasonic waves in air,” *Ultragarsas*, vol. 50, no. 1, pp. 46–49, 2004.
- [11] D. Ruiz, E. Garcia, J. Urena, D. De Diego, D. Gualda, and J. C. Garcia, “Extensive Ultrasonic Local Positioning System for navigating with mobile robots,” *2013 10th Work. Positioning, Navig. Commun. WPNC 2013 - Proc.*, pp. 0–5, 2013.

- [12] M. Hazas and A. Hopper, "Broadband Ultrasonic Location Systems for Improved Indoor Positioning," *IEEE Trans. Mob. Comput.*, vol. 5, no. 5, pp. 536–547, 2006.
- [13] G. N. DeSouza and A. C. Kak, "Vision for mobile robot navigation: A survey," *IEEE Trans. Pattern Anal. Mach. Intell.*, vol. 24, no. 2, pp. 237–267, 2002.
- [14] R. Mautz and S. Tilch, "Survey of optical indoor positioning systems," in *2011 Int. Conf. Indoor Position. Indoor Navig. IPIN 2011*. IEEE, Sep. 2011, pp. 1–7.
- [15] Y. Nakazato, M. Kanbara, and N. Yokoya, "Localization system for large indoor environments using invisible markers," in *Proc. 2008 ACM Symp. Virtual Real. Softw. Technol.*, 2008, pp. 295–296.
- [16] R. Mautz, "Indoor Positioning Technologies," Ph.D. dissertation, ETH Zurich, 2012.
- [17] OptiTrack, "OptiTrack - General FAQs," 2017. [Online]. Available: <http://optitrack.com/support/faq/general.html> [Accessed 2017-03-12].
- [18] Microsoft, "Kinect - Windows app development," 2017. [Online]. Available: <https://developer.microsoft.com/en-us/windows/kinect> [Accessed 2017-03-12].
- [19] Infineon, "Smallest 3D camera worldwide brings Augmented Reality to a smartphone - Infineon Technologies," 2016. [Online]. Available: <https://www.infineon.com/cms/en/about-infineon/press/press-releases/2016/INFXX201606-064.html> [Accessed 2017-03-12].
- [20] SICK AG, "SICK Germany," 2016. [Online]. Available: <https://sick.com>
- [21] Velodyne, "Velodyne LiDAR," 2017. [Online]. Available: <http://velodynelidar.com/> [Accessed 2017-03-12].
- [22] C. Ye and J. Borenstein, "Characterization of a 2 - D Laser Scanner for Mobile Robot Obstacle Negotiation," *Proc. 2002 IEEE Int. Conf. Robot. Autom.*, no. May, pp. 2512–2518, 2002.
- [23] D. Fox, W. Burgard, F. Dellaert, and S. Thrun, "Monte Carlo Localization: Efficient Position Estimation for Mobile Robots," *Aaai-99*, no. Handschin 1970, pp. 343–349, 1999.

- [24] ROS, “amcl - ROS Wiki,” 2017. [Online]. Available: <http://wiki.ros.org/amcl> [Accessed 2017-03-12].
- [25] T. Stoyanov, R. Mojtabahedzadeh, H. Andreasson, and A. J. Lilienthal, “Comparative evaluation of range sensor accuracy for indoor mobile robotics and automated logistics applications,” *Rob. Auton. Syst.*, vol. 61, pp. 1094–1105, 2013.
- [26] J. Hightower, G. Borriello, and R. Want, “SpotON: An indoor 3D location sensing technology based on RF signal strength,” *Uw Cse*, p. 16, 2000.
- [27] P. B. Padmanabhan and V. N., “RADAR: An in-building RF based user location and tracking system,” *Proc. IEEE INFOCOM 2000. Conf. Comput. Commun. Ninet. Annu. Jt. Conf. IEEE Comput. Commun. Soc. (Cat. No.00CH37064)*, vol. 2, no. c, pp. 775–784, 2000.
- [28] J. Hightower and G. Borriello, “Location systems for ubiquitous computing,” *IEEE Comput.*, vol. 34, no. 8, pp. 57–66, 2001.
- [29] M. Vossiek, L. Wiebking, P. Gulden, J. Wieghardt, C. Hoffmann, and P. Heide, “Wireless local positioning,” *IEEE Microw. Mag.*, vol. 4, no. 4, pp. 77–86, Dec. 2003.
- [30] S. Goswami, “Some Real-World Indoor Location Systems,” in *Indoor Locat. Technol.* New York, NY: Springer New York, 2013, pp. 83–104.
- [31] J. Sachs, *Handbook of Ultra-Wideband Short-Range Sensing: Theory, Sensors, Applications.* Weinheim, Germany: Wiley-VCH Verlag GmbH & Co. KGaA, Nov. 2012.
- [32] Zebra, “Zebra Technologies | Transparenz und Datenerfassung in Unternehmen,” 2017. [Online]. Available: <https://www.zebra.com/de/de.html> [Accessed 2017-03-12].
- [33] M. Mahfouz, M. Kuhn, and G. To, “The Future of Ultra Wideband Systems in Medicine: Orthopedic Surgical Navigation,” in *Nov. Appl. UWB Technol.* InTech, Aug. 2011.
- [34] Time Domain, “Time Domain,” 2017. [Online]. Available: <https://timedomain.com/> [Accessed 2017-03-12].
- [35] A. Petroff, R. Reinhardt, R. Stanley, and B. Beeler, “PulsON P200 UWB radio: simulation and performance results,” in *IEEE Conf. Ultra Wideband Syst. Technol. 2003.* IEEE, 2003, pp. 344–348.

- [36] Ubisense, “Location Intelligence Solutions and Software Platforms | Ubisense,” 2017. [Online]. Available: <https://ubisense.net/en> [Accessed 2017-03-12].
- [37] P. Steggles and S. Gschwind, “The Ubisense smart space platform,” in *Adjunct. Proc. Third Int. Conf. Pervasive Comput.*, 2005, pp. 73–76.
- [38] C. Rörig, “Lokalisierungsverfahren für drahtlose Sensornetzwerke,” in *Wirel. Commun. Inf. – Radio Eng. Multimed. Appl.*, J. Sieck and M. Herzog, Eds. Verlag Werner Hülsbusch, 2009, pp. 81–97.
- [39] DecaWave, “Indoor Positioning Systems (IPS) - RTLS Solutions | DecaWave,” 2017. [Online]. Available: <https://www.decawave.com/> [Accessed 2017-03-12].
- [40] M. Malajner, P. Planinsic, and D. Gleich, “UWB ranging accuracy,” in *2015 Int. Conf. Syst. Signals Image Process.*, vol. 15. IEEE, Sep. 2015, pp. 61–64.
- [41] C. Rizos, “Locata : A Positioning System for Indoor and Outdoor Applications Where GNSS Does Not Work,” *Proc. 18th Assoc. Public Auth. Surv. Conf.*, no. March, pp. 73–83, 2013.
- [42] Abatec Group AG, “abatec group AG,” 2017. [Online]. Available: <https://www.abatec-ag.com/> [Accessed 2017-03-12].
- [43] A. Stelzer, “Concept and application of LPM-a novel 3-D local position measurement system,” *IEEE Trans. Microw. Theory Tech.*, vol. 52, no. 12, pp. 2664–2669, 2004.
- [44] Symeo GmbH, “Symeo GmbH - Absolute Positioning,” 2017. [Online]. Available: <https://www.symeo.com> [Accessed 2017-03-12].
- [45] S. Roehr, P. Gulden, D. Shmakov, and I. Bilous, “Wireless local positioning - existing solutions and novel system concepts,” in *2015 IEEE MTT-S Int. Conf. Microwaves Intell. Mobil.* IEEE, Apr. 2015, pp. 1–4.
- [46] Y. Dobrev, M. Vossiek, M. Christmann, I. Bilous, and P. Gulden, “Steady Delivery: Wireless Local Positioning Systems for Tracking and Autonomous Navigation of Transport Vehicles and Mobile Robots,” *IEEE Microw. Mag.*, vol. 18, no. 6, pp. 26–37, Sep. 2017.
- [47] H. Liu, H. Darabi, P. Banerjee, and J. Liu, “Survey of wireless indoor positioning techniques and systems,” *IEEE Trans. Syst. Man Cybern. Part C Appl. Rev.*, vol. 37, no. 6, pp. 1067–1080, 2007.

- [48] D. Dardari, P. Closas, and P. M. Djuric, "Indoor Tracking: Theory, Methods, and Technologies," *IEEE Trans. Veh. Technol.*, vol. 64, no. 4, pp. 1263–1278, Apr. 2015.
- [49] R. Kaune, "Accuracy studies for TDOA and TOA localization," *2012 15th Int. Conf. Inf. Fusion*, pp. 408 –415, 2012.
- [50] A. Norrdine, "An Algebraic Solution to the Multilateration Problem," in *2012 Int. Conf. Indoor Position. Indoor Navig.*, 2012, p. 2012.
- [51] Y. Dobrev, P. Gulden, and M. Vossiek, "An Indoor Positioning System Based on Wireless Range and Angle Measurements Assisted by Multi-Modal Sensor Fusion for Service Robot Applications," *IEEE Access*, pp. 1–17, Nov. 2018.
- [52] A. G. Stove, "Linear FMCW radar techniques," *IEE Proc. F Radar Signal Process.*, vol. 140, no. 2, p. 137, 1993.
- [53] D. Shmakov, R. Ebelt, and M. Vossiek, "Wireless sensor network with 24 GHz local positioning transceiver," in *2012 IEEE/MTT-S Int. Microw. Symp. Dig.*. IEEE, June 2012, pp. 1–3.
- [54] S. Roehr, P. Gulden, and M. Vossiek, "Precise Distance and Velocity Measurement for Real Time Locating in Multipath Environments Using a Frequency-Modulated Continuous-Wave Secondary Radar Approach," *IEEE Trans. Microw. Theory Tech.*, vol. 56, no. 10, pp. 2329–2339, Oct. 2008.
- [55] Y. Dobrev, M. Vossiek, and D. Shmakov, "A Bilateral 24 GHz Wireless Positioning System for 3D Real-Time Localization of People and Mobile Robots," in *2015 IEEE MTT-S Int. Conf. Microwaves Intell. Mobil.*. IEEE, Apr. 2015, pp. 1–4.
- [56] C. Reustle, D. Shmakov, and M. Vossiek, "A 24 GHz SIMO radar tachymeter for precise transponder localization," in *2015 IEEE MTT-S Int. Microw. Symp.*. IEEE, May 2015, pp. 1–4.
- [57] S. M. Kay, *Fundamentals of statistical signal processing : estimation theory*. Prentice-Hall, Inc., 1993.
- [58] S. Scheiblhofer, S. Schuster, M. Jahn, R. Feger, and A. Stelzer, "Performance analysis of cooperative FMCW radar distance measurement systems," in *2008 IEEE MTT-S Int. Microw. Symp. Dig.*, no. 1. IEEE, June 2008, pp. 121–124.

- [59] R. Ebelt, D. Shmakov, and M. Vossiek, "The effect of phase noise on ranging uncertainty in FMCW secondary radar-based local positioning systems," *Radar Conf.*, pp. 258–261, 2012.
- [60] S. Lanzisera and K. S. J. Pister, "Burst mode two-way ranging with cramer-rao bound noise performance," in *GLOBECOM - IEEE Glob. Telecommun. Conf.*, 2008, pp. 859–863.
- [61] D. Rife and R. Boorstyn, "Single tone parameter estimation from discrete-time observations," *IEEE Trans. Inf. Theory*, vol. 20, no. 5, pp. 591–598, Sep. 1974.
- [62] S. Schuster, S. Scheiblhofer, and A. Stelzer, "The influence of windowing on bias and variance of DFT-based frequency and phase estimation," *IEEE Trans. Instrum. Meas.*, vol. 58, no. 6, pp. 1975–1990, 2009.
- [63] B. Brannon, "Sampled systems and the effects of clock phase noise and jitter," p. 12, 2004. [Online]. Available: <http://qtwork.tudelft.nl/~schouten/linkload/jitter-appnote-andev.pdf>
- [64] A. Nazar, Z. M., and F. A., "Frequency Estimation of Single-Tone Sinusoids Under Additive and Phase Noise," *Int. J. Adv. Comput. Sci. Appl.*, vol. 5, no. 9, pp. 101–106, 2014.
- [65] A. Frischen, J. Hasch, and C. Waldschmidt, "A Cooperative MIMO Radar Network Using Highly Integrated FMCW Radar Sensors," *IEEE Trans. Microw. Theory Tech.*, vol. 65, no. 4, pp. 1355–1366, Apr. 2017.
- [66] A. Barbieri and G. Colavolpe, "On the cramer-rao bound for carrier frequency estimation in the presence of phase noise," *IEEE Trans. Wirel. Commun.*, vol. 6, no. 2, pp. 575–582, Feb. 2007.
- [67] B. Widrow and I. Kollár, *Quantization Noise Roundoff Error in Digital Computation, Signal Processing, Control, and Communications*. Cambridge University Press, 2008.
- [68] K. Thurn, R. Ebelt, and M. Vossiek, "Noise in Homodyne FMCW radar systems and its effects on ranging precision," in *2013 IEEE MTT-S Int. Microw. Symp. Dig.* IEEE, June 2013, pp. 1–3.
- [69] H. Boche and M. Schubert, "On the Narrow-Band Assumption for Array Signal Processing," *AEU - Int. J. Electron. Commun.*, vol. 53, no. 2, pp. 117–120, 1999.

- [70] C. Gentner, B. Ma, M. Ulmschneider, T. Jost, and A. Dammann, “Simultaneous Localization and Mapping in Multipath Environments,” in *2016 IEEE/ION Position, Locat. Navig. Symp.* IEEE, Apr. 2016, pp. 807–815.
- [71] Q. Wang, B. AI, K. Guan, Y. Li, and Z. Zhong, “Ray-based analysis of small-scale fading for indoor corridor scenarios at 15 GHz,” in *2015 Asia-Pacific Int. Symp. Electromagn. Compat. APEMC 2015*, 2015, pp. 181–184.
- [72] G. Li, D. Arnitz, R. Ebelt, U. Muehlmann, K. Witrisal, and M. Vossiek, “Bandwidth dependence of CW ranging to UHF RFID tags in severe multipath environments,” *2011 IEEE Int. Conf. RFID*, pp. 19–25, Apr. 2011.
- [73] A. Saleh and R. Valenzuela, “A Statistical Model for Indoor Multipath Propagation,” *IEEE J. Sel. Areas Commun.*, vol. 5, no. 2, pp. 128–137, Feb. 1987.
- [74] A. F. Molisch, D. Cassioli, C. C. Chong, S. Emami, A. Fort, B. Kannan, J. Karedal, J. Kunisch, H. G. Schantz, K. Siwiak, and M. Z. Win, “A comprehensive standardized model for ultrawideband propagation channels,” *IEEE Trans. Antennas Propag.*, vol. 54, no. 11, pp. 3151–3166, Nov. 2006.
- [75] T. Pavlenko, C. Reustle, Y. Dobrev, M. Gottinger, L. Jassoume, and M. Vossiek, “Design and Optimization of Sparse Planar Antenna Arrays for Wireless 3D Local Positioning Systems,” *IEEE Trans. Antennas Propag.*, pp. 7288–7297, 2017.
- [76] Z. Chen, G. Gokeda, and Y. Yu, *Introduction to Direction-of-Arrival Estimation*. Norwood, MA: Artech House, 2010.
- [77] J. Vijn, “Another fast fixed-point sine approximation,” 2009. [Online]. Available: <http://www.coranac.com/2009/07/sines/> [Accessed 2018-02-18].
- [78] S. Boyd and L. Vandenberghe, *Convex Optimization*. Cambridge University Press, 2004.
- [79] S. Gratton, A. S. Lawless, and N. K. Nichols, “Approximate Gauss–Newton Methods for Nonlinear Least Squares Problems,” *SIAM J. Optim.*, vol. 18, no. 1, pp. 106–132, Jan. 2007.

- [80] M. Schütz and M. Vossiek, “A Robust Real-Time Demodulation Scheme for Backscatter Transponder Based Wireless Positioning Systems - to be published,” in *Proc. GeMiC 2018 - 11th Ger. Microw. Conf. (GeMiC 2018)*, Freiburg, Germany, 2018, pp. 1–4.
- [81] A. Mirkin and L. Sibul, “Cramer-Rao bounds on angle estimation with a two-dimensional array,” *IEEE Trans. Signal Process.*, vol. 39, no. 2, pp. 515–517, 1991.
- [82] R. Nielsen, “Azimuth and elevation angle estimation with a three-dimensional array,” *IEEE J. Ocean. Eng.*, vol. 19, no. 1, pp. 84–86, 1994.
- [83] L. Kühnke, “Realisierung und Kalibrierung aktiver Antennensysteme mit digitaler Strahlformung,” Ph.D. dissertation, Universität Hannover, 2001.
- [84] D. Zankl, S. Schuster, R. Feger, A. Stelzer, S. Scheiblhofer, C. M. Schmid, G. Ossberger, L. Stegfellner, G. Lengauer, C. Feilmayr, B. Lackner, and T. Burgler, “BLASTDAR—A Large Radar Sensor Array System for Blast Furnace Burden Surface Imaging,” *IEEE Sens. J.*, vol. 15, no. 10, pp. 5893–5909, Oct. 2015.
- [85] M. Lanne, A. Lundgren, and M. Viberg, “Calibrating an array with scan dependent errors using a sparse grid,” *Signals, Syst. . .*, pp. 2242–2246, 2006.
- [86] J. Pierre and M. Kaveh, “Experimental performance of calibration and direction-finding algorithms,” in [*Proceedings*] ICASSP 91 1991 Int. Conf. Acoust. Speech, Signal Process. IEEE, 1991, pp. 1365–1368 vol.2.
- [87] C. M. Schmid, C. Pfeffer, R. Feger, and A. Stelzer, “An FMCW MIMO radar calibration and mutual coupling compensation approach,” in *Radar Conf. (EuRAD), 2013 Eur.*, 2013, pp. 13–16.
- [88] G. Strang, *Linear Algebra and Its Applications*. Brooks/Cole, 2005.
- [89] Boon Chong Ng and Chong Meng Samson See, “Sensor-array calibration using a maximum-likelihood approach,” *IEEE Trans. Antennas Propag.*, vol. 44, no. 6, pp. 827–835, June 1996.
- [90] M. Moebus, H. Degenhardt, and A. Zoubir, “Local array calibration using parametric modeling of position errors and a sparse calibration grid,” in *2009 IEEE/SP 15th Work. Stat. Signal Process.*, no. 1. IEEE, Aug. 2009, pp. 453–456.

- [91] C. M. Schmid, S. Schuster, R. Feger, and A. Stelzer, "On the Effects of Calibration Errors and Mutual Coupling on the Beam Pattern of an Antenna Array," *IEEE Trans. Antennas Propag.*, vol. 61, no. 8, pp. 4063–4072, Aug. 2013.
- [92] A. Kumar, A. D. Sarma, E. Ansari, and K. Yedukondalu, "Improved Phase Center Estimation for GNSS Patch Antenna," *Antennas Propagation, IEEE Trans.*, vol. 61, no. 4, pp. 1909–1915, 2013.
- [93] G. Bartels, *GPS-Antenna Phase Center Measurements Performed in an Anechoic Chamber*. Delft University Press, 1997.
- [94] S. M. Sherman, *Monopulse principles and techniques*. Boston: Artech House, 2011.
- [95] W. Kederer and J. Detlefsen, "Direction of arrival (DOA) determination based on monopulse concepts," in *2000 Asia-Pacific Microw. Conf. Proc. (Cat. No.00TH8522)*, 2000, pp. 120–123.
- [96] W. Kederer and J. Detlefsen, "Comparison of amplitude-matching and complex monopulse algorithms with respect to SNR," *Aeu-International J. Electron. Commun.*, vol. 57, no. 3, pp. 168–172, 2003.
- [97] S. A. R. Zekavat and R. M. Buehrer, Eds., *Handbook of Position Location*. Hoboken, NJ, USA: John Wiley & Sons, Inc., Sep. 2011.
- [98] P. J. Bevelacqua and C. Balanis, "Antenna Arrays: Performance Limits and Geometry Optimization," Ph.D. dissertation, Arizona State University, 2008.
- [99] P. Bajorski, *Statistics for Imaging, Optics, and Photonics*. Cambridge: Wiley, 2011, vol. 808.
- [100] D. Lerro and Y. Bar-Shalom, "Tracking With Debiased Consistent Converted Measurements Versus EKF," *IEEE Trans. Aerosp. Electron. Syst.*, vol. 29, no. 3, pp. 1015–1022, 1993.
- [101] Mo Longbin, Song Xiaoquan, Zhou Yiyu, Sun Zhong Kang, and Y. Bar-Shalom, "Unbiased converted measurements for tracking," *IEEE Trans. Aerosp. Electron. Syst.*, vol. 34, no. 3, pp. 1023–1027, July 1998.
- [102] Z. Duan, C. Han, and X. R. Li, "Comments on "unbiased converted measurements for tracking"," pp. 1374–1377, 2004.

- [103] W. Mei and Y. Bar-Shalom, "Unbiased Kalman filter using converted measurements: revisit," in *Signal Data Process. Small Targets*, O. E. Drummond and R. D. Teichgraeber, Eds., vol. 7445, no. AUGUST 2009, Aug. 2009, p. 74450U.
- [104] S. Bordonaro, P. Willett, and Y. Bar-Shalom, "Decorrelated unbiased converted measurement Kalman filter," *IEEE Trans. Aerosp. Electron. Syst.*, vol. 50, no. 2, pp. 1431–1444, 2014.
- [105] L. Mailaender, "Comparing Geo-Location Bounds for TOA, TDOA, and Round-Trip Toa," in *2007 IEEE 18th Int. Symp. Pers. Indoor Mob. Radio Commun.* IEEE, Sep. 2007, pp. 1–5.
- [106] X. Lv, K. Liu, and P. Hu, "Geometry influence on GDOP in TOA and AOA positioning systems," *NSWCTC 2010 - 2nd Int. Conf. Networks Secur. Wirel. Commun. Trust. Comput.*, vol. 2, no. 1, pp. 58–61, 2010.
- [107] S. Thrun, W. Burgard, and D. Fox, *Probabilistic robotics*. The MIT Press, 2005.
- [108] F. Martinelli, "Robot localization: comparable performance of EKF and UKF in some interesting indoor settings," in *2008 16th Mediterr. Conf. Control Autom.* IEEE, June 2008, pp. 499–504.
- [109] F. Martinelli, "DubLez," 2010. [Online]. Available: <http://robot2.dsp.uniroma2.it/~fmartine/FiltRob/DubLez.ppt>
- [110] V. Spruyt, "A geometric interpretation of the covariance matrix," 2014. [Online]. Available: http://www.visiondummy.com/2014/04/geometric-interpretation-covariance-matrix/#Eigendecomposition_of_a_covariance_matrix [Accessed 2017-08-21].
- [111] R. Rojas, "The Secret Life of the Covariance Matrix," 2009. [Online]. Available: http://www.inf.fu-berlin.de/inst/ag-ki/rojas_home/documents/tutorials/secretcovariance.pdf
- [112] K. O. Arras, "An Introduction To Error Propagation," Autonomous Systems Lab, Institute of Robotic Systems, Swiss Federal Institute of Technology Lausanne (EPFL), Lausanne, Switzerland, Tech. Rep. September, 1998.
- [113] H. Moradi, K. Kawamura, E. Prassler, G. Muscato, P. Fiorini, T. Sato, and R. Rusu, "Service robotics (the rise and bloom of service robots [tc spotlight])," *IEEE Robot. Autom. Mag.*, vol. 20, no. 3, pp. 22–24, Sep. 2013.

- [114] U. Backes-Gellner, C. Böhringer, U. Cantner, D. Harhoff, I. Ott, and M. Schnitzer, “Gutachten zu Forschung, Innovation und technologischer Leistungsfähigkeit Deutschlands,” Expertenkommission Forschung und Innovation (EFI), Berlin, Germany, Tech. Rep., 2016.
- [115] Henrik I. Christensen, “A Roadmap for U.S. Robotics: From Internet to Robotics,” Robotics - VO, Tech. Rep., 2013.
- [116] H. Christensen, “From Internet to Robotics 2016 Edition,” Robotics - VO, Tech. Rep., 2016.
- [117] E. Poulin, “Benchmarking the hospital logistics process: A potential cure for the ailing health care sector,” *C. Manag.*, vol. 77, no. 1, pp. 20–23, 2003.
- [118] J. Evans, “HelpMate: an autonomous mobile robot courier for hospitals,” in *Proc. IEEE/RSJ Int. Conf. Intell. Robot. Syst.*, vol. 3, no. 203. IEEE, 1994, pp. 1695–1700.
- [119] S. O’Keefe, “A Robot to Help Make the Rounds,” 2003. [Online]. Available: https://spinoff.nasa.gov/spinoff2003/hm_4.html [Accessed 2017-02-06].
- [120] CSS Robotics, “Efficient specimen delivery SpeciMinder™,” 2008. [Online]. Available: http://www.cssrobotics.com/Resources/SpeciMinder_trifold290403.pdf [Accessed 2017-02-06].
- [121] Aethon, “TUG Robots in Healthcare,” 2017. [Online]. Available: <http://www.aethon.com/tug/how-it-works> [Accessed 2017-02-06].
- [122] Swisslog, “TransCar® Automated Guided Vehicle System,” 2016. [Online]. Available: http://www.swisslog.com/-/media/Swisslog/Documents/HCS/TransCar_Automated_Guided_Vehicles/Brochures/AGV-100_AGV_Overview.pdf [Accessed 2017-02-06].
- [123] R. Mautz, “The challenges of indoor environments and specification on some alternative positioning systems,” *Proc. - 6th Work. Positioning, Navig. Commun. WPNC 2009*, vol. 2009, pp. 29–36, 2009.
- [124] L. Mainetti, L. Patrono, and I. Sergi, “A survey on indoor positioning systems,” *2014 22nd Int. Conf. Software, Telecommun. Comput. Networks*, pp. 111–120, 2014.

- [125] D. Schneider, "You are here," *IEEE Spectr.*, vol. 50, no. 12, pp. 34–39, 2013.
- [126] D. Lymberopoulos, J. Liu, X. Yang, R. R. Choudhury, V. Handziski, and S. Sen, "A realistic evaluation and comparison of indoor location technologies," in *Proc. 14th Int. Conf. Inf. Process. Sens. Networks - IPSN '15*, no. Table 1. New York, New York, USA: ACM Press, 2015, pp. 178–189.
- [127] J. Torres-Sospedra, A. Jiménez, S. Knauth, A. Moreira, Y. Beer, T. Fetzer, V.-C. Ta, R. Montoliu, F. Seco, G. Mendoza-Silva, O. Belmonte, A. Koukofikis, M. Nicolau, A. Costa, F. Meneses, F. Ebner, F. Deinzer, D. Vaufreydaz, T.-K. Dao, and E. Castelli, "The Smartphone-Based Offline Indoor Location Competition at IPIN 2016: Analysis and Future Work," *Sensors*, vol. 17, no. 3, p. 557, Mar. 2017.
- [128] R. D'Andrea, "Guest Editorial: A Revolution in the Warehouse: A Retrospective on Kiva Systems and the Grand Challenges Ahead," *IEEE Trans. Autom. Sci. Eng.*, vol. 9, no. 4, pp. 638–639, Oct. 2012.
- [129] N. Nourani-Vatani, "Multi-modal Sensor Fusion," 2017. [Online]. Available: <http://journal.frontiersin.org/researchtopic/5597/multi-modal-sensor-fusion#overview> [Accessed 2017-05-21].
- [130] Y. Dobrev, S. Flores, and M. Vossiek, "Multi-modal sensor fusion for indoor mobile robot pose estimation," in *2016 IEEE/ION Position, Locat. Navig. Symp.* IEEE, Apr. 2016, pp. 553–556.
- [131] S. Flores and M. Vossiek, "A Robust Air Coupled Ultrasonic Piezoelectric-Carbon Fiber Reinforced Polymer (CFRP) Sensor for Mobile Robot Navigation," in *Proc. Int. Ultrason. Symp.*, Chicago, 2014, pp. 858–861.
- [132] J. Traa, "Least-Squares Intersection of Lines," 2013.
- [133] R. De Maesschalck, D. Jouan-Rimbaud, and D. Massart, "The Mahalanobis distance," *Chemom. Intell. Lab. Syst.*, vol. 50, no. 1, pp. 1–18, Jan. 2000.
- [134] H. Durrant-Whyte, D. Pagac, and B. Rogers, "An Autonomous Straddle Carrier for Movement of Shipping Containers," *IEEE Robot. Autom. Mag.*, vol. 14, no. 3, pp. 1–1, 2007.
- [135] Y. Bar-Shalom, X. R. Li, and T. Kirubarajan, *Estimation with Applications to Tracking and Navigation*. Wiley Interscience, 2001.

- [136] C. Schlegel, “Service Robotics Ulm,” 2017. [Online]. Available: <http://www.servicerobotik-ulm.de> [Accessed 2017-11-25].
- [137] Open Source Robotics Foundation, “ROS.org | Powering the world’s robots,” 2017. [Online]. Available: <http://www.ros.org/>
- [138] Y. Bar-Shalom, “Update with out-of-sequence measurements in tracking: exact solution,” *IEEE Trans. Aerosp. Electron. Syst.*, vol. 38, no. 3, pp. 769–777, July 2002.
- [139] Festo, “Robotino® - Services - Festo Didactic,” 2017. [Online]. Available: <http://www.festo-didactic.com/int-en/services/robotino/> [Accessed 2017-11-25].
- [140] L. Omron Adept MobileRobots, “MobileRobots Robot Platforms: Programmable Mobile Robots for Research, Engineering and Education,” 2017. [Online]. Available: <http://www.mobilerobots.com/ResearchRobots.aspx> [Accessed 2017-11-25].
- [141] F. Cordes, C. Oekermann, A. Babu, D. Kuehn, T. Stark, and F. Kirchner, “An Active Suspension System for a Planetary Rover,” *iSAIRAS*, 2014.
- [142] DFKI GmbH, “Space Exploration Hall - Robotics Innovation Center - DFKI GmbH,” 2017. [Online]. Available: <https://robotik.dfki-bremen.de/en/research/research-facilities/space-exploration-hall.html> [Accessed 2018-03-03].
- [143] Y. Dobrev, C. Reustle, T. Pavlenko, F. Cordes, and M. Vossiek, “Mobile robot 6D pose estimation using a wireless localization network,” in *2016 IEEE MTT-S Int. Conf. Microwaves Intell. Mobil.* IEEE, May 2016, pp. 1–4.
- [144] M. Powell, T. Crockett, J. Fox, J. Joswig, J. Norris, and K. Rabe, “Targeting and Localization for Mars Rover Operations,” in *2006 IEEE Int. Conf. Inf. Reuse & Integr.* IEEE, Sep. 2006, pp. 23–27.
- [145] H. Flämig, “Autonomous Vehicles and Autonomous Driving in Freight Transport,” in *Auton. Driv.* Berlin, Heidelberg: Springer Berlin Heidelberg, 2016, pp. 365–385.
- [146] Proxaut SRL – Italy, “AGV Autonomous Guided Vehicles – Industrial warehousing logistics machine handling system realization,” 2017. [Online]. Available: <http://www.proxaut.com/agv-autonomous-guided-vehicles-assistance-reparation.html> [Accessed 2018-02-24].

- [147] G. Ullrich, "Effizientes Fulfillment mit Fahrerlosen Transportfahrzeugen," *LOGISTIK für Unternehm.*, vol. 1, no. 4/5, pp. 22–25, 2012.
- [148] SEW EURODRIVE, "Industry 4.0 showcase factory | SEW-EURODRIVE," 2017. [Online]. Available: https://www.sew-eurodrive.de/company/your_success/future_trends/industry-40/basics/showcase_factory/showcase_factory.html [Accessed 2018-02-28].
- [149] L. Schulze, S. Behling, and S. Buhrs, "Automated Guided Vehicle Systems: a driver for increased business performance," *Proc. Int. MultiConference Eng. Comput. Sci.*, vol. II, pp. 19–21, 2008.
- [150] Y. Dobrev, C. Reustle, and M. Vossiek, "Self-organizing 3D Wireless Local Positioning Networks for Robot Swarms," presented in Autonomous Vehicles Workshop at the IEEE MTT-S International Microwave Symposium 2016 (IMS 2016), San Francisco, CA, 2016.
- [151] W. Murphy and W. Hereman, "Determination of a position in three dimensions using trilateration and approximate distances," Master's Thesis, Colorado School of Mines, Golden, Colorado, 1995.
- [152] Q. Quan, "Low Bounds of The GDOP in Absolute-Range based 2-D Wireless Location Systems," in *Inf. Sci. Digit. Content Technol. (ICIDT), 2012 8th Int. Conf.*, 2012, pp. 135–138.
- [153] A. Dempster, "Dilution of precision in angle-of-arrival positioning systems," *Electron. Lett.*, vol. 42, no. 5, p. 291, 2006.
- [154] Y. Zhong, S. C. Huang, and X. Y. Wu, "Geometric dilution of precision for bearing-only passive location in three-dimensional space," *Electron. Lett.*, vol. 51, no. 6, pp. 518–519, Mar. 2015.
- [155] S. Julier and J. Uhlmann, "A non-divergent estimation algorithm in the presence of unknown correlations," in *Proc. 1997 Am. Control Conf. (Cat. No.97CH36041)*, vol. 4. IEEE, 1997, pp. 2369–2373 vol.4.
- [156] H. V. Henderson and S. R. Searle, "On deriving the inverse of a sum of matrices," *Siam Rev.*, vol. 23, no. 1, pp. 53–60, 1981.
- [157] S. M. LaValle, *Planning Algorithms*. New York, NY, USA: Cambridge University Press, 2006.

- [158] Y. Dobrev, D. Shmakov, I. Bilous, T. Pavlenko, C. Reustle, and M. Vossiek, "A Wireless Localization Network for 6D Pose Estimation," pp. 1–2, 2016. [Online]. Available: <https://www.microsoft.com/en-us/research/wp-content/uploads/2015/10/dobrev.pdf> [Accessed 2017-02-06].
- [159] S. Sarkka, V. V. Viikari, M. Huusko, and K. Jaakkola, "Phase-Based UHF RFID Tracking With Nonlinear Kalman Filtering and Smoothing," *IEEE Sens. J.*, vol. 12, no. 5, pp. 904–910, May 2012.
- [160] Microsoft Corporation, "Microsoft Indoor Localization Competition – IPSN 2016 – Microsoft Research," 2016. [Online]. Available: <https://www.microsoft.com/en-us/research/event/microsoft-indoor-localization-competition-ipsn-2016/>
- [161] D. Lymeropoulos and J. Liu, "The Microsoft Indoor Localization Competition: Experiences and Lessons Learned," *IEEE Signal Process. Mag.*, vol. 34, no. 5, pp. 125–140, Sep. 2017.
- [162] J. Holsten, P. Hartmann, M. Schütt, and D. Moormann, "Automatische unbemannte Flüge außerhalb der Sichtweite zwischen zwei Packstationen mit einem Tiltwing-Fluggerät," in *Dtsch. Luft- und Raumfahrtkongress*, Braunschweig, 2016.
- [163] Y. Dobrev, M. Schütt, P. Hartmann, and D. Moormann, "Entwurf und Validierung eines Präzisionslandesystems für unbemannte Tiltwing-Fluggeräte," in *Dtsch. Luft- und Raumfahrtkongress*, Braunschweig, 2016.
- [164] E. Semsch, M. Jakob, D. Pavlicek, and M. Pechoucek, "Autonomous UAV Surveillance in Complex Urban Environments," in *2009 IEEE/WIC/ACM Int. Jt. Conf. Web Intell. Intell. Agent Technol.* IEEE, 2009, pp. 82–85.
- [165] J. H. Ong, A. Sanchez, and J. Williams, "Multi-UAV System for Inventory Automation," in *2007 1st Annu. RFID Eurasia*. IEEE, Sep. 2007, pp. 1–6.
- [166] D. Borio, J. Fortuny Guasch, and C. O'Driscoll, "Spectral and Spatial Characterization of GNSS Jammers," in *7th GNSS Vulnerabilities Solut. Conf.*, Baska, Croatia, 2013.
- [167] P. Pace, "FMCW Radar, Electronic Attack Considerations," in *Detect. Classifying Low Probab. Intercept Radar*, 2nd ed. Boston: Artech House, May 2009.

- [168] Y. Dobrev, Y. Dobrev, P. Gulden, M. Lipka, T. Pavlenko, D. Moormann, and M. Vossiek, “Radar-Based High-Accuracy 3D Localization of UAVs for Landing in GNSS-Denied Environments,” in *2018 IEEE MTT-S Int. Conf. Microwaves Intell. Mobility, ICMIM 2018*, 2018.
- [169] A. Stelzer, M. Jahn, and S. Scheiblhofer, “Precise distance measurement with cooperative FMCW radar units,” in *2008 IEEE Radio Wirel. Symp.* IEEE, Jan. 2008, pp. 771–774.
- [170] F. Martinelli, “A Robot Localization System Combining RSSI and Phase Shift in UHF-RFID Signals,” *IEEE Trans. Control Syst. Technol.*, vol. 23, no. 5, pp. 1782–1796, 2015.
- [171] H.-M. Zogg, W. Lienhart, and D. Nindl, “Leica TS30 The Art of Achieving Highest Accuracy and Performance,” 2009.
- [172] J. M. Rueger, *Electronic Distance Measurement*. Springer-Verlag Berlin Heidelberg, 1990.
- [173] F. Bayoud, “Leica’s pinpoint EDM technology with modified signal processing and novel optomechanical features,” *Proc. 2006 Conf. Int. Fed. Surv.*, pp. 1–16, 2006.
- [174] Leica Geosystems, “Leica TS30 Technical Data,” 2009.
- [175] G. Bradski and A. Kaehler, *Learning OpenCV*. O’Reilly, 2008.
- [176] A. Menditto, M. Patriarca, and B. Magnusson, “Understanding the meaning of accuracy, trueness and precision,” *Accredit. Qual. Assur.*, vol. 12, no. 1, pp. 45–47, Jan. 2007.
- [177] R. B. Langley, “Dilution of Precision,” *GPS World*, vol. 10, no. May, pp. 52–59, 1999.



Yassen Dobrev

Born 1987, Sofia (Bulgaria)
Contact yassen.dobrev@gmail.com
<http://yassen.antday.com>

Work Experience

- since 05/17 Senior engineer imaging radar, Symeo GmbH (since 02/18 part of Analog Devices Inc.), Munich, Germany
07/16-09/16 Intern, flat panel display division, Apple Inc., Cupertino, CA, USA
07/13-03/17 Research assistant, wireless local positioning systems, Institute of Microwaves and Photonics (LHFT), Friedrich-Alexander-University Erlangen-Nürnberg (FAU), Germany
05/11-06/13 Research assistant, display technology, Chair of Microelectronics (LME), Saarland University, Germany
05/09-07/09 Intern, wireless sensors & RF-technology division, Siemens AG, Munich, Germany

Education

- 10/09-02/10 Visiting student, Electronic & Electrical Engineering, The University of Sheffield, UK
09/05-04/11 Dipl.-Ing. Mechatronics (MEMS), Saarland University, Germany

Nürnberg (Germany), April 1, 2018